UNIVERSITY OF EXETER

DOCTORAL THESIS

Microfluidic Elasto-Magnetic Materials For Controlled Swimming And Pumping

---

Elizabeth Lucy Martin

A thesis submitted for the degree of
Doctor of Philosophy in Physics

EPSRC Centre for Doctoral Training in Metamaterials
College of Engineering, Mathematics, and Physical Sciences

May 2021

Declaration

Microfluidic Elasto-Magnetic Materials For Controlled Swimming And Pumping

Submitted by Elizabeth Lucy Martin to the University of Exeter as a thesis for the degree of Doctor of Philosophy in Physics in May 2021.

This thesis is available for Library use on the understanding that it is copyright material and that no quotation from the thesis may be published without proper acknowledgement.

I certify that all material in this thesis which is not my own work has been identified and that no material has previously been submitted and approved for the award of a degree by this or any other University.

I acknowledge financial support from the Engineering and Physical Sciences Research Council (EPSRC) of the United Kingdom, via the EPSRC Centre for Doctoral Training in Metamaterials (Grant No. EP/L015331/1).

(Signature) ....

Abstract

This thesis presents the results from investigating the behavior of different magnetically actuated systems capable of creating motion or activating fluid flow within a low Reynolds number regime. It demonstrates a number of designs where magnetic materials are integrated into elastic networks and the systems are activated by an oscillating magnetic field. The elasto-magnetic systems rely on magnetic and elastic interactions to generate their movement and are designed in such a way as to induce non-reciprocal motion that could be used to manipulate fluid. The thesis demonstrates the capability of these devices and investigates its potential application in microfluidic systems. The presented research is primarily focused on three elasto-magnetic designs.

The first design was based on two interacting ferromagnetic particles with different properties connected by an elastic link. The devices produced were that of a 68 µm microswimmer and a membrane or network spanning 12 mm with feature sizes of the order of micrometers. Ellipsoidal CoNiP (major and minor diameters of 30 µm and 10 µm) and cylindrical Co (diameter 10 µm) particles were produced by electrodeposition. The electrodeposition parameters have been optimised on deposition of CoNiP films to produce an out-plane coercivity for CoNiP elements of 54 kA/m. A fabrication process was created using lithographic techniques to produce a highly structured network of a silicon-based organic polymer, Polydimethylsiloxane (PDMS), embedded with the described magnets. Although this design did not demonstrate active pumping, important conclusions were derived

regarding the improvements required to make it more practically suited.

The second design consisted of a series of magnetic discs connected to a frame via elastic axles. The paddles had the same magnetic properties but different elastic properties, due to the different widths of their connecting axles. These introduced a phase difference in the motion of the paddles when actuated. This phase difference was reminiscent of metachronal waves that commonly exist in cilia carpets. In order to understand this design further, a theoretical model was developed and various parameters were investigated, such as frequency and rotational stiffness of the paddles, which was implicative to the width of the axles. For the dimensionless parameters investigated, the maximum speed was generated when the center-to-center separation was 0.9, the frequency was 1.4, ℓ_{p1} = 0.130 and ℓ_{p2} = 0.225, achieving maximum angles of 45° and 148° respectively.

The third design comprised of only a single ferromagnetic component, which was at the 'head' of the device, connected to an asymmetric 'tail'. This 3-linked 'tail' was inspired by Purcell's 3-link swimmer. The head of the device was actively driven while the elastic links followed. This introduced a phase difference in the generated motion of the device. The 3-linked structure was integrated within a microfluidic device to produce an enclosed pumping system. In this section, the properties of the path drawn by the head during its cycle and the flow rate generated by this device were researched for different fluid viscosities and driving frequencies. It was found that this system could provide a tuneable fluid flow with a flow rate of up to 700 µlh^{-1}. The fluid flow was able to be reversed by adjusting the driving frequency.

Acknowledgements

The research in this thesis, and this thesis itself, would not have been possible without the support and guidance of many of my colleagues, friends and family. Therefore, I would like to take this opportunity to thank several of them.

Firstly, I would like to thank my supervisors, Prof. Feodor Ogrin and Dr. Stefano Pagliara, they have helped shape me into the researcher that I am today. I would also like to extend my gratitude to all the past and present members of the ABIOMATER Team, especially Prof. Andrew D. Gilbert, Dr. Matthew T. Bryan, Peter D. Inzani and Jacob L. Binsley, for all of our collaborations and invaluable discussions.

I would like to thank all of the summer students that I have had the pleasure of working alongside during my studies, Tom Moynihan, Aleksandra Pac and Anna Saracino. I wish Tom and Aleks all the best for their research in their current Ph.D. studies.

Many thanks to the Engineering and Physical Sciences Research Council (EPSRC) of the United Kingdom and the Centre for Doctoral Training (CDT) in Metamaterials (XM^2), including the director, Prof. Alastair Hibbins, and the Programme Manager, Dr. Anja Roeding, of the (XM^2).

I further wish to thank all the past and present members of the Magnetism and Magnetic Materials Research group at the University of Exeter, for their advice, insightful observations and encouragement during my studies. Particularly to

Prof. Volodymyr Kruglyak, Prof. Robert Hicken, Dr. Paul Keatley, Dr. Thomas Loughran, Dr. Natalie Whitehead, Emily Glover and David Newman, for their continued interest in my work.

I would like to express my sincere gratitude for the training, information and guidance provided by the technical and support staff within the Physics department at the University of Exeter, including but not limited to, Mark Heath, Nick Cole, Peter Savage and George Ricketts.

Finally, I would like to thank all of my family and friends for their continued support.

To Ned, Frank, Milo, Ros, Austin and David, I am very grateful to have started my Ph.D. studies alongside all of you and this journey would not have been the same without all of our time spent together over the last few years, in and out of the physics building.

I would also like to thank everyone at St Thomas Baptist Church, Exeter, and at Sardis Baptist Church, Resolven, for all of their support, encouragement and prayers throughout my PhD.

To James, Sam, Suzie, Tom and Stuart, thank you for all of your support, friendship, fun and laughter over the years, as well as all of those useful questions about my research.

Last but not least, I would like to especially thank my loving parents and sister, Rachel, without whom I would not have even applied for this Ph.D. position in the first place.

Contents

List of Figures

List of Tables

List of Symbols

A	Cross-sectional area of a channel.
A_{ext}	Dimensionless external magnetic field parameter.
$\boldsymbol{B}$	Magnetic flux density.
B	Magnitude of magnetic flux density.
b	The time dependant amplitude of the external magnetic field in the paddle system.
$\boldsymbol{B}_a$	The magnetic flux density generated by a magnetic moment ($\boldsymbol{m}_a$) acting on another ($\boldsymbol{m}_b$).
$\boldsymbol{B}_{ext}$	The external magnetic field vector of the paddle system.
B_{ext}	A constant of amplitude of the external magnetic field vector of the paddle system.
$\boldsymbol{B}_k$	The magnetic flux density generated by bead k in the two ferromagnetic particle system.
b_x	The time dependant x directional amplitude of the external magnetic field in the paddle system.
b_y	The time dependant y directional amplitude of the external magnetic field in the paddle system.

c_1	Arbitrary constant of rotational stiffness in the paddle system.
c_2	Arbitrary constant of rotational stiffness in the paddle system.
D	Distance travelled by a swimmer.
D_a	Distance travelled by the *“pushmepullyou”* swimmer.
D_b	Distance travelled by the three linked spheres swimmer.
D_{body}	The number of body-lengths a swimmer has travelled in a period of time.
d_y	The dampening y component of external magnetic field in the paddle system.
E	Electroplating voltage.
E_{ani}	Anisotropy energy due to crystal anisotropy.
E_b	Euler-Bernoulli filament of bending stiffness.
E_{mag}	The magnetostatic energy for each particle in the two ferromagnetic particle system.
$\hat{\boldsymbol{F}}$	Direction of the external force acting on a device/swimmer.
f	Frequency.
$\boldsymbol{F}_{add}$	Additional force term per unit volume.
$\boldsymbol{F}_{bend,i}$	Bending force acting on bead i in the bead triplet ijk in the paddle system.
$\boldsymbol{F}_{bend,j}$	Bending force acting on bead j in the bead triplet ijk in the paddle system.
$\boldsymbol{F}_{bend,k}$	Bending force acting on bead k in the bead triplet ijk in the paddle system.

$\boldsymbol{F}_{dip}$	The force exerted by a magnetic moment on another magnetic moment.
$\boldsymbol{F}_{drag,k}$	Fluidic drag force acting on bead i.
$\boldsymbol{F}_{E}$	Elastic force between the two particles in the two ferromagnetic particle system.
$\boldsymbol{F}_{ext,i}$	Magnetic torque force from the external magnetic field acting on bead i in the paddle system.
$\boldsymbol{F}_{head}$	Viscous drag force of a sperm-like swimmer.
$\boldsymbol{F}_{interact,i}$	Fluidic interactions force from other beads in the fluid acting on bead i in the paddle system.
$\boldsymbol{F}_{m1}$	Magnetic dipole force experienced by the ‘hard’ particle of the two ferromagnetic particle system.
$\boldsymbol{F}_{m2}$	Magnetic dipole force experienced by the ‘soft’ particle of the two ferromagnetic particle system.
$\boldsymbol{F}_{M,j}$	Magnetic force acting on one particle, j, from another, k, in the two ferromagnetic particle system.
$\boldsymbol{F}_{spring,i}$	Spring force acting on bead i in the paddle system.
$\boldsymbol{F}_{\delta}$	Point force.
$\boldsymbol{G}$	General tensor depending on the shape of the body and on the boundary conditions at infinity.
g	Arbitrary function of time.
$\boldsymbol{H}$	External applied magnetic field.
h	Height of a channel.
H_c	Coercive Field.

H_x	Time dependant amplitude of the external magnetic field in the x direction.
H_x^0	Maximum Amplitude of the external magnetic field in the x direction.
H_y	Time dependant amplitude of the external magnetic field in the y direction.
H_y^0	Maximum Amplitude of the external magnetic field in the y direction.
$\mathbf{I}$	Electroplating current.
i	bead indicator.
I_n	Identity matrix.
$\boldsymbol{J}$	Green's function of Stokes flow (Stokeslet).
j	bead indicator.
K	Effective anisotropy field constant of a particles in the two ferromagnetic particle system.
k	bead indicator.
K_0	Magnetocrystalline anisotropy constant of the zero order.
k_0	Typical value of the link spring constant k_{ij} in the paddle system.
K_1	Magnetocrystalline anisotropy constant of the first order.
K_2	Magnetocrystalline anisotropy constant of the second order.
K_h	Effective anisotropy field constant of the 'hard' particle in the two ferromagnetic particle system.
K_i	Magnetocrystalline anisotropy constants.
k_{ij}	Effective spring constant between beads i and j in the paddle system.
K_s	Effective anisotropy field constant of the 'soft' particle in the two ferromagnetic particle system.

k_s	Effective spring constant between the two particles in the two ferromagnetic particle system.
K^V	Uni-axial volume magnetocrystalline anisotropy constant.
L	Characteristic length.
L1	First link of the single-ferromagnetic 3-linked pump.
L2	Second link of the single-ferromagnetic 3-linked pump.
L3	Third link of the single-ferromagnetic 3-linked pump.
L_{arc}	Arclength of the closed width path drawn by the head of the single-ferromagnetic 3-linked pump.
L_b	The body-length of a swimmer.
L_c	Length of a channel.
ℓ_{ijk}	Rotational stiffness of the angle between the bead triplet ijk in the paddle system.
ℓ_p	Rotational stiffnesses of paddles in the paddle system.
ℓ_{p1}	Rotational stiffness of paddle 1 in the paddle system.
ℓ_{p2}	Rotational stiffness of paddle 2 in the paddle system.
$\mathcal{M}$	Characteristic mass.
$\boldsymbol{M}$	Magnetisation.
M	Magnitude of magnetisation vector.
$\boldsymbol{m}$	Magnetic moment.
m_0	Typical magnetic moment magnitude of the beads in the paddle system.
M_1	Magnitude of magnetisation vector of the first particle in the two ferromagnetic particle system.

M_2	Magnitude of magnetisation vector of the second particle in the two ferromagnetic particle system.
m_1	Magnetic moment of the first particle in the two ferromagnetic particle system.
m_2	Magnetic moment of the second particle in the two ferromagnetic particle system.
$\boldsymbol{m}_a$	An arbitrary magnetic moment.
$\boldsymbol{m}_b$	A second arbitrary magnetic moment.
$\boldsymbol{M}_{head}$	Magnetic moment at the head of a sperm-like swimmer.
$\boldsymbol{m}_i$	Magnetic moment of bead i.
m_i	Magnitude of the magnetic moment of bead i in the paddle system.
$\boldsymbol{m}_j$	Magnetic moment of particle j in the two ferromagnetic particle system.
$\boldsymbol{M}_k$	Magnetisation vector of particle k in the two ferromagnetic particle system.
$\boldsymbol{m}_k$	Magnetic moment of particle k in the two ferromagnetic particle system.
M_r	Magnetic remanence.
M_s	Magnetic saturation.
M_x	Magnetisation at a certain applied magnetic field.
N	Number to sum over.
$\hat{\boldsymbol{n}}$	Unit normal direction.
$\boldsymbol{n}$	Outward normal vector.
P	Pressure.
Q	Volumetric flow rate.

$\mathcal{R}$	Dimensionless grand resistance matrix of the magnetic head of a sperm-like swimmer.
R	Average bead radius in the paddle system.
$\boldsymbol{r}$	Position vector.
r	Magnitude of position vector.
r_{0ij}	Initial distance between the beads i and j in the paddle system, representing a relaxed spring.
$\boldsymbol{r}_{b0}$	Initial distance between the particles in the two ferromagnetic particle system, representing a relaxed spring.
$\boldsymbol{r}_{b1}$	Position vector of the first particle in the two ferromagnetic particle system.
$\boldsymbol{r}_{b2}$	Position vector of the second particle in the two ferromagnetic particle system.
Re	Reynolds number.
R_i	Radius of bead i.
R_i	Radius of bead j.
$\boldsymbol{r}_i$	Position vector of bead i.
$\dot{\boldsymbol{r}}_i$	Velocity vector of bead i.
$\ddot{\boldsymbol{r}}_i$	Acceleration vector of bead i.
$\hat{\boldsymbol{r}}_{ij}$	Directional unit vector of the position vector of bead i to bead j in the paddle system.
$\boldsymbol{r}_{ij}$	Position vector of bead i to bead j in the paddle system.
r_{ij}	Distance between bead i and bead j in the paddle system.
$\boldsymbol{r}_j$	Position vector of bead j.

$\dot{\boldsymbol{r}}_j$	Velocity vector of bead j.
r_{jk}	Distance between bead j and bead k in the paddle system.
$\boldsymbol{r}_k$	Position vector of particle k.
r_k	Magnitude of position vector of particle k.
r_{p0}	Typical value of r_{0ij} the distance between beads in the paddle system.
$\boldsymbol{r}_s$	The positions of points on the surface of the swimmer.
$\dot{\boldsymbol{r}}_s$	Swimming gait.
S	Surface.
$S_1 - S_5$	Configurations of Purcell's two hinge swimmer.
$S_a - S_c$	Configurations of Purcell's two hinge swimmer.
S_h	The shape of a swimmer.
S_p	Sperm compliance number.
$\mathcal{T}$	Characteristic time period.
T	Time period of a complete stroke cycle of a swimmer.
t	Time.
t_0	Initial time.
t_1	An arbitrary time after a set number of stroke cycles of a swimmer.
t_a	An arbitrary time after a set number of stroke cycles of a swimmer.
t_f	The time period of a single stroke cycle of a swimmer after t_0.
t_m	Time between t_0 and t_f in the stroke cycle of a swimmer that separates sequence of shapes into the forward and backward.
T_N	A particular time period in terms of the number of cycle time periods that occur.
T_{off}	Time the rest voltage is applied in electrodeposition.

T_{on}	Time the active voltage is applied in electrodeposition.
U	Characteristic flow velocity.
$\boldsymbol{u}$	Velocity.
$\boldsymbol{u}_{f1}$	A velocity field.
$\boldsymbol{u}_{f2}$	A velocity field.
$\boldsymbol{u}_{fh}$	Velocity fields at the head of a sperm-like swimmer.
V	Volume.
$\boldsymbol{v}$	Instantaneous swimming velocity.
$v_{average}$	The average velocity of the flow in a channel.
V_{bend}	Total bending potential in the paddle system.
$V_{bend,ijk}$	The bending potential for in the bead triplet ijk in the paddle system.
V_{ext}	Total potential from the magnetic moment of the beads and the external magnetic field in the paddle system.
$V_{ext,i}$	The potential from the magnetic moment of the bead i and the external magnetic field in the paddle system.
v_{peak}	The peak velocity of the flow in a channel.
V_{spring}	Total elastic potential in the paddle system.
$V_{spring,ij}$	The elastic potential for the link between bead i and bead j in the paddle system.
v_x	The velocity of the flow at a given position in the rectangular channel.
W	Width of the closed width path drawn by the head of the single-ferromagnetic 3-linked pump.
w	Width of a channel.
$\boldsymbol{\mathcal{X}}$	Centre of reaction position vector.

$\dot{\boldsymbol{x}}$	Centre of reaction velocity vector.
X	Centre of reaction position in x direction.
x	Axis direction.
x_i	Position in x direction of bead i.
x_j	Position in x direction of bead j.
x_k	Position in x direction of bead k.
Y	Centre of reaction position in y direction.
y	Axis direction.
y_i	Position in y direction of bead i.
y_j	Position in y direction of bead j.
y_k	Position in y direction of bead k.
z	Axis direction.
α	A constant of the y direction amplitude of the external magnetic field in the paddle system.
α_{0i}	Angle of the easy axis of bead i with respect to link ij in the paddle system.
α_i	Angle of the magnetic moment of bead i with respect to link ij in the paddle system.
α_{p1}	Orientation of the initial magnetic moment of paddle 1 in the paddle system.
α_{p2}	Orientation of the initial magnetic moment of paddle 2 in the paddle system.
β	A constant of the x direction amplitude of the external magnetic field in the paddle system.

Γ	Internal magnetic time-scale in the paddle system.
γ	Electroplating duty cycle.
Δ	Difference.
ϵ	Dimensionless ratio between average bead radius and characteristic length in the paddle system.
θ_{0ijk}	Initial angle of bead triplet ijk in the paddle system.
θ_1	Angle of right hinge in Purcell's two hinge swimmer.
θ_2	Angle of left hinge in Purcell's two hinge swimmer.
θ_E	The angle between the uni-axial and the direction of magnetisation.
θ_{ij}	Angle between $\boldsymbol{r}_{ij}$, the position vector from bead j to bead i and the x-axis in the paddle system.
θ_{jk}	Angle between $\boldsymbol{r}_{jk}$, the position vector from bead k to bead j and the x-axis in the paddle system.
θ_m	Angle between the magnetic moment of the particle and the orientation of the easy axis with respect to the direction of magnetisation in the in the two ferromagnetic particle system.
κ	Effective anisotropy field constant of all magnetic beads in the paddle system.
κ_i	Effective anisotropy field constant of bead i in the paddle system.
λ_i	Mass of bead i in the paddle system.
μ	Dynamic viscosity.
μ_0	Permeability of free space.
ν	Kinematic viscosity.

$\xi_\perp$	Perpendicular fluid dynamic resistance coefficients related to a sperm-like swimmer.
ρ	Density.
ϱ_x	Directional cosines of the normalised magnetisation with respect to the x axis of the lattice.
ϱ_y	Directional cosines of the normalised magnetisation with respect to the y axis of the lattice.
ϱ_z	Directional cosines of the normalised magnetisation with respect to the x axis of the lattice.
σ_s	Stress field.
σ_{s1}	An arbitrary stress field.
σ_{s2}	An arbitrary stress field.
ς	Dimensionless parameter related to the time in the paddle system.
τ	Magnetic torque.
Υ	Body-lengths travelled per cycle for a swimming device.
υ	Dimensionless parameter related to the mass of the paddle system.
Φ	Example angle used in vector identities.
Φ_1	Arbitrary orientation of the initial magnetic moment in the paddle system.
Φ_2	Arbitrary orientation of the initial magnetic moment in the paddle system.
Φ_3	Arbitrary orientation of the initial magnetic moment in the paddle system.

Φ_4	Arbitrary orientation of the initial magnetic moment in the paddle system.
ϕ	Phase difference angle in the dampening y component of external magnetic field in the paddle system.
χ_m	Magnetic susceptibility.
ψ	Angle of the external magnetic field with respect to the x axis.
Ω	Imposed magnetic torque at the head of the sperm-like swimmer.
ω	Angular frequency of oscillation of the magnetic field.
ϖ	Dimensionless parameter related to the fluidic forces in the paddle system.

List of Publications & Conferences

Publications

- Elizabeth L. Martin*, Matthew T. Bryan, Stefano Pagliara and Feodor Y. Ogrin, *Advanced Processing of Micropatterned Elasto-Magnetic Membranes*, IEEE Transactions in Magnetics, (2019), **55**, 2900406.
- Matthew T. Bryan*, Jose Garcia-Torres, Elizabeth L. Martin, Joshua K. Hamilton, Carles Calero, Peter G. Petrov, C. Peter Winlove, Ignacio Pagonabarraga, P. Tierno,Francesc Sagués and Feodor Y. Ogrin, *Microscale magneto-elastic composite swimmers at the air-water and water-solid interfaces under a uniaxial field.*, Physical Review, (2019), **11**, 044019.
- Daiki Matsunaga*, Joshua K. Hamilton*, Fanlong Meng, Nick Bukin, Elizabeth L. Martin, Feodor Y. Ogrin, Julia M. Yeomans and Ramin Golestanian, *Controlling collective rotational patterns of magnetic rotors*, Nature Communications, (2019), **10**, 044019.
- Jacob L Binsley*, Elizabeth L. Martin, Thomas O. Myers, Stefano Pagliara and Feodor Y. Ogrin, *Microfluidic devices powered by integrated elasto-*

magnetic pumps, Lab on a Chip, (2020), 4285–4295.

- Matthew T. Bryan*, Elizabeth L. Martin*, Aleksandra Pac, Andrew D. Gilbert and Feodor Y. Ogrin, *Metachronal waves in magnetic micro-robotic paddles for artificial cilia*, Communications Materials, (2020), **2** 14.

Conferences

Organised Conferences

- Bio-inspired Magnetic Systems 2018, Exeter, UK (9th - 11th July 2018).

Oral Presentations

- Magnetism 2018, Manchester UK (9th-10th April 2018) - "Development of novel magnetic-elastic membranes for microfluidic applications".
- Bio-inspired Magnetic Systems (BIMS) 2018, Exeter UK (9th-11th July 2018) - "Development of novel magnetic-elastic membranes for microfluidic applications".
- Magnetism 2019, Leeds UK (8th-9th April 2019) - "Investigation of Coupled Elasto-Magnetic Pumps for Microfluidic Applications".
- INTERMAG 2020, Montreal Canada (4th-8th May 2020) - "Investigation of a Network of Structured Elasto-Magnetic Discs for Low Reynolds Number

Pumps" - *(Accepted but the Conference was cancelled due to COVID - 19)*.

Poster Presentations

- Magnetism 2017, York UK (3rd-4th April 2017) - "The investigation of the coercive field and saturation magnetisation of microscopic CoNiP elements produced by electrodeposition".
- Micromotors Summer School, Dresden Germany (13th-18th August 2017) - "The investigation of the coercive field and saturation magnetisation of microscopic CoNiP elemetns produced by electrodeposition".
- 62nd Annual Conference on Magnetism and Magnetic Materials (MMM 2017), Pittsburgh USA (6th-10th November 2017) - "Development of novel magneto-elastic membranes for microfluidic applications".
- Bio-inspired Magnetic Systems (BIMS) 2018, Exeter UK (9th-11th July 2018) - "Development of novel magnetic-elastic membranes for microfluidic applications".
- 2019 Joint MMM-Intermag Conference, Washington DC (14th-18th January 2019) - "Advanced Processing of Bio-Inspired Magnetic Metamaterials".
- 65th Annual Conference on Magnetism and Magnetic Materials (MMM 2020), Virtual (originally Florida, USA), (2nd-6th November 2020) - "Investigation of a Coupled Elasto-Magnetic Discs for Low Reynolds Number Pumps" - Best Poster Award.

Chapter 1

Introduction

1.1 Motivation

More than half a century ago, Richard Feynman in his lecture entitled *"There's Plenty of Room at the Bottom"* speculated that "although it is a very wild idea, it would be interesting in surgery if you could swallow the surgeon". This concept also inspired several science fiction films such as *Fantastic Voyage* (1966) and *Innerspace* (1987), in which a submarine with its human crew were shrunk down to a microscopic size, injected into a human and then they proceeded to travel around the body undertaking delicate surgery. Although this may appear to be an inconceivable idea, the notion of performing medical procedures at microscopic scales is now slowly coming out of the realm of science fiction.

The study of microfluidic devices is a growing research area, primarily due to the promising applications in the biomedical field. These are devices that concern the manipulation of small volumes of fluids. Recently, there has been a significant research effort focused on devices that can propel themselves in microfluidic environments, often called microswimmers, with the hope of realising elements of the *Fantastic Voyage*.

A particular area of application that promises a great impact is lab-on-a-chip-technology (LOC). LOC is widely anticipated to be used for on-site diagnostics, drug release and sample preparation, as well as non-biological functions such as inkjet printing. LOC devices are envisioned to be able to perform tasks such as mixing a blood sample with the buffer solution, as well as monitoring and releasing glucose in diabetic patients, to name but a few.

The term 'lab-on-a-chip technology' refers to devices which would allow several laboratory functions (such as synthesis and analysis of chemicals) on a portable handheld device. These devices are a promising avenue to progress point-of-care testing. There are several imaginable benefits, such as less required sample volumes for diagnostics, less required reagents, more compact systems and a safer platform for chemical, radioactive or biological studies, to name but a few. An additional key advantage is that the analysis of a sample can take place where the sample is generated, rather than being transported to a large laboratory facility, which can take a significant amount of time. Lab-on-a-chip incorporates many different areas of technology but the one which ties them altogether and makes the whole concept possible is microfluidics.

Therefore, there is a growing need for active microscopic devices which could be integrated as a part of the standard microfluidic chip environment. This would enable a range of functionalities such as pumping, stirring, and valving, which are otherwise impossible at this scale of the fluidic geometry.

Microfluidic devices operating on the order of a microscale are dependant on very different rules. Pumping and swimming in these conditions are subjected to a low Reynolds number environment. Edward Mills Purcell in *"Life at Low Reynolds Number", American Journal of Physics, January 1977* explained that "Motion at low Reynolds number is very majestic, slow, and regular." This is because systems at low Reynolds number regimes are subject to what is know as the “Scallop Theorem”, which states that there is no net fluid flow for time-reversible motions. Therefore, a device whether artificial or natural requires at least two degrees of freedom to pump or swim in this regime.

Despite the great promise of microfluidic devices that could open up many doors in fields, such as biomedical, designing and fabricating such devices has been met with many challenges. A great deal of effort has been invested in devising various shape sequences that would lead to translational motion. However, this is only part of the problem. The second essential requirement for a successful pump or swimmer is an actuation mechanism generating the necessary shape sequence and the requisite energy. The third challenge, once a design and actuation method is established, is to find suitable fabrication methods, since traditional machining methods are insufficient to produce the devices at this scale.

A number of actuation methods have been researched to propel microswimmers such as chemical, acoustic, light and magnetic and each of these methods have their advantages as well as disadvantages. Although the actuation method dictates some of the design features, there is still significant variation within these categories.

1.2 Thesis Outline

The aim of this thesis was to theoretically and experimentally investigate magnetically actuated systems that are able to manipulate fluid. Such systems include low Reynolds numbers swimmers, pumps and magnetically controlled membranes. Magnetic actuation provides a wireless transmittable energy source that possesses several properties that could be varied (i.e. frequency, orientation, strength).

This thesis is organised in the following way. Chapter 2 provides an historical background. It introduces the relevant concepts of fluid dynamics and the basics of magnetism. This is alongside Chapter 3 which is a review of the relevant literature on the study of low Reynolds number swimmers, pumps and membranes and the different fabrication techniques using magnetic materials.

Chapter 4 focuses on the work undertaken to produce a micro-patterned elasto-magnetic membrane and microswimmer. These devices are comprised of pairs of two different interacting ferromagnetic particles that were connected together via an elastic material. The devices required an in-depth fabrication process involving several lithographic and electrodeposition steps which are discussed in this chapter.

In Chapter 5 a similar fabrication method to that of Chapter 4 is used to create a ferromagnetic paddle based pump. The pump comprises of an array of ferromagnetic discs of a single material connected together via elastic axles. The paddles are allowed to rotate to a varying degree due to the different elastic properties of their axles. In the presence of an oscillating magnetic field they form metachronal motion which is similar to that of a cilia. To understand this system further, a number of theoretical investigations are presented.

Chapter 6 focuses on the fabrication and experimental investigation of a single elasto-magnetic pump. The geometry of this pump is based on Purcell's theoretical 3-linked swimmer. The 3-linked device is attached at one end to allow it to pump rather than swim. As an actuation method, a single ferromagnet was attached to the head of the 3-linked device and actuated via a uni-axial oscillating magnetic field. The geometry of the design is the key factor in forming a motion that is able to pump fluid in a low Reynolds number regime.

Chapter 7 is centralised on the further developments of elasto-magnetic paddle devices, first discussing experimental research, concentrating on their fabrication, and then theoretical work. The theoretical investigations primarily focus on the effect of the magnetic orientations of the paddles on the overall system. This chapter also highlights some of the future work to be undertaken based on the results described in this thesis.

The final chapter of this thesis contains the overall conclusions that can be derived from the work presented in this thesis.

1.3 Central Development Of Thesis

The primary aim of this research was to investigate and develop magnetically actuated systems that are able to manipulate fluid in a low Reynolds number regime. In this thesis it has been shown that magnetically actuated devices with elastic components (known as elasto-magnetic devices) can pump fluid in a low Reynolds number regime. These devices all comprised of ferromagnets embedded within an elastic structure. The designs have shown that a device can have a non-reciprocal stroke cycle while being actuated via a uni-axial oscillating magnetic field. The elastic interactions, provided by the elastic component, are key in achieving the non-reciprocal motion of a magnetic device actuated via a uni-axial oscillating magnetic field. The described devices are able to be produced using lithographic and electroplating fabrication techniques.

1.4 Contributions

This section details the work undertaken by the author of this thesis, Elizabeth L. Martin, and the contributions of other academics are stated for the research focused chapters, Chapter 4, Chapter 5, Chapter 6 and Chapter 7.

In Chapter 4, the research described in the introduction sections, Section 4.1.1 and Section 4.1.2 were undertaken primarily by Prof. Feodor Y. Ogrin, Prof. Andrew D. Gilbert, Dr. Joshua K. Hamilton and Dr. Matthew T. Bryan before the research in this thesis had began. The electrodeposition investigations were conducted by the author of this thesis, Section 4.2.1. This includes the designs of two of the electrodeposition cells (Figure 4.6(b) and (c)), while the other cell Figure 4.6(a) was created before this research. The electrolyte solution recipes used were cited accordingly. The microscale elasto-magnetic swimmer was designed in collaboration with Dr. Matthew T. Bryan, Section 4.2.2, while the microscale elasto-magnetic membrane was designed solely by the author of this thesis, Section 4.2.3. The author of this thesis created a fabrication procedure for the microscale elasto-magnetic swimmers and membranes Section 4.2.4. The author of this thesis produced the membranes, however the swimmers were produced by Dr. Matthew T. Bryan. The author of this thesis performed and analysed the actuation investigations on the membrane, Section 4.2.5.

In Chapter 5, the design of the paddle membrane was created collaboratively by Dr. Matthew T. Bryan and the author of this thesis (Section 5.1). The fabrication procedure (discussed in Section 5.2) was developed by Dr. Matthew T. Bryan and the author of this thesis, it was based on the fabrication method described in Chapter 4. The experimental measurements described in Section 5.2 were taken by taken by Dr. Matthew T. Bryan and Aleksandra Pac. The analytical model described in Section 5.3 was developed by Prof. Andrew D. Gilbert and myself. The foundations of the analytical model was created by Prof. Andrew D. Gilbert and then further developed by the author of this thesis to investigate the paddle design with different width axles and orientations of the disc's magnetic moment. All results and investigations shown in Section 5.3.1, Section 5.3.2, Section 5.3.3, Section 5.3.4 and Section 5.3.5 was undertaken solely by the author of this thesis. In Section 5.4 the fabrication and experimental tests of the macro-paddle design were performed by Tom Moynihan (who undertook an 8-week summer project hosted by the author of this thesis) and the author of this thesis collaboratively. However the design, fabrication procedure and analysis in Section 5.4 was conducted solely by the author of this thesis.

The research in Chapter 6 was accomplished in collaboration with Jacob L. Binsley. In Section 6.2, the design and actuation of the swimmer was completed cooperatively and Jacob L. Binsley solely designed the enclosed pump system encasing the swimmer. Initial fabrication tests with SU-8 and PDMS was conducted by the author of this thesis. The fabrication procedure (Section 6.3) was created by the author of this thesis and Jacob L. Binsley, with the author of this thesis focusing on the fabrication of the middle section of the pump (Figure 6.3) and Jacob L. Binsley on the production of the overall pump (Figure 6.2(e)). The fabrication of the pump was conducted by Jacob L. Binsley. The raw data when testing the pump was recorded by Jacob L. Binsley and as well as the collection of the data using 'Tracker' [2] (discussed in Section 6.4). Calculating the average velocity and flow rate (discussed in Section 6.4) was undertaken by the author of this thesis. The discussion in Section 6.5 was completed by the author of this thesis. The research on the hysteretic area of the closed loop path of the swimmer was conducted collaboratively, again by Jacob L. Binsley and the author of this thesis, however all data presented Section 6.6.1 was analysed by the author of this thesis. The other elements of the data analysis in this thesis (Section 6.6.2, Section 6.6.3 and Section 6.6.4) were undertaken by the author of this thesis.

In Chapter 7, the experimental tests of the macro-paddle design were performed by Tom Moynihan and the author of this thesis, while the design, fabrication method and analysis was conducted solely by the author of this thesis (Section 7.3.2). All other sections of this chapter (Section 7.2.1, Section 7.2.2, Section 7.2.3, Section 7.3.1 and Section 7.4) was completed by the author of this thesis.

Chapter 2

Background

"Motion at low Reynolds number is very majestic, slow, and regular"

- Edward Mills Purcell.

2.1 Fluid Dynamics

This chapter presents the development of ferromagnetic microfluidic devices. These devices have the potential to be incorporated into a number applications such as biological or medical fields. In all the desired applications the ferromagnetic microfluidic devices would be surrounded by a fluid. Therefore, it is important to study some of the fundamental concepts that govern fluid dynamics to understand the systems it resides in.

Conservation of mass leads to the continuity equation. If you consider volume V bounded by a surface S. For the conservation of mass to hold, the rate of change of mass inside V is equal to that of the mass flux inwards over the surface S

$$\frac{\partial}{\partial t}\int_V \rho(\boldsymbol{r},t)\,dV = -\int_S \rho(\boldsymbol{r},t)\boldsymbol{u}\cdot\hat{\boldsymbol{n}}\,dS. \tag{2.1}$$

Where $\boldsymbol{u}\cdot\hat{\boldsymbol{n}}$ is the flow in the perpendicular direction of S and $\rho(\boldsymbol{r},t)$ is the density of the fluid. Using the divergence theorem this becomes

$$\frac{\partial}{\partial t}\int_V \rho(\boldsymbol{r},t)\,dV = -\int_V \nabla\cdot(\rho(\boldsymbol{r},t)\boldsymbol{u})\,dV, \tag{2.2}$$

$$\int_V \left[\frac{\partial\rho(\boldsymbol{r},t)}{\partial t} + \nabla\cdot(\rho(\boldsymbol{r},t)\boldsymbol{u})\right]\,dV = 0.$$

For the mass to be conserved everywhere, there must be equal for any volume, leading to

$$\frac{\partial\rho}{\partial t} + \nabla\cdot(\rho\boldsymbol{u}) = 0. \tag{2.3}$$

This is the continuity equation for a general fluid. An incompressible fluid is a fluid where the density of which remains constant in space and time, i.e. during flow. For the case of an incompressible fluid, (assuming conservation of mass and the density within a moving volume of fluid remains constant) the above equation simplifies to

$$\nabla\cdot\boldsymbol{u} = 0. \tag{2.4}$$

2.1.1 The Navier-Stokes Equation

The key equation that governs the motion of a fluid is described by the Navier-Stokes equation, which was formulated by Claude-Lauis Navier in 1822, but this was developed further by George Gabriel Stokes in 1845. This equation was deduced from various physical hypotheses, and in various forms, by Navier (1827), Poisson (1831), Saint-Venant (1843) and Stokes (1845). Stokes (1846) himself reviewed the methods and hypotheses of these authors, and presented a short rational derivation of the equations. It was developed from applying Newton's second law to a small element of fluid. A fluid is said to be Newtonian if the viscous stress is linearly proportional to the strain rate. Where strain is a measure of deformation, which is dimensionless, and it is in terms of the relative displacement of particles in a body.

The Navier-Stokes equation for an incompressible fluid ($\nabla \cdot \boldsymbol{u}$) is given by

$$\frac{\partial \boldsymbol{u}}{\partial t} + \boldsymbol{u} \cdot \nabla \boldsymbol{u} = -\frac{\nabla P}{\rho} + \nu \nabla^2 \boldsymbol{u} + \frac{\boldsymbol{F}_{add}}{\rho}. \tag{2.5}$$

Where $\boldsymbol{u}$ is the velocity of the fluid, P is the pressure of the fluid, ρ is the density of the fluid, ν is the kinematic viscosity of the fluid and $\boldsymbol{F}_{add}$ is an additional force per unit volume term which would include forces such as gravity, Coriolis or an electromagnetic force. The kinematic viscosity of the fluid can be expressed as $\nu = \frac{\mu}{\rho}$ where μ is the dynamic viscosity of a fluid.

The Navier-Stokes equation can be converted to a dimensionless form, where the characteristic length and flow velocity of the system are taken to be L and U respectively. Following this method time could be expressed as $\frac{L}{U}$. Using these, the following dimensionless parameters are defined

$$\begin{aligned}
\boldsymbol{r}^* &= \frac{\boldsymbol{r}}{L}, \\
\boldsymbol{u}^* &= \frac{\boldsymbol{u}}{U}, \\
t^* &= \frac{Ut}{L}, \\
P^* &= \frac{PL}{\mu U}, \\
\nabla^* &= L\nabla.
\end{aligned} \tag{2.6}$$

Using these dimensionless variables the dimensionless Naiver Stokes equation is

$$\begin{aligned}
\frac{\partial \boldsymbol{u}}{\partial t} &= \frac{U^2}{L}\frac{\partial \boldsymbol{u}^*}{\partial t^*}, \\
\boldsymbol{u}\cdot\nabla\boldsymbol{u} &= \frac{U^2}{L}(\boldsymbol{u}^*\cdot\nabla^*\boldsymbol{u}^*), \\
\frac{\nabla P}{\rho} &= \frac{U}{L^2}(\nu\nabla^* P^*), \\
\nu\nabla^2\boldsymbol{u} &= \frac{U}{L^2}(\nu\nabla^{*2}\boldsymbol{u}^*).
\end{aligned} \tag{2.7}$$

Using these terms and assuming the absence of gravitational effects, the Navier-Stokes equation can be stated as

$$\frac{U^2}{L}\left(\frac{\partial \boldsymbol{u}^*}{\partial t^*} + \boldsymbol{u}^*\cdot\nabla^*\boldsymbol{u}^*\right) = \frac{U\nu}{L^2}(-\nabla^* P^* + \nabla^{*2}\boldsymbol{u}^*). \tag{2.8}$$

Finally, parameter known as Reynolds number (Re) can be introduced into the dimensionless Navier-Stokes equation

$$Re\left(\frac{\partial \boldsymbol{u}^*}{\partial t^*} + \boldsymbol{u}^*\cdot\nabla^*\boldsymbol{u}^*\right) = (-\nabla^* P^* + \nabla^{*2}\boldsymbol{u}^*). \tag{2.9}$$

Where Re is

$$Re = \frac{UL}{\nu} = \frac{\rho UL}{\mu}. \tag{2.10}$$

The Reynolds number is a useful parameter within fluid dynamics as it indicates the regime of the fluid and therefore, its behaviour. Reynolds number is a dimensionless criterion that determines the relative importance of inertia and viscous effects. It was first introduced by George Gabriel Stokes in 1851, however Osborne Reynolds popularised its use in 1883. It can be derived from the Navier-Stokes Equation (2.5) by neglecting the additional force term. As Re tends to zero the viscous terms in the Navier-Stokes equation dominate whilst at larger values of the Reynolds number inertia forces dominate. However, inertial effects always exist so when the Reynolds number is zero there is no flow. Due to these reasons, Reynolds number is a useful indicator of what forces are the most important in any given fluid.

In general terms there are two main regimes of fluid flow. The first is when $Re \gg 1$, this regime is know as inviscid flow (also known as Euler flow), the other is when $Re \ll 1$.

2.1.2 Low Reynolds Number

Reynolds number indicates the relative importance of inertia to viscous effects. The lower the Reynolds number the less important inertia forces are compared with the viscous forces on the flow, until the inertia effects are presumed to be negligible. When the Reynolds number is $\ll 1$ the system is know as being in a low Reynolds number regime. There is no finite number that below which is a low Reynolds number and above which it is not. In the paper entitled *"Life in Low Reynolds Number"* by Edward M. Purcell, the Reynolds numbers considered as low Reynolds numbers were $\sim 10^{-4}$ or 10^{-5} [1], whereas, Sir Geoffrey Taylor in his famous lecture, *"Low-Reynolds-Number Flows"*, quotes 0.05 as being "small compared with 1.0 so that inertia plays no appreciable part in the situation" [3]. A system that flows at a low Reynolds number ($\ll 1$) is also likely to produce a flow at a slightly larger Reynolds number when viscous forces are still dominant but inertia forces have a very small effect (e.g. $Re < 1$). Therefore the value of a low Reynolds number is related to tolerance.

When the Reynolds number is much less than 1 ($Re \ll 1$), one enters the approximation that is known as the Stokes regime. This regime can be achieved by having a very viscous fluid, very small length scales or slow fluid flow. This is also known as creeping flow. The Navier-Stokes equation can then be simplified to:

$$0 = -\nabla^* P^* + \nabla^{*2} \boldsymbol{u}^*. \tag{2.11}$$

Returning to the dimensional form gives Stokes equation of the flow for an incompressible fluid ($\nabla \cdot \boldsymbol{u}$),

$$0 = -\nabla P + \mu \nabla^2 \boldsymbol{u}. \tag{2.12}$$

Comparing this to the complete Navier-Stokes Equation (2.5), it can be seen that the non linear and time dependant terms are not present. This means that only the forces that are being applied to the fluid at that particular instant in time are important and that the system has no memory of what forces had occurred in previous time stamps. It follows that as soon as the force applied to the fluid is removed, the fluid returns to being at rest. In addition to this, the equation does not have any time dependence, which implies that reversing the direction of the flow is equivalent to reversing time. This lack of time dependence in Equation (2.12) presents a challenge in producing a net flow of fluid in Stokes regime based on a cyclic motion. If an element of the fluid is displaced by a forward stroke of an object and this object subsequently performs a reverse stroke, the fluid will again

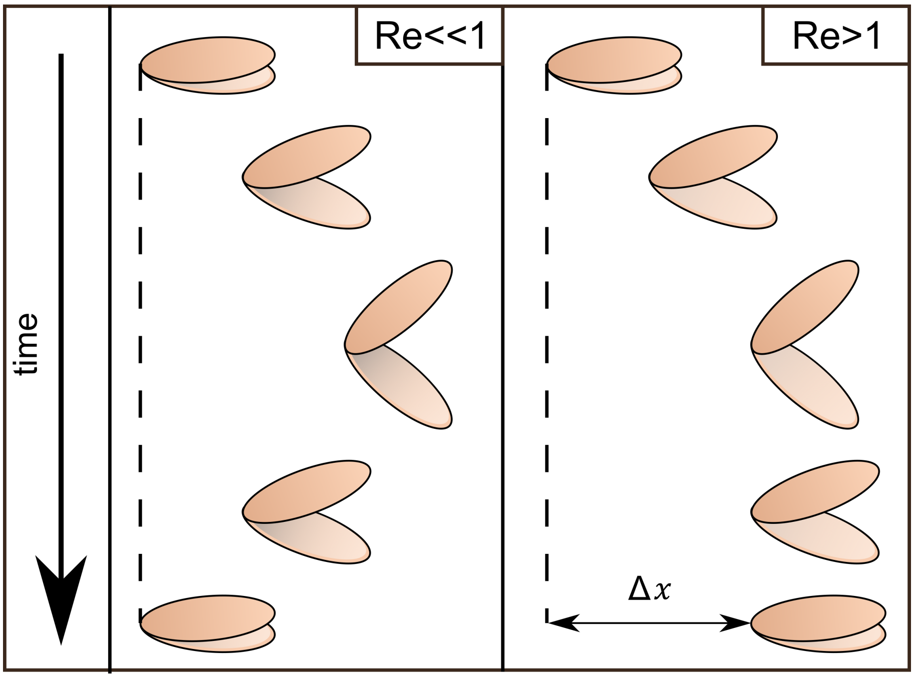

Figure 2.1: A diagram describing the Scallop Theorem by E. Purcell [1]. It shows that in a low Reynolds number regime, if there is only one degree of freedom in the configuration of space, in this case a hinge, and the motion performed is reciprocal, it does not achieve a net motion. This is not the case in a larger Reynolds number system.

be displaced but the fluid will return to it's initial position, from before any strokes had occurred, thus there is no net motion.

The motion can be best described by Edward M. Purcell in the paper entitled *"Life in Low Reynolds Number"*, in which he first introduced the "Scallop" Theorem [1] (see Figure 2.1). Purcell's scallop is effectively a simple hinge that generates motion through opening and closing. The motion of a simple hinge only has one degree of freedom and is confined to reciprocal motion. Although in a higher Reynolds number regime this motion is sufficient to provide a net movement in the fluid, this is not the case when $Re \ll 1$. In this regime, the "Scallop" would effectively be stuck, moving backwards and forwards about one point. This is due to time-reversal symmetry and this needs to be broken in order to provide a net motion. Thus at least two degrees of freedom are required to produce a net movement and in a fixed case to produce a flow.

Purcell introduced the idea of a two-hinged system, which is the simplest design he thought of that would have two degrees of freedom and thus could achieve a net movement in a low Reynolds number regime Figure 2.2 (a). This is commonly known as Purcell's swimmer. This swimmer can move, altering angles θ_1 and θ_2 relative to the hinge. However, if the arms move in sync ($\theta_1 = -\theta_2$) which is shown in case Figure 2.2(b), the swimmer is producing a reciprocal motion. It can be seen in Figure 2.2(b) and Figure 2.2(d) that the motion is symmetric.

This theory can be generalised to swimmers not based on scallops. One important property of the Scallop Theorem, is that if a body undergoes surface deformation, the distance travelled by the swimmer between two different surface configurations does not depend on the rate at which the surface deformation occurs but only on its geometry, known as rate independence. It has been shown mathematically by E. Lauga and T. R. Powers [4] that for any swimmer in a low Reynolds number regime, locomotion is independent of swimming rate. This mathematical proof will be discussed below.

Firstly, the reciprocal theorem describes the relationship between two flows in the same geometry where inertial effects are insignificant compared to viscous effects.

$$\iint_S \boldsymbol{u_{f1}} \cdot \boldsymbol{\sigma_{s2}} \cdot \boldsymbol{n} \, dS = \iint_S \boldsymbol{u_{f2}} \cdot \boldsymbol{\sigma_{s1}} \cdot \boldsymbol{n} \, dS, \tag{2.13}$$

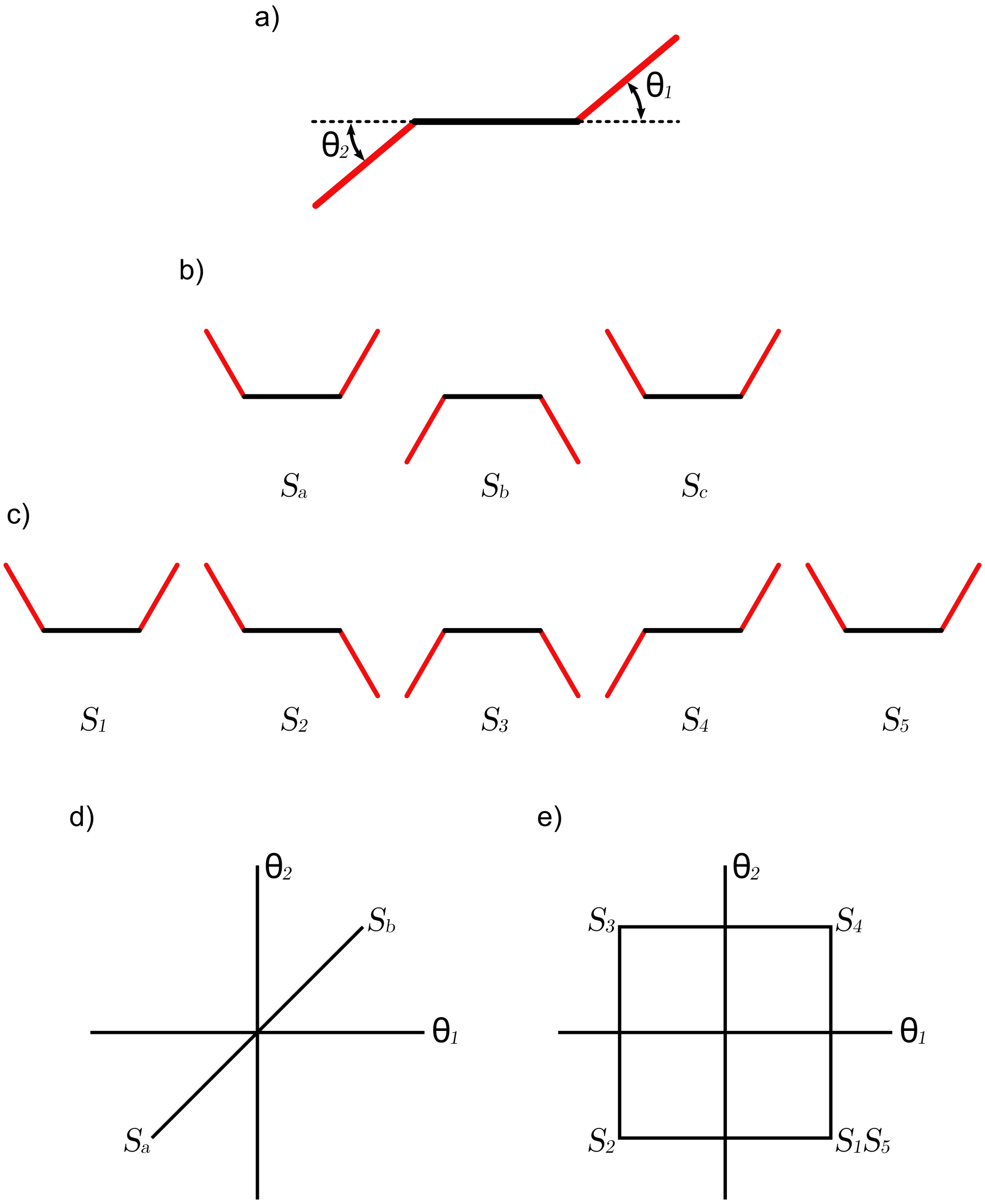

Figure 2.2: The two hinge swimmer proposed by E. Purcell. (a) Shows the two dimensions in configuration space, θ_1 and θ_2. (b) For the configuration sequence S_a, S_b, S_c, there will be no net displacement after one cycle. (c) For the configuration sequence S_1, S_2, S_3, S_4, S_5, there will be displacement after one cycle. (d) The configuration space for the stroke pattern in (b). (e) The closed loop in configuration space for the stroke pattern in (c).

where $\boldsymbol{u_{f1}}$ and $\boldsymbol{u_{f2}}$ are the velocity fields, $\boldsymbol{\sigma_{s1}}$ and $\boldsymbol{\sigma_{s2}}$ are the stress fields of two flows, S is the bounding surface of volume of fluid with outward normal $\boldsymbol{n}$. This equation can be to obtain information about a certain flow by using information from another flow. (This is preferable to solving Stokes equations, which is difficult due to not having a known boundary condition.)

The linearity of Stokes equations allows the reciprocal theorem to be used to relate the swimming velocity of the swimmer to the velocity field of the fluid around its surface (known as the swimming gait, $\dot{\boldsymbol{r}}_{\boldsymbol{s}}(t)$), which changes according to the periodic motion it exhibits. This can be used to show the relationship between the instantaneous swimming velocity ($\boldsymbol{v}(t)$) in the direction of the external force ($\hat{\boldsymbol{F}}$) acting on a body and its swimming gate ($\dot{\boldsymbol{r}}_{\boldsymbol{s}}(t)$), $\hat{\boldsymbol{F}}\cdot\boldsymbol{v}(t) = \iint_{Sh} \dot{\boldsymbol{r}}_{\boldsymbol{s}}(t)\cdot(\boldsymbol{\sigma_s}\cdot\boldsymbol{n})\,dS_h$ [4], where σ_s is the stress field, $\boldsymbol{n}$ is a direction and S_h is the shape.

Following this, a low Reynolds number swimmer's instantaneous speed of locomotion is given by a general integral in the form of $\boldsymbol{v}(t) = \iint_{Sh} \dot{\boldsymbol{r}}_{\boldsymbol{s}}(t) \cdot \boldsymbol{G}(\boldsymbol{r_s})\,dS_h$, where $\boldsymbol{r_s}(t)$ denote the positions of points on the surface of the swimmer and the function $\boldsymbol{G}(\boldsymbol{r_s})$ is a general tensor depending on the shape of the body and on the boundary conditions at infinity [4].

Considering the forward stroke of the cycle, where $\boldsymbol{v}(t)$ is an instantaneous prescribed velocity of the swimmer, the distance travelled can be described as

$$\Delta D_{t_0 \to t_1} = \int_{t_0}^{t_1} \boldsymbol{v}(t)\,dt. \tag{2.14}$$

Now consider the swimmer deforming in the same manner but at a different rate with $t' = g(t)$ and $\boldsymbol{r}'_s(t') = \boldsymbol{r}_s(t)$ [4].

$$\begin{aligned}
\Delta D'_{t_0\to t_a} &= \int_{t_0}^{t_a} \boldsymbol{v'}(t')\,dt' = \int_{t_0}^{t_a} \boldsymbol{v'}(t')\dot{g}(t)\,dt \\
&= \int_{t_0}^{t_a} \iint_S \dot{g}(t)\dot{\boldsymbol{r}}'_{\boldsymbol{s}}(t') \cdot \boldsymbol{G}(\boldsymbol{r}'_{\boldsymbol{s}})\,dS\,dt \\
&= \int_{t_0}^{t_a} \iint_S \dot{g}(t)\frac{\dot{\boldsymbol{r}}_{\boldsymbol{s}}(t)}{\dot{g}(t)} \cdot \boldsymbol{G}(\boldsymbol{r}_{\boldsymbol{s}})\,dS\,dt \\
&= \int_{t_0}^{t_a} \boldsymbol{v}(t)\,dt = \Delta D
\end{aligned} \tag{2.15}$$

This result means that the net distance traveled by the swimmer does not depend on the rate at which it is being deformed, but only on the geometrical sequence of shape.

Another important property of the Scallop Theorem is that if the sequence of shapes displayed by a swimmer deforming in a time–periodic fashion is identical when viewed after a time-reversal transformation, then the swimmer does not achieve a net distance.

Let t_0 occur at a position such as S_a and t_f a period later at a position such as S_c with a sequence of shapes $\boldsymbol{r}_s(t)$ and $\boldsymbol{r}_s(t_0) = \boldsymbol{r}_s(t_f)$. Let t_m be a time instant between that of t_0 and t_f that divides the sequence of shapes into the forward and backward, for example when S_b occurs in the sequence S_a, S_b, S_c. Let t' occur between t_m and t_f and t between t_0 and t_m. Due to the sequence of shapes they can be expressed as $t' = f(t)$ with $t_m = f(t_m)$ and $t_f = f(t_0)$. The distance the swimmer travels over the backwards stroke can be expressed as the following,

$$\begin{aligned}
\Delta D'_{t_m\to t_f} &= \int_{t_m}^{t_f} \boldsymbol{v'}(t')\,dt' = \int_{t_m}^{t_0} \boldsymbol{v}(t)\,dt \\
&= -\int_{t_0}^{t_m} \boldsymbol{v}(t)\,dt = -\Delta D_{t_0\to t_1}.
\end{aligned} \tag{2.16}$$

Following this, the net distance travelled in a period is $\Delta D_{t_0\to t_1} + \Delta D'_{t_1\to t_f} =$

$\Delta D_{t_0 \to t_1} - \Delta D_{t_0 \to t_1} = 0$. Therefore, for a sequence such as S_a, S_b, S_c there will be no net motion.

However, for the case when the hinges move in a configuration similar to that of Figure 2.2(c), it can be seen that the links move out of phase with each other. This is clear in the configuration of space Figure 2.2(e) as it displays a loop rather than a straight line, due to the motion being asymmetric. This asymmetry causes the motion to be non-reciprocal. This means the swimmer attains a net motion in a Re$\ll$1 regime.

2.1.3 Low Reynolds Number Swimming Systems

There has been a large amount of interest in creating models and devices that can propel in low Reynolds number environments. Such devices are often called swimmers, swimming devices, microbots or micromotors. As previously mentioned, swimmers have the potential to be incorporated into biological and medical applications.

In modern medical practice, diagnostic investigations and medicinal treatment are often balanced against their invasiveness; the degree to which surgical and medicinal implements must invade the body to achieve their desired therapeutic outcome. Synthetic swimmers have a great potential for providing minimally invasive alternatives in these roles, allowing physicians greater degrees of access and specificity without resorting to more inherently time consuming and invasive procedures, such as surgery. Synthetic swimming devices could be directed to a particular area of the body such as liver, stomach or reproductive tract to aid with diagnostic tests. In addition to diagnostic applications, they could transport and deliver drugs to specific regions within the body, which could be life saving for the patients that have multiple symptoms that require opposite treatments. This is not only important for swimming devices active within the body, but also for externally used microfluidic systems such as pumps and mixers which need to overcome the same restrictions outlined by a low Reynolds number system. Since the work by Edward Purcell [1] there have been large variety of techniques that propose different mechanisms for time-irreversible motion [5–10].

Some swimming methods are based on kinematics. One of the simplest examples of a proposed swimming model that was based on Purcell's two hinge motion comprised of a push-me-pull-you motion [11]. This consisted of two identical spherical bladders linked together via a rod. These bladders exchanged volumes and their mutual separation in each stroke. When one expands it acts as a force pushing the other away, which in turn, pulls the first sphere. This *"pushmepullyou"* motion is repeated to form a swimming cycle, see Figure 2.3(a). A. Najafi *et al.* described another device known as the "three linked spheres" swimmer [12]. This design consisted of three hard spheres that are linked through two arms/links that alter their length, Figure 2.3(b). The length of the arms would decrease/increase in turn with a constant velocity in a sequence of four steps before returning to its original orientation. The device gained a displacement of ΔD_b, due to its movement sequence and the fluidic forces. The *"pushmepullyou"* swimmer was thought to be both more intuitive, due to its simpler design, and more efficient, as $\Delta D_a > \Delta D_b$ than the "three linked spheres" swimmer.

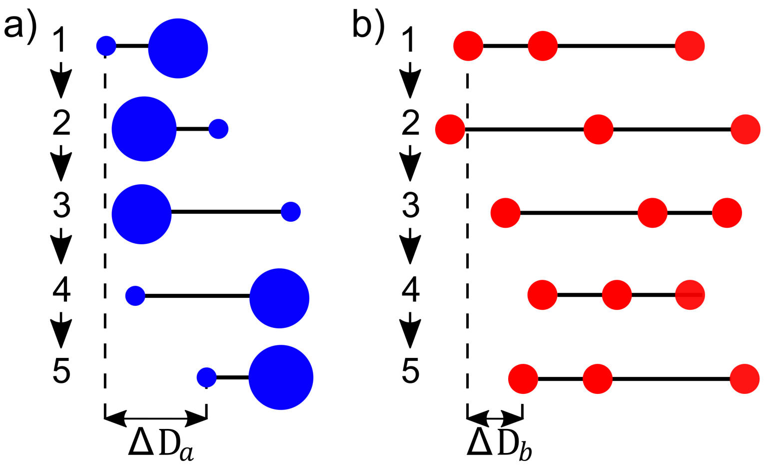

Figure 2.3: a) Five snapshots of the *"pushmepullyou"* swimming stoke. The stroke starts from image 1 and continues to 5, this picture shows one complete cycle, after which the swimmers return to its original configuration but it has been displaced by ΔD_a. Figure adapted from [11]. b) The corresponding strokes of three linked spheres based on the *"pushmepullyou"* swimmer. After a full cycle, following the order 1-5, the swimmer returns to its original shape and it has been displaced by a distance ΔD_b. Figure adapted from [11, 12].

A large number of synthetic swimmer designs take inspiration from existing organisms in nature. This is because many biological swimmers use intricate ways of deforming their shape to produce non-reciprocal motion. An example of this is the sperm cell. Its design consists of a (roughly spherical) head and a single eukaryotic flagellum, the tail. The cell is propelled through a fluid by a snake-like wiggling of its flagellum, as shown in Figure 2.4(c). The flagella beat in a propagating bending wave, with wavelengths smaller than the flagellum length.

A wide variety of bacteria use several helical filaments also known as flagella for their motion. Examples of this are *E. coli* and *Salmonella* bacteria, which have multiple flagella, Figure 2.4(b). These bacteria operate under a "run" and

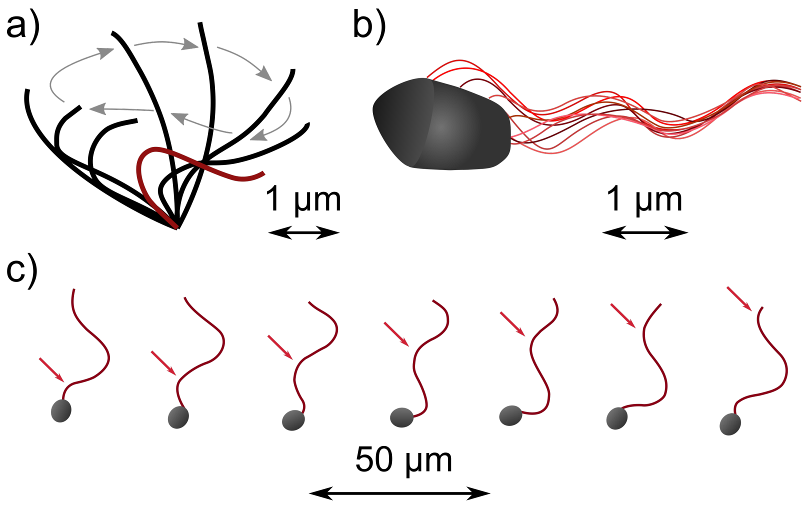

Figure 2.4: a) A diagram showing the motion of a cilium. b) A diagram of *Salmonella*. c) A diagram showing the motion of a sperm cell.

"tumble" motion. In the "run" phase the flagella wind up (left-handed, rotate counterclockwise) to form a bundle and the bacterium moves forward. Following this, in the "tumble" phase, one flagellum reverses its rotational direction to clockwise and leaves the bundle, which gives a more random orientation to the bacterium. The reversal of the rotational direction is accompanied by a change of the helical handedness from left-handed to right-handed and the flagella undergoes a polymorphic transition. At the end of the tumbling phase, all flagella start to rotate again in the same counterclockwise direction, the bundle reforms, and the bacterium returns to a directional motion.

Another example in nature, that is mimicked by researchers creating synthetic swimmers, is cilia. For example Paramecium, another form of single cell organism, feature these cilia. There are several differences between cilia and flagella, such as location and density on cells, but the main structural variation is their length, cilia are typically 10 µm long while sperm flagella are about 50 µm. However, their other significant distinction is their pattern of movement.

As mentioned, flagella beat with an almost perfect propagating sinusoidal bending wave with each flagellum beating independently of any other. Whereas the beat of a cilium is more rotational and fast moving compared to that of a flagellum, in addition to this groups of cilia beat in a coordinated rhythm. A cilium has two distinct phases, a power stroke and a recovery stroke. During the power stroke the cilium stretches out straight and moves quickly in one direction as it bends. In the recovery stroke it bends to the side by a small amount and retracts slowly. What is of particular interest with regards to cilia is that a collection of them can cause a 'metachronal wave'. This is when the cilia do not beat in synchronization but there is a slight delay between a particular cilium and the cilium next to it (this is similar motion to that of a Mexican wave). Due to the different stroke styles the direction of motion for flagella and cilia are different, for flagella it is parallel to the length of the flagella, while with cilia is is perpendicular to it.

All of these biological swimmers have complex chemical motors or internal energy systems, such as the mitochondria, causing their movement, which is difficult to replicate externally outside of nature.

2.2 Magnetic Actuation

When designing synthetic swimmers, a key consideration is the method of actuation used to generate motion in the low Reynolds number regimes. There is significant interest in utilising magnetic fields to instigate this movement due to it's ability to have wireless control. This makes it attractive for a number of biomedical applications.

2.2.1 Magnetic Materials

There are five main types of magnetic materials, ferromagnetic materials, ferrimagnetic materials, antiferromagnetic materials, paramagnetic materials and diamagnetic materials. Materials are divided into these groups depending on how they respond in the presence of an external magnetic field. In ferromagnetic materials, when an external magnetic field is applied, the magnetic moments in the material spontaneously align parallel to each other. Once they are magnetised by the field, they then act as a source of a magnetic field, which may persist after the removal of the external magnetic field. Examples of ferromagnetic materials include Cobalt (Co), Nickel (Ni) and Iron (Fe). Ferrimagnetic materials have two different magnetic moments that are anti-parallel to each other but they have a different magnitude so there is a net magnetisation. An example of where this occurs is ferrites, such as magnetite (Fe_3O_4). Antiferromagnetic materials are similar to that of ferrimagnetic materials, but the magnetic moments are of similar magnitude so there is no net magnetisation. Generally, this occurs at sufficiently low temperatures and theses materials become paramagnetic, an example of this includes Nickel(II) oxide (NiO). Paramagnetic materials exhibit a weak form of magnetism and have magnetic moments parallel to an external magnetic field when it is applied, but do not retain these moments after the external field is removed. Examples of paramagnetic materials are Aluminium (Al), Platinum (Pt)

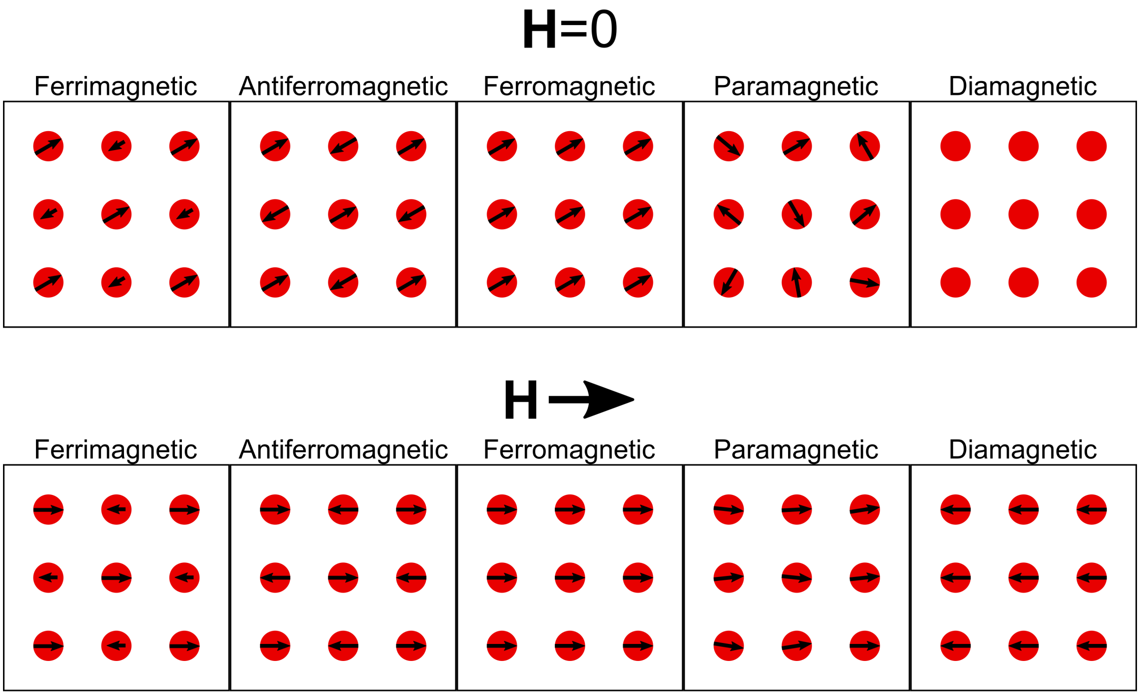

Figure 2.5: Schematic representation of diamagnetic, paramagnetic, ferrimagnetic and antiferromagnetic and ferromagnetic materials' microscopic structures at rest and in the presence of a magnetic field $\boldsymbol{H}$. The red circles are an approximate representation of atoms.

and Tin (Sn). Lastly, diamagnetic materials have magnetic moments anti-parallel to the direction of an applied external magnetic field which creates an induced magnetic field in then in the opposite direction, causing a repulsive force. Diamagnetism is a property of most materials in varying degrees, examples of diamagnetic materials are Silicon (Si), Gold (Au), and Copper (Cu).

These different categories are related to the magnetic susceptibility (χ_m), which gives the relationship with the magnetisation of a material in the presence of an external magnetic field, given by:

$$\boldsymbol{M} = \chi_m \boldsymbol{H}. \tag{2.17}$$

This in turn relates to the induced magnetic flux density ($\boldsymbol{B}$),

$$\boldsymbol{B} = \mu_0(\boldsymbol{H} + \boldsymbol{M}). \tag{2.18}$$

Equation (2.18) shows how the different material's magnetic susceptibility has an effect on the induced magnetic flux density. For paramagnetic materials χ_m >0 which increases the strength of the induced magnetic flux density. Alternatively for diamagnetic materials χ_m <0 which decreases the strength of the induced magnetic flux density, in both of these cases $|\chi_m|$ ≪1. Ferromagnetic materials have a significantly large magnetic susceptibility. The following discussions will now be focused on ferromagnetic materials.

2.2.2 Introduction To Magnetism

On a macroscopic scale, the bulk magnetisation $\boldsymbol{M}$ is field induced. However, on a microscopic scale, the magnetisation varies within a ferromagnet. The exact configuration of the magnetisation depends on the contribution of different energies, Zeeman, magnetostatic energy, anisotropy, magnetoelastic and exchange energies. The total energy related to the magnetic material is the sum of all these energies. The most stable structure is obtained when the overall potential energy is a minimum.

Zeeman energy is named after Pieter Zeeman [13], it is the potential energy of the magnetic moments in the applied magnetic field. The Zeeman energy is at a minimum when all the magnetic moments in a sample are in alignment with the applied field. Magnetostatic energy is the magnetic potential energy due to the external magnetic field surrounding a ferromagnet, this potential energy can be minimised by small domain formation and domain splitting [14]. (Magnetocrystalline) Anisotropy energy is the energy required during magnetisation of ferromagnetic materials to rotate the magnetic domains due to crystalline anisotropy. Magnetoelastic energy is due to an anisotropy with respect to the external elastic tensions. Lastly the exchange energy is the energy due to the exchange interaction. It is associated with the coupling of individual dipole into a single domain, it is a potential energy within a domain and is minimised when all dipole as aligned in one direction. This energy can be positive or negative depending on the atomic structure [14]. Only positive exchange energy results in the dipole alignment in one direction, and therefore, magnetic domains and ferromagnetism. The exchange interaction is quantum mechanical effect that is a short-range effect and occurs between identical particles that are usually nearest-neighbour atoms. The exchange interaction is electrostatic in origin and is a result of the Pauli exclusion principle [15]. The interaction defines the spin system in a magnetic material. In ferromagnetic it is minimised at parallel orientation of all electron spin moments of 3d and 4f shells [15].

Atomic magnetic moments originate from two main sources, the movement of electrons in orbits around the nucleus, i.e. orbital angular momentum, and due to the spin of the electrons, i.e. due to the spin angular momentum and there is a small contribution due to the spin angular momentum of the nucleus. Ferromagnetic materials have a net magnetic moment at the atomic level but display a strong coupling between internal magnetic moments. This causes domains, which are regions within a magnetic material where the magnetisation direction is the same due to the aligned moments, which is a consequence of the exchange interaction.

The direction of the alignment varies from domain to domain in a more or less random manner, although certain crystallographic axes may be preferred by the magnetic moments, which in the absence of an external magnetic field will align with one of these equivalent ‘easy axes’. The reason these domains form is to minimise internal energy. The magnetic domains only occur in ferromagnetic, ferromagnetic and antiferromagnetic materials where there is magnetic ordering. The net magnetisation M is the sum of these moments within the domains. When in the presence of an external magnetic field, domains that are parallel or close to parallel to the field become larger in the expense of those which are not so favourably orientated, i.e. more atomic magnetic moments align themselves towards the direction of the field so that favourable domains become larger.

In ferromagnetic materials, the relationship between the internal magnetic field and the induced magnetic flux density can be shown by the hysteresis loop (or hysteresis curve) of a material. This can also give a large amount of information about the materials magnetic properties. Ferromagnetic materials can be permanently magnetised because they can retain a residual magnetisation, even after the external field is removed. A typical magnetisation curve ("*oa*"), also known as a virgin curve, and a hysteresis loop ("*abcdef*") for a ferromagnetic material are shown in Figure 2.6. As the magnetic field is increased, the magnetisation increases in magnitude in an orientation that is in the direction of the applied field (as regions in which the magnetisation lies in a more energy favourable direction

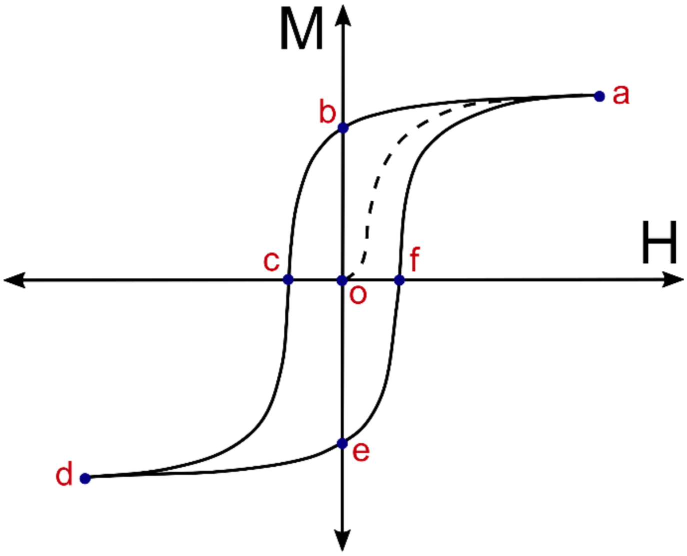

Figure 2.6: The dependence of a ferromagnetic sample's magnetisation M on the applied field H, with "*oa*" showing a virgin loop and "*abcdef*" a hysteresis loop. Where "*o*" is when the sample has not previously been in a magnetic field and is not magnetised, "*a*" and "*d*" show the saturation, "*c*" and "*f*" indicate the coercivity and "*b*" and "*e*" show the remanence of the sample.

will grow at the expense of unfavourable ones by the movement of domain walls). For a sample that is initially not magnetised, due to the random-like nature of the domains, when it is in the presence of a magnetic field it will become magnetised.

For example, for an external magnetic field in the positive direction, a demagnetised ferromagnetic material will follow the path "*oa*". The applied magnetic field at which the material is fully magnetised is known as the saturation field, at which the domain structure is removed shown at "*a*" and "*d*". After the external applied field is increased and the magnetisation is at a maximum, the external field is decreased, the magnetic response of the material will follow the path "*abc*". The residual magnetisation or remanence is the magnetisation that remains if the applied field is decreased to zero, "*b*" and "*e*". The coercive field is the size of the demagnetising field needed to reduce the magnetisation from the remanent field value to zero show at "*c*" and "*f*".

The ratio of the remanence to magnetisation saturation, which can sometimes be called the “squareness” ratio of a sample, indicates how much the magnetisation has decreased from saturation to when no external magnetic field is applied. For a number of applications the perfect ratio would be one, this means it has kept its magnetisation, however in produced materials this is rarely the case.

Ferromagnetic materials are often referred to as hard or soft, these are relative terms. Hard magnetic materials are materials that require a relatively large demagnetising field to reverse its magnetisation direction and therefore, have a larger coercivity and retain their magnetisation in larger external magnetic fields in the opposing direction. On the contrary, soft magnetic materials require a relatively small demagnetising field to reverse its magnetisation direction. Therefore, have relatively small coercivites and are more likely to change their magnetisation to the direction of an external field. An example of a hard magnetic material is neodymium iron boron (NdFeB) and an example of a magnetic material that is considered to be soft is cobalt (Co). Both of these materials are used in this research since they have a larger remanence compared to that of other ferromagnetic materials.

Magnetic anisotropy is the directional dependence of a material’s magnetic moment. Due to anisotropy, there are preferred orientations of the magnetic moment. These are commonly known as "easy" axes and can incorporate several different types of anisotropy. These are the most energy favourable directions and deviations from these directions imposes an additional energy penalty on the system. This magnetic anisotropy is generated from various properties such as, magnetocrystalline, shape, magnetostriction, surface and interface anisotropy.

The anisotropy of most magnetic materials have a magnetocrystalline origin [16]. This is determined by the crystal structure of a material and is an intrinsic anisotropy. Most other types of anisotropy are mainly related to the geometry of the given sample. Magnetocrystaline anisotropy is the preferred alignment of the atomic magnetic moments along a particular crystal direction and primarily arises from the spin orbit interaction of the electrons.

From a phenomenological approach, it was proposed by Akulov, that the anisotropy energy can be expressed in the form of a power series in projections of the magnetisation on the crystal axes and the expressions must be compatible with the symmetry of the crystal lattice [15]. For example, in cubic structures the energy density due to the crystal anisotropy is [15],

$$E_{ani} = K_0 + K_1(\varrho_x^2\varrho_y^2. + \varrho_y^2\varrho_z^2 + \varrho_z^2\varrho_x^2) + K_2\varrho_x^2\varrho_y^2\varrho_z^2 + ... \tag{2.19}$$

where ϱ_x, ϱ_y and ϱ_z are the directional cosines of the normalised magnetisation with respect to the Cartesian axes of the lattice. K_i's are the magnetocrystalline anisotropy constants, i.e., K_0, K_1, and K_2 are the crystalline anisotropy constants of zero, first and second order, respectively. Some crystal systems have a single axis of high symmetry, this is called uni-axial anisotropy. The energy density is represented by [15],

$$E_{ani} = K^V \sin^2\theta_E + ... \tag{2.20}$$

where K^V is the uni-axial volume magnetocrystalline anisotropy constant and θ_E is the angle between the uni-axial and the direction of magnetisation.

Shape anisotropy is the preference for the magnetisation to lie along a particular geometric axis, the shape creates a demagnetising field that is not equal in all directions, creating one or more easy axes.

On a simplistic level, magnetostrictive anisotropy is the physical shrinking or expansion of a ferromagnet in the direction of the magnetisation when it is magnetised by an external field. It is due to the magneto-elastic constants of the crystal lattice. Surface and interface anisotropy are induced by the broken symmetry at surfaces and interfaces of magnetic thin films and multilayer and therefore, are not relevant for this study due to the nature of the samples.

A large remanence field can be obtained by providing a large anisotropy field which can be achieved either by using a certain geometry or by choosing a material that has a strong crystalline anisotropy. Studies have shown that in the second case, materials like sintered NdFeB permanent magnets or cobalt based alloys are particularly good candidates due to their ideal crystalline structure. Sintered NdFeB is shown to have a tetragonal crystalline structure [17], while cobalt-based alloys utilise the high crystalline anisotropy of the hexagonal close-packed (hcp) structure of Co and a suitable microstructure [18].

There are two key types of magnetic forces present in most magnetic-fluidic systems. These are the torque and dipole interactions. When a magnetic element is in the presence of a constant external magnetic field ($\boldsymbol{H}$) a torque is exerted ($\boldsymbol{\tau}$), given by [19],

$$\boldsymbol{\tau} = \mu_0 \boldsymbol{m} \times \boldsymbol{H}. \tag{2.21}$$

Where μ_0 is the permeability of free space with the value $4\pi \times 10^{-7}$ Hm^{-1} and $\boldsymbol{m}$ is the magnetic moment of an element. The magnetic moment has a relationship with magnetisation ($\boldsymbol{M}$), given by

$$\boldsymbol{m} = \int_V \boldsymbol{M}\, dV, \tag{2.22}$$

where dV is the volume element. Looking at Equation (2.21) and Equation (2.22), it can be seen that the torque experienced by an object is dependent of the orientation of the object and the external magnetic field (i.e. the angle between $\boldsymbol{m}$ and $\boldsymbol{H}$), the strength of the external magnetic field, the magnetisation and volume of the object.

Another equation in this research is the magnetic flux density. Any system with a magnetic moment will produce an induced magnetic flux density ($\boldsymbol{B}$). For a point dipole magnetic moment the magnetic flux density is given (in tesla) by [19]

$$\boldsymbol{B} = \frac{\mu_0}{4\pi} \left(\frac{3(\boldsymbol{m} \cdot \boldsymbol{r})\boldsymbol{r}}{r^5} - \frac{\boldsymbol{m}}{r^3} \right). \tag{2.23}$$

Where $\boldsymbol{r}$ is the position vector originating from the point of the magnetic moment. When considering two magnetic moments, the force $\boldsymbol{F}_{dip}$ exerted by a magnetic moment ($\boldsymbol{m}_a$) on another magnetic moment ($\boldsymbol{m}_b$) separated in space by a vector $\boldsymbol{r}$ is defined by [20]:

$$\boldsymbol{F}_{dip} = \nabla(\boldsymbol{m}_b \cdot \boldsymbol{B}_a). \tag{2.24}$$

The derivative is then taken to obtain [20]

$$\boldsymbol{F}_{dip}(\boldsymbol{r},\boldsymbol{m_a},\boldsymbol{m_b}) = \frac{3\mu_0}{4\pi r^5}\Bigg((\boldsymbol{m_a}\cdot\boldsymbol{r})\boldsymbol{m_b} + (\boldsymbol{m_b}\cdot\boldsymbol{r})\boldsymbol{m_a} + (\boldsymbol{m_a}\cdot\boldsymbol{m_b})\boldsymbol{r} - \frac{5(\boldsymbol{m_a}\cdot\boldsymbol{r})(\boldsymbol{m_b}\cdot\boldsymbol{r})}{r^2}\Bigg). \tag{2.25}$$

2.3 Summary

In this chapter, the fundamental concepts that underpin this research area have been covered. Initially beginning with the relevant fluid dynamic concepts, including the Navier-Stokes equation and Reynolds number. This has then focused on low Reynolds number systems and the underlining issue of producing net motion in such a regime. This is due to the time independent nature of the system which is shown by Purcell's Scallop Theorem. Many biological organisms, including bacteria and sperm cells, are able to swim in low Reynolds number environments, which is why many researchers attempt to mimic these designs artificially.

The chosen method of actuation for the work presented in this thesis is by using magnetic fields. Therefore, a section has been dedicated to the underpinning physics of magnetic materials and the relevant forces, focusing on ferromagnetism.

Chapter 3

Review Of Current Devices & Fabrication Techniques

3.1 Microfluidic Swimming Devices

There has been a large interest in adapting biological and theoretical swimming mechanisms for the creation of artificial devices that achieve a net movement in low Reynolds number regimes. These devices could lead the way for a number of potential applications, such transport and delivery of substances to specific sites. This includes targeted drug delivery or active pumps in microfluidic technology such as lab-on-a-chip devices and diagnostic tests. It has been discussed in Section 2.1.3 that there is a requirement for a non-reciprocal motion to generate a net movement in a low Reynolds number environment, but this is only part of the problem. This leads to the key question: how to generate this sequence of

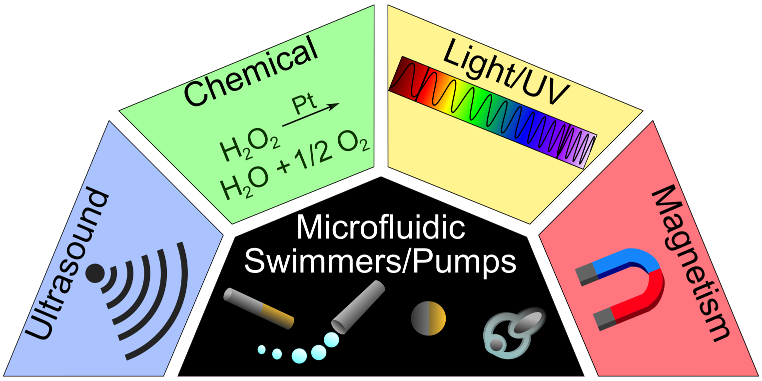

Figure 3.1: Diagram indicating the different types of actuation used for microswimmers with some microswimmer examples.

movements? There have been a few proposed mechanisms involving chemicals, electrical fields, ultrasound, light and magnetic actuation.

3.1.1 Microscale Swimming Devices

Chemically Actuated Micromotors

Micromotors which use chemical reactions for their actuation transform the fuel energy into kinetic energy. Often, a part of the micromotor consists of a catalyst, such as platinum, silver or palladium and this reacts with the fluid it is in, usually hydrogen peroxide or organic compounds. However, these motors can be difficult to control. Some of these chemical micromotors act like microjets, expelling gas bubbles from one end of an asymmetrical tube [21–24]. An example of this uses a rolled up microtube consisting of Pt/Au/Fe/Ti multilayers in Hydrogen peroxide [21]. Due to the magnetic layer in the microtube, the trajectories of the swimmer could be controlled by applying external rotating magnetic fields. This microtube system was able to produce a swimming speed of 2 mms^{-1} (approximately 50 body-lengths per second) [21]. Other designs use two different metals, often platinum/gold (as platinum is catalytic and gold is not) in hydrogen peroxide and use whats known as self-electrophoresis [25–27]. The decomposition of the hydrogen peroxide, due to the catalyst, produces positively charged hydrogen ions at the surface of the anode (Pt) and they are consumed them at the cathode (Au).This causes a different ion distribution each side of the motor. The attraction between these oppositely charged ions brings them towards each other, and the effect of this within the surrounding fluid causes the swimmer to propel.

Another method of using chemicals for propelling micromotors is using a design known as Janus particles/spheres. These are nano/micro particles whose surfaces have two distinct physical properties, normally by using two different materials. These often use spheres made of a nonconducting material, e.g. polystyrene [28] or silica [29–31], of the order of a few micrometers capped with Pt, of the order of nanometres in thickness, over the hemisphere. Again, these are surrounded in hydrogen peroxide. The Janus particles/spheres work similarly to the other chemical motors discussed previously as their motion is connected to diffusiophoresis. At short intervals, the particles move predominantly in a directed way, with a velocity that depends on the concentration of the fuel molecules. However as time increases, the motion reverts to a random path. Efforts have been made to lower the concentration of the hydrogen peroxide [32,33] as well as utilising other fuels, such as glucose or urea [8,10,34,35], however the concentrations of these fluids is higher than physiological levels and the velocities have been slower than that of other chemical swimmers. Water has even been used with Ga/Al [36]. Others use different materials such as manganese, zinc or carbon-based materials that decompose in acidic environments [10,35,37,38].

Although these motors can be relatively fast compared to motors actuated via other methods, their direction is influenced by random fluctuations due to the nature of a chemical reaction. Additionally, there is no on/off mechanism to these swimmers so there is no control for when they are activated. In addition to this, many of these devices require hydrogen peroxide to work, the toxicity of the concentrated solution is not suitable for applications in many fields, especially biomedical areas.

Light Actuated Micromotors

Light, as a wireless transmittable energy source that is easy to control, has been used to propel micromotors. Many organisms depend on light to move using a biochemical process, photo-taxis. Due to light being used by many organisms and that it is a wireless transmittable energy source, there has been a large amount of interest in light induced micromotors. Overall there are two main categories of light propelled micromotors, those using photocatalytic processes and those using the heating effect, thermophoresis. Using thermoresponsive materials has acquired significant interest, while it is possible to directly exploit the thermal response of materials or induce it by inductive heating of embedded magnetic particles, a more practical and versatile solutions is to trigger this response using light. The most common photoresponsive materials for soft microbots are hydrogels based on lower critical solution temperature polymers and liquid-crystal elastomers [7]. Some of these photo catalytic processes cause bubble propulsion or self-electrophoresis for example, and have similar limitations as the chemical micromotors, such as fuel, but display more control in terms of on/off and direction of motion. An example of these are tubular structures, which are similar to the chemical micromotors and propel via bubbles that are actuated by light [39, 40]. These require fuel similar to the chemical swimmers but with more control in terms of on/off and motion.

Popular light controlled micromotors are "Janus" particles. Similar to those discussed with chemical micromotors, they have two different surfaces, a light-active and an inactive surface on opposing sides. The light can initiate a local reaction via a photocatalytic process [9, 41–44] or a photo thermal effect [45, 46], the active surface of the colloid breaks the symmetry and local fluid flows resulting in a response which causes the motion of the particle [7].

There are also designs different to that seen in chemical swimmers, such as using a polymer film containing azobenzene chromophore [47]. The azobenzene chromophore reacts in UV light and is connected to the flagellum which is made up of flexible polymer [47]. Switching between UV and white light drives the flagellum to swing in an oscillatory motion which results in propelling the swimmer at an average swimming speed of 142 μms^{-1} [47].

Other approaches use induced temperature gradients to drive thermophoretic swimmers. One design has been produced using liquid-crystal elastomers to create cylindrically shaped (200 µm diameter and 1 mm length) micro-robots which are driven by structured monochromatic light [48]. This light can create travelling waves along the surface of the device, and propel at 200 µms^{-1} [48]. In addition to these structures, some use a helical ribbon structure made of a hydrogel with gold nanorods (helical contour length 160 µm) and actuate via plasmonic heating, achieving longitudinal speeds of 20 µms^{-1} [49].

Although light-based control has several advantages, like the remote manoeuvre on demand with excellent spatial and temporal resolution, etc., there are some limitations, such as these systems can only have 2D control whereas magnetic fields can be used to control in 3D. In addition to this, light-based control requires that the micro-devices move in a clear transparent medium which limits the applications.

Ultrasound Actuated Micromotors

Progress has been made toward the fabrication of micromotors that can be propelled using ultrasound. This is an attractive option as high frequency sound waves, in particular in the MHz regime, are known have minimal deleterious effects on biological systems [50]. In addition to this, ultrasound is already known to be used in medical diagnostics tests for decades, an obvious example of this is ultrasound scans. Some micromotor examples use nano/microrods, that are typically metallic rods that are a few micrometres in length propelled via pulsed or continuous ultrasound that translates along and rotate around the long axis [51–53], others use ultrasound to vaporise a perfluorocarbon compound on a "microbullet" to trigger a force to penetrate cellular tissue [26]. Looking more in depth into the microrods, it has been shown that standing waves in the MHz frequency can levitate, rotate, align, assemble and propel at speeds of 200 µms^{-1} these microrods of AuRu or AuPt [51]. These systems are assumed to have a directional motion due to the asymmetric shape of the rods, leading to the longitudinal asymmetric distribution of microrod and the acoustic pressure created [51, 53]. As commented on, these systems have several benefits, such as no required fuel and bio-compatible actuation. However they have limitations in their directionality. Methods have been studied to solve this by using a magnetic field to guide the rods with an added nickel strip [52]. However, then two different external pieces of equipment are needed to actuate and direct the micromotor rather than one. This leads onto the question: why not only use magnetic fields for actuation?

Electromagnetically Actuated Micromotors

Over the last decade, the idea of using magnetism to actuate micromotors has attracted a significant amount of interest due to its promising properties. Similarly to light, magnetic actuation provides a wireless transmittable energy source that possesses several properties that could be varied (i.e. frequency, orientation, strength). These properties could then be used to control and turn on/off the swimmers and do not require a transparent medium like light does. Similarly to ultrasound, magnetic fields are already known to be used in medical diagnostic tests, such as MRI (field strengths usually between 0.5 - 1.5 T [54]) and present no clear and convincing evidence from animal or cellular studies that demonstrates deleterious biological effects for the fields investigated (a few Tesla and below) [55–57]. In addition to this, other methods of actuation (chemical and ultrasound) have also incorporated magnetic components into their designs to aid them in their direction of propagation. However, using magnetic actuation does not come without it's own challenges. A permanent magnet or electromagnet could be used to actuate a micromotor but magnetic fields decas with distance rapidly and this has to be accounted for when designing magnetic actuation setups and choosing magnetic propulsion methods. Magnetically actuated microfluidic systems will be expanded on in Section 3.1.4.

3.1.2 Pumping Actuation Methods

From biology, to medicine, to space exploration, microelectronics cooling, pumps and valves are common components in most industrial or scientific systems involving fluid. For many microfluidic systems, active, self-contained small pumps are highly desirable [58]. In most laboratory experimental set-ups external pumps are often used as they allow for accurate control which is user friendly.

Micropumps are active devices embedded on a chip that aim at generating and maintaining a microfluidic flow. These micropumps are most commonly fabricated using pre-existing micro-electro-mechanical systems (MEMS) techniques on substrates such as silicon, glass or polymers (e.g polyymethylmethacrylate (PMMA), polydimethylsiloxane (PDMS), or SU-8 photo resist) [59].

Most microfluidic systems operate under a low Reynolds regime (where viscous forces dominate over inertia, Section 2.1.2). This is due to the length scale of the systems and the viscosity of the fluids used. These systems are required to function under the same restrictions as that of their swimming counterparts, that being that a time independent motion is required. Therefore, the micropump requires more than one degree of freedom.

The first accepted micropumps, initially reported in the 70s, were based on the actuation of both the pump diaphragm and the valves [60–62]. However, only after the fabrications of Smits [63] and Van Lintel [64] in the 90s, more intensive research in this area began.

Mechanical and Non-mechanical Micropumps

Most of the produced micropumps fall in either of the groups "mechanical" or "non-mechanical" (sometimes called dynamic pumps [65]) [59, 66, 67]. Non-mechanical micropumps do not require any moving components. They use specific mechanisms to transform a form of non-mechanical energy into kinetic momentum so as to drive the fluid contained within an arrangement of microchannels. These types of pumps cannot be found on a macro-scale and make use of physical properties of the fluid which can only be utilised when operating within a microscale or smaller. Examples of this include electro-chemical, electro-wetting, electro-osmotic, magneto-hydrodynamic, electro-hydrodynamic, bubble type and evaporation type pumps [59, 65, 66].

Whereas, mechanical micropumps use physical actuation or a mechanism, such as a diaphragm or a closing/opening valve, etc., to perform the pumping action. For a mechanical micropump to function within a low Reynolds number regime, the micropump must execute an asymmetric stroke. This means the stroke, in returning to its original position must not trace the exact path of the original stroke in a particular direction (i.e. backward stroke must not be the exact reverse of the forward stroke) if a net movement of fluid is to be achieved.

This could be achieved using a system of valves, but a design such as this would likely increase complexity and the space occupied by a structure. Both of these factors would likely increase the production cost involved in the process. Currently a range of available micro actuation techniques have been used to design micropumps. Some of the most common principles include piezoelectric, thermo-pneumatic, electrostatic and electromagnetic actuation.

Piezoelectric Micropumps

Micropumps based on a piezoelectric diaphragm are the most common types of mechanical micropumps. Piezoelectric materials deform when subjected to an external voltage. This effect is utilised by attaching a piezoelectric material to a pump diaphragm with an AC voltage to induce an oscillatory motion which produces the pressure required to generate suction and discharge flow alternately. The advantages of this design are the fast response and simple structure but the drawbacks include a complex fabrication process, high actuation voltage and a small stroke [6, 59, 65, 66].

Thermo-pneumatic Micropumps

Thermo-pneumatic type actuation mechanisms for micropumps are also an important category. Thermo-pneumatic actuators commonly consist of a heater and a diaphragm connecting two chambers (one main driving chamber and another to aid actuation normally filled with air). These micropumps utilise a change in volume of the chamber or a change in phase of the fluid within the chamber due to heat. In the case of volume, a periodical change of the volume within the chamber induces a corresponding change in pressure within the cavity. This in turn actuates the flexible diaphragm, which in turn deforms the "main" chamber. Alternating between heating and cooling causes an oscillatory movement of the diaphragm which results in a pumping action. These have the advantage of being relatively simple in design, having a low actuation volume and a large diaphragm displacement, to name a few. The main limitation relates to the high temperature sensitivity of the working fluid and when used for biological application, a high temperature elevation can damage the working fluid, such as coagulation of protein, damaging blood cells, etc., [65]. As well as other disadvantages, such as high power consumption and long response times, further limiting the applications [6].

Electrostatic Micropumps

Another major category of mechanical micropumps use electrostatic actuation. These micropumps are most commonly based on the principle of Parallel Plate Capacitors [59,65]. The diaphragm or membrane associated with the electrostatic micropump gets attracted or repelled by an electrostatic force that is produced by an applied electric field, this mechanical movement will be interpreted as the pumping action [66]. These have the advantage of low power consumption (as it required a low actuation voltage), fast response, high actuating force generation and good control on its diaphragm deflection but has a key disadvantage which is its small stroke length [6, 65].

Electromagnetic Micropumps

The last major category of mechanical micropumps discussed here use electromagnetic actuation. The basic mechanism of this actuation involves the interaction between a magnet and a produced magnetic field which creates a dipole force between them. A commonly used structure is a system that consists of a magnetic field source (the electromagnetic coil) and the membrane component which is a flexible structure with an attached magnet [6]. The generated magnetic field is able to cause the membrane to deform, due to the attached magnet, and provide the pump actuation. This has the attractive features of producing a high force generation with relatively low operating voltage, contactless actuation, a large frequency range, ease of control and the ability to produce a large stroke. Some of the limitations are the requirement of an external magnetic field, thermal effect and high power consumption [6, 65, 68] (Electromagnetic Micropumps have a power consumption within the range of 13 mW to 7 W [6] whereas electrostatic pumps are typically in the order of 1 mW [65]). In addition to these advantages, it has been reported that "The combination of nozzle/diffuser elements with an electromagnetically actuated PDMS (Polydimethylsiloxane) membrane provides large deflection amplitude and flow rates both for water and air which could be successfully applied for low cost and disposable lab-on-a-chip systems." [65]. Although these devices offer a practical solution for pumping, they would be unable to operate in a low Reynolds number regime due to the reciprocal motion of the pumping mechanism.

Pumping Methods Conclusion

Producing a valve-free pump is not a trivial problem, as previously mentioned it requires an asymmetric stroke cycle. This challenge is similar to that of a swimming device in a low Reynolds number regime. Swimming and pumping are related by a "change of reference". A low Reynolds number swimming system can become a micropump by spatially restricting the swimmer in some way in order for it to drive the flow rather than propel itself.

3.1.3 Lab-On-A-Chip Technology

One of the key technological advancements that has changed the way we live over the past half century is miniaturisation. An example of this includes transistors, which are incorporated into electronics such as the modern mobile telephone. Lab-on-a-chip (LOC) technology has become an increasingly stimulating area of research over the last couple of decades due to the similarly shared goal of downsizing technology. This term is utilised for small, handheld devices that

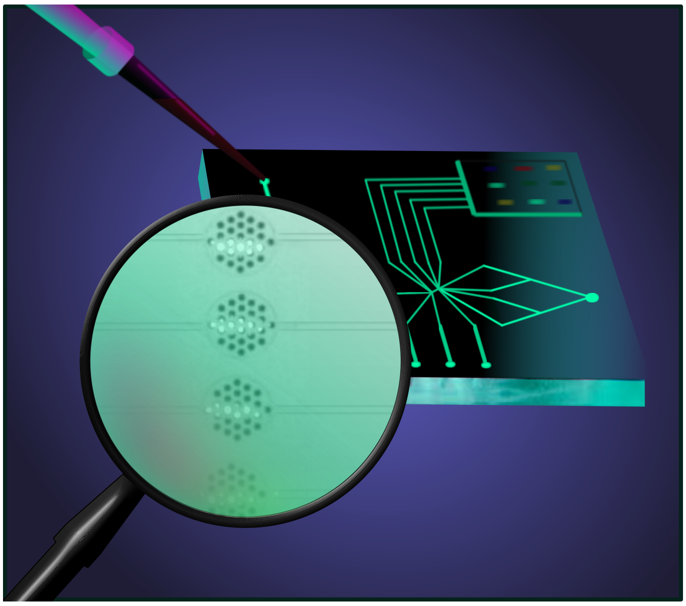

Figure 3.2: Diagram indicating how micromotors/swimmers could be used in lab-on-a-chip devices.

integrate singular or several laboratory functions that are scaled down to within one unit or ‘chip’. The term chip in LOC technology does not necessarily refer to a ‘traditional’ chip, such as a silicon chip in electronics [69]. These chips range in sizes of millimetres to a few centimetres in scale [70] and so remain being hand-held. They are fabricated using a wide variety of materials which can include silicon, but also includes materials such as glass or polymers compared to the traditional fabrication of traditional chips [69]. For LOC technology, a much wider variety of fabrication technologies are used for the production of the devices [69].

LOC technology has the potential to be used in a diverse range of biomedical and other analytical applications. Examples would include rapid pathogen detection, forensic science, electrophoresis, environmental monitoring and undoubtedly medical diagnostics, to name but a few [69, 70]. However, the vast majority of LOC devices are connected to microfluidics and sensing capabilities [69]. The microfluidic sections of LOC devices refer to the areas where physics related to the flow of fluids is important within these devices. These are sections such as channels, pumps, mixers and valves, which to be incorporated into these LOCs.

The interest with these devices is partly due to their potential to be used within different point-of-care (POC) devices. POC devices perform analytical or diagnostic tests at the "point of care", such as by a patient in a hospital, at a local doctor's surgery, or even in the field. This is in order to provide rapid, on-site results without the need of being sent to an external laboratory. This caused many researchers to begin to explore microfluidics further and try to miniaturize biochemical operation in the 90s.

A POC device is defined as a medical diagnostic testing device which can be performed near the patient. In addition to this, these devices aim to have a short turn around time and to be user friendly [71]. The importance of these POC devices has been particularly evident within the last year due to the COVID-19 pandemic. Over 34,500,000 coronavirus tests were conducted in March 2021 alone [72]. The benefit of tests not requiring a laboratory has being principal in reducing the time needed to provide the result. It has been seen that the speed of providing the result can reduce the spread of infection.

Arguably, the first lab-on-a-chip was created in 1979 at Stanford University for a gas chromatographic air analyzer, fabricated on a 2 inch silicon wafer [73]. Since then there has been a growing interest in this field, though this novel LOC technology is not fully developed yet. However the growth of these technologies can be partly attributed to the rapidly evolving field of micro-fabrication technologies, including lithographic techniques, which were essential to the manufacture of the first few LOC devices.

The concurrent development of novel materials would greatly aid the development of LOC technology. An example of this co-development benefit could be found in materials aiding the flow of fluids between areas on the device, the release of chemicals within the device and the mixing of fluids around the sensors so localised concentration does not affect the results. In addition to this, they have the potential to be integrated into devices for refined drug delivery for controlled drug release, controlling the flow of fluids and advanced pumping mechanisms.

3.1.4 Magnetically Actuated Microfluidic Devices

In this section magnetically actuated swimmers, membranes and array systems will be discussed. The vast majority of these devices rely on magnetic torque in some part, for their actuation. The majority of these devices are actuated by either rotating magnetic fields or oscillating magnetic fields. In a rotating field the flux density $\boldsymbol{B}$ rotates around a central axis, whereas, in an oscillating field the flux density $\boldsymbol{B}$ changes direction in plane. These magnetically actuated devices can be separated into several groups, magnetic swimming devices incorporated with rigid components (referred to as rigid swimmers), magnetic swimming devices incorporated with flexible components (referred to as flexible swimmers) and array or membrane-like magnetic systems.

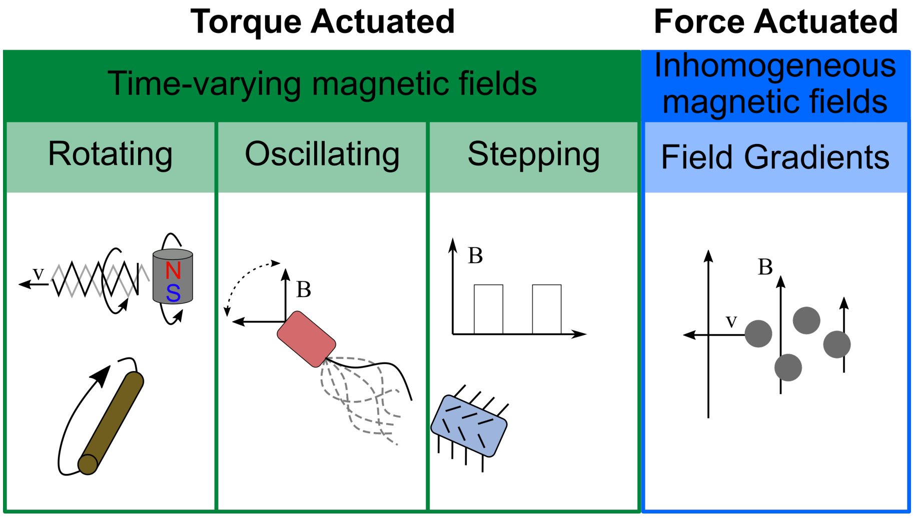

Figure 3.3: Different magnetic fields used for the actuation of different designs of magnetic micro/nano swimmers.

Rigid Swimmers

Rigid devices rely on their complex geometry, intricate field or delicate design, which may involve a number of detached components, in order to achieve their asymmetric motion. One of the most well studied and experimentally investigated rigid magnetic microswimmers are known as helical swimmers or helices. The helical structure was inspired by the rotating bacteria's flagella, that have a cork screw like shape. Helical microswimmers are actuated using rotating magnetic fields, the swimmer is rotated around its helical axis and the direction of motion is perpendicular to the plane of rotation [5]. Due to this, the micromotor can be propelled forwards or backwards simply by reversing the direction of rotation of the magnetic field. The first low Reynolds number helical rigid swimmer was a few centimeters in range and comprised of a $SmCo_5$ cubic magnet attached to a spiral of copper wire (a low Reynolds number was achieved by using a viscous oil) [74]. Since then many experimental micro-helices have been reported

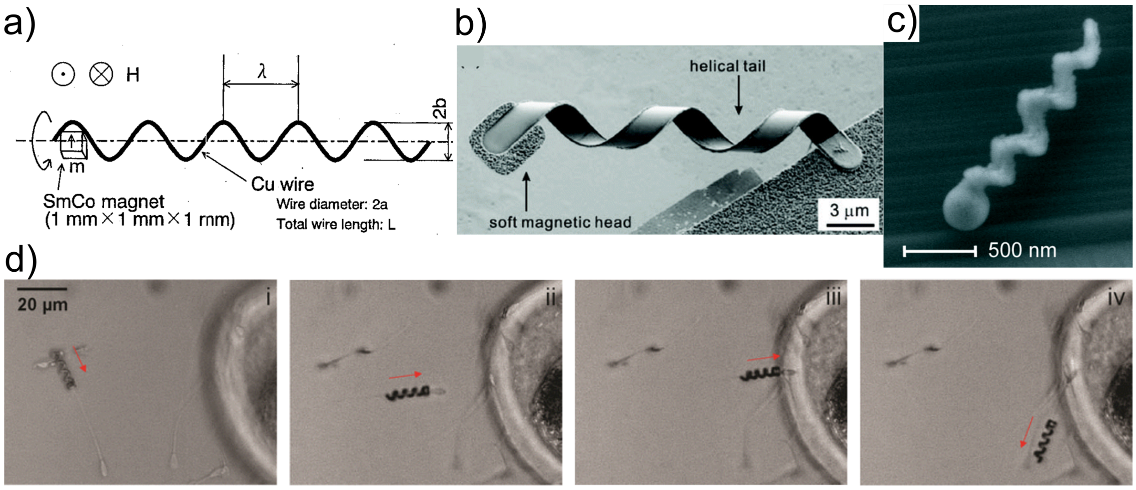

Figure 3.4: Examples of helical swimmers. a) Schematic view of the first low Reynolds number helical rigid swimmer, figure from [74]. b) SEM image of GaAs/GaAs/Cr trilayer helical swimmer with a soft Cr/Ni/Au trilayer "head", figure from [75]. c) SEM image of an individual nanostructured helix, figure from [76]. d) Showing that a spermbot was able to (i), transport (ii), approach to the oocyte membrane (iii), and release (iv) the sperm cell, figure from [77].

in literature, varying in size, fabrication method and anticipated application. Even through helices can be considered a fundamental shape of nature, one of the main challenges with these swimmers is creating a fabrication process for these helices that is repeatable, has control over the design parameters and is suitable for the application of the magnetic material necessary for the swimmer.

In 2007, Nelson's group developed the first micro-scaled helical swimmer mimicking bacterial propulsion [78] and was further characterised in 2009 [75, 79]. Their artificial bacterial flagellum consisted of a rigid helical tail attached to a soft magnetic metal "head" and the swimmer was in a reservoir of either water or paraffin oil.

The tail had a diameter of 2.8 µm, lengths of 30-100 µm, and was initially a GaAs/GaAs bilayer but later developed to be a GaAs/GaAs/Cr trilayer while the head was initially Ni but developed to be Cr/Ni/Au trilayer 4.5 µm $\times$ 4.5 µm with thickness of 200 nm.

The fabrication of the swimmer incorporates a number of techniques, including lithographic, epigrowth and e-beam evaporation and was based on the self-scrolling technique, this relies on the (controlled) internal stress of thin material layers to roll into a desired 3D shape which is defined by the crystal orientation. In 2009 smaller helices (200-300 nm width, 1-2 µm length) were fabricated using glancing angle deposition (GLAD) by P. Fischer's group [76]. This method uses spherical seeds on which helical pillars are grown through the rotation of a tilted stage during evaporation of the SiO$_2$, this step is followed by depositing a thin (30 nm) layer of cobalt onto the surface (which covers half the helix). This fabrication method allows for a number of micromotors to be produced simultaneously. It was observed that for frequencies around 150 Hz with a field of $\sim$5 mT, the micromotors achieved a speed of $\sim$40 µms^{-1}. This type of swimmers have been a large point of focus for several groups. A particular example is the so-called "Spermbots" produced by M. Median-Sanchez group [77]. These were fabricated using Direct Laser Writing and were coated with a soft-magnetic NiTi layer. These helical swimmers were used for the capture, transport, and release a single immotile living sperm cell (without damaging the cell) and have a peak speed of 70 µms^{-1}.

Helices are not the only rigid magnetic microswimmers. A smaller subset of mi-

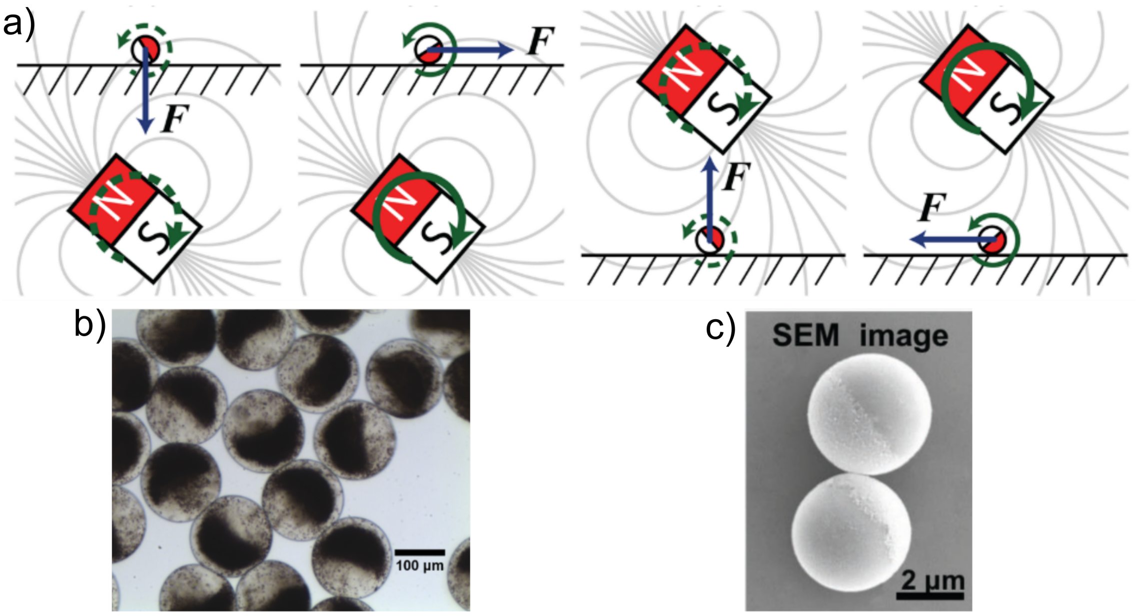

Figure 3.5: Examples of surface walkers. a) Schematic view of the simplest design of surface walker, figure from [80]. b) Bright field image of artificial cells surface walkers containing Fe_2O_3 nanoparticles in one hemisphere and live cells in the other, figure from [81]. c) SEM image of a pair of microdimers, highlighting its staggered shape and the magnetic hemispheres, figure from [82].

cromotors/swimmers are known as surface walkers. These devices rely on surface interactions and require an air-fluid or fluid-fluid boundary to propel (but the device may not need direct contact). The need for a near surface remains to be the fields biggest issue with regards to applications. These devices can be activated using a rotating field or an oscillating on/off field depending on their design. Their movement stroke is can be thought of as a "roll" or tumble along the boundary, which is due to the fluid drag imbalance [5]. One of the simplest examples of a surface walker is a permanently magnetised sphere in a rotating magnetic field [80, 81], see Figure 3.5. A recent example of a magnetically actuated micro-surface walker is the Janus microdimer surface walker, consisting of two Ni/SiO_2

Janus spheres connected by magnetic forces [82]. Under the influence of a planar oscillating magnetic field and near a surface, the spheres roll over each other in an asymmetric fashion that can be thought of as feet walking. These can achieve speeds of up to 18.6 µms^{-1} ($\sim$4 body-lengths s^{-1}) in an oscillating magnetic field operated at 25 Hz and $\sim$2.7 mT.

Very often biological microswimmers appear in large groups rather than as individual swimmers. If their density is sufficiently high, interactions between the swimmers become important. This has been mimicked in laboratories by investigating the collective behavior of active self-propelled microswimmers (sometimes known as swarm microswimmers) [83,83–91,91,92]. In this case, collisions have a large effect on the movement and these collisions depend on the shape of the colliding swimmers and on their self-propulsion. This has become a popular area of research within magnetic microswimmers as magnetic actuation lends itself to the uniform control of swarms, as all would receive the same magnetic field input and no addition power is required to actuate one or many within a certain area. It does however, remain a challenge to steer control/steer groups or individual swimmers from the bulk. This could be archived by the different groups being designed differently.

Several different groups have dedicated their research into investigating magnetic swarms. Some of these swarm swimmers have been designed to be activated by rotating magnetic fields [83–89], while others oscillating magnetic fields [90–92]. A number of different designs have been created, some are similar to that of surface walkers and require a surface [83,90,91], while others based on helical

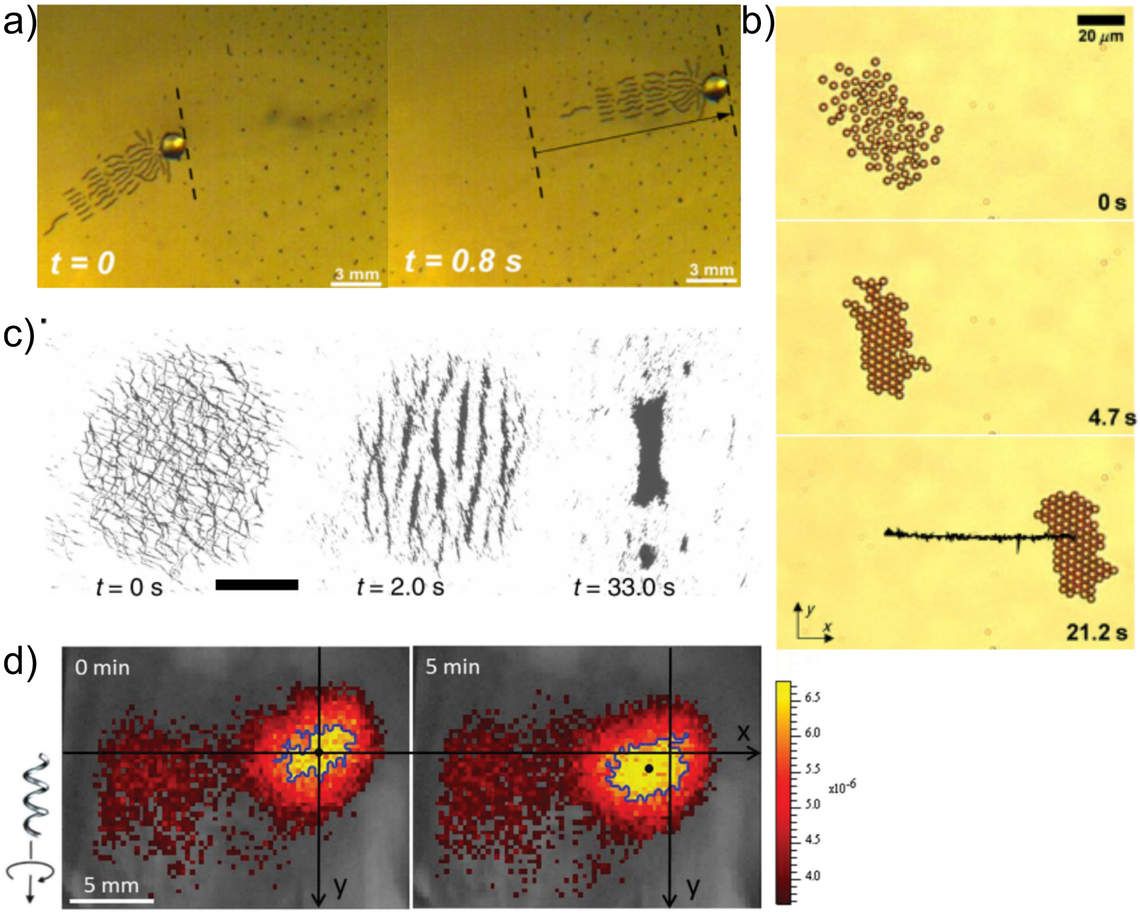

Figure 3.6: Examples of swarm swimmers, a) snake-particle hybrid comprising of nickel microparticles at a liquid-air surface activated by a 80 Hz, applied field 8 kA/m moving a glass bead, figure adapted from [91]. b) Snapshots of a colloidal carpet comprising of paramagnetic micro colloids and propelled by an applied field, $\boldsymbol{H}$ amplitude in (xy) plane 1800 Am^{-1} and z direction 1400 Am^{-1}, frequencies 942.5 rad s^{-1}, figure from [86]. c) The generation process of a reconfigurable ribbon-like paramagnetic nano-particle swarm (scale bar 800 µm) figure from [92]. d) A swarm of functionalised magnetic helical structures (80,000 in number in 400 µl) in the intra peritoneal cavity of a Balb-C mouse swimming downward under the actuation of a rotating magnetic field (9 mT, 90 Hz), (The yellow contour was used to determine the movement of the swarm of magnetic helical swimmers, calculated by the author's Matlab code), figure from [89].

swimmers [84, 88, 89] and others on spherical magnetic particles [85–87] or even ribbons [92].

An example produced by A. Snezhko [91, 93] displays a novel snake-like self-assembled structure. These are comprised of nickel microparticles at a liquid-air surface and are induced by a vertical alternating magnetic field. However, an additional in-plane DC magnetic field was applied to probe the magnetic properties of the structure. These snake-like structures emerge as a result of the competition between the magnetic and hydrodynamic forces. It is worth noting that above a certain frequency some of the structures break symmetry and turn to swimmers [91]. Structures like these are of great interest, however designs like this rely on the surface interactions, making them impractical for many of the desired bulk fluid applications similarly to many other "surface walkers".

A further example of swarm swimmers are magnetic colloidal carpets [86]. These are comprised of paramagnetic micro colloids that are linked together via a dipole force. This is induced by applying a conical oscillating magnetic field which can be used to steer the carpet. These are suspended in high-deionized water which is then sandwiched between a glass side and cover slip along with with tracer beads. The field induces the hydrodynamic propulsion of the structure. While this device is interesting for transport of biological cargo such as cells, the surface still plays a part in the interaction so would not be suitable in bulk. Some devices within this category rely on a comparatively small number in chain-like structures compared to the bulk designs previously mentioned [94]. This design was very similar to [86] but instead of carpets, these particles formed chains that can transport a vesicle. The vesicle contains a particle which is linked to those outside the vesicle by a dipole force. An elliptical polarized magnetic field rotating in plane perpendicular to the ground again induces propulsion of the hybrid composite.

Flexible Swimmers

Flexible magnetic devices are attractive due to the potential to further advance a wide number of technological areas. Flexible swimmers, as the name suggests, have flexible components usually joints, tails or links, allowing for deformations in the presence of a magnetic field. These devices are propelled because of an undulatory motion and are usually actuated by oscillating or rotating magnetic fields [95].

The fabrication of these devices offer a number of challenges, this is partly due to the fabrication of ferromagnetic materials on a microscale and then the incorporation of these within elastic structures. A large number of these magnetic materials with elastic elements have Polydimethylsiloxane (PDMS) components, which is a silicon based elastic polymer largely used in microfluidics. Although a large proportion of these fabricated devices use PDMS combined with magnetic components; the structures, patterns, overall size and magnetic materials vary in many ways among the devices.

One of the earliest examples of a magnetic flexible device was produced by Saotome *et al.* [96]. It was created using two small NdFeB magnets (0.7 mm × 0.7 mm × 2 mm), with a rubber film connecting them and additional "fins" attached to

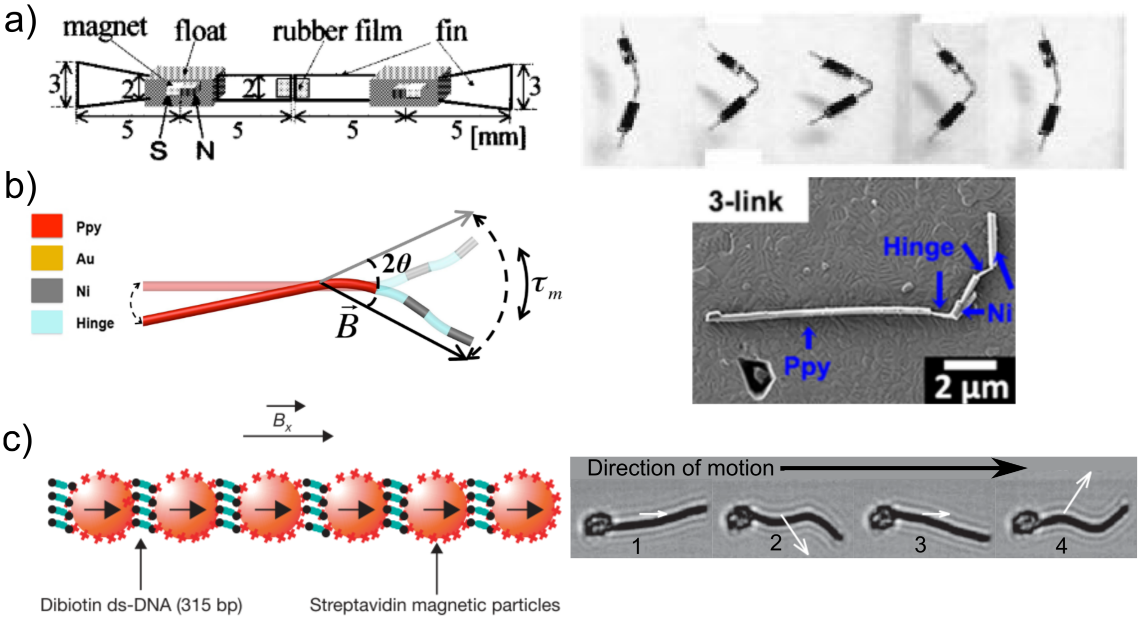

Figure 3.7: Examples of flexible swimmers with the schematic diagram alongside photos of the device. a) The structure of one of the earliest examples of a magnetic flexible device with photographs of the movement of the device when an DC and AC magnetic field is applied, figure adapted from [96]. b) Schematic of a 3-link nanoswimmer with a SEM image of the device, figure adapted from [97]. c) Schematic representation of a flexible magnetic filament based on a sperm cell with the beating pattern of the motion of the filament, the white arrows represent the magnetic field ($\boldsymbol{B}$ amplitude in x and y direction 8.3 mT and 13.7 mT respectively with an frequency of 10 Hz). The black arrow on the top shows the direction of motion. The filament length is 24 mm, figure adapted from [98].

the magnet. It was activated by an AC sinusoidal magnetic field combined with a DC magnetic field, the magnetic torque, magnetic dipole and elastic forces acting on the system generated a stroke cycle. The novel actuator was 20 mm in length. In water it reached a maximum velocity of 37 mms^{-1}. This design is similar to a hinge and would not be sufficient to provide motion in a low Reynolds number regime.

Due to their success in nature a number of flexible-based swimmers are based on sperm cells or bacteria. These designs rely on a flexible 'tail' for their swimming mechanism. Dreyfus *et al.* is widely accepted to be the first to generate non-reciprocal deformation of an artificial swimmer via a magnetic field [98]. The swimmer's stroke cycle, similar to that of a sperm cell, enables the swimmer to gain a net distance. The design is made of commercially available micrometre-scale superparamagnetic (1 mm diameter) colloids coated with streptavidin and linked together via biotinylated double-stranded DNA to act as a 'flagellum'. This is combined with a red blood cell, which looks like the head of a sperm cell, that is being transported, see Figure 3.7. As the particles are superparamagnetic, they gain a magnetic dipole force when subjected to a magnetic field as well as a torque. The chain would align with an external uniform magnetic field and would be actuated by an oscillating transverse field. They found that the actuation induced a beating pattern that was able to propel the structure, and that by varying the external fields, the velocity and direction of motion could be controlled. The swimmers reach a maximum speed of 0.015 body-lengths per cycle [98].

One of the first to investigate external actuation of Purcell's three-link swimmer was Jang *et al.* [97]. The design of this device consisted of Nickel (Ni) links with flexible poly(allylamine hydrochloride) and poly(styrenesulfonate) polymer hinges. The three-link swimmer produced an average speed of 14.44 µms^{-1} or 0.93 body-lengths per second under an oscillating magnetic field resulting from the superimposition of two sinusoidal magnetic fields on x and y axis.

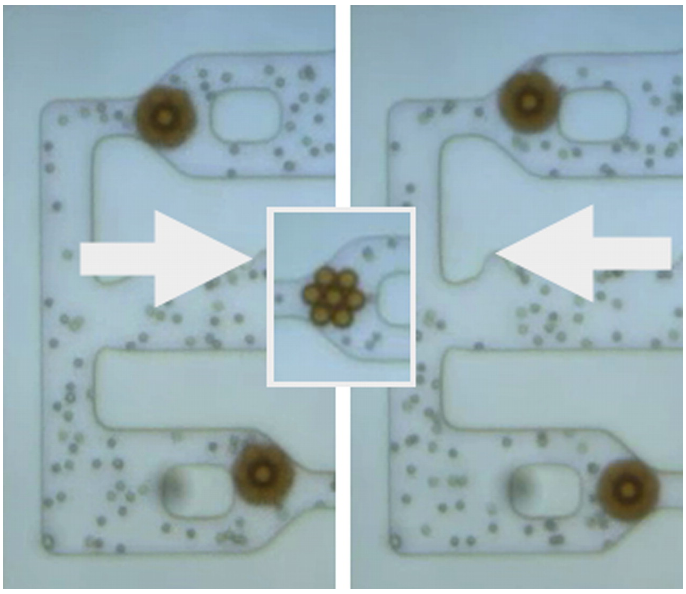

Figure 3.8: Check valve position as a function of applied flow for the colloidal cluster composed of 4.5 µm superparamagnetic particles, arrows indicate the direction of flow and insert shows when the field is turned off. (Note that 1.5 µm particles are used here as flow tracers.) Figure taken from [107].

These three different approaches gave rise to a number of flexible magnetic swimmers being investigated theoretically [99–102] and experimentally [102–105] but the majority of these are based on the sperm type design.

Pumping Swimmers

As previously mentioned some of magnetic swimmers have been used to produce pumps by constraining the swimmer in some way. This technique has been achieved by several different groups to produce valves, pumps and mixers/stirrers [106–109].

In one example, commercially available 4.5 µm dynabeads (superparamagnetic spherical polymer particles) were used alongside an externally generated rotating magnetic field [107]. These particles were superparamagnetic and the field caused an attraction between individual particles in the sample plane. This would cause the dynabeads to form the clusters initially. However once a cluster is formed, the field would exerts a net force on it, which in turn causes the cluster to spin. This device, along with PDMS channels, has been shown to be able to be used as a valve, mixer or pump for an aqueous solution with polystyrene tracer particles.

Arrays and Membranes

The production and investigation of elastic magnetic arrays and membranes is not so widely researched or established, compared to that of purely magnetic materials or magnetic swimming devices. However these systems have the potential to be used as pumps, mixers or valves. Some of these devices are made on a much larger scale than that of their swimmer counterparts. As such, they could be more suitable than their swimming counter-part for certain applications. These devices can be attached to the top surface of a channel or built in the walls.

The work by P. Tseng *et al.* produced a device that comprised of PDMS and permalloy for tunable biointerfacing [110]. They demonstrated a method of integrating permalloy features of varying size into PDMS of varying elastic properties. In this fabrication process, photolithographic techniques with SU-8 was used to produce moulds to electroplate permalloy onto the substrate in a cuboid shape. Several devices were produced with the dimensions of the Permalloy cuboids

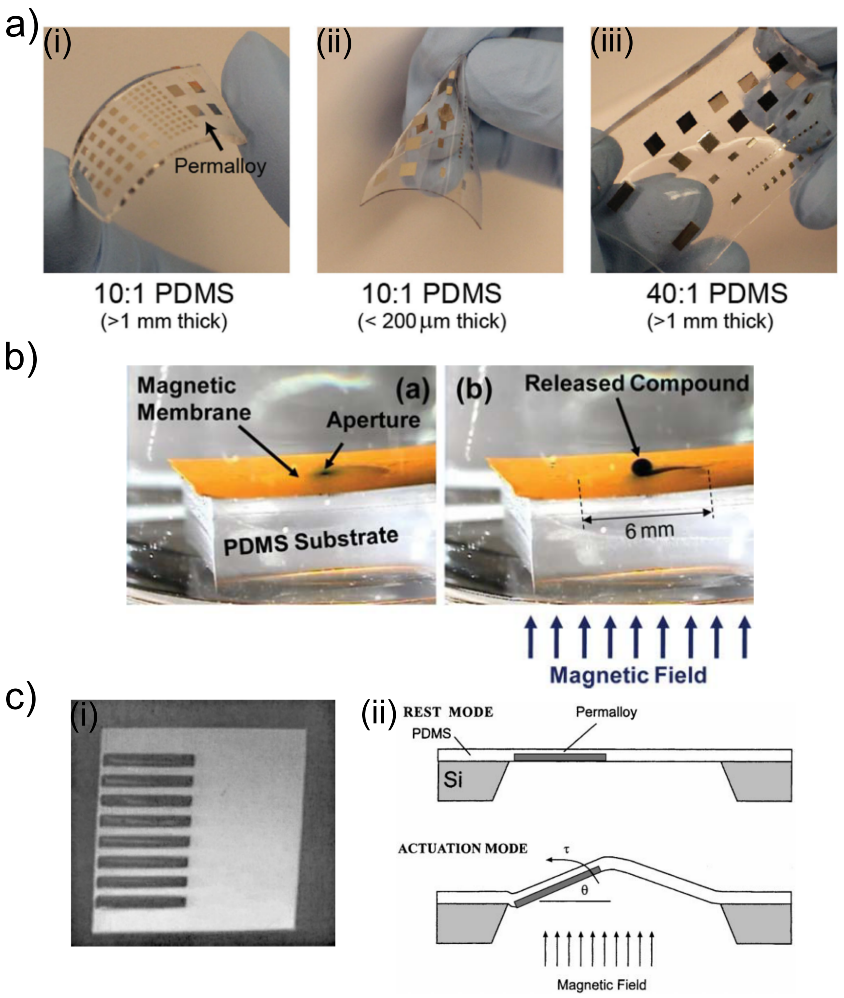

Figure 3.9: Examples of magnetically controlled membranes. a) 3 mm Permalloy elements within a PDMS membrane being manipulated. Figure from [110]. b) A magnetic membrane consisting of PDMS and iron oxide nanoparticles in water showing magnetic actuation of a 200 mT from underneath results in a discharge of powder dye, figure from [111]. c) Front view of the micro magnetic membrane actuator with eight Permalloy flaps embedded in the transparent membrane and a schematic illustration of the actuation principle of a magnetic membrane actuator. In the rest mode there is no external applied magnetic field and the membrane lies flat and when an external magnetic field is applied the Permalloy there is a magnetic torque, which causes the movement of the membrane. Figures from [112].

varying in size (4 µm to 5 mm), with thicknesses of 1-70 µm. The elastic properties of PDMS were varied by altering the ratio of curing agent (10:1 to 50:1) with thicknesses on a millimetre scale. These were shown to be able to be integrated with cover-slips and microfluidic channels to micro-manipulate magnetic particles within these channels. Application of an external magnetic gradient led to a deformation of the permalloy array embedded into PDMS. Although in this application a continuous film is advantageous for channels, in terms of flexibility a continuous film is not always suitable.

Another device made on a large scale also used electroplated Permalloy and PDMS [112]. This device used Permalloy pieces (100 µm wide, 870 µm long and 22 µm thick) positioned in a 2 mm square, 40 µm thick PDMS. In the presence of an external field the membrane displaced. The displacements were shown to be of the order of 80 µm in the largest field experimented with (1.85 $\times$ 10^5 Am^{-1}). These experiments were conducted in air with the hope that this type of membrane could be applied to the fabrication of micro-pumps. It has the advantage of being simple to fabricate [112] but has not yet been investigated as a pump where fluidic forces could hinder its movement.

Other such devices have been produced to create this pump-like motion [111, 113, 114]. These have been produced using a ferrofluid and the membrane was actuated by an oscillating magnetic field. In this case the ferrofluid was PDMS incorporated with coated iron oxide nanoparticles, which were mixed using a sonicator. This membrane made of ferrofluid has a diameter of 6 mm and a thickness of 40 µm with a laser-drilled aperture ($\sim$ 100 $\times$ 100 $\mu\mathrm{m}^2$). When the device was actuated, the membrane deforms and discharges the drug solution out of the reservoir due to the expanding of the aperture. These devices were produced by using lithography and PDMS, to create the reservoir and to produce the membrane separately. These were then bonded together using an oxygen plasma, after the drug (a docetaxel (DTX), a taxane-based drug) was put into the reservoirs. The work showed that the magnetic field had an almost linearly effect on the amount of DXT released in their device (field range used was 0-255 mT) when using 10 actuations. Then using the largest field, it was found that the number of actuations almost linearly increased the amount of released DTX (number of actuations ranging from 1 to 20). For each actuation, the magnetic field was on for 100 s. Where 20 actuations were conducted at 255 mT, the amount of DTX released was of the order of 300 ng. Given that these have already been shown to pump fluid, it is a viable option for microfluidic devices. However, some of the drug does seep out over time when there is no magnetic field and it would not be so easy to adapt this device for other applications, such as mixing.

The other most common magnetic microfluidic array structures are those based on cilia [115–126]. Similarly to swarm swimmers their combined motion causes a net effect. Like biological cilia, the design aims to produce a metachronal wave which could induce a flow. Most of these artificial magnetic cilia also use a type of ferrofluid but on a smaller scale than that of the membranes previously discussed. Most use an elastic polymer with a magnetic material such as NdFeB microparticles [118,123,124], maghemite nanoparticles [115,116], Co nano/microparticles [117,126] or even Co nanowires [119]. While the vast majority use PDMS [115,116,118,119,126], some use other materials such as silicone

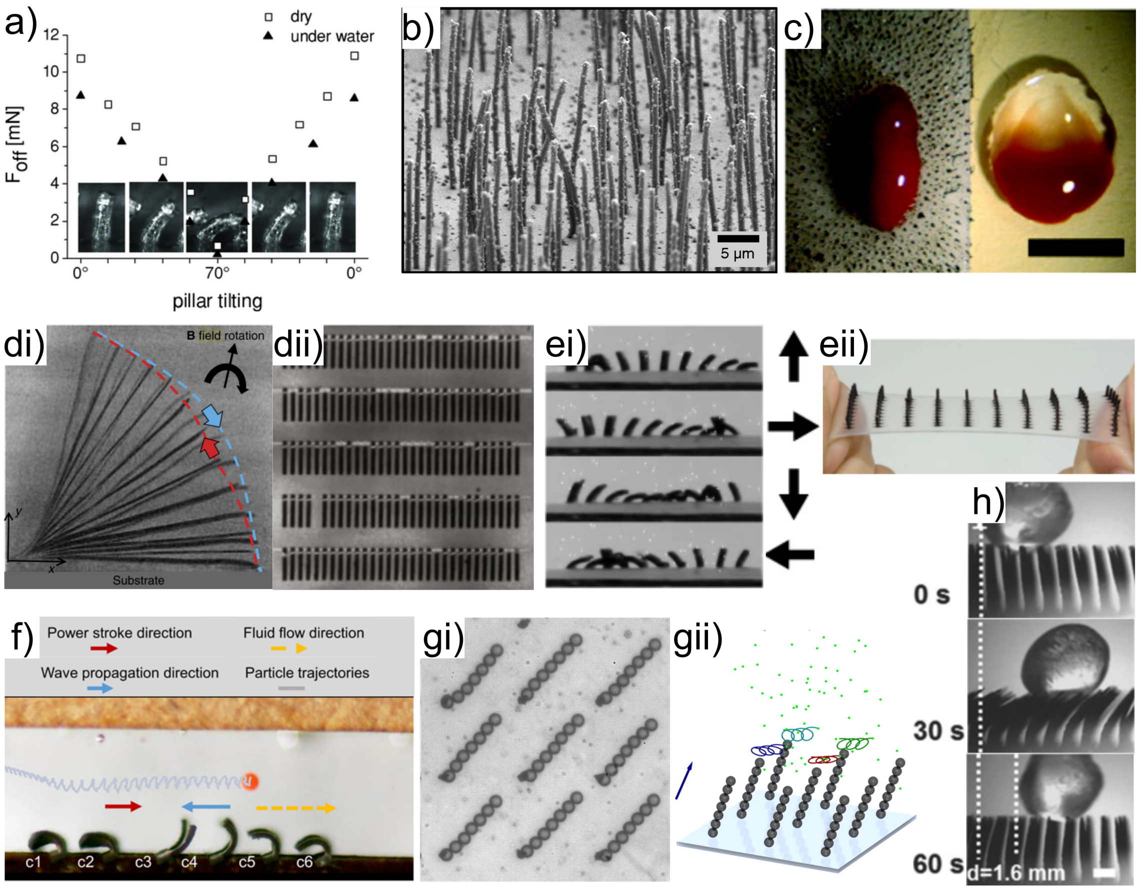

Figure 3.10: Some examples of magnetic cilia. a) From [118], the change of the adhesion force with the bending of the NdFeB and PDMS pillars caused by higher field gradients. b) From [115], SEM image of a biomimetic maghemite and PDMS cilia array. c) Adapted from [117], mixing two drops of glycerol (one clear and one red) by periodic actuation of Co nanoparticles and elastic polymer cilia. d) Adapted from [121], NiFe cilia with a Ti anchor to the substrate. e) Adapted from [123], snapshots of NdFeB and silicon rubber cilia carpets under a magnetic field (80 mT, arrows to indicate the direction) during pumping experiments. f) Adapted from [124], pumping glycerol in channel using NdFeB and silicone rubber cilia with a rotating magnetic field, visualized by particle transportation. g) Adapted from [125], chains of superparamagnetic beads attached to a substrate by nickel anchoring sites. h) Adapted from [126], transporting PS microsphere using an array of Co and PDMS cilia activated by an external magnet field (~0.7 T).

rubber (Ecoflex 00-30, Smooth-On Inc.) [123, 124] and dissolved elastomeric poly(styrene-block-isoprene-block-styrene) (Kraton D1113BT) [117]. Others do not rely on an elastic polymer for the flexibility but rather a thin layer of metal [120–122] or chains of superparamagnetic beads [125]. The fabrication method for these structures often rely on creating a mould, lithographically or manually making one using a porous material, or even using the effects of gravity to the researchers advantage. Most of these require a rotating field for actuation [115–117, 120–125], while others use an oscillating on/off field [118, 119] or even horizontally moving a permanent magnet back and forth [126]. These cilia have been reported to be able to pump [115, 121, 123–125], mix [115, 117, 124], as well as transport objects [117, 126].

It is worth noting that other flexible magnetic devices have been produced for applications other than microfluidics, such as magnetic field mapping [127]. These microcantilevers have been produced by lithographic techniques and sputtering. These cantilevers have a thickness of 100 nm of Permalloy on 3 nm of titanium. These have been fabricated to allow visualisation of magnetic field lines and to be able to map and quantify non-uniform fields (8 to 160 kA/m). However, it is worth noting that similar techniques could be used to produce devices for microfluidic applications.

3.1.5 Comparison of Swimming Devices

It has been shown in this chapter that there are many different types of swimming devices. These devices are numerous sizes, have been investigated in different fluids and have been actuated using a variety of methods. The swimming devices can be compared simply by looking at their swim speed, although it is worth creating a figure-of-merit variable that can be used to compare their effectiveness at swimming. The used figure-of-merit is the number of body-lengths swam per cycle of actuation,

$$\Upsilon = \frac{D_{body}}{T_N} = \frac{U_{swim}T}{L_b}. = \frac{U_{swim}}{L_b f}. \tag{3.1}$$

Where D_{body} is the number of body-lengths traveled, T is the time period of a cycle, T_N is the time period in terms of number of time periods of a cycle T, U_{swim} is the swimming speed of the device, L_b is the body-length of a swimmer and f is the frequency of actuation in Hz. This figure-of-merit Υ is also know as dimensionless speed [103]. Υ is a key parameter when comparing different devices, however this parameter does not include any information about the fluid or actuation. Therefore Table 3.1 has been created which is summary of a variety of examples of swimming devices discussed in this thesis. Table 3.1 includes information regarding the actuation method of the swimmer, (when known) the fluid the swimmer resides in, as well as Υ and Re calculated from information given in the relevant paper. This table has not included information regarding chemically actuated devices, as they do not have a cycle, neither has it included swimmers that rely on surface interactions as they are not directly comparable to those in the bulk of a fluid.

Table 3.1: Comparing various swimming devices described in Chapter 3.

Description & Citation	Actuation	Fluid	Υ	Re
Flexible Swimmer (Sperm-like) [47]	Light	n/a	1.1×10^{-2}	n/a
Body-Shape Changing Swimmer [48]	Light	Glycerol-Water Solution	1.1×10^{-3}	n/a
Flexible Swimmer (Microhydrogels) [49]	Light (Providing Heat)	Water	4.6×10^{-3}	3×10^{-3}
Rigid Microrod Chains [51]	Ultrasound	Water	4.0×10^{-5}	4×10^{-4}
Rigid Microrods [53]	Ultrasound	Water	3.7×10^{-3}	4×10^{-5}
Rigid Helical Swimmers [74]	Magnetic $H \sim 80$ kA/m	Silicone Oil	4.6×10^{-2}	1×10^{-3}
Rigid Helical Swimmers [75]	Magnetic $B \sim 2$ mT	Water	1.6×10^{-2}	7×10^{-4}

Rigid Helical Swimmers [76]	Magnetic $B \sim$ 5 mT	Water	1.3×10^{-1}	8×10^{-5}
Rigid Helical Swimmers (Spermbots) [77]	Magnetic $B \sim$ n/a	Water	4.2×10^{-2}	1×10^{-3}
Rigid Helical Swimmers [78]	Magnetic $B \sim$ 40 mT	Water	1.2×10^{-1}	2×10^{-4}
Flexible Swimmer (2-links) [96]	Magnetic $H \sim$ 1030 A/m DC & 1680 A/m AC	Water	3.1×10^{-1}	7×10^{2}
Flexible Swimmer (3-linked) [97]	Magnetic $B \sim$ 8.4 mT	65% Glycerol & Water	4.7×10^{-2}	2×10^{-5} [a]
Flexible Swimmer (Sperm-like) [98]	Magnetic $B \sim$ 8.9 mT in x & 10.3 mT in y	n/a	9.4×10^{-2}	n/a
Flexible Swimmer (Sperm-like) [103]	Magnetic $H \sim$ n/a	Water	1.0×10^{-1}	1×10^{-4}

Flexible Swimmer (Sperm-like) [105]	Magnetic $B \sim 0.5$ mT	Urine	6.1×10^{-2}	4×10^{-5} [b]

[a] Fluid dynamic viscosity taken from [128].

[b] Fluid kinematic viscosity taken from [129].

It can be seen in Table 3.1 that the different swimmer produce a range of values of Υ. It can be seen that generally the magnetically actuated swimmers produce a larger value of Υ than that of the other swimmers with different actuation methods looked at in this table. Other than actuation method, there is no clear trend between the value of Υ and the other parameters investigated. Therefore, it is worth noting that the specific design is important when creating a swimming device.

3.2 Magnetic Fabrication Techniques

Magnets can be fabricated or manufactured in several different ways. The main methods of production include sputtering, using magnetic particles, 3D printing and general industrial manufacturing methods such as sintering.

However, not all of these methods are suitable for all applications. Each system has a particular need and different constraints, such as size, performance, temperature range, cost and process limitations, to name a few. Therefore, no single magnetic material or process will be perfect for all the diverse needs. However, there is seen to be some general challenges across micro-electromechanical systems which are similar to those of microswimmming devices. These are magnet size (typically few micrometers to hundreds of micrometers), material magnetic performance and process integration [130]. Process integration can be one of the biggest challenges for these devices as it places limitations on the material selection, fabrication methods and especially the constraints on device design. For example, some are required to be of the order of a few micrometres or/and be produced in a particular shape.

Macroscale magnets are commonly created by a powder metallurgical process and sometimes casting [130]. These have the limitation of the size they are produced at, which are typically not much smaller than 1 mm [130]. This is due to the particle sizes of the powder ranging from a few micrometers to up to a few hundred micrometers [130]. Firstly, the desired magnetic alloy is mixed by melting appropriate quantities of the raw elements in large furnaces. This molten mixture is poured into a mould and allowed to cool for cast magnets. For powder-based macromagnets, the alloy is allowed to cool, and then ball milled or jet milled to form fine powders. These powders are then pressed into molds to create the desired shape. Heat treatments are used to bond the powder (either subsequent or simultaneously to the pressing) also to induce precipitation, diffusion, or microstructural changes to enhance the magnetic properties [130]. After this, a magnetic field can be applied to encourage the preferred magnetic orientation. Due to the process and machinery required these magnets are often commercially available and are produced at a set shape and size which may not be suitable for a particular design.

Sputtering and electrodeposition are among the most widespread techniques for metallic thin film deposition. These have the advantage of producing uniform elements with uniform surfaces and it is fast to operate but the deposition rates attainable are quite low. This process is very useful for making planar films but is not advantageous for depositing into a deep structure/mould. Especially with regards to sputtering, the elements produced are often too thin to be used to produce magnetic elements on a microscale. This limit is due to the to intrinsic stresses that develop during depositions. In addition to this, the magnetic performance of a film has been reported to degrade with thickness due to variations in the microstructure (the grain size and shape) [130].

Multilayered materials can produce uniform structures that have a microscale thickness. These structures can improve the magnetic properties of the material, compared to that same magnetic material in bulk form, and allows for an out of plane magnetisation. Due to the structure of multiple layers of alternating magnetic and non-magnetic layers, the quality of these structures degrades with thickness. This would not benefit all systems. In addition to this, the multilayer can add further steps to the fabrication process making the process more time consuming.

However, with regards to electrodeposition, relatively thick films have been demonstrated [131]. It is a useful technique for achieving diverse materials with a relatively low cost, as it is a low temperature, low power, "single step" process. It is also compatible with other fabrication techniques as it is flexible with regards to the shape able to be produced. Compared with that of sputtering it has relatively fast deposition rates and does not require a vacuum system. Similarly to sputtering, the main challenges of electroplating are the often high residual stresses in the deposited materials and the control of a variety of parameters that affect the properties of the deposited films. Even with these promising prospects, it still remains a challenge to electrodeposit hard magnetic materials with large magnetic strength (BH_{max}) and a large coercivity field (H_c) suitable for generating a larger but stable magnetic torque for microstructure actuation.

Attempts have been made at producing micromagnets using magnetic powders [130]. Using magnetic powders is attractive because it offers the opportunity to produce magnets with dimensions that are not commonly produced via bulk-manufacturing methods (not commonly much smaller than 1 mm) or standard microfabrications techniques like sputtered or electroplated magnets (which are often limited to a few micrometers in thickness). However, this still depends on the particle size which varies for different materials but are typically a few micrometres [130]. Thus, microscale powder processing methods may be well suited for magnets in the range of 10 µm – 1 mm. Unfortunately using powders has the potential to cause segregation/contamination issues depending on the situation.

Other approaches try to replicate macroscale bonded magnetic powder methods using polymers/resins/inks mixed with magnetic particles or nanowires. This is sometimes called a "ferrofluid". At times this is done via 3D printing, [132] or using PDMS with magnetic particles [111, 113, 114] or nanowires with a silicon-based organic polymer, Polydimethylsiloxane (PDMS), [118]. These all have a similar production methods. The composite is made and can be spin coated, screen printed, or put into put into moulds to form magnets with micrometer to millimeter scale features. These methods gain the flexibility of shape but similarly to in bulk-manufactured bonded magnets, the final magnet properties are usually weaker than those of the original magnetic powder. The coercivity generally remains consistent but the remanence is proportional to the fill factor (the amount of magnetic material) which typically 60%–80% at best [130]. It has been reported that for higher fill factors, the magnet/particle mixtures are too viscous, so screen printing and spin casting are no longer feasible [130]. In cases such as 3D printing magnets, it requires a dedicated machine to be used and the size is limited to the resolution of the 3D printer. In addition to this, due to the random nature of pouring not all structures would be uniform, using an applied magnetic field would help the particles align but not every structure would have the same amount of magnetic material. This would lead to different interactions in different areas of the device, which would not be advantageous as it would be relatively randomised and difficult to replicate.

Due to the advantages of electrodeposition, this technique has been chosen to approach the challenge of making the majority of magnetic elements within this project. (Electrodeposition is also referred to as either electroplating or electrophoretic deposition). This technique can be used for decorative purposes, for corrosive purposes or to alter the properties of a metal, however in some cases it can be used to produce magnetic elements. In general, it is a process of coating one metal object with another metal by electrolysis. A metal, in this case the substrate, is surrounded by an aqueous solution containing metal ions, an electrolyte/ electrolytic bath. An electric current is passed through the solution, causing the transfer of ions onto the cathodic surface, plating the metal onto the substrate. The process is often conducted in an electroplating cell. The anode can be made of the metal that is being plated or an inert conductive material used to complete the circuit (this applies in this research). Before a current is applied, there is already a potential difference, the open circuit voltage (Eoc). When a current is applied, i.e. there is a flow of electrons, the electrodes gain a charge, anode positive and cathode negative. This causes the hydrated ions in the electrolyte to be attracted to the cathode, through ionic migration. When at the cathode, the hydrated metal ions enter the diffusion double layer and the water molecules of the hydrated ion are aligned by the electric field in this layer. Next, the ions to be deposited enter the layer where the hydrated shield is lost due to the higher field that is present in the layer. Then, on the surface of the cathode, the individual ion is neutralised and adhered. The absorbed atom moves to the growth point of the cathode and is incorporated into the growing lattice, which is known as incorporation. When the anode is made of the metal that is intending to be plated, the ions in the solution get replenished over time, whereas with an inert anode, the concentration of metal ions in the solution decreases over time when the reaction occurs. The temperature of the bath has a significant affect on the speed of the reaction and structure of the material. The pH value, which is significant to the free ions, and the electrolyte composition also greatly affects the material's structure.

Electroplating can be performed with a constant potential or an alternating or varying potential. One type of electroplating is pulsed electroplating, this is when the potential or current rapidly alternates between two different values [131, 133–

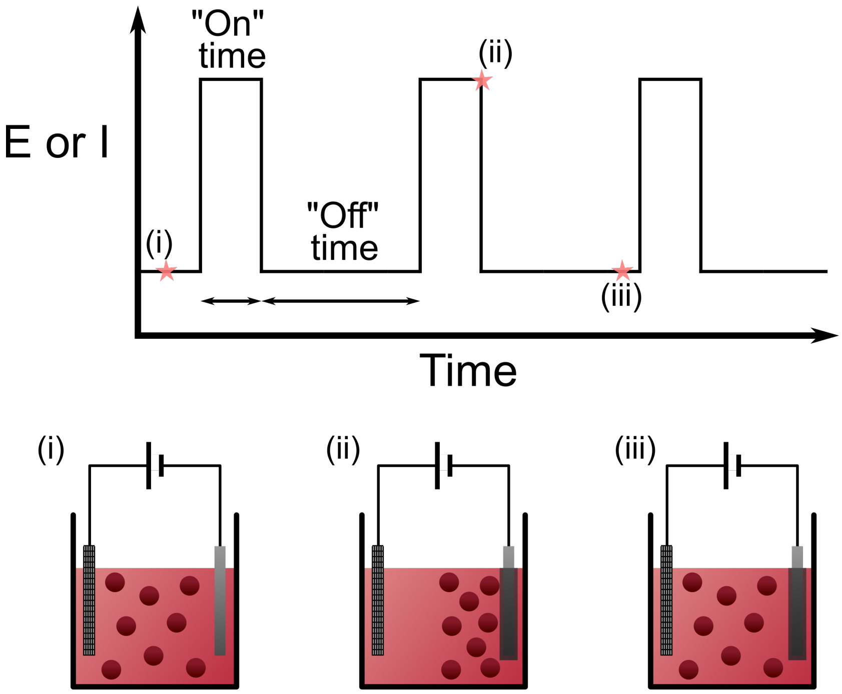

Figure 3.11: Diagram showing the shape of pulsing scheme for electrodeposition, with illustrations of the different situations.

136]. This results in a rectangular potential waveform, which alternates between two applied voltages, an active voltage and a rest voltage, Figure 3.11. The first voltage, the active voltage, is the larger of the two and the rest voltage is when the current is zero or significantly lower than during the active part of the cycle. The cycle can be defined by the duty cycle and the frequency [135, 136]

$$\gamma = \frac{T_{on}}{T_{on} + T_{off}}. \tag{3.2}$$

Where the duty cycle (γ) is the relationship between the time the active voltage is applied (T_{on}) and the time the rest voltage is applied (T_{off}).

This technique has been developed to retain the advantages of electroplating and to reduce the stress on the structure, with the aim of maintaining the magnetic performance similar to that of thin films. When a constant voltage is used during electrodeposition, areas of the solution that have a high current density have a lower concentration of ions than that of other areas as time increases. This still occurs during the time when the active voltage is applied, however when the rest voltage is applied there is a lower current allowing the ions from the bulk to diffuse to less concentrated areas of the solution [134,135]. A diagram of this can be seen Figure 3.11. When the active voltage is again applied, the ions are more evenly distributed for the deposition compared to that of a constant voltage [134].

In addition to this, when electroplating, a negatively charged layer forms around the cathode. This thickens over time, and when a constant voltage is applied this layer changes to a thickness which can block the ions from reaching the cathode. The period when the rest voltage is applied allows this layer to discharge, which allows the ions to pass through the layer and reach the cathode with greater ease. Pulsed-deposition techniques can also influence the structure and composition of an alloy. Materials that are produced by pulse form more compact layers and performs less stress in the surface coating than that of a constant potential [137].

NdFeB and SmCo are known as the largest remanence field rare earth magnets. Both of which produce alloys with transition metal and an element from the Lanthanide series of metals. They both have extremely high coercivities in comparison to other magnet materials. With regards to commercially producing hard magnets NdFeB (or sometimes called NIB) is the most popular choice, this is due to the material's high remanence at room temperature and its lower cost. However, rare earth metals are difficult to electrodeposit with aqueous solutions, though SmCo has reportedly been possible [138].

Cobalt-based alloys are good candidates for providing sufficient magnetic properties for microfluidic materials. Adding a non-magnetic element to a magnetic alloy can increase the coercivity of the material [139]. The non-magnetic elements are usually a small relative quantity of the alloy but are very important factor in the magnetic properties of the material. This is due to segregation of these elements at the grain boundaries during the electrodeposition process [130]. This creates pinning sites for the domain walls when a magnetic field is applied and therefore, increasing the coercivity. It has been shown by Luborsky [140] through experiments on electrodepositing CoNi that P is the most effective element of group VA and VIB elements to increase the coercivity of the material, though they are all capable of increasing the coercivity. CoNiP has previously shown a good promise for electroplated films [131,140–143] and thus is a promising candidate for micromagnets that could be integrated into microfluidic materials.

3.3 Summary

A brief history of swimming devices in low Reynolds number environments was discussed and how the environment has affected the devices produced at a microscale. This including discussing a number of different propulsion mechanisms, such as light, ultrasound, chemical reactions to name but a few. Different researchers have designed swimmers with different materials, geometries and actuation systems with complementary physics for generating non-reciprocal motion in the regime. In addition to swimmers, pumping actuation methods have been reviewed.

There is a significant number of designed magnetically actuated microfluidic devices which is in part due to the advantages actuation via a magnetic field has in this research area. Firstly, magnetically actuated swimmers can be categorised into two groups, swimmers with a flexible element and swimmers without, which have been called flexible and rigid swimmers respectively. This led onto a number of magnetically actuated arrays, networks and devices. Finally, a variety of swimmers have been compared.

The chosen method of actuation for the work presented in this thesis is by using magnetic fields. There are several advantages to using magnetic actuation rather than other methods. For example, magnetic fields possess various parameters such as frequency and orientation that could be used to control a device. There are several different techniques used to fabricate magnetic structures, such as sputtering, sintering and electrodeposition, to name but a few. The methods all have their associated advantages and disadvantages, however, different methods are optimal in different cases depending on the desired purpose of the magnetic structure.

Chapter 4

Advanced Processing Of Micropatterned Elasto-Magnetic Devices

4.1 Introduction

This chapter focuses on the development of elasto-magnetic devices using two-magnetic particles. The network or membrane and the microswimmer are based on similar theoretical concepts. These devices are comprised of pairs of interacting ferromagnetic particles connected together via an elastic material. The link serves two purposes, firstly to maintain average separation between the particles and secondly to aid the transport of fluid.

The pair of particles possess different magnetic properties with an anisotropically

’hard’ and an anisotropically ’soft’ ferromagnetic particle. They are set sufficiently close in space as to interact with each other. When the pair of magnetic elements are within the presence of an alternating uniform external magnetic field, it causes hysteresis-dependent orientation of the average magnetic moments. The amplitude of the external magnetic field is chosen so that it is sufficiently large to cause the magnetic orientation of the soft particle to switch to the opposite direction, so it aligns in the direction of the external magnetic field, but not large enough to cause the hard magnetic particle to also switch. The hard magnetic particle’s moment will remain close to its initial position at equilibrium. This will cause alternating attraction and repulsion between the two magnetic particles due to dipole gradient forces as the soft particle changes the orientation of its magnetic moment due to the external field. If the motion of the particles was only due to this attraction-repulsion force, it would not be sufficient to produce a device which can propel as this motion is still reciprocal. However, the attraction-repulsion force, as well as the magnetic torque generated by the external field, causes non-reciprocal motion within a fluid.

4.1.1 Theoretical Model Of The Two-Ferromagnetic Particle Swimmers

A theoretical model of a two-magnetic particle system was developed by F. Ogrin *et al.* [144] and later investigated by A. Gilbert *et al.* [145, 146]. A schematic representation of the system consisting of both a hard and soft magnetic particle is shown in Figure 4.1.

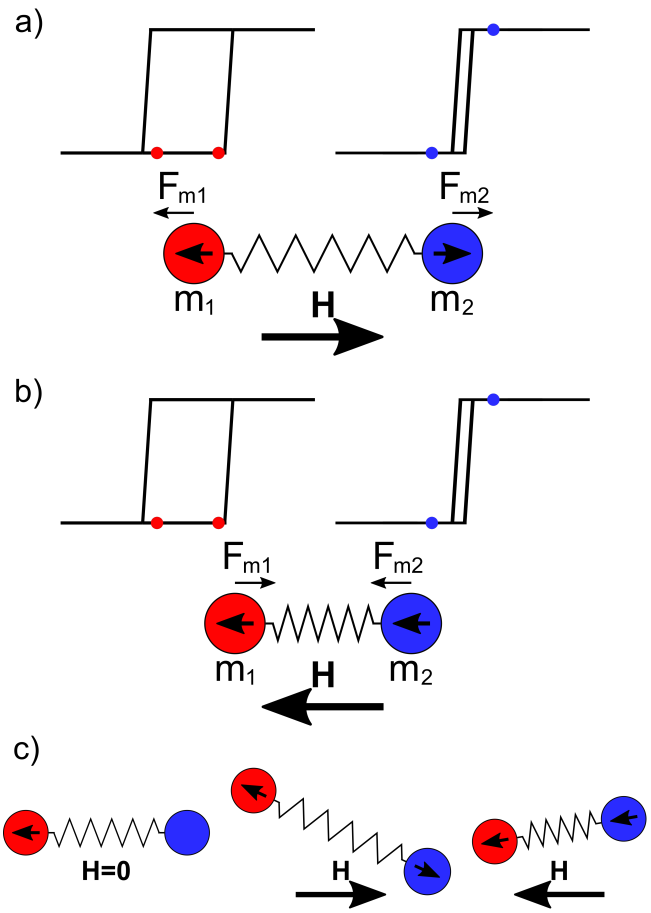

Figure 4.1: A diagram of a ferromagnetic couple consisting of a hard (red) and a soft (blue) magnetic particle connected by an elastic element, with the magnetic forces between the particles in two orientations of an external field $\boldsymbol{H}$ and hysteresis loops showing how the magnetisation changes in the two different orientations for the external field. (a) External magnetic field anti-parallel to the magnetic moment of the hard particle. (b) External magnetic field parallel to the magnetic moment of the hard particle. (c) Indicates the effects of magnetic torque on the system.

Using Equation (2.23) and Equation (2.24), and assuming both the magnetic particles are “point dipoles” the flux density for each individual particle, $\boldsymbol{B}_k$, and the magnetic force between the two particles, $\boldsymbol{F}_{Mj}$, [144] can be found to be

$$\boldsymbol{B}_k = \frac{\mu_0}{4\pi}\left(\frac{3(\boldsymbol{m}_k \cdot \boldsymbol{r}_k)\boldsymbol{r}_k}{r_k^5} - \frac{\boldsymbol{m}_k}{r_k^3}\right), \qquad \boldsymbol{F}_{Mj} = \nabla(\boldsymbol{m}_j \cdot \boldsymbol{B}_k). \tag{4.1}$$

Where $\boldsymbol{m}_k$ is the magnetic moment of the particle k, ($\boldsymbol{m}_k = \boldsymbol{M}_k V_k$), and $\boldsymbol{r}_k$ is the position vector of the particles j and k. Here, j denotes a particle number $j = 1$ or $j = 2$ and $k = 3 - j$.

The switching magnetic force of attraction or repulsion between the particles results in a physical displacement of the particles relative to each other, see Figure 4.1(a) and (b). This provides the first degree of freedom for the system.

To determine the orientation of the dipole moments in the external field, $\boldsymbol{H}$, the model used a standard magnetostatic approach [147] in which the interaction energy is minimised to find the local minima with stable positions of both moments. For simplicity, the magnetostatic energy density for each particle was represented by

$$E_{mag} = -\boldsymbol{M} \cdot \boldsymbol{H} + K \sin^2 \theta_m. \tag{4.2}$$

Where $-\boldsymbol{M} \cdot \boldsymbol{H}$ corresponds to the Zeeman energy representing the interaction of the magnetic moments with the applied field $\boldsymbol{H}$. The second term is the uni-axial magnetic anisotropy term and it describes the combined effects of shape and/or crystalline anisotropy. Here, θ_m is the angle between the magnetic moment of the particle and the orientation of the easy axis with respect to the vector $\boldsymbol{M}$. K is the effective anisotropy field constant. For the hard particle K was chosen so that the effective anisotropy field was higher than the applied magnetic field ($2K/M > H$), whereas for the soft particle $K = 0$. (It was also assumed that the time of magnetic switching/relaxation is significantly shorter than the period of the applied field oscillation.) The different anisotropy constants are not only key in obtaining different switching characteristics but also for generating asymmetric torques. The torques are generated as the system is in the presence of an external elliptical magnetic field. The hard particle (with higher anisotropy) can rotate to align its easy axis with the direction of the applied field. The soft particle does not contribute to the torque as its anisotropy is negligible. If the particles are rigidly connected to each other, the torque applied to the hard particle will lead to a rotation of the whole dipole pair, which will provide another degree of freedom in the configuration space.

In the model, an elliptical oscillating magnetic field was applied in the xy plane, with $H_x = H_x^0 \cos(\omega t)$ and $H_y = H_y^0 \sin(\omega t)$. Where H_x and H_y are the amplitudes of the field, ω is the angular frequency of the field and t is time.

Although the magnetic interactions are key components of the system, the device is also subjected to elastic forces and hydrodynamic friction. As mentioned previously, the particles are connected by an elastic link, the extension or compression of this generates an elastic force $\boldsymbol{F}_E$,

$$\boldsymbol{F}_E = k_s[(\boldsymbol{r}_{b2} - \boldsymbol{r}_{b1}) - \boldsymbol{r}_{b0}]. \tag{4.3}$$

Where k_s is the effective spring constant and $\boldsymbol{r}_{b0}$ is the vector representing the relaxed spring. (With the bending modulus of the spring being assumed to be infinitely large). The viscous resistance on each particle was calculated using the Stokes approximation, in which the drag force $\boldsymbol{F}_{drag,i}$ is proportional to the ith particle velocity $\dot{\boldsymbol{r}}_i$, radius R_i, and the dynamic viscosity of the fluid μ,

$$\boldsymbol{F}_{drag,i} = -6\pi\mu R_i \dot{\boldsymbol{r}}_i. \tag{4.4}$$

The developed computer model calculated the trajectories of the two particles under certain conditions of environment and geometry, this could provide a realistic representation of possible swimmers. The trajectory of motion and thus the characteristics of swimming of the dipole pair depend on the parameters of both the particles and the external environment.

The motion of the system has been calculated using the following parameters; μ =10^{-3} Pa s (which is the viscosity of water), $R_1 =$ 1.6 µm, $R_2 =$ 0.8 µm, $r_{b0} =$ 20 µm, k_s =3 $\times 10^{-3}$ Nm^{-1}, $H_x^0 =$ 398 kA/m (5 kOe), $H_y^0 =$ 80 kA/m (1 kOe), f =230 Hz, $M_1 = M_2$ =1.4 $\times$ 10^6 Am^{-1}, $2K_h/M_1 =$ 1 T (10 kG), $2K_s/M_2 =$ 0 T (0 kG). This gives a Reynolds number of $\sim 10^{-3}$.

Figure 4.2(a) demonstrates the different phases over one cycle together with the corresponding orientation of the magnetic moments and the magnetic dipole gradient forces calculated by the model. After a full cycle, the original configuration of the system is recovered, but the shape sequence executed is nonreciprocal; therefore, the conditions for swimming are fulfilled allowing a net translation of the centre of mass. The proposed system showed promise for a reliable method to propel a swimming device in a low Reynolds number regime.

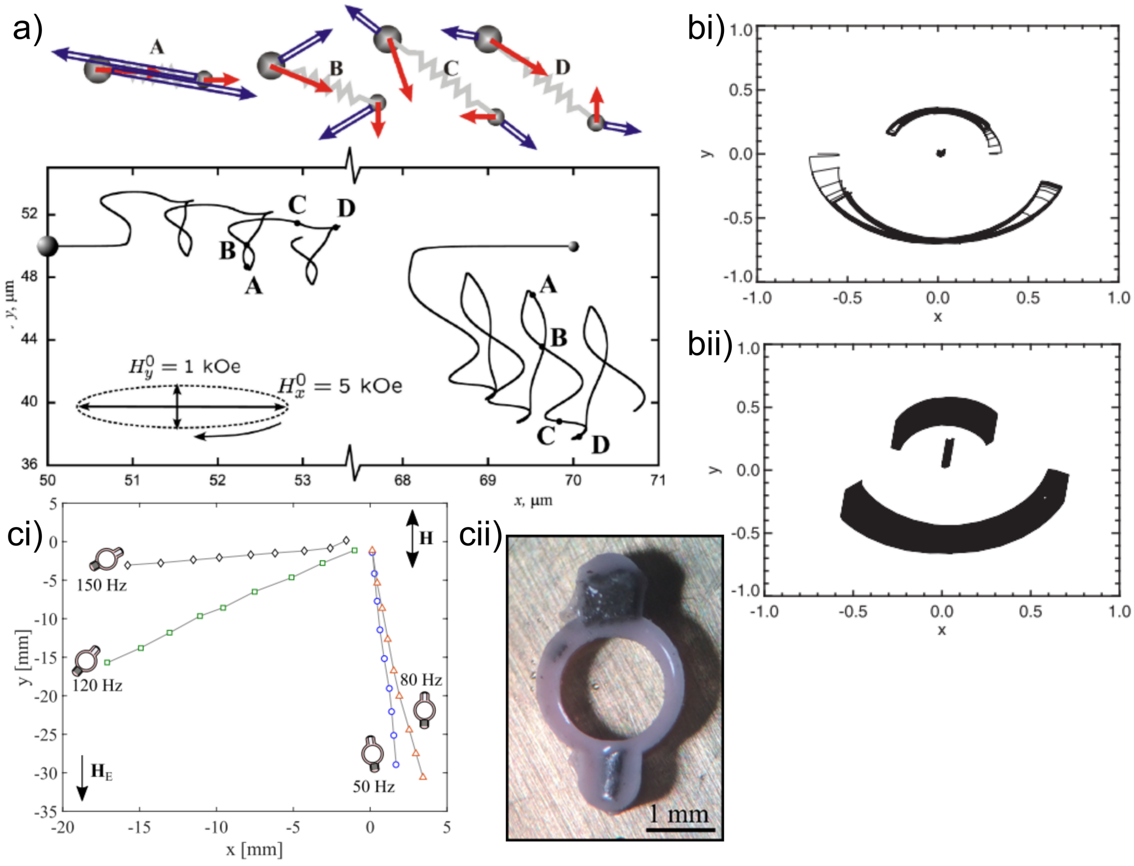

Figure 4.2: The movement of the theoretical two ferromagnetic particle swimmer and the 3.6 mm experimental device. *(See next page for the full figure caption)*.

4.1.2 Macro Design Of The Two-Ferromagnetic Particle Swimmers

The two ferromagnetic particle design was first produced experimentally on a millimetre-scale by J. Hamilton *et al.* [148]. The macro swimmer had an overall length of 3.6 mm. It was comprised of a hard NdFeB cubic particle (0.6 × 0.6 × 0.45 mm) and a soft Fe cylindrical particle (0.7 mm long, diameter 0.5 mm) connected together via a silicone rubber link (Polycraft), see Figure 4.2(cii). The swimmer was constructed in a mould, the magnets were manually placed in and the liquid rubber was poured into the mould and left to cure. To test the device,

Figure 4.2: a) Figure taken from [144] discussing the movement of the theoretical ferromagnetic swimmer. Particle trajectories (solid lines) at different phases of the field cycle. The diagram shows the orientations of the magnetisation for each particle (top single arrows), the magnetic gradient forces (double-line arrows), and the orientation of the dipole pair at the same points of the cycle. The anisotropy easy axis of the hard particle coincides with the line connecting the particles. b) Figure taken from [145] showing the theoretical position of the soft particle, hard particle and centre of reaction. bi) for $0 \leq t \leq 10T$, bii) for $10T \leq t \leq 60T$, where T is the length of 1 cycle of the magnetic field. c) Details of the ferromagnetic swimmer in [148, 149]. ci) Direction of the motion as a function of frequency at 2.0 mT for a perpendicular alignment between applied field ($\boldsymbol{H}$) and Earth's Field ($\sim$0.02 mT). The mean orientation of the swimmer is shown schematically for each frequency. The final point on each trajectory is at 1.9 s. Figure taken from [148]. cii) The overall length of the swimmer is the movement of the theoretical ferromagnetic swimmer with a 2.2 mm centre to centre separation between the NdFeB cubic particle and Fe cylindrical particle. Image provided by J. K. Hamilton.

it was placed at the fluid-air interface in a Petri dish containing water or aqueous sucrose solution. The swimmer was then observed by a video camera (20 s with 1080p HD 30 fps) when within a pair of Helmholtz coils powered with a sinusoidal signal via a standard audio amplifier to activate the device. The driving frequency of the magnetic field was varied between 20–200 Hz with a field strength in the range of 0.5-2.5 mT. The swimmer was able to propel in a range of Reynolds number environments (Re=$\sim 6 \times 10^{-5}$ to ~ 20 [148]) and it was shown that its speed and direction of motion could be controlled using different magnetic field parameters, such as frequency Figure 4.2(ci). In addition to propelling in these environments, by confining the swimmer, it was possible to pump fluid through a channel [149].

4.2 Microscale Elasto-Magnetic Devices

Although the concept was successfully demonstrated on a millimetre scale it was significantly more difficult to create devices at a microscale. Furthermore, the current fabrication method was not suitable for creating arrays or multiple swimmers at once. This would be a disadvantage for industrial applications as producing devices can become very time consuming and as a result of this, becomes cost inefficient. Thus, a microscale elasto-magnetic swimmer and an elasto-magnetic membrane were proposed. These were again based on the two ferromagnetic particle concept, see Section 4.1.1 and Section 4.1.2.

The mould-based fabrication method used for the macro swimmers could not easily be scaled down to the microscale dimensions needed. Therefore, a new fabrication strategy was required. One of the first fabrication challenges was the production and placement of the magnetic elements used in the design. Due to the scale of the magnets, it was not not possible to place them manually in the desired locations. The magnets had a number of constraints including their shape, dimension and uniform surface. It was also important to create a procedure that would allow multiple magnets to be produced simultaneously during the same process. Due to the constraints, it was evident that electrodeposition would be the most optimal strategy for producing the magnets. However not all materials can be electrodeposited, hence a suitable material needed to be found.

4.2.1 Electrodeposition

As stated above, both types of anisotropic magnetic elements were favoured to be produced using electrodeposition. The main requirement in this case is that the magnet should provide a sufficient total magnetic moment, but with a minimal hysteresis to an applied magnetic field.

Electrodeposition Material

As described above, the main challenge of this work lay in finding a material that would be possible to deposit with electrodeposition that would be able to achieve microscopic dimensions whilst maintaining a high anisotropy. This is very often lost due to the polycrystalline nature of compounds deposited with this method.

A number of groups have attempted similar research efforts to produce microstructured magnets and examined several different candidates. This includes compounds such as NdFeB and SmCo, which can provide coercive fields above 1 T and higher in its bulk form [150, 151]. However, to date, there are as of yet no compelling results demonstrating a similar performance from equivalent materials produced by electrodeposition.

Before producing micro magnets, electroplating solutions and parameters were first explored by depositing films onto copper substrates (~24 mm × 24 mm and 35 µm thick). These substrates would be placed in an electroplating cell, situated in a beaker of electrolyte solution. The solution would first be heated to the desired temperature while located within a water bath. Post the electrodeposition process, a vibrating-sample-magnetometer (VSM) was used to evaluate the magnetic properties of the samples.

Initially, SmCo indicated to be a promising candidate, however, this material became a challenge to electrodeposit. Initial deposition tests were conducted on copper substrates at a temperature of 60°C ± 0.3°C. The solution was based on a recipe from J. Chen *et al.* [138], made with a mix of Samarium(III) sulphate [$Sm_2S_3O_{12}\cdot 8H_2O$] (440 g /L), Cobalt(II) sulphate [$CoSO_4\cdot 7H_2O$] (18.6 g /L), glycine [$C_2H_5NO_2$] (27 g /L) and boric acid [H_3BO_3] (30.9 g /L) in water to form an electrolyte. Several tests were conducted, first using pulsed electrodeposition, with a duty cycle (γ) of $\frac{2}{9}$ and frequency of $\sim$ 11.1 Hz, and later using DC electrodeposition, both with an active voltage of 0.2 V and a total active electrodeposition time of 90 s. These tests did not result in a sufficient deposit on the substrate. Unfortunately, the solution became liable to separate, this was postulated to be a contributing reason that the electrodeposition was not successful. The separation was thought to be due to the mixture producing the salt or ester sulphamate, however agitation nor heating seemed to improve the solution.

Due to the premise of cobalt-based alloys as good candidates to provide hard magnetic properties, later tests were performed on cobalt-based materials. The aqueous solution used to deposit CoNiP was made of 33 g /L of cobalt (II) sulphate heptahydrate ($CoSO_4 \cdot 7H_2O$), 60 g /L of nickel (II) sulphate hexahydrate ($NiSO_4 \cdot 6H_2O$), 3.9 g /L of sodium hypophosphite monohydrate ($NaPO_2H_2{\cdot}H_2O$) and 60 g /L of ammonium chloride (NH_4Cl) [142], with a pH of 5.

Electroplating parameters of CoNiP were first explored by depositing thin films ($\sim$1 µm thick) of CoNiP onto thick (35 µm) copper substrates. The substrates were all electrodeposited for the same time period (120 s), but the applied voltage was altered to change the current density. Average current density was found by measuring the average current during the deposition and dividing by the surface area that was electrodeposited. Figure 4.3 showed that the coercivity varied with a generally exponentially decreasing trend apart from at low current densities. Typically, low current densities produced hard magnets, whereas large current densities resulted in soft magnetic properties (Figure 4.3). There was also a visual indication of the quality of the material, as can be seen in Figure 4.3, which shows photographs of the films with the highest and lowest coercivity. Films with a small coercivity visually had a rough surface and were almost black in colour, Figure 4.3(i). In addition to this, films with larger coercive fields possessed more

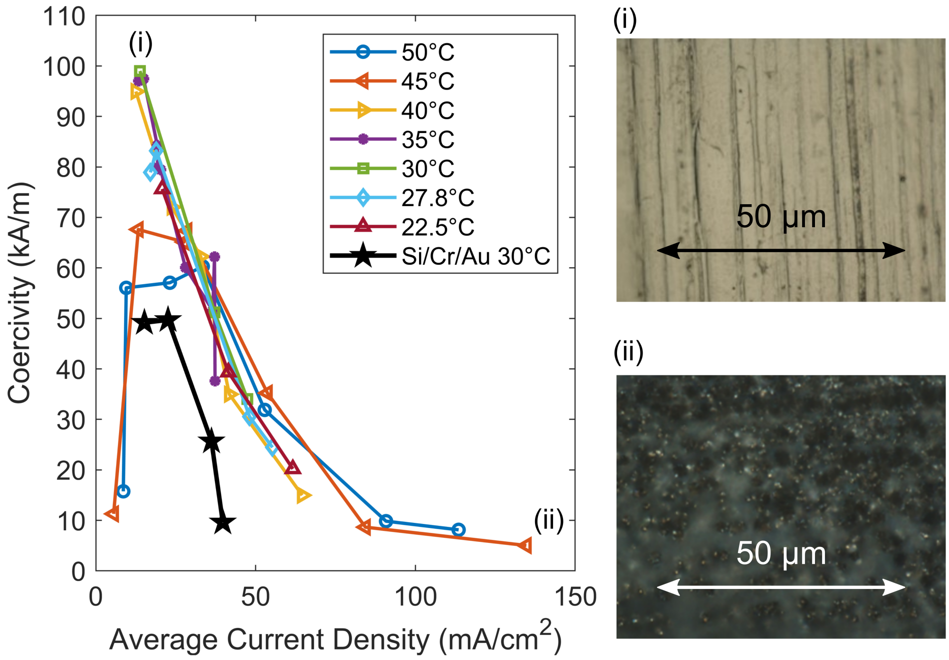

Figure 4.3: Dependence of coercivity on the electrodeposition current density for CoNiP films on copper substrates for different temperatures (°C) and Cr/Au-coated silicon substrates for 30°C with (i) a photo showing the CoNiP on copper substrate for the highest coercivity found and (ii) a photo showing the CoNiP on copper substrate for the lowest coercivity found in this investigation.

uniform surfaces and displayed much lighter colours compared with that of films with small coercive fields, Figure 4.3(ii). It is worth noting that the film in possession of the smallest coercivity was electroplated at the largest current density.

Although the colour of the film was a good indication of its properties, the structure could provide further understanding. At low current densities the deposit was uniform and grey in colour (Figure 4.3(i)), as the current density increased, in general, the deposit became darker and irregular structures would form out-of-plane of the substrate (Figure 4.3(ii)). It was hypothesised that these non-uniform pillars were formed due to the material being deposited so rapidly that it was accumulating in certain areas. These tall pillars would produce a smaller in-plane coercivity compared to that of a continuous film due to their structure. However, looking at the film with the smallest in-plane coercivity, it was found that its out-of-plane coercivity was more that three times larger than its in-plane coercivity Pillar-like shapes have the potential for producing a larger out-of-plane coercivity than that of a continuous film.

The dependence of temperature on the film was also investigated, which had a much smaller affect on coercivity than that of current density. However, it can be seen that there is a softening affect at the highest temperatures ($>$40°C) and lowest current densities. Since the investigation was focusing on films with a larger coercivity, measurements were ceased once increasing the current density consistently caused significant reductions in the coercivity. The largest coercive field (99 kA/m) was produced at a temperature of 30°C with an average current density of 13.8 mAcm^{-2}.

To examine the effect of depositing onto different substrates, it was investigated whether deposition on to gold-coated silicon affected the relationship between average current density and coercive field. While the overall trend appeared to be similar to that of the copper substrates, deposition onto silicon produced smaller coercivites (Figure 4.3), with a maximum coercive field of 50 kA/m. It is likely that this reduction in coercivity is due to the lower surface roughness of silicon [152].

Using the same films, the dependence of current density on the squareness ratio (M_r/M_s) was investigated, Figure 4.4(a). There is not such an obvious trend

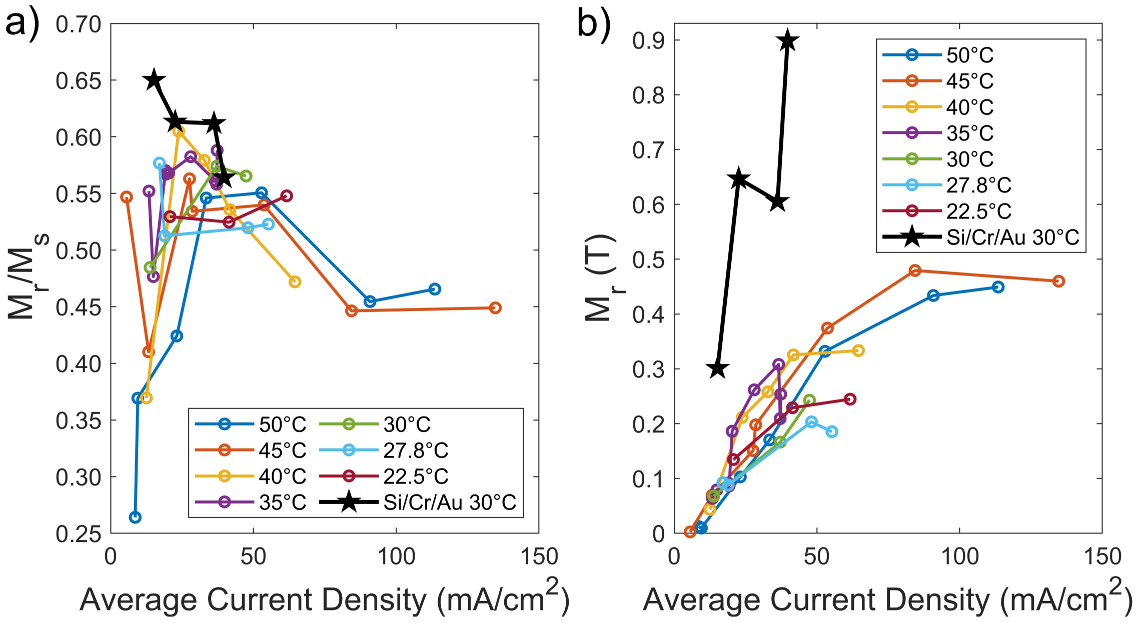

Figure 4.4: Dependence of a) squareness ratio M_r/M_s and b) remanence field M_r on the electrodeposition current density for CoNiP films on copper substrates for different temperatures (°C) and Cr/Au-coated silicon substrates for 30°C.

between the two than that of current density and coercivity, however there does seem to be a region of current density where the ratio is larger. For lower temperatures ($\leq$40°C) the majority of the films ($>$80%) had a squareness ratio between 0.5 and 0.6. The higher temperatures ($>$40°C) and larger current density still displayed a much reduced squareness compared to that of other films. The film with the largest ratio of 0.6 on a copper substrate was produced at a temperature of 40°C with an average current density of 23.8 mAcm^{-2}. The Si/Cr/Au substrates displayed a larger squareness ratio than that of the copper substrates, with a maximum ratio of 0.65 at a current density of 15.2 mAcm^{-2}. The remanence was shown to increase with current density, Figure 4.4(b), therefore, a balance in the current density was required for producing micromagnets.

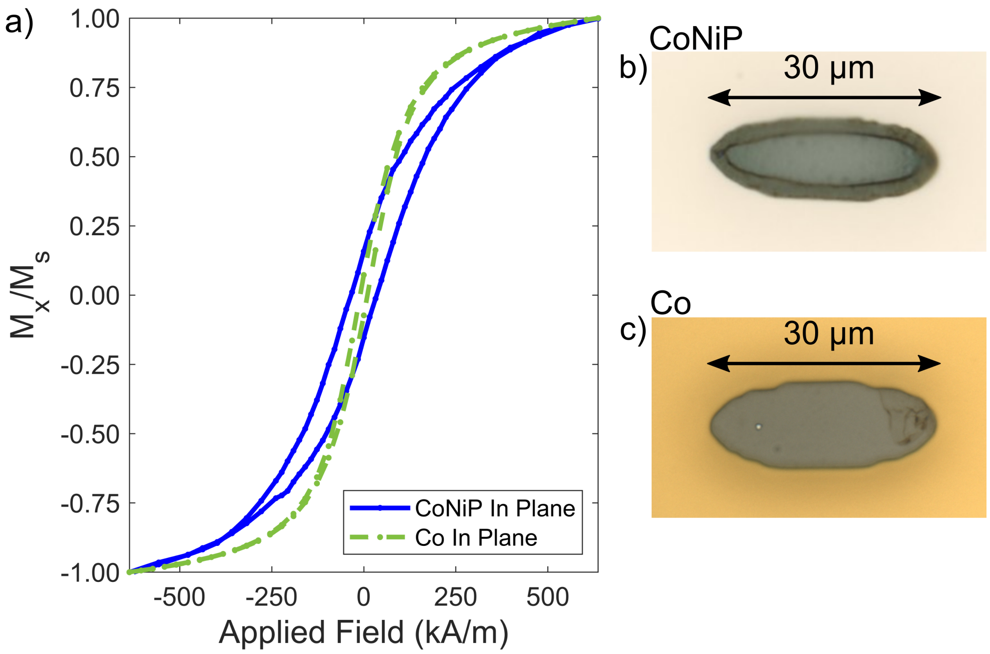

Figure 4.5: a) Normalised VSM hysteresis curves comparing the coercive fields of Co and CoNiP microstructures. Photographs of a single element of an array of b) CoNiP elements and c) Co elements.

In order to generate dipole interactions between magnetic elements, the elasto-magnetic membranes required the soft particles to be electrodeposited as well as the hard particles. The soft elements were designed based on a Co solution, with the choice of electroplating parameters taken from earlier work undertaken at the same research group at the University of Exeter [153]. For the electrodeposition of the particles a pulsed-electrodeposition technique was used due to the decrease in stress it would have on the smaller shapes [135]. The pulsed deposition process had a duty cycle (γ) of $\frac{2}{9}$ and a frequency of $\sim$ 11.1 Hz. Following these methods, circular Co microstructures were produced through electrodeposition at 50°C in an aqueous solution of cobalt(II) sulphate heptahydrate ($CoSO_4 \cdot 7H_2O$) mixed at 200g/l with boric acid (40g/l) (pH 4). Figure 4.5(a) compares the hysteresis curves from arrays of CoNiP and Co microstructures grown on gold-coated silicon, while Figure 4.5(b) and Figure 4.5(c) show the electrodeposited elements. The average coercive field for Co elements was around 10 kA/m (electroplated at a current density of 11 ± 2 mAcm^{-2}) with the saturation magnetisation similar to standard values for polycrystalline cobalt. The in-plane coercivity of the CoNiP microstructures was 35 kA/m (produced at 30°C with an average current density of 30 ± 12 mAcm^{-2}) with an out-of-plane coercivity of 54 kA/m. Although this is smaller than the coercive field of CoNiP films, it is still larger that the Co microstructures, which reached only 10 kA/m.

The measurements were performed on a macroscopic array of elements of the same shape and size, to be implemented in a further fabrication of membranes (Section 4.2.3) and microswimmers (Section 4.2.2).

Electrodeposition Cell

Three different electrodeposition cells were used in this piece of research. Each have their advantages and disadvantages and were appropriate for different substrates.

A cell for electroplating Co (shown in Figure 4.6(a)) had previously been created before this research. This cell consisted of a large metal frame, cover and screws with a window for a 24 mm square substrate. Due to the majority of the cell being comprised of conductive material, a large section of the frame was being electroplated each time it was used. This meant that the current density was able to be kept very consistent each time of use. However, due to the size of the cell and

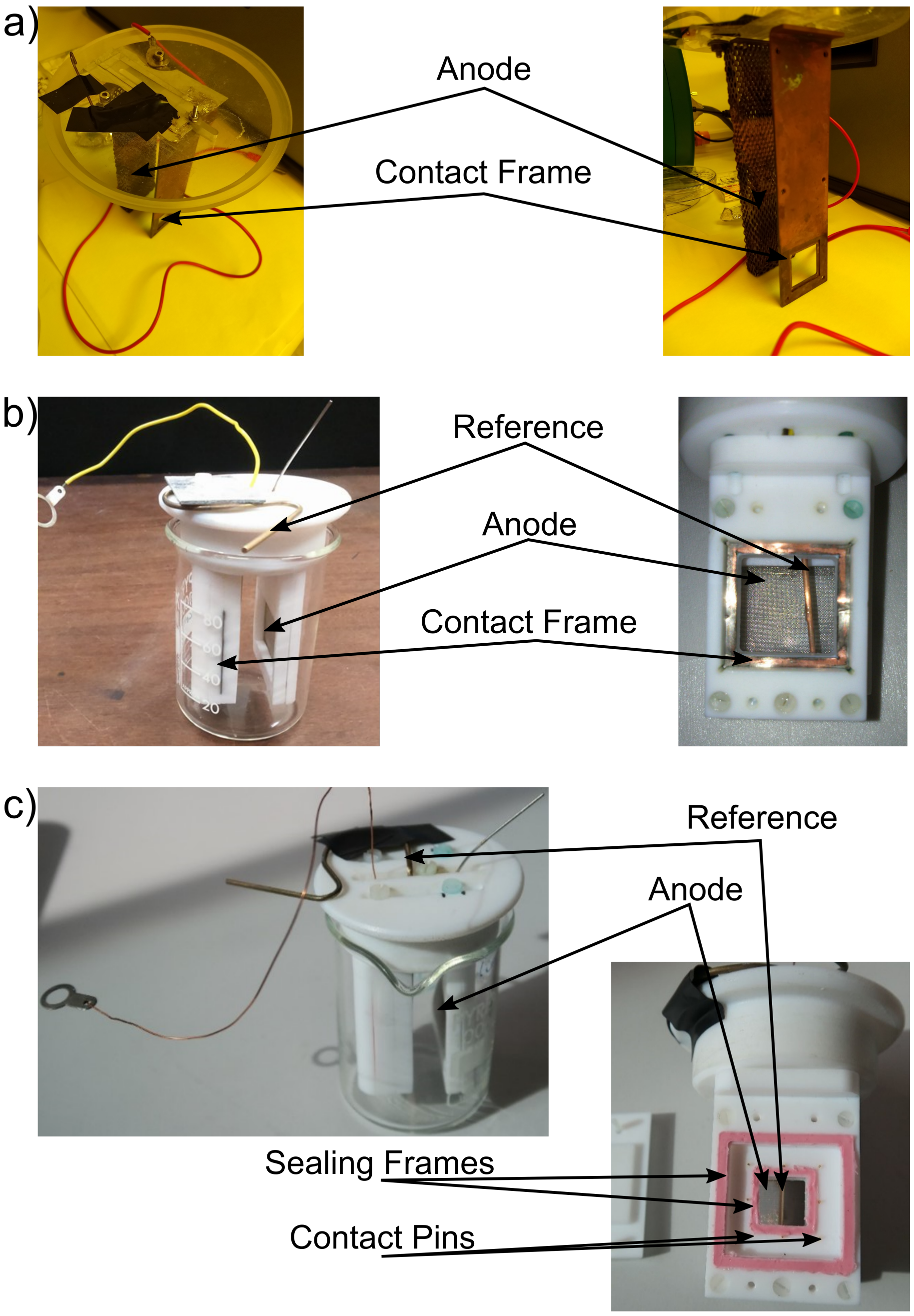

Figure 4.6: a) Photographs of the pre-existing large electrodeposition cell. b) Photographs of the first design of the cell used for SmCo and CoNiP copper substrates. c) Photographs of the cell produced for making arrays of small CoNiP elements. All cells have a window suitable for a 24 mm square substrate.

therefore, the beaker that was needed, a large volume of solution was necessary for the electrodeposition process, which in turn required more resources and took a significant time to heat to the desired temperature of deposition.

To avoid contamination, a new electrodeposition cell was produced for electroplating CoNiP. This cell was primarily made of a Teflon base with a platinum mesh anode, a brass rod acting as a reference wire and a cathode made from a copper frame to which the samples were connected to. As can be seen in Figure 4.6(b), this cell is significantly smaller than the larger Co cell. As a consequence of this, a smaller amount of solution was required to cover that of the substrate window, which decreased preparation time and the amount of resources used. In addition to this, the non-conductive base meant that the frame of the cell wasn't being plated as well as the substrate each time, unlike that of the larger cell. As a result of this the area being plated could be controlled. However, it was noted that the copper frame was also being deposited on, which over time would change the resistance. Also, with regards to the copper substrates, if the back of the cell was not sufficiently sealed tight enough, then fluid would seep through the casing of the cell and come into contact with the back of the substrate causing the back as well as the front to be electroplated. This cell was satisfactory for the copper substrates as the copper frame would be in direct contact with the copper substrate. However, when moving to the arrays of particles, this cell did not provide sufficient contact to complete the circuit. This was due to the added depth between the conducting surface of the substrate and the copper frame which was cause by the mould created for the particles. Due to these reasons a new cell was produced.

The third cell can be seen in Figure 4.6(c). Firstly, this cell was designed with a smaller window than that of the previous cell, which was due to the limited area required to be electroplated when producing the designed arrays. Secondly, sealing frames were added, as can be seen in Figure 4.6(c). These were comprised of Polycraft silicone rubber and were produced using a 3D printed mould. The purpose of these sealing frames were to limit the amount of solution coming into contact with parts of the substrate outside of the window, such as contact points. Another addition to the cell was the adoption of using gold contact pins rather than a copper frame for the connection to the substrate. These gold pins possess a spring within them, this would allow the contact points to make contact with the substrate no matter the depth added by the lithographic process. All of these additions aided in the creation of electrodeposition of micro magnets.

4.2.2 Microscale Elasto-Magnetic Swimmer

The design for the two ferromagnetic microswimmers were based on that of the macro version [148], with the microswimmers being less than a fifth of the size of the macro swimmers. The microswimmer contained a circular soft magnetic particle (Co) and an ellipsoidal hard magnetic particle (CoNiP). These magnetic particles were linked together via an elastic material in the form of a ring. This would allow the device to deform and subsequently swim. The elastic material chosen was a silicon-based organic elastomer polydimethylsiloxane (PDMS), this was due to its flexibility, ability to be moulded into a desired shape, the material properties and its popularity of use in the field of microfluidics. The magnetic

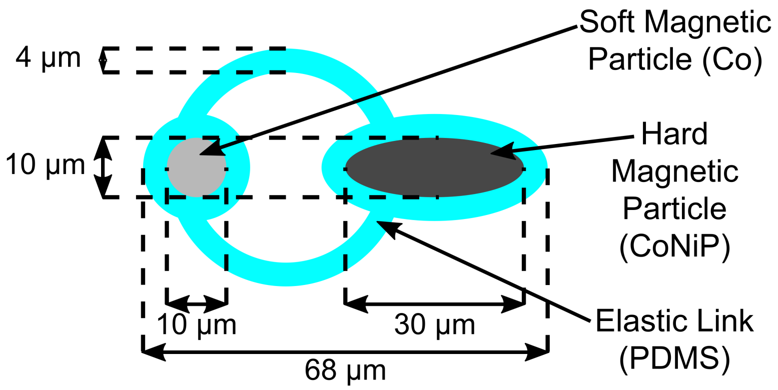

Figure 4.7: A schematic of the microswimmer design with magnetic elements and the elastic links, drawn in scale with each other.

elements would need to be encased in PDMS to keep them within the device. The design can be seen in Figure 4.7. It has a width of 40 µm, a body-length of 68 µm and an overall thickness $\sim$ 6 µm. The design and the produced fabrication process of the microswimmer was completed in collaboration with Dr. Matthew T. Bryan.

4.2.3 Microscale Elasto-Magnetic Membranes Design

The design of the proposed elasto-magnetic membrane is based on the geometry of a ferromagnetic swimmer detailed in Section 4.2.2. The same materials as that of the microswimmer were used in the design. The single cell of the material contains three pairs of hard and soft ferromagnetic particles linked with elastic beams, as shown in Figure 4.8. The magnetic elements were arranged in alternating columns of CoNiP and Co elements horizontally with vertical elements being of the same material, as shown in Figure 4.8. It is worth noting that the distance between a neighbouring hard and soft particle in the same row and unit was

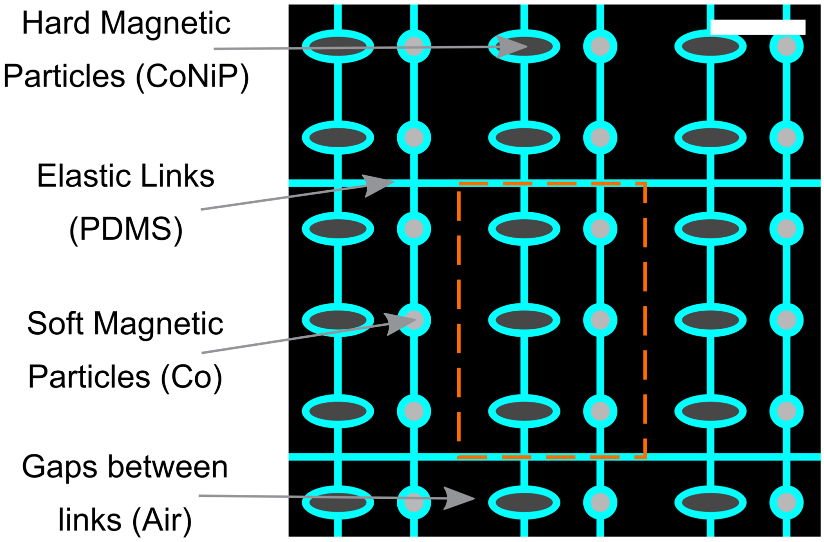

Figure 4.8: A schematic of the elasto-magnetic membrane design with magnetic elements and the elastic links, drawn in scale with each other. The scale bar at the top right of the diagram indicates 50 µm. A unit cell (dotted) is comprised of three pairs of ferromagnetic swimmers joined together.

significantly less than that of a neighbouring hard and soft particle in the same row but in different neighbouring units. This was designed so that the dipole force would be more dominant between these pairs than the other particles around.

The feature size of the design is in the tens of micrometres range with typical thicknesses of around 6-10 µm. Here, an example is demonstrated with the following dimensions (as shown on Figure 4.8). The size of the ellipsoidal CoNiP element was 30 µm in the major axis and 10 µm in the minor axis. The circular Co elements have a diameter of 10 µm. The width of the links around the elements and connecting elements together were 4 µm. The dimensions of this unit cell were 98 µm horizontally and 144 µm vertically. The centre-to-centre distance between a CoNiP and Co particle in the same row and the same unit was 40 µm, while between a Co and CoNiP particle in the same row in but different neighbouring units was 58 µm. The vertical distance between the rows of particles was set to be 48 µm. The overall size of the membrane was 4 mm × 4 mm, attached to a frame with a 2 mm circular aperture diameter.

The membrane's movement, like that of the swimmers, would be controlled by torque and dipole interactions. However, while the whole structure of the swimmer would be able to physically rotate, this is not the case with the membrane. The non-reciprocal motion would be caused by the attraction/repulsion of the magnetic elements and the twisting movement of the harder magnetic element due to torque.

4.2.4 Fabrication Of The Membrane

The next objective in this project was to integrate the magnetic components into the elastic material so that the structure could be deformed in the presence of a magnetic field. This meant that the elastic material has to be structured to provide sufficient elasticity while still having enough volume to encapsulate the magnetic elements. Due to these requirements, the employed fabrication procedure of the elasto-magnetic device required an intricate step-by-step process involving several different techniques. There are five main fabrication sections during the process: substrate preparation, fabrication of hard magnetic elements, fabrication of soft magnetic elements, production of the elastic structure and the liberation of the device. The major steps in the fabrication process of the membrane are illustrated in Figure 4.9.

Although the microswimmer's fabrication process was required to be more complex than that of the macro-swimmer, it did not require the same number of steps as that of the membrane. However, the fabrication process was similar to that of the membrane. Therefore, the fabrication process of the membrane will be discussed first and the differences between this process and that of the microswimmer will later be expanded upon.

To prepare the substrate for the patterning of the magnetic particles, a 1 mm thick glass substrate with an area of 24 mm × 24 mm was coated with a 600 nm layer of 950K A6 polymethyl methacrylate (PMMA) via spin coating. This was a sacrificial layer that was used in the liberation of the membrane at the end of the fabrication process. The substrate was plated with 100 nm of aluminum, 5 nm of chromium and 50 nm of gold using a thermal evaporator, forming a multilayer of glass/PMMA/Al/Cr/Au (Figure 4.9(a)). These metal layers were required to produce a conductive layer for the electrodeposition process but needed to be removed prior to membrane liberation in order to enable membrane actuation. Due to the harmful nature of the Cr and Au etchants with the CoNiP elements, it was decided to partially etch the Cr and Au layers before the magnetic particles were produced. This involved using photolithography patterns that were the inverse of where the particles and contacts would be, enabling electrodeposition to take place without hindering later fabrication steps. To do this, a layer of Shipley S1828 photo resist was spun at 2000 rpm and baked at 120°C for 90 s. This was the first of the four lithographic processes in the fabrication method.

A Durham Magneto Optics MicroWriter ML2 was used to expose the inverse pat-

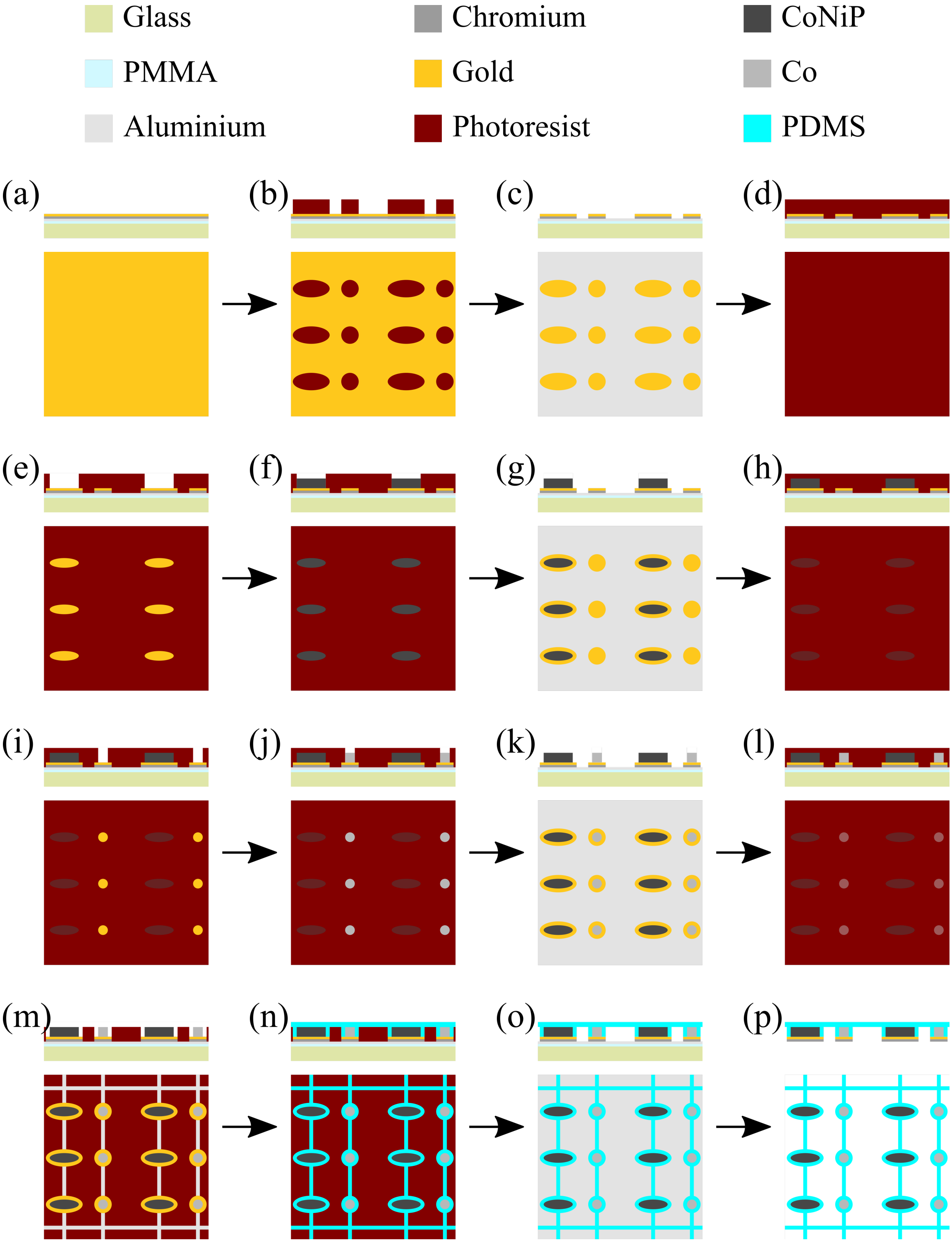

Figure 4.9: Fabrication steps of the elasto-magnetic membrane. *(See next page for the full figure caption).*

Figure 4.9: Diagram showing the fabrication steps to produce an elasto-magnetic membrane. The upmost diagram for each letter shows the cross-section with the below diagram showing the view from directly above the sample. (a-c) are substrate preparation steps. (a) Glass substrate with 600 nm PMMA spun on, followed by 100 nm of aluminium, 5 nm of chromium and 50 nm of gold layered on top (via thermal evaporator). (b) Lithographic step for the inverse of the magnetic particles (c) The Au and Cr are then etched away and the resist is removed. (d-g) are steps connected to the production and integration of CoNiP. (d) A further layer of resist is spun onto the glass/PMMA/Al/Cr/Au substrate. (e) Another lithographic step to create moulds for the CoNiP particles.(f) Electrodeposition of the CoNiP particles. (g) The resist is removed. (h-k) are part of the similar electrodeposition process for the Co particles. (h) Spinning on resist, (i) writing and developing the resist to produce a mould. (j) Electrodeposition of Co. (k) The removal of this resist. (l-o) are all related to the process that produces the links. (l) Resist is added again for the lithographic process (m) creating the mould for the links. (n) PDMS is added to the sample to produce these links. (o) The PDMS is etched down to produce links of appropriate thickness and the resist is again removed. (p) This is the final step which is the removal of the membrane from the substrate by etching the Al and removing the PMMA.

tern onto the resist. Initially, cross-shaped markers were written and developed into the resist in order to align future lithographic steps. Subsequently, the inverse pattern of the particles and contacts for the electrodeposition was written. The resist was developed using the solution MF319 and the exposed Au and Cr was removed by etching in standard gold etchant (Sigma-Aldrich) for 4 s and chromium etchant (Sigma-Aldrich) for 7 s, respectively. After the removal of the resist with acetone, the substrate remained coated in PMMA and aluminum with chromium and gold layered features (Figure 4.9(c)). Note that the presence of the Al layer prevented the acetone from removing the sacrificial PMMA layer at this stage and connected (the now segregated) Cr/Au areas.

The patterning of the CoNiP particles was produced with photolithography. However, three layers of photo-resist were applied in order to be able to electrodeposit thicker structures (the tri-layered resist was approximately 8 µm thick in total), (Figure 4.9(d)). After the shapes of the CoNiP magnetic elements were written and developed (Figure 4.9(e)), an oxygen plasma (50 sccm) was used to etch residual resist in the patterned area to ensure the gold surface was clear for electrodeposition. After this process, the sample was prepared for the electrodeposition of CoNiP (which is discussed in the previous section), this produced a 6 µm thick layer of the ellipsoidal particles (Figure 4.9(f)). The resist was required to be removed (Figure 4.9(g)) for the production of the Co particles. Co particles were produced following similar steps (Figure 4.9(h-k)), using the same electrodeposition parameters as the previous section, Section 4.2.1.

The next steps take on the fabrication process of creating the elastic structure that connects the magnetic elements. A further three layers of photo-resist were spun (Figure 4.9(l)) and the link pattern photolithography was performed (Figure 4.9(m)), which created a mould for the elastic link material. As discussed previously, the links were required to be capable of elastic deformation under magnetic forces, but rigid enough to hold the magnetic elements embedded in it. Due to this Sylgard 184 polydimethylsiloxane (PDMS, mixed in a 10:1 ratio of base:curing agent) was selected as the link material. Not only could this be spin-coated to a thickness less than 100 µm but also it has a relatively low Young's moduli (2.1-4.2 MPa [154, 155]) and a high Poisson's ratio (0.495 [156]). This would allow the device to deform more under a certain force, which would therefore provide a greater response.

The PDMS was spun at 7500 rpm and cured by baking on a hotplate at 115°C for 35 minutes. While filling the mould created by the photo-resist, it also left excess PDMS on top of the resist, forming a continuous film above the patterned area. To remove the excess PDMS the sample was exposed to 75 W, 20 mTorr inductively coupled plasma (ICP) etch with SF6 (10 sccm) [157] and O2 (2 sccm). To avoid overheating and consequent damage to the sample, the ICP etch was applied in pulses of 30 s, followed by a 30 s rest, until the PDMS thickness had been reduced to just below the level of the resist, (Figure 4.9(n)).

After the removal of the resist (Figure 4.9(o)), the membrane was essentially complete, but remained attached to the substrate. Since MF319 (the photo-resist developer) etches aluminum but does not affect the patterned magnets, it was used to remove the Al layer underneath the membrane, exposing the sacrificial layer

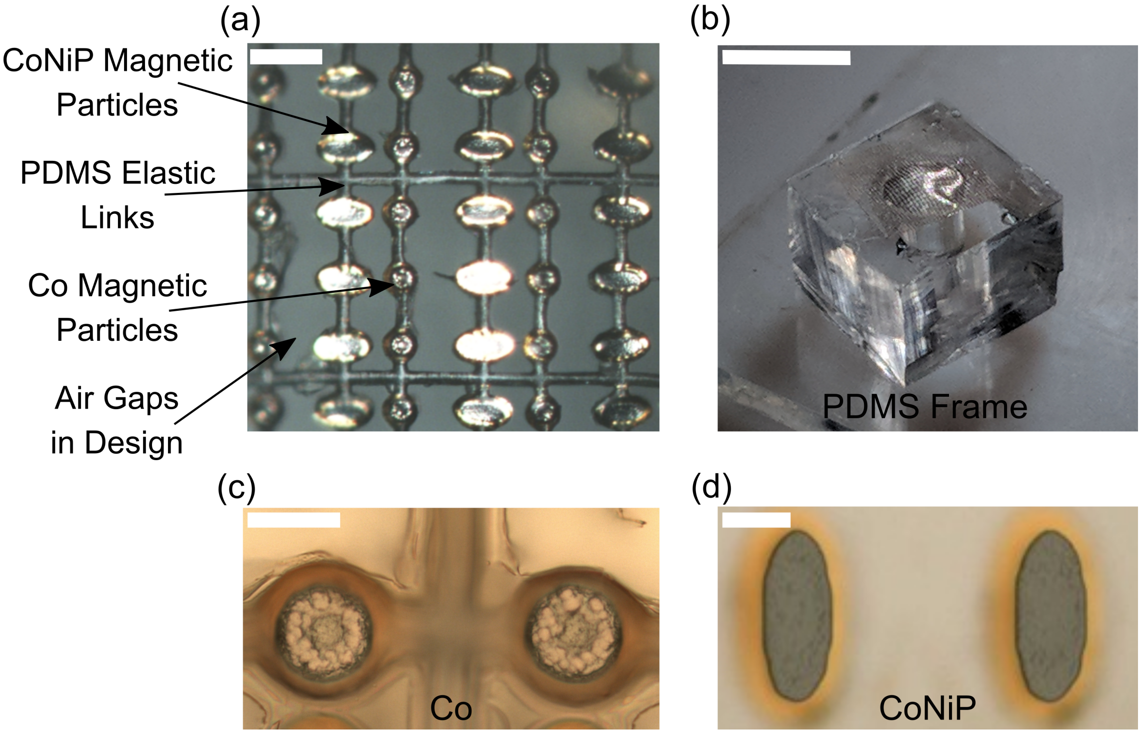

Figure 4.10: (a) Photograph of the elasto-magnetic membrane with a scale bar at the top left indicating 100 µm. (b) A photograph of the membrane on its PDMS frame with a scale bar at the top left indicating 5 mm. (c) Photograph of two of the electroplated circular Co elements with a scale bar in the top left indicating 10 µm. (d) Photograph of two of the electroplated CoNiP ellipsoidal elements with a scale bar in the top left indicating 10 µm.

of PMMA. A thick PDMS frame was attached to the edges of the sample with uncured PDMS, which was then cured in situ to create adhesion. This frame had a 2 mm aperture in the centre, which the membrane was attached across after liberation. The sample was then ready for the removal process from the substrate. Liberation of the membrane from the fabrication substrate was achieved by soaking in acetone to dissolve the sacrificial PMMA layer and free the device (Figure 4.9(p)). At this stage the elasto-magnetic membrane was comprised of a network of CoNiP and Co particles embedded in PDMS links connecting the

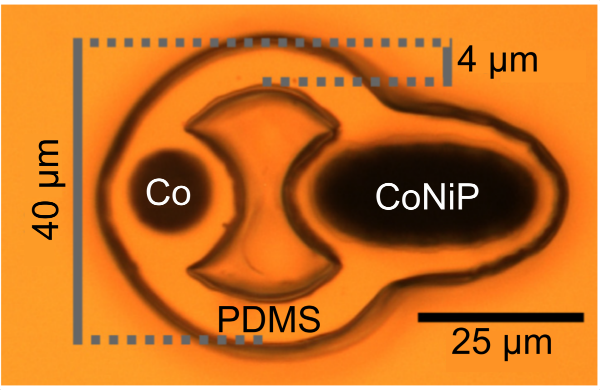

Figure 4.11: This shows an optical microscopy image of a two ferromagnetic particle swimmer with a circular soft magnetic particle (Co) and an ellipsoidal hard magnetic particle (CoNiP) with the clear linking material being PDMS. This image is also used in [158].

particles together, to form a microscale patterned membrane that was attached to a macroscale frame, (Figure 4.10(b)). To fix the magnetisation direction of the particles, the membrane was saturated in a 1.8 T field, (in this case using a VSM).

As previously mentioned the fabrication process for the membrane and microswimmer were very similar. The differences between these two fabrication processes will now be described. The microswimmers could be manually removed from a substrate using tweezers. Therefore, certain steps that were realised for the membrane fabrication process due to the sacrificial layer were not required during the fabrication process of the swimmer. Similarly to the membrane, a 1 mm thick glass substrate with an area of 24 mm × 24 mm was used. The substrate was plated with 5 nm of chromium and 100 nm of gold using a thermal evaporator, forming a multilayer of glass/Cr/Au. The aluminium was not needed in this process as its purpose in the membrane fabrication process was to protect the sacrificial layer. The Cr/Au layers did not need to be etched due to the swimmer removal process. Therefore, the lithographic processes to write the markers and CoNiP particles' moulds could be executed immediately after the Cr/Au layers were added. The next steps are the same as that of the membrane until the liberation process. After the final layer of resist was removed, the microswimmers could be manually detached from the glass/Cr/Au substrate using tweezers. The final device can be see in Figure 4.11.

4.2.5 Membrane Actuation

The completed membrane on its frame can be seen in Figure 4.10(b). A section of the membrane in the centre of the frame can be seen in Figure 4.10(a), with photographs of the Co and CoNiP particles taken during the fabrication process, Figure 4.10(c) and (d) respectively.

To test the performance of the elasto-magnetic membrane, it was placed into a microscope system with video camera (1000 fps) housing a single axis Helmholtz coil pair (Platform Kinetics Ltd). The system can be seen in Appendix C. Observing the membrane in air, its behavior was imaged under an oscillating magnetic field. The oscillating magnetic field was tested with a range of frequencies from 1-45 Hz applied on the surface of the membrane. Consistent behavior was observed in this range and although the field was applied in the plane of the membrane surface, it produced an out-of-plane actuation, such that the membrane moved in and out of focus. The oscillations of the particles were assessed optically to estimate the mechanical displacements by measuring the reflected intensity from the membrane. Figure 4.12(a) shows a trace of when the magnetic field

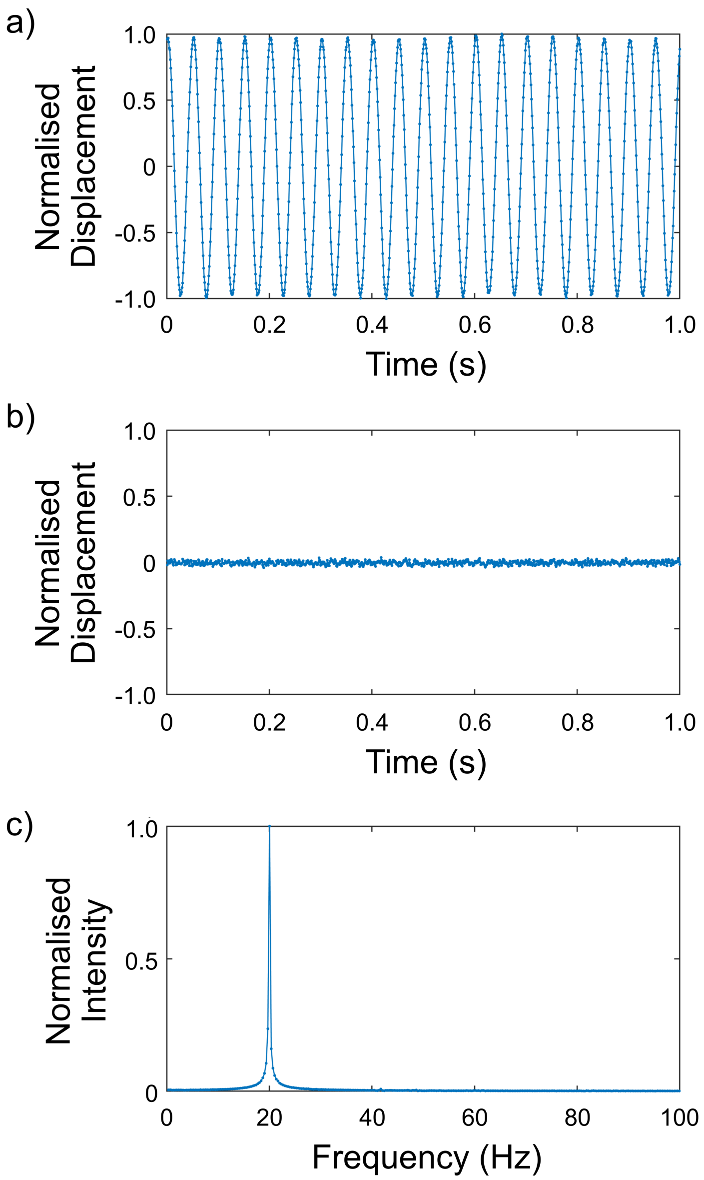

Figure 4.12: (a) The normalised z displacement against time of elasto-magnetic membrane in a 20 mT 20 Hz magnetic field (b) The normalised z displacement against time of elasto-magnetic membrane when no magnetic field is present. (c) Fourier transform of the motion in (a).

(20 mT 20 Hz) was applied compared to when there was no applied field (Figure 4.12(b)). The frequency of oscillation of the membrane matches that of the applied field (Figure 4.12(c)). It was found that, for a given amplitude of the applied

field (20 mT) at 20 Hz, the rotation of the particles were reaching 15°, with the main degree of motion perpendicular to the surface of the membrane. This system had a Reynolds number of 10^{-3}. This motion seemed to be mainly caused by the torque generated but there was no visible movement from the dipole force. This was thought to be due to the design of the structure inhibiting this movement. However the motion shows promise for future developments.

4.3 Summary

This work has successfully shown how ferromagnetic elements can be incorporated into a microscale elastic structure. This has been achieved in microswimmers with two ferromagnetic elements of different materials, as well as with a network system with arrays of magnetic elements. This was achieved via a multistage process with a number of photolithographic steps, as well as electrodeposition and PDMS etching. It has been shown that microscale CoNiP elements can be produced via electrodeposition to be suitably hard for MEMS applications, with coercive fields of 35 kA/m. As a proof-of-principle demonstration, the membrane was shown to deform in the presence of an alternating magnetic field. While future challenges will be required to focus on establishing the correct geometry and actuation for particular applications, this work has addressed major difficulties in device fabrication and establishes a strong basis for research in this area.

Chapter 5

Metachronal Waves Produced By Elasto-Magnetic Paddles

5.1 Introduction

As mentioned in the previous chapters, many researchers have found inspiration from strategies employed by biological organisms in order to introduce asymmetry into microfluidic devices. Some organisms use hair-like cilia that beat in a metachronal fashion to actively transport fluid and suspended particles. Metachronal motion emerges due to the phase difference between beating cycles of neighboring cilia and it appears as traveling waves propagating along a ciliary carpet. A more widely-known and large scale example of a metachronal wave is that of a Mexican wave travelling across a stadium full of spectators. In order to create metachronal motion artificially, it is essential to impose a phase difference in the stroke cycles of multiple individual components of a system.

To implement such a design, an experimental device was created to pump fluid in a low Reynolds number regime. The design comprised of a series of ferromagnetic discs with the same magnetic properties which were connected to a frame. The links or axles were in possession of different elastic properties to each other, which was key in achieving a phase difference between the discs. When actuated by an oscillating magnetic field while within a fluid, the magnetic discs would initially experience the same magnetic torque and fluidic drag but different elastic forces. These led to a phase difference between the angles achieved by the discs. As the magnetic torque is highly non-linear with time (being dependent on both the paddle rotation and a time-dependent field amplitude), the small differences were amplified to produce large phase difference between paddles. In an experimental set-up the different elastic properties could be obtained by altering the width of each link/axle connecting the disc to the frame. The magnetic disc and its corresponding link/axle was referred to as a paddle. These paddles would have had two equilibrium orientations, one stable at 0° under the forward field and one rotated under the reversed field.

5.2 Experimental Investigations On A Microscale

An experimental device was designed with feature sizes on the order of micrometres. The device was comprised of a 2D array of units, 650 µm × 500 µm and 10 µm in thickness to fill a frame with a 5 mm aperture. The frame was similar

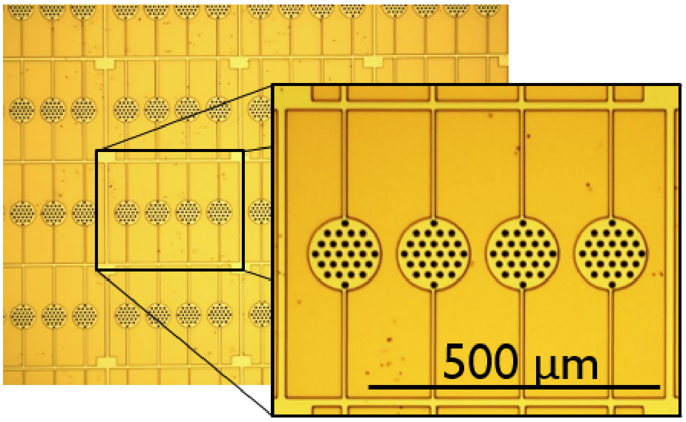

Figure 5.1: Microscopy images of a paddle membrane, highlighting a single unit of the paddle cell. The device was comprised on PDMS and CoNiP cylinders. The four axles in the unit connecting the discs to the network were different widths.

to that previously discussed in Chapter 4. The layout can be seen in Figure 5.2. Each unit consisted of four paddles with a disc diameter of 120 µm and a centre-to-centre spacing of 150 µm. Each paddle comprised of a PDMS disc and its corresponding link/axle with a hexagonal pattern of 26 cylindrical CoNiP pieces within the disc. The CoNiP cylinders were 6 µm thick and had a diameter of 10 µm and a pitch of 20 µm (discs $\sim$ 10% CoNiP). The device is shown in Figure 5.1, each paddle had a different axle width, 3, 6, 9, 12 µm going from left to right respectively.

The following fabrication method was developed by Dr. Matthew T. Bryan and the author of this thesis. It was based on the procedures discussed in Chapter 4. The differences between the two methods are briefly discussed in this section.

Following the procedure, a substrate of glass/PMMA/Au was used with a 10 µm resist, AZ9260, to produce a mould via photolithography. The solution and method of electrodeposition of the CoNiP magnets were the same as discussed in Chapter 4. The PDMS membrane was then patterned by performing further photolithography steps with the same resist. Other steps, such as the production and spinning of the PDMS were the same as those described Chapter 4, however to maximise the elasticity it was left to cure at room temperature rather than baked. For the details of etching the PDMS to the base of the resist, please see Chapter 4. The liberation of the membrane from the substrate was achieved by using a nickel-compatible gold etchant to expose the sacrificial layer of PMMA underneath the sample. After attaching the membrane to a frame, the membrane was soaked in acetone to dissolve the PMMA. The residual gold layer was then removed by the second use of the nickle-compatible etchant. To achieve a consistent magnetisation across the sample the structure was magnetised in an applied field of 80 kA/m.

The paddle membrane was attached to a PDMS frame with a 5 mm inner aperture diameter and imaged in water under a uni-axial magnetic field. The experimental measurements were taken by Dr. Matthew T. Bryan and Aleksandra Pac (using the ABIOMATER system, Appendix C).

It was found that for this particular design, the paddles of different widths of axles had different maximum rotation angles, with the thinner achieving the larger span. However, as the magnetic field strength was increased, the maximum angle of rotation for all paddles was constrained at a maximum limit of 180°, Figure 5.2. As a control device, a membrane was made with identical axles (all 3 µm in width). It was found that in in contrast to those with varying widths, all paddles rotated in unison.

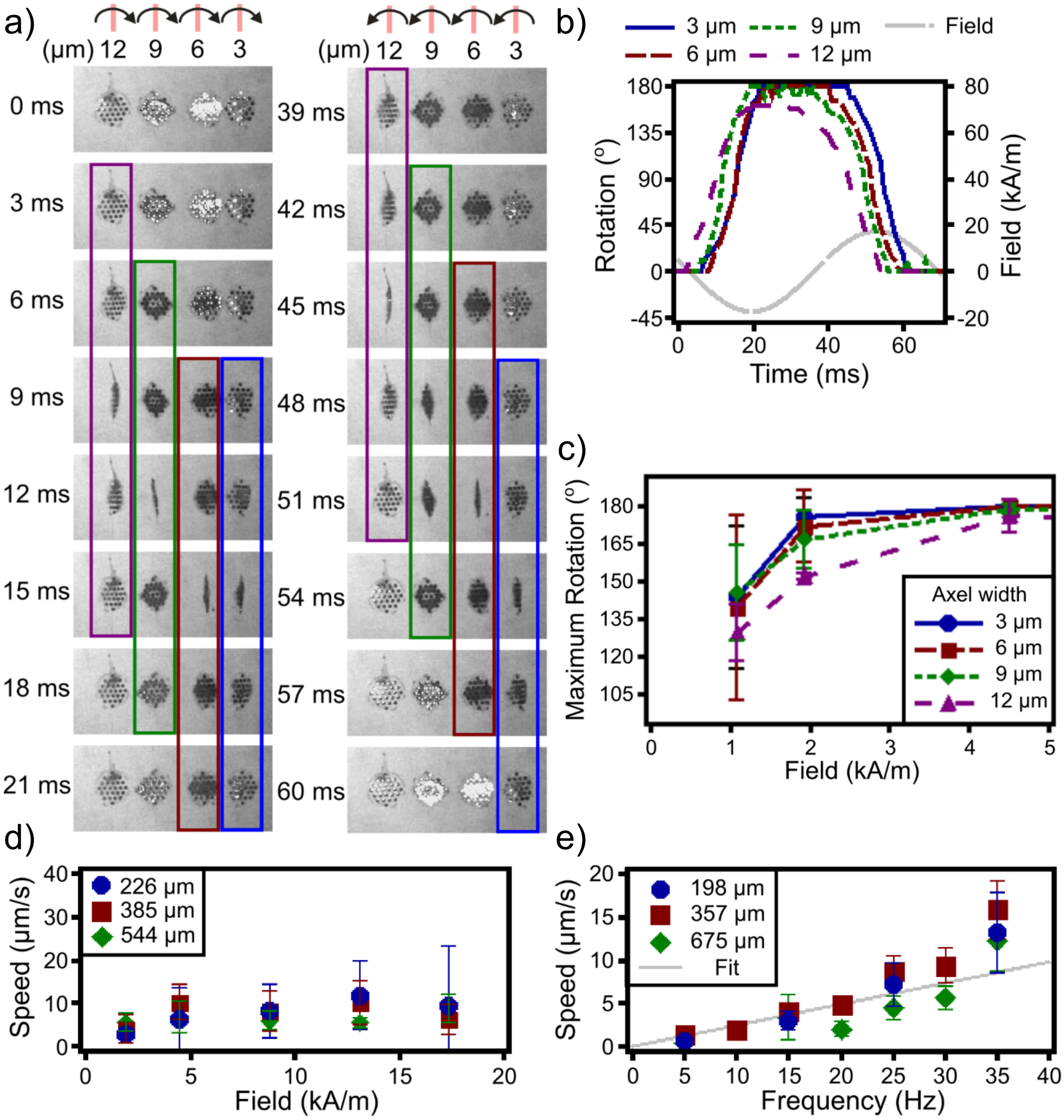

Figure 5.2: Experimental results from the micro paddle membrane, *(see the next page for the full caption).*

The details of the methods for finding the flow rate measurements and the statistical analysis method can be found in [159]. The fluid motion generated by the paddle membrane was measured from the motion of polystyrene tracer beads on the surface of the water. Negligible bead motion occurred in the absence of a magnetic field. However, actuating the paddle membrane with a magnetic field generated persistent movement. The flow was predominantly observed to be

Figure 5.2: a) Microscopic time-sequence images of a unit showing the motion of the paddles of a forward and backward stroke actuated by a 15 Hz 1.9 kA/m field. b) Individual paddle rotations with respect to time and the applied field for the cycle shown in (a). c) The effect of the different axle width and magnetic field amplitude on the maximum angle of rotation of a paddle (15 Hz field, the data points are the average of three paddles in separate units with error bars indicating the standard deviation). d) The effect of field amplitude (15 Hz) on the flow speed at different heights. e) The effect of field frequency (11.2 kA/m)) on the flow speed at different heights, with the line a linear fit to h=357 µm data for frequencies $\leq$ 20 Hz. Diagram showing the experimental paddle membrane. The figures here are adapted from [159]

perpendicular to the axles and along the direction of decreasing axle width. The measurements were repeated under both high fields, 17.4 kA/m, and low fields, 1.9 kA/m, and both generated a much faster flow than that which occurred due to random drift prior to any field actuation.

It was measured how the net flow speed could be controlled using the amplitude and frequency of the applied field across a range of fluid heights. At a constant 15 Hz frequency, net flow speed was independent of the field amplitude and averaging 7.3 $\pm$ 2.5 µms^{-1}. The field strength only altered the speed of paddle rotation, not the sequence of actuation. This means that provided with a sufficient oscillation magnetic field to function, this device would always work in a low Reynolds number regime. On the other hand, increasing the frequency of the magnetic field caused a rise in the flow speed, following a linear trend up to 20

Hz (Figure 5.2(e)). This does not alter the paddle sequence but it proportionally increases the flow speed with the frequency of the magnetic field, which is still consistent with low Reynolds number regime, assuming a similar amount of fluid has moved during each cycle. The Reynolds number was calculated to be less than 1 (10^{-5}). At frequencies above that of 20 Hz there is a deviation from the linear increase with frequency, this could be due to the effects of inertial that have caused a greater than proportional increase in the flow speed.

5.3 Analytical Model

To understand how time-reversal symmetry of paddle rotation could be broken to produce metachronal waves and therefore, generate flow in a low Reynolds number environment, Prof. Andrew D. Gilbert and I developed a simplified model of the membrane consisting of periodically repeating two-paddle cells. The full details of the model can be found in Appendix A.

In the model, the membrane frame connecting the paddles was modelled as a series of non- magnetic beads joined by inflexible links to form a backbone structure, see Figure 5.3. Each paddle was represented by two hard magnetic beads connected by inflexible links about a pivoting axis. All links in the model were elastically stiff, producing negligible change in length under tension or compression. The movement of the membrane in a fluid was modelled, but its translational motion was pinned. Due to the restricted translational freedom, actuation that would otherwise produce propagation instead resulted in a flow. Torques produced by a

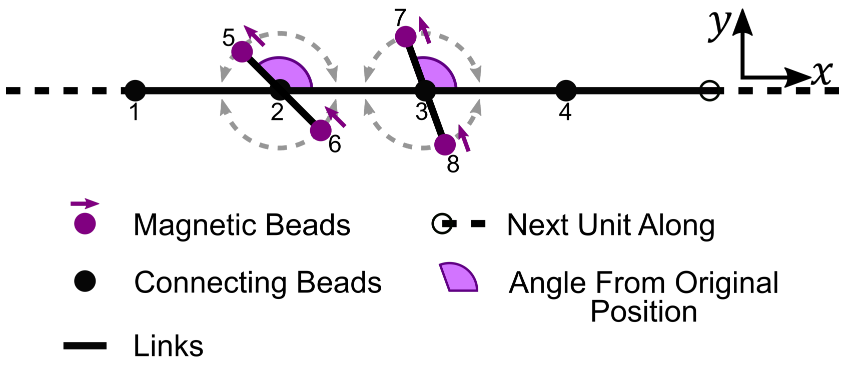

Figure 5.3: Diagram showing theoretical representation of the paddle membrane, with numbered beads.

magnetic field caused the magnetic beads to rotate around their respective paddle axes, with resultant flow due to each bead determined by Stokes' law (the hydrodynamic resistance of the links was neglected). To describe the mechanical twisting of the paddle axles, rotation of each paddle around its pivot away from its rest position was resisted by a restoring elastic torsion proportional to a (non-dimensional) rotational stiffness or bending stiffness. Each paddle was modelled with an individual rotational stiffness, ℓ_{p1} and ℓ_{p2}, enabling the paddles to respond independently to the applied field.

The described model includes several different categories of forces from the system. These forces are elastic forces, bending forces, external magnetic forces, fluidic drag forces and the fluidic interaction forces. The elastic forces on the links in the system are similar to that of a spring. The bending forces on an angle opposes a difference from the initial angle geometry. The external magnetic forces is related to magnetic torque and is minimised when the magnetic moment of a bead is in the same orientation as that of the external applied magnetic field. The fluidic drag force relates to the Stokes drag on a sphere and the fluidic interaction forces are the effect other beads have on the flow of a particular bead, (using stokeslets to approximate this). A non-dimensional equation of motion for the system is solved using the described forces and it calculates the flow generated by the model of the paddle system.

5.3.1 Paddle Behaviour

It was shown that varying ℓ_p for a particular paddle varied the maximum angle of rotation. In Figure 5.4 the angles achieved by the experimental system at certain widths of axles were mapped to the angles achieved by certain ℓ_p values. This was used to calculate an approximate ℓ_p value for an experimental paddle with a particular axle width.

To investigate the behaviour of the paddles, ℓ_{p1} and ℓ_{p2} were set to be constants approximating the rotational stiffness for the 3 µm and 6 µm paddles, as shown in Figure 5.4(b). Each of the paddles position's was monitored over a period of the magnetic field oscillation cycle (Figure 5.5).

In Figure 5.5(a), the paddles were in their initial orientation, therefore the elastic forces would be at their minimum. In addition to this, the orientation of the magnetic moment of both of the paddles was in the same orientation as the orientation of the $x-$component of the magnetic field. Therefore, due to these reasons, the paddles did not alter their position. In Figure 5.5(b), the $x-$component of the magnetic field was in the opposite orientation, this caused the paddles to start rotating (clockwise) due to magnetic torque, against the drag and elastic forces. Due to

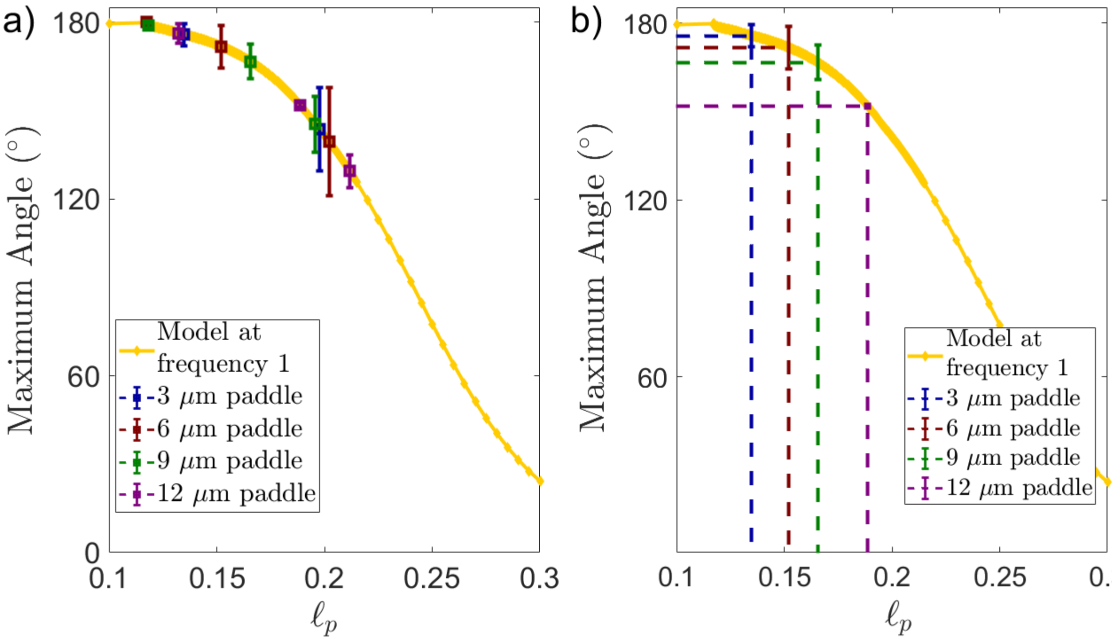

Figure 5.4: a) A graph showing the different angles achieved by changing ℓ_p in the model when the frequency was set to 1 with markers indicating the different angles the experimental paddles reached mapped to the curve to calculate their approximate ℓ_p values. b) This shows the approximate ℓ_{p1} the experimental paddles correspond to when actuated by a 15 Hz, 1.9 kA/m field due to the angles the paddles reached at this actuation.

the different values of ℓ_{p1} and ℓ_{p2} each paddle had different elastic forces acting on them (with initially similar magnetic and fluidic forces acting on them). Therefore the paddle with the smaller ℓ_p reached a larger difference in angle. In Figure 5.5(c), the $x-$component of the magnetic field was maintained in the same orientation as in Figure 5.5(b) and the paddles continued to rotate (clockwise) reaching their maximum angle, which was different for the two paddles due to the different values of ℓ_{p1} and ℓ_{p2}. In Figure 5.5(d), the orientation of the $x-$component of the magnetic field returned to its initial position. The paddles then rotated in the opp-

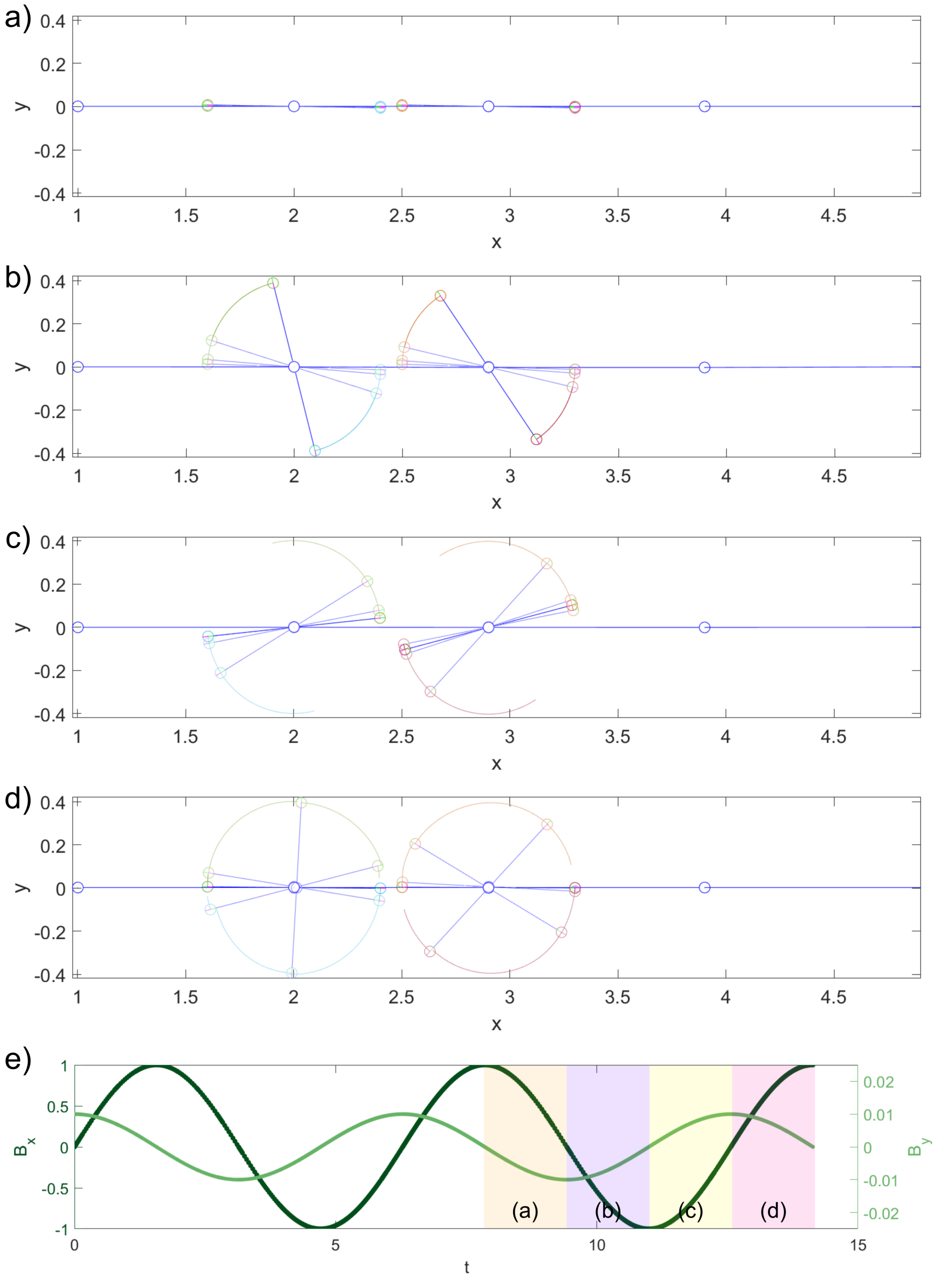

Figure 5.5: This figure shows how the paddles in the model behave when ℓ_{p1}=0.135 and ℓ_{p2}=0.152. a-d) shows the motion of the two paddles, with each showing a trajectory for the beads in its region and traces of the paddles position with the darkest trace showing the paddles position at the end of the region shown in (e). e) Shows the magnetic field amplitude and indicates the region in which (a-d) is from.

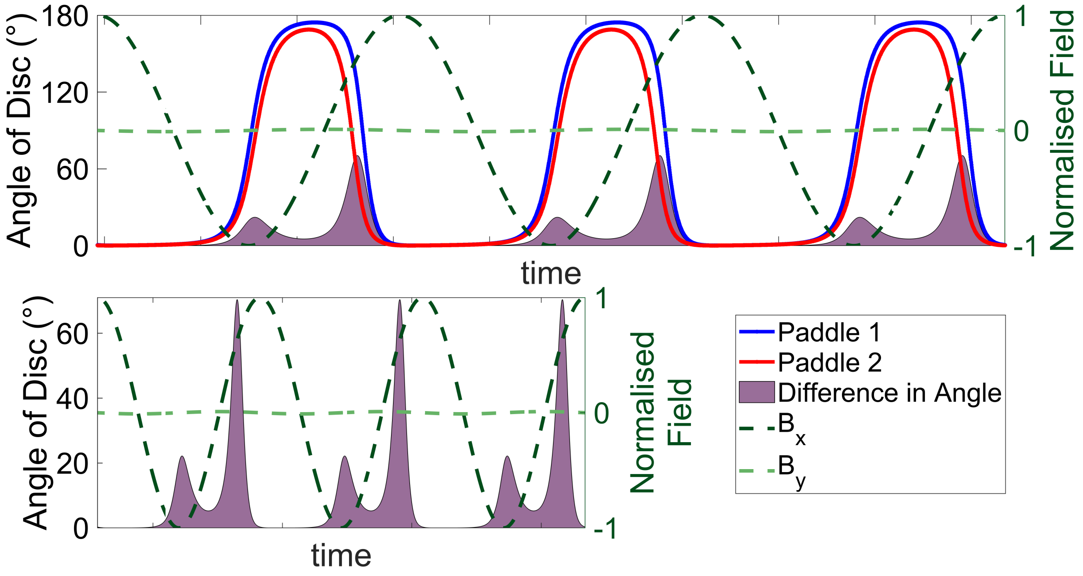

Figure 5.6: These graphs show how the angles of the two paddles and the difference between them varied over 3 periods of the magnetic field oscillation when ℓ_{p1}=0.135 and ℓ_{p2}=0.152.

osite direction to their initial rotation (anticlockwise), due to the orientation of their magnetic moment. The magnetic and elastic forces were then working together against the fluidic drag force. The paddles then reached their initial position and a full cycle has been completed. Once the orientation of the field was altered again, the cycle would repeat.

The angles of both of the paddles were observed over multiple periods as shown in Figure 5.6. It can be clearly seen that the paddles reached different angles, with paddle 1 reaching a greater maximum angle as $\ell_{p1} < \ell_{p2}$. It was also shown that the paddles had a difference in angle with each other over the period of oscillation, apart from when they were both at their initial position. The difference in the angle was not symmetric in time. The difference in angle was greater when the paddles were returning to their initial position. The angle of the two paddles

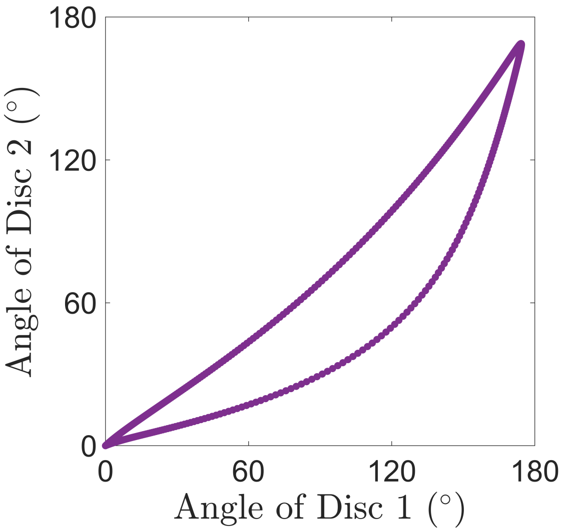

Figure 5.7: The angles of the two paddles when ℓ_{p1}=0.135 and ℓ_{p2}=0.152.

can be plotted against each other, as shown in Figure 5.7. This graph is similar to that of Figure 2.2 in Chapter 2, which is used to show that the motion of Purcell's 3-linked swimmer is non-reciprocal, thus confirming that the angle difference here is the key component in creating a flow in this system.

5.3.2 Generated Flow

As discussed in the previous section it is important to understand how the paddle system generates two degrees of freedom. It is also valuable to understand how the various parameters of the system could affect the generated flow.

The values of ℓ_{p1} and ℓ_{p2} were varied (between 0.125-0.500) to observe how this affects the flow generated by the system. The effect of this is shown in Figure 5.8 where the frequency was set to 1.4 ($\sim$ 21 Hz). It was found that the value ℓ_p of each paddle had a large effect on the magnitude and direction of the flow. It was shown that when both paddles were reasonably stiff there was very little or

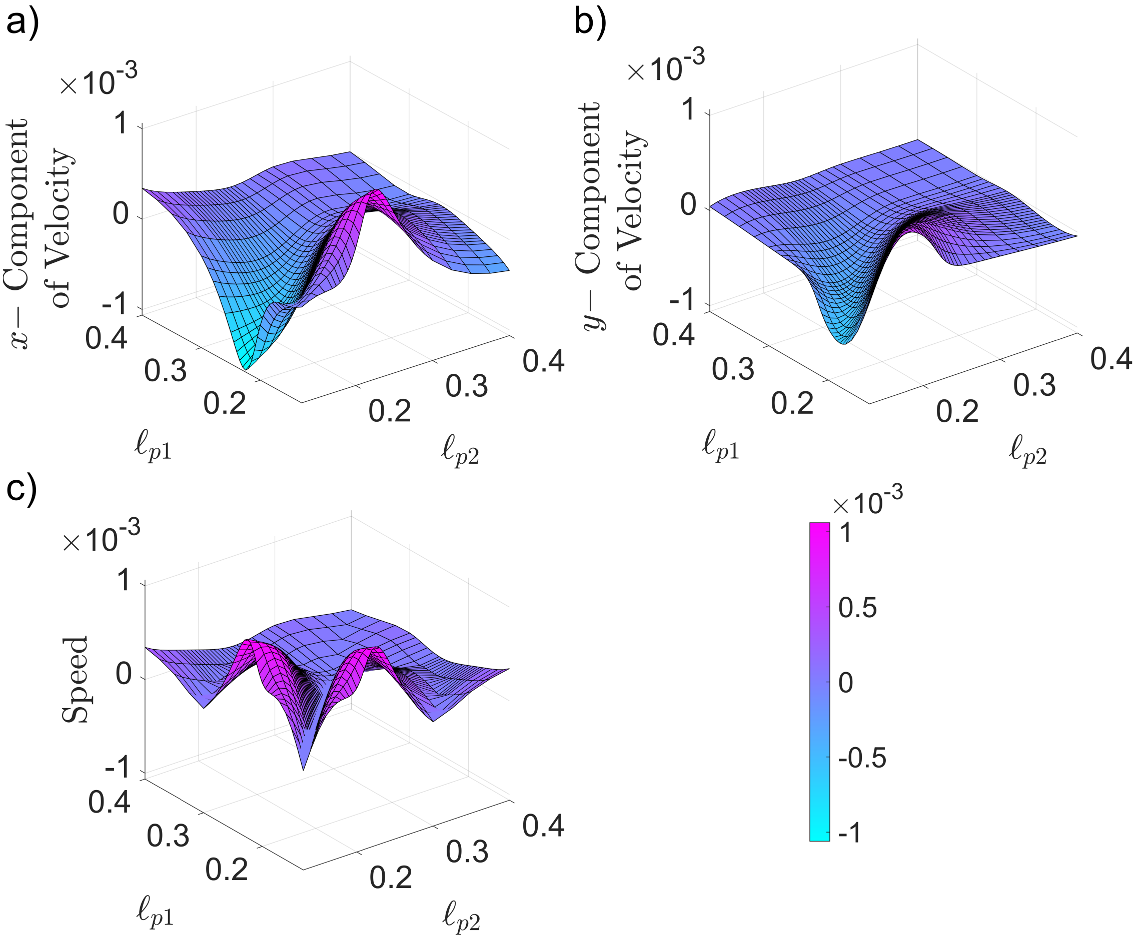

Figure 5.8: Surface plots indicating how varying ℓ_{p1} and ℓ_{p2} affects a) the $x-$component of the velocity, b) the $y-$component of the velocity and c) the speed of the generated flow when the frequency was set to 1.4 ($\sim$ 21 Hz).

no flow generated, which was as expected. The larger velocities were produced when one or both of the paddles were able to rotate more easily.

In order to understand the system more, the speed and velocity was investigated when ℓ_{p2} was fixed to certain values and ℓ_{p1} was varied. This can be seen in Figure 5.9. The maximum speed was observed at the smallest ℓ_{p2} shown. However its peak did not occur at the smallest value of ℓ_{p1}.

The peak at which the maximum $x-$component of velocity occurred, decreased

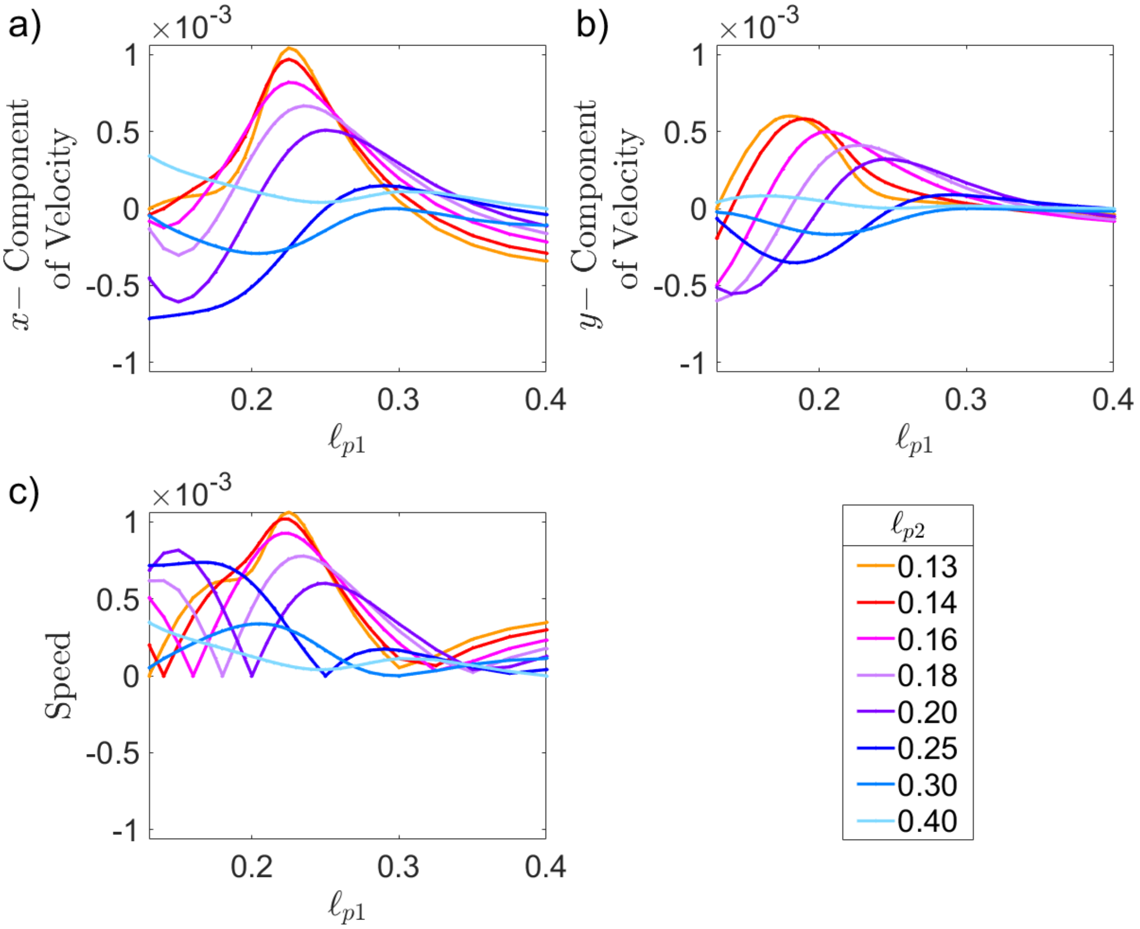

Figure 5.9: Profile plots indicating how varying ℓ_{p1} affects a) the $x-$component of the velocity, b) the $y-$component of the velocity and c) the speed of the generated flow when the frequency was set to 1.4 and and ℓ_{p2} was set to a particular value.

in magnitude with the value of ℓ_{p2}. The value of ℓ_{p1} at this maximum increased as ℓ_{p2} was reduced. When both paddles became stiff their velocity was significantly smaller.

As can be seen in Figure 5.10, when ℓ_{p1}=ℓ_{p2} no flow was achieved. This was due to the paddles' movement being the same as each other in the oscillating magnetic field. Therefore, they were behaving like a system with one degree of freedom and no net motion would be achieved. The graph shows how the velocity

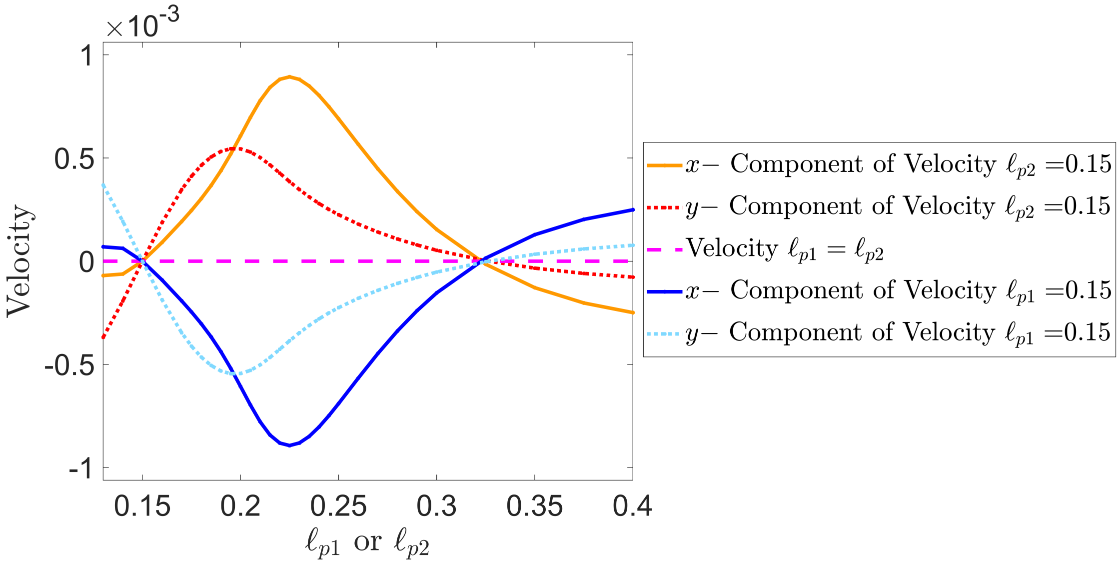

Figure 5.10: Indicates how the velocity of the generated flow varies when ℓ_{p1} = 0.15 (light and dark blue) and ℓ_{p2} was varied, when ℓ_{p2} = 0.15 (orange and red) and ℓ_{p1} was varied, and when ℓ_{p1}=ℓ_{p2} and their value was varied (pink).

was affected when ℓ_{p1} =0.15 and ℓ_{p2} was varied and when ℓ_{p2} =0.15 and ℓ_{p1} was varied. The velocity generated by a pair of ℓ_{p1} and ℓ_{p2} was equal in magnitude but opposing in direction to that of the same pair of ℓ_p when their positions were reversed (i.e. $\boldsymbol{u}(\ell_{p1} = c_1, \ell_{p2} = c_2)$=-$\boldsymbol{u}(\ell_{p1} = c_1, \ell_{p2} = c_2)$, where $\boldsymbol{u}$ is velocity).

5.3.3 Investigating The Relationship Between Angle Reached & The Generated Flow Rate

Figure 5.8 and Figure 5.9 demonstrated the dependence on the values of ℓ_{p1} and ℓ_{p2} on the flow. It has been shown that ℓ_p alters the maximum angle of the paddle, Section 5.3.1. Keeping this in mind and noting the magnitude of the generated flow rate due to ℓ_p, it can be investigated now how the behaviour of the paddle

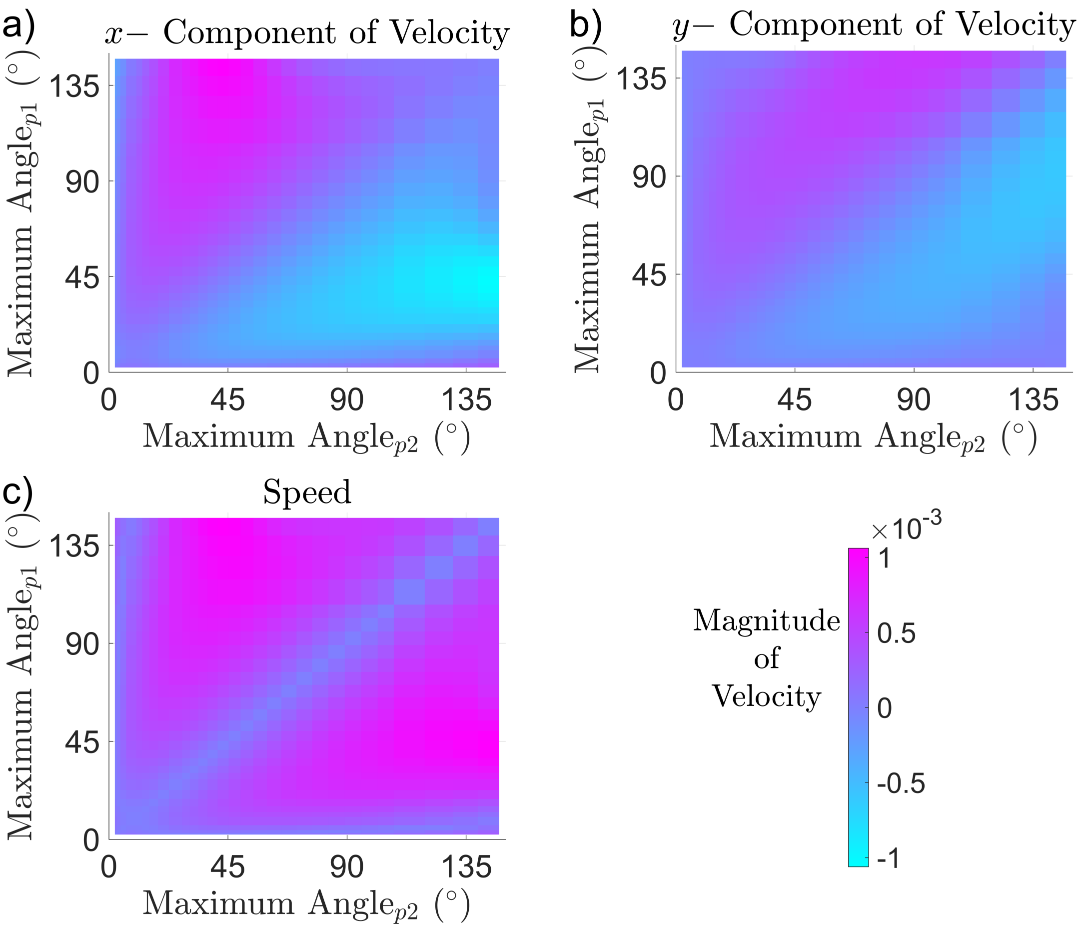

Figure 5.11: Using Figure 5.8 and information regarding the angle achieved by a value of ℓ_p to investigate how the angle reached by each paddle affects a) the $x-$component of the velocity, b) the $y-$component of the velocity and c) the speed of the generated flow when the frequency was set to 1.4.

can affect the flow.

The described information can be calculated and is shown in Figure 5.11 and Figure 5.12. These display the relationship between maximum angle of the paddles and the generated velocity. It can be seen that the larger speeds were generated when one paddle reached an angle above that of 90° whereas the other's remained significantly less than 90°. This was also true for the $x-$component of the

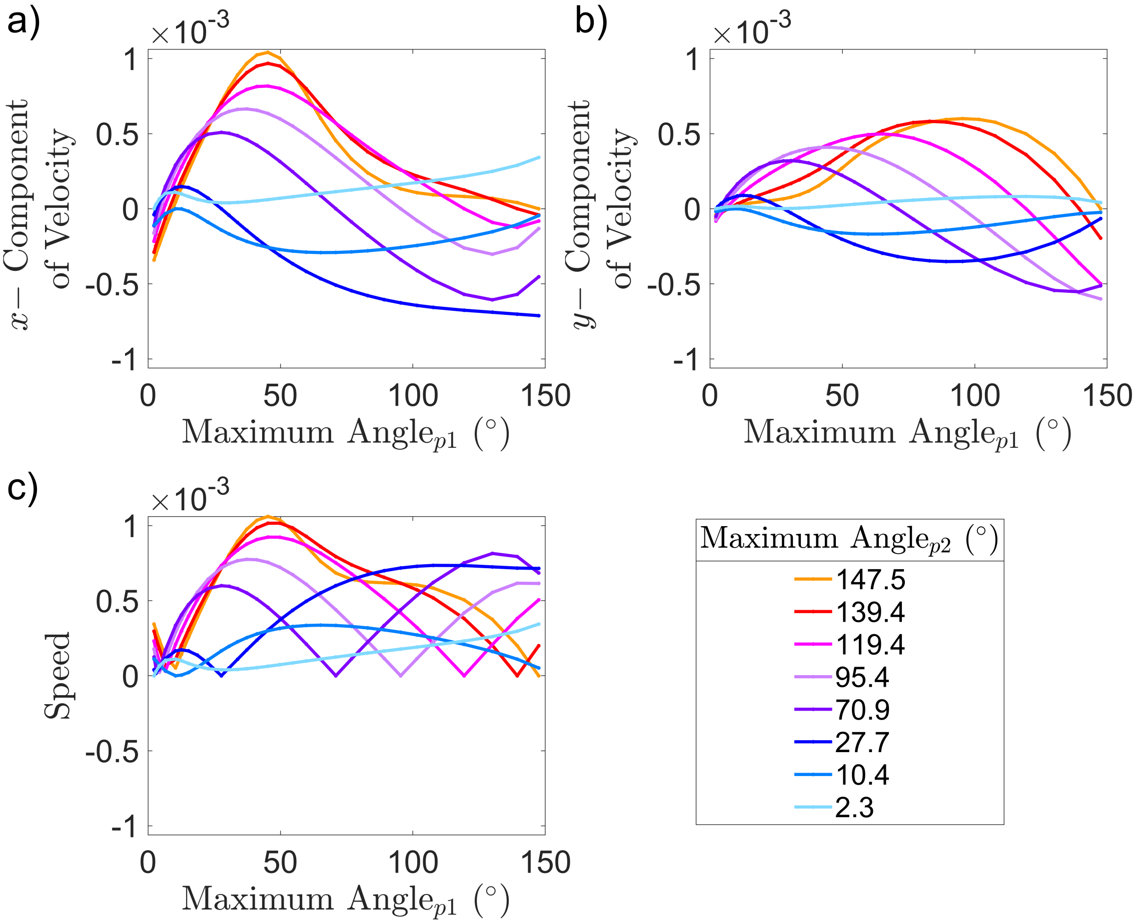

Figure 5.12: Using Figure 5.9 to investigate how the angle reached by the first paddle affects a) the $x-$component of the velocity, b) the $y-$component of the velocity and c) the speed of the generated flow when the frequency was set to 1.4 and ℓ_{p2} was set at a particular value that would have reached a certain angle.

velocity. The average magnitude of the $x-$component velocity was considerably larger than that of the $y-$component. The $x-$component of the velocity does not benefit from both paddles being able to rotate by a large angle. This was not the case with the $y-$component, for which it was advantageous for both paddles to be able to rotate by a large angle.

Figure 5.13 shows the dependence of velocity on the calculated difference in

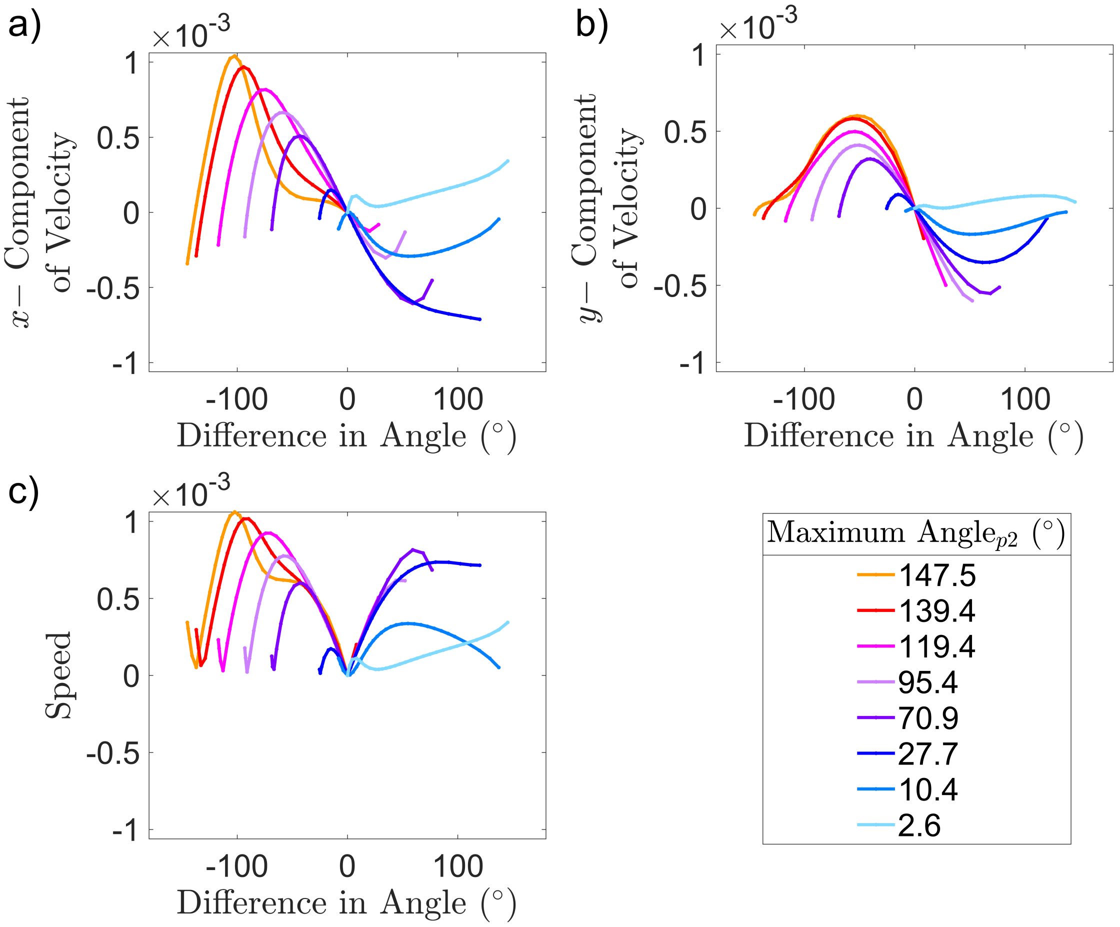

Figure 5.13: Using Figure 5.9 to investigate how the angle reached by the first paddle affects the a) $x-$component of the velocity, b) $y-$component of the velocity and c) speed of the generated flow when the frequency was set to 1.4 and ℓ_{p2} was set at a particular value.

maximum angle between the paddles. From this, it can be seen that a significant difference in angle was required to obtain a large speed. However, the maximum velocity and the difference at which this occurred depends strongly on the angle achieved by the paddle. Therefore, while it is useful to consider the different in the maximum angle for the paddles, the maximum angle itself is a more important factor.

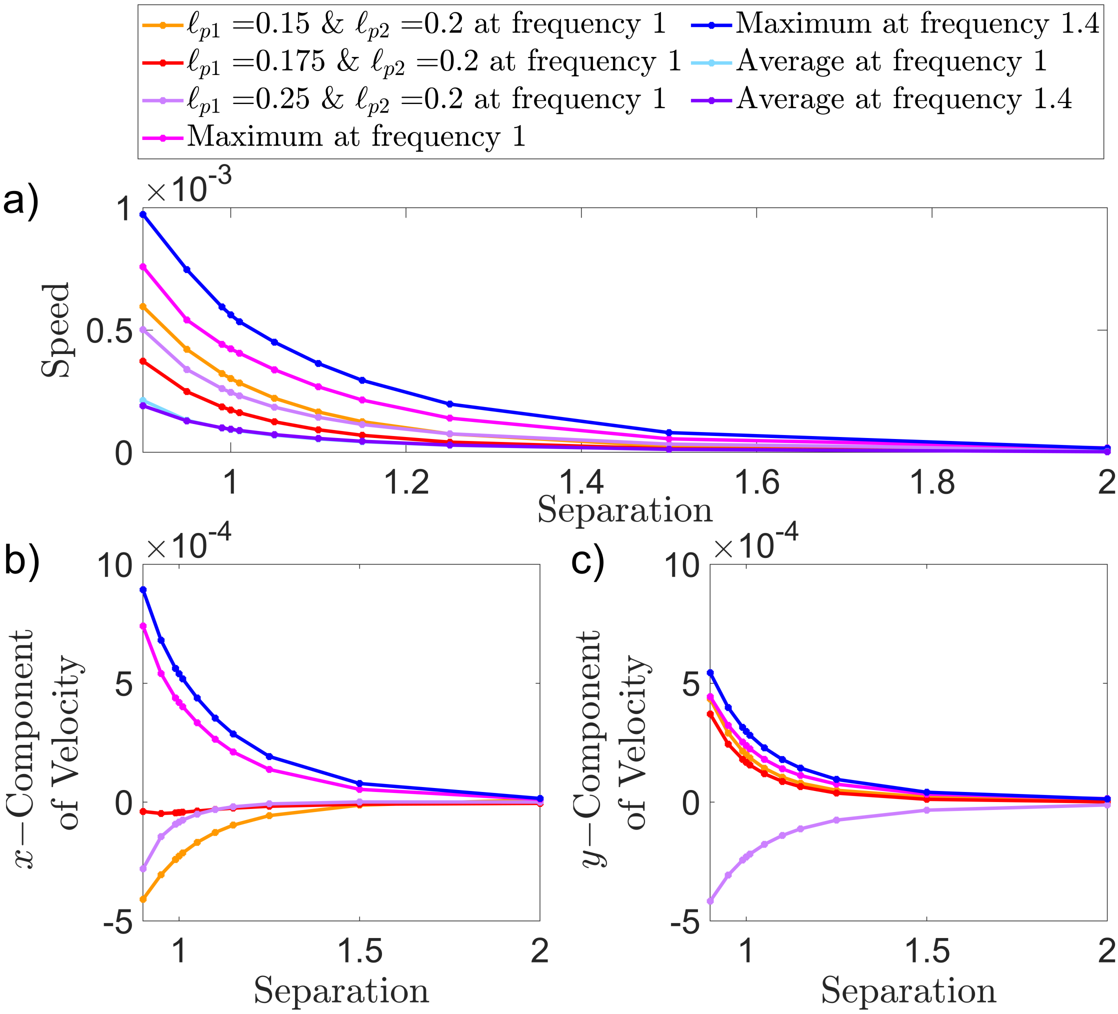

Figure 5.14: a) How the speed, b) the $x-$component of velocity and c) the $y-$component of velocity generated by the paddle system was affected by increasing the separation between the paddles for specific pairs of ℓ_p, maximum values and average values over a range of ℓ_p values.

5.3.4 Altering The Separation Between The Paddles

The paddles in the theoretical model had a dimensionless diameter of 0.8, where the dimensionless distance between the frame-like beads is 1 and the diameter of a disc is 120 µm. In the results above their centre-to-centre separation distance was set to 0.9, as at this distance the paddles were sufficiently close to

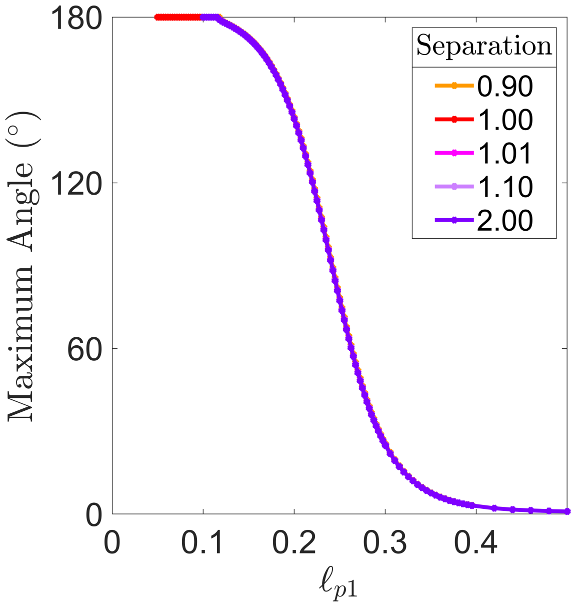

Figure 5.15: This shows how the maximum angles of a paddle varies with ℓ_p for different separations.

each other without coming into contact. As the separation between the paddles expanded, the speed and magnitude of the x and y components of velocity for a particular pair of ℓ_{p1} and ℓ_{p2} decreased. This can be seen in Figure 5.14 where pairs ℓ_{p1}=0.150, 0.175 & 0.250 and ℓ_{p2}=0.200 are shown as examples. When the maximum and average velocity over a range of ℓ_{p1} and ℓ_{p2} (0.1 - 0.5) were calculated, their values reduced with separation. This trend at which this declines closely resembles an exponential decay. The behaviour of the paddles do not change as the separation expanded, Figure 5.15. This was to be expected as the separation does not affect the forces that primarily cause the paddle to rotate.

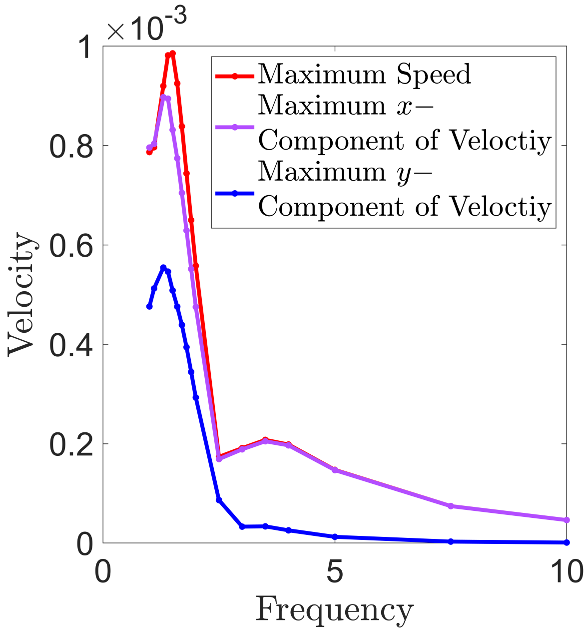

Figure 5.16: a) Displays the effect of frequency on the maximum generated speed, $x-$component and $y-$component of velocity achieved within a range of pairs of paddles (ℓ_p=0.1 - 0.5).

5.3.5 The Actuation Frequency Dependence

Figure 5.16 shows the variation of maximum speed, $x-$component and $y-$component of velocity with actuation frequency for values of ℓ_{p1} and ℓ_{p2} in the range of 0.1 to 0.5. This was investigated in more detail for particular pairs of paddles with ℓ_{p2} = 0.2, Figure 5.17. Varying the frequency does not affect all of the pairs of paddles in the same way, like altering the separation. As can be seen in Figure 5.17(b) the change in frequency can alter the direction and magnitude of the flow.

It was found that the frequency greatly affects the maximum angle reached at a particular ℓ_p value, Figure 5.18. This indicates that changing frequency alters the behaviour of the paddles. This is consistent with the experimental investigations, that angle of rotation of a axle width varies with frequency and that it affects the

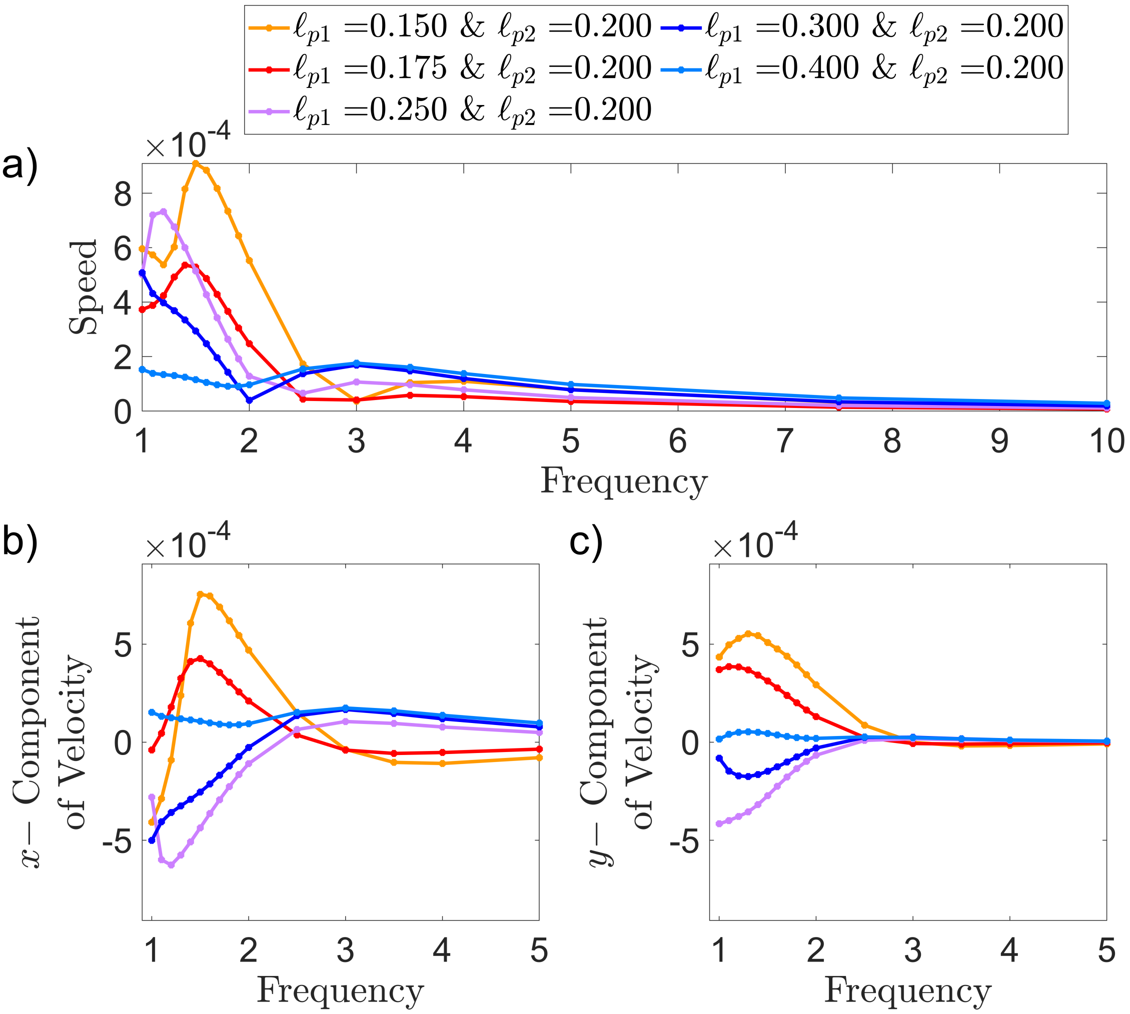

Figure 5.17: a) How the speed, b) the $x-$component of velocity and c) the $y-$component of velocity generated by the paddle system was affected by altering the actuation frequency for specific pairs of paddles when ℓ_{p2} = 0.200.

generated flow rate.

At lower frequencies, there was a larger amount of time for the paddle to rotate to a greater angle. As frequency was raised, the paddle was unable to keep up with the phase of the field and changed its direction of rotation at a smaller angle. Therefore, the maximum angle reached was greater at lower frequencies than that at larger values. It was worth noting that for the parameters investigated,

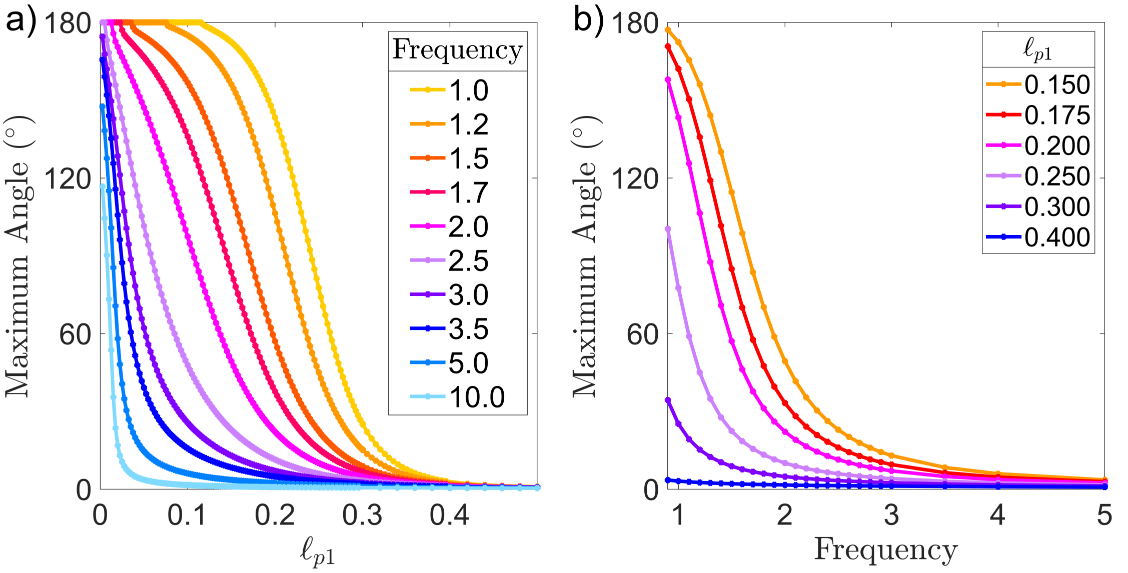

Figure 5.18: a) Displays the effect of ℓ_p on the maximum angle achieved of a paddle for various frequencies. b) The effect of actuation frequency on the maximum angle reached for certain values of ℓ_p used in Figure 5.17.

there seems to be an optimum value for a particular pair of paddles at which the system generates its maximum flow speed.

It has already been shown that, frequency affects the generated flow speed and the angle achieved by a set ℓ_p. Therefore, it was worth investigating whether the maximum angle achieved by a pair, irrelevant of the value of ℓ_p, affected the flow. The data from Figure 5.18 was used to modify the values of ℓ_{p1} and ℓ_{p2} over a range of frequencies so that the paddle maintained a certain consistent maximum angle achieved in a period. In order to maintain a consistent maximum angle over all frequencies, the value of ℓ_p would decline and the paddles would become less stiff as frequency was increased.

Figure 5.19 shows that the velocity generated still varies with frequency even when a consistent maximum angle was achieved for all values. It was clearly

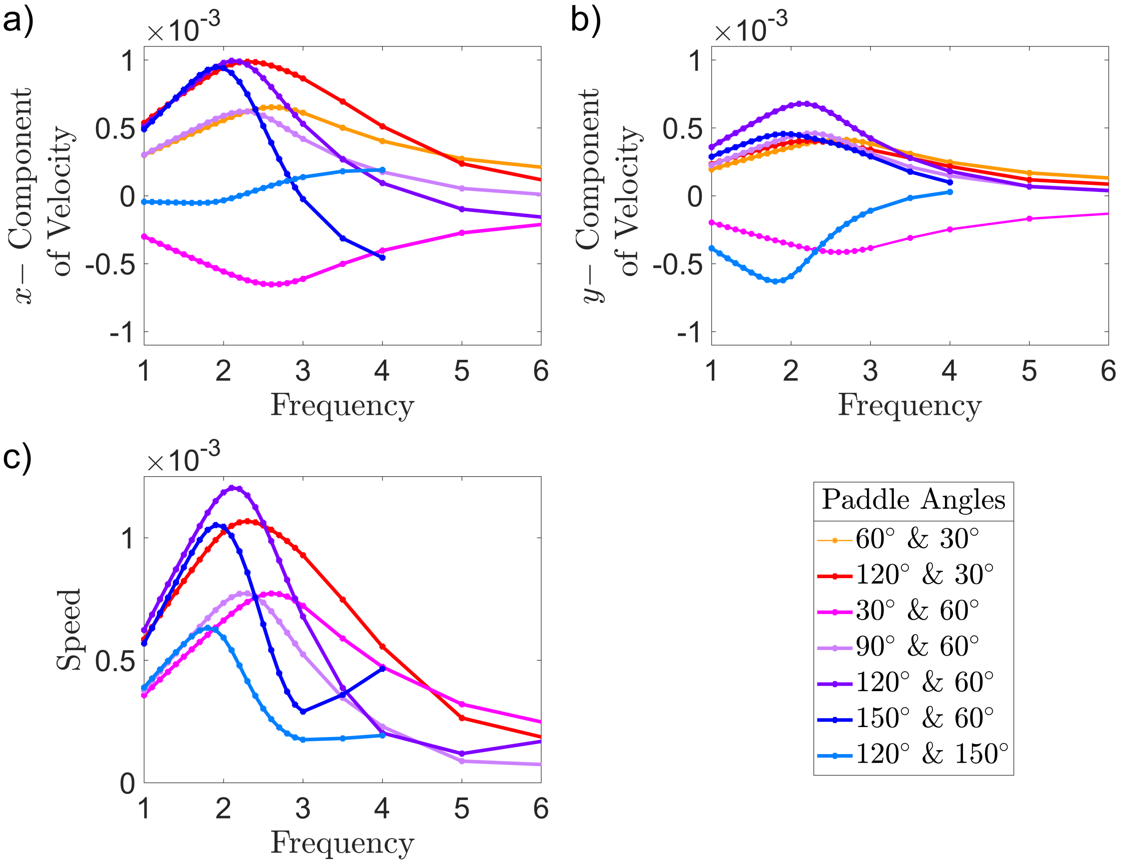

Figure 5.19: This displays how a) the $x-$component of velocity, b) the $y-$component of velocity and c) the speed generated by the paddle system with varying frequency when the maximum angle achieved was controlled by setting certain ℓ_{p1} and ℓ_{p2} values. In the legend the first angle corresponds to the maximum angle of the first paddle and the second to the second paddle.

shown that setting the angles does not mean a consistent speed was achieved over the different frequencies. This was because the value of ℓ_p was important, not just the angle achieved. Similar to the ℓ_p values, reversing the order of the paddles reverses the direction of the flow while maintaining the same magnitude, this can be seen for paddle pairs 60° & 30° (orange) and 30° & 60° (pink).

Several points are worth noting for the situation, when second angle was 60° and the first was varied between 30° (pink), 90° (lilac), 120° (purple) and 150° (dark blue). Firstly, the direction of the flow was different depending on if the maximum angle of the first paddle was greater or lesser than that of the second. When one angle $<$90° and the other was $>$90°, a larger maximum velocity was observed.

For the pairs which are within the category described above, 120° & 30° (red), 120° & 60° (purple) and 150° & 60° (dark blue), their $x-$component of velocity was initially very similar, see Figure 5.19(a). However for these pairs, it started to decrease at different frequencies. The frequency at which this occurred and the gradient was related to the stiffness of the paddles. The $x-$component of the least stiff pair of paddles in this set, (the pair with the greatest maximum angles), had the steepest gradient and started to decline at a lowest frequency than that of the others. The reverse was true for the stiffest pair of the discussed group. The $y-$component of velocity of these three pairs had a similar trend when frequency was varied, Figure 5.19(b). The pair with their maximum angle closest to 90°, (120° & 60°) exhibited the largest magnitude of the $y-$component.

The results from 60° & 30° (orange) and 120° & 150° (light blue) highlight that the difference in maximum angle was not the key factor, because if this was so it would be expected that the velocity of these pairs would be similar.

When altering the driving frequency of a system it was important to consider the flow generated per cycle. It can be seen from Figure 5.20 that this is not consistent over all frequencies. Initially, the flow per cycle remains almost constant but at a certain frequency range there is a rapid reduction in the speed.

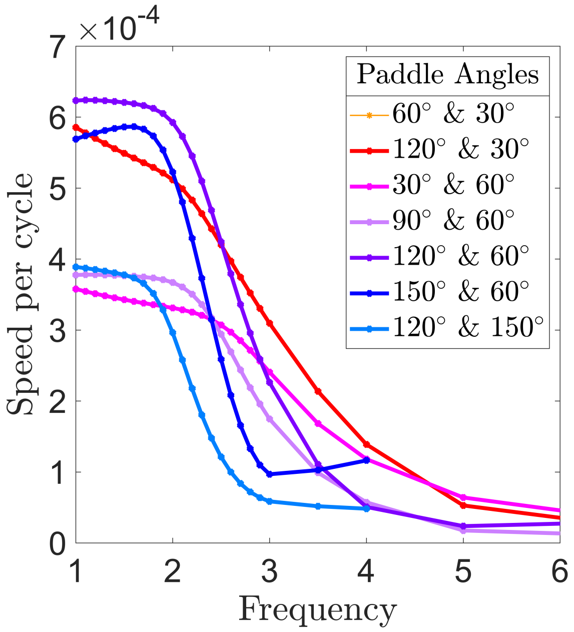

Figure 5.20: Displays the speed per cycle for the different paddle pairs in Figure 5.19.

It was also investigated how the behaviour of the paddles depended on other parameters such as k_{ij} (spring-like constant) and α (y component of the field amplitude). This was not included in this chapter as these investigations were to ensure the system was reliable. The results from this can be found in Appendix A.

5.4 Macro Two-Paddle Experimental Results

To further investigate the paddles experimentally, additional samples were produced. This was done in collaboration with Tom Moynihan who undertook an 8 week summer project hosted by the author of this thesis during his undergraduate studies.

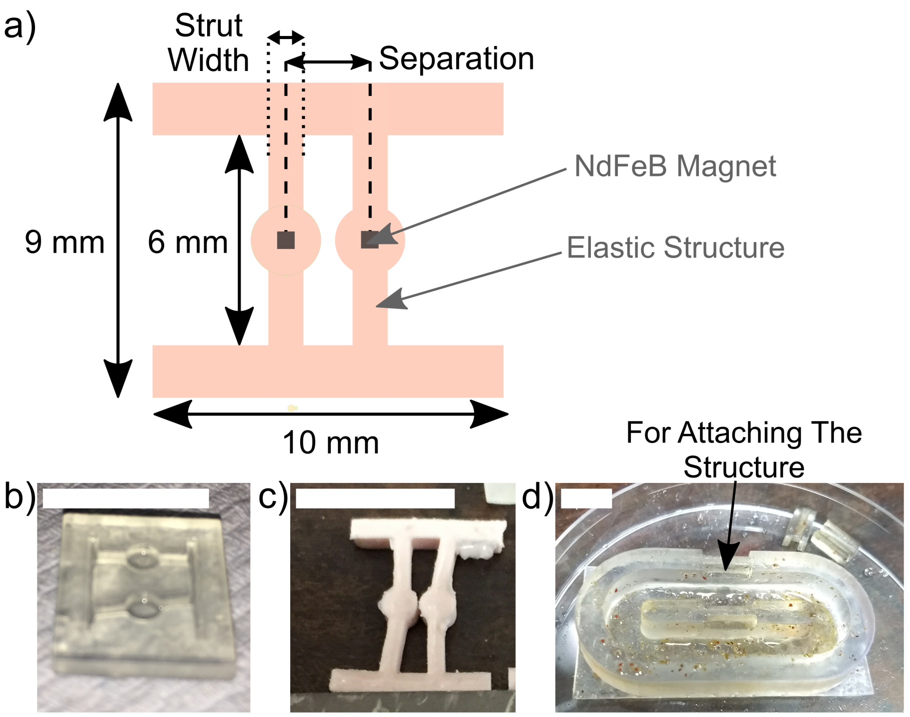

Figure 5.21: a) The design of the macro paddle structure. Photographs with a scale bar of 10 mm of b) the 3D printed mould c) the macro paddle structure and d) the channel.

Paddle devices were made with different widths of axles. The overall design of the samples were similar to that of the previously discussed micro paddle system. However, these were made on a larger scale using a different fabrication method to limit the fabrication time and enable tests to be conducted on a shorter timescale.

The macro paddle device consisted of an elastic structure of two paddles with different widths of axles and a magnet incorporated into each of the discs. The design can be seen in Figure 5.21(a) and the thickness of the overall structure was 0.5 mm. The centre-to-centre separation was 2.4 mm to agree with the ratio of the theoretical results. To fabricate these structures, a mould was created via 3D printing (Formlabs Form 2), as can be seen in Figure 5.21(b). The liquid silicone rubber (Polycraft with fast cure catalyst GP-3481-F agent 10:1 ratio by weight) was placed into the mould. NdFeB cubic 0.5 mm magnets, provided by the company SuperMagnetMan, were manually placed into the their desired locations in the mould. The magnets were orientated to have an in-plane magnetic moment using an external magnet, (which was not removed until the structure had cured). It was cured at room temperature for approximately 24 hours before it was removed. The final structure can be seen in Figure 5.21(c).

This fabrication method was less time consuming and therefore, a larger variation of sample parameters could be explored. However, this method also led to more defects in the samples, such as small air pockets in the elastic structure. Therefore, this method was suitable for initial tests to observe trends related to the model but less technologically favourable for practical applications.

Several types of paddle devices were produced and these could be categorised into two groups. One group of devices had one axle with a width of 0.5 mm, whereas the other group, a width of 1.0 mm. In both of these groups, the other axle's width was varied between 0.5 - 1.2 mm.

A fluidic channel was created via 3D printing. Within the design there were special notches to ensure the paddle structure was securely adhered to the channel walls, shown in Figure 5.21(d). The paddle structures were placed at the air-fluid interface within the channel. As a fluid, a mixture of 50% glycerol and 50% water was used, which had a viscosity of 5.04 mPa s [128]. The devices were actuated with a uni-axial oscillating magnetic field at frequencies 10-60 Hz with a strength

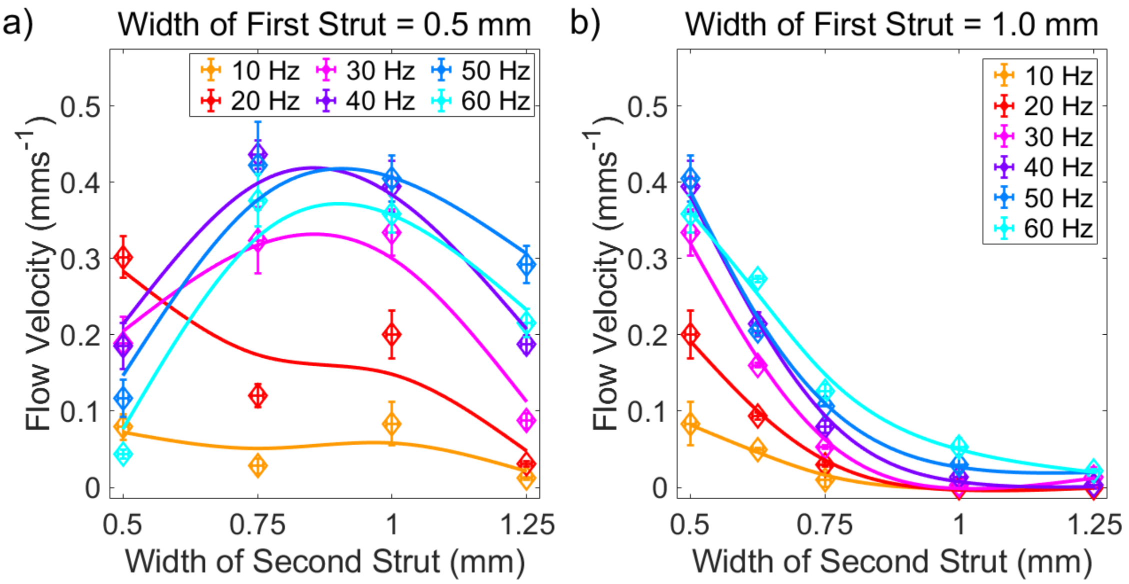

Figure 5.22: Average flow velocity as a function of width of the second axle for a two paddle system with the first axle with a width of a) 0.50 mm and b) 1.00 mm for various driving frequencies.There is a simple smoothing spline between the data points to act as a visual guide.

of 6 mT (using the ABIOMATER system, Appendix C).

Videos of the channel with the fluid and tracer particles were taken on a high speed camera (1000 fps). The videos were then converted into sets of images which were analysed with a software 'Tracker' [2] to obtain the generated flow rates. The results from these videos can be seen in Figure 5.22 and Figure 5.23.

This system had an approximate Reynolds number of 10^{-1}. In Figure 5.22 it can be seen that the width of the axles affected the flow generated by the paddles. In both sets, the pair of paddles that displayed the greatest flow rate were the pair that had the smallest width of the second axle that was not the same as that of the set width (i.e when the first axle width = 0.50 mm, and second = 0.75 mm, and when the first axle width = 1.00 mm, and second = 0.50 mm).

When looking at Figure 5.22(b), it can be seen that increasing the width of the second axle rapidly reduces the generated flow for all frequencies. Whereas for Figure 5.22(a) this was not the case.

It can be observed that there was a general trend that as the width of the second axle broadens (from the widths being the same), the generated flow rate becomes larger, before diminishing again as the paddle becomes sufficiently stiff.

The model predicted that the width of the axles of the paddles would affect the flow rate, as displayed by the experimental results. They were also in agreement that as the width of the second paddle's axle becomes significantly thicker (while keeping the width of the first paddle constant) the flow rate diminishes. In both investigations, the maximum flow rate was observed when a paddle was at the smallest set width.

It can be seen, particularly with Figure 5.22(a), that when the paddles have the same width they were still able to generate flow which does not agree with the theoretical model. The model did not take into account dipole magnetic moments, which could alter the difference in angle and therefore, the generated flow. In addition to this, the paddles were on the air-fluid surface boundary which adds additional forces into the system that could be adding an additional degree of freedom.

Similarly to the theoretical results, the frequency affected the flow generated by a pair of paddles, Figure 5.23. The stiffer the paddles, the less frequency affected the flow rate, which is in agreement with the model. The theoretical data implied

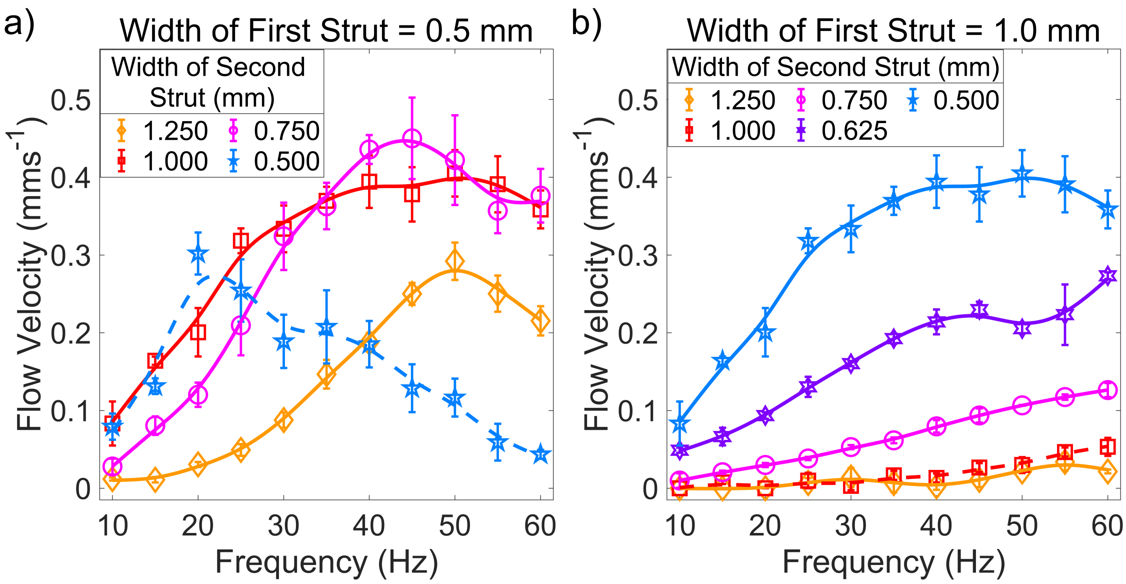

Figure 5.23: Average flow velocity as a function of frequency for a two paddle system with one axle with a width of a) 0.50 mm and b) 1.00 mm and the other with various widths (0.50-1.25 mm). The dotted line indicates the device where both the axles had the same width. There is a simple smoothing spline between the data points to act as a visual guide.

that there was an optimal frequency for a pair of paddles. The trends displayed in the experimental data agree with this theory. However experiments would need to be conducted at a larger frequency range to confirm this, which was not possible due to the experimental limitations.

5.5 Summary

This chapter demonstrates that spatially varying the axle width of paddle-based elasto-magnetic structures enables metachronal waves to emerge spontaneously. This occurred as the paddles rotated between bi-stable states defined by the field direction. A micro-paddle device was fabricated with PDMS and electroplated CoNiP cylinders and was able to generate flow speeds of up to 16 μms^{-1}.

To understand how time-reversal symmetry of paddle rotation could be broken to produce metachronal waves and therefore, generate flow in a low Reynolds number environment, a model of the device was developed. It consisted of periodically repeating two-paddle cells. The model was able to reproduce experimental features of actuation and to predict design paradigms for generating flow in a low Reynolds number environment. When both paddles had identical rotational stiffness, the maximum angle of rotation was the same as that of each other and no flow was achieved, which is in agreement with the mechanical experiments. However, flow could be achieved by paddles of different rotational stiffness, provided they were still able to rotate a certain amount. The experimental and theoretical results were also in agreement that altering the frequency affects the angle of rotation of the paddles and therefore, the generated flow. Further theoretical investigations were conducted on the behaviour of the paddles over a cycle, indicating that the non-reciprocal motion was caused by the difference in angle by the two paddles over a period.

For the parameters investigated, the maximum speed was generated when the centre-to-centre separation was 0.9, the frequency was 1.4, ℓ_{p1} = 0.130 and ℓ_{p2} = 0.225, achieving maximum angles of 45° and 148° respectively. It was found that greater speeds were generated when one paddle's maximum angle was greater than 90° and the others was less than that. This ensured there was a significant difference in angle throughout the cycle to create the non-reciprocal motion.

Considering the experimental design and set-up in Section 5.2, maintaining the same disc geometry, magnetic moment and magnitude of actuation field, the model suggests that a greater flow speed would be produced if the separation between was 135 µm, the widths of pairs of paddle axles were thicker ($\sim$ 13 µm and 35 µm) and the actuation frequency was $\sim$ 21 Hz.

Chapter 6

Single-Ferromagnet Elasto-Magnetic Pumps

6.1 Introduction

This chapter focuses on the fabrication and experimental investigation of a single elasto-magnetic pump. In previous chapters, the results of a two ferromagnetic particle swimmer (with one "hard" and one "soft" magnetic particle) have been described. In addition to this, swimmers and pumps comprised of multiple ferromagnets consisting of a single magnetic material have also been explored. In this section, creating a pump using a single ferromagnet will be studied. In order to obtain the two degrees of freedom using a single structure with a single magnetic particle, either the shape of the link/tail would need to be more complex than that of other designs investigated in previous chapters or the actuation needs to be multi-directional, e.g a rotating magnetic field. As a uni-axial coil system has been chosen as the activation method for a device with a single ferromagnet, the geometry of the link would need to be such that a phase difference could be obtained.

The publication on this work can be found in [160] and it was accomplished in collaboration with Jacob L. Binsley. He designed the enclosed pump system encasing the swimmer and recorded the raw data. The fabrication of the swimmer, certain elements of the data analysis and understanding the swimmer was undertaken cooperatively. While other elements of the data analysis were solely undertaken by the author of this thesis (all results in sections Section 6.6.2 and Section 6.6.4).

6.2 Design

The design of the swimmer encased within the pump was similar to that of Purcell's 3-linked swimmer. As stated in section 2.1.2, Purcell's swimmer is the simplest design able to swim in the Stokes regime and it consists of three links attached via two hinges that have a controlled rotation, see Figure 6.1(a). However this stroke pattern of the swimmer is difficult to control externally in practice.

The design of the discussed 3-link swimmer is similar to Purcell's swimmer but it differs in certain aspects, such as its geometry. The design differences between Purcell's swimmer and the created 3-link swimmer model can be seen in Figure 6.1.

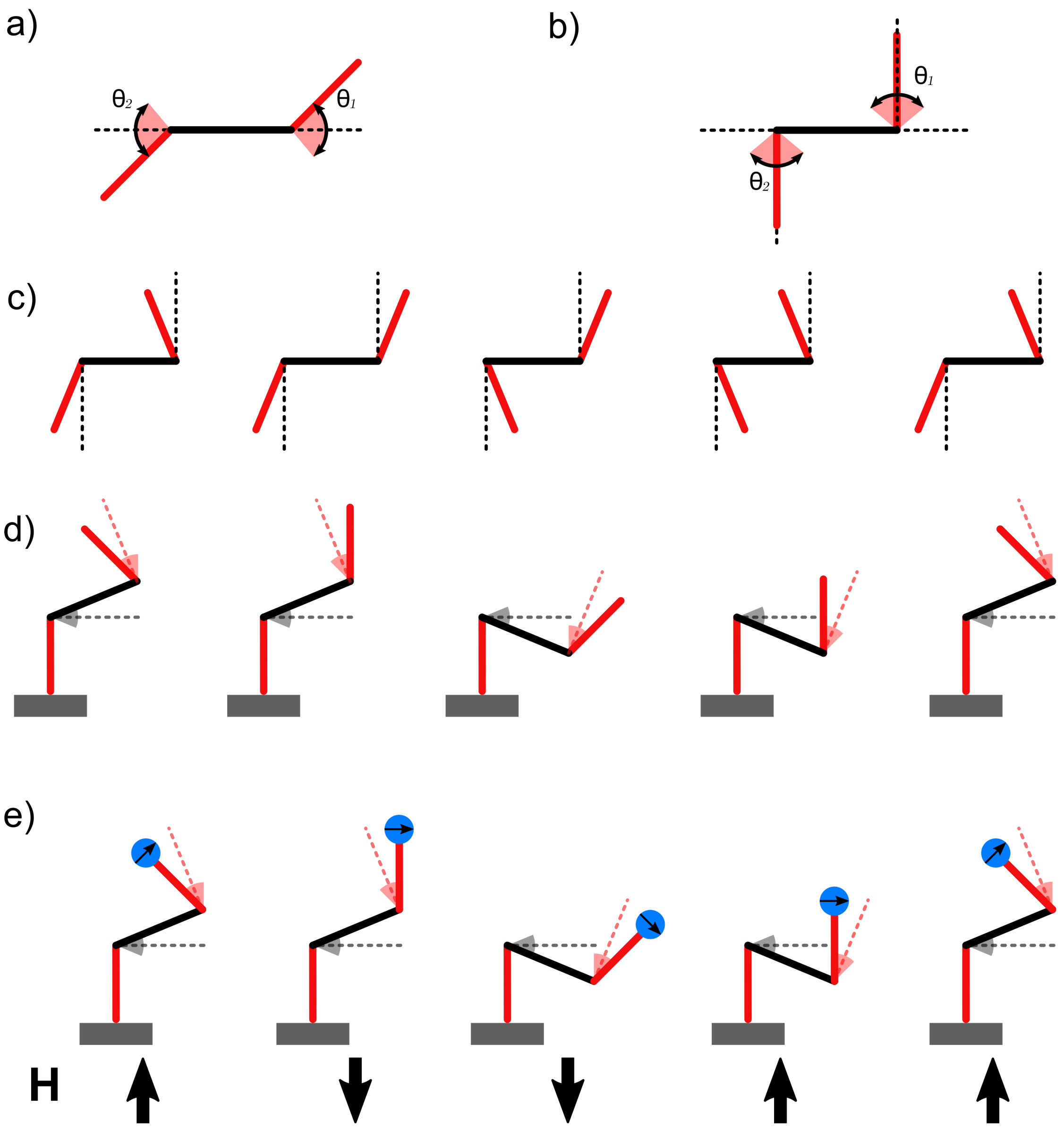

Figure 6.1: a) A schematic view of Purcell's 3-link swimmer. b) A schematic view of an adapted 3-link swimmer. c) A configuration sequence with the adapted 3-link swimmer that is non-reciprocal. d) How this sequence would look like if the bottom link was fixed to a surface. e) The proposed method to achieve this movement sequence with an external applied magnetic field and a magnet at the "head" of the swimmer. In cases (c)-(e) the last diagram the same as the first completing the cycle.

For the swimmer to be able to pump rather than swim it needs to be confined. One method would be to attach it to a fixed point, although a non-reciprocal stroke pattern would need to be maintained. It has been shown in Figure 6.1(d) that if the swimmer is attached to a surface by the end of a link, a non-reciprocal stroke pattern could still be obtained. However while this is achievable, a suitable method of magnetic activation is still required. The most simple approach would be to use a uni-axial magnetic field provided by electromagnetic coils. By adding a ferromagnetic "head" to the 3-linked elastic beam, an externally driven oscillating uni-axial magnetic field would generate a torque. With this configuration, a stroke pattern similar to that found in Figure 6.1(e) was predicted.

As mentioned previously, a swimmer that comprises of a single ferromagnet attached to straight link could also create an asymmetric response. Using a driving torque which is asymmetric in time, as seen in Section 3.1.4, it would be possible to activate such a swimmer. However this method increases the complexity of the external actuation equipment used to power the device. In the interest of limiting this complexity, the optimal solution is to actuate a geometrically asymmetric pump using a simple symmetric driving torque.

Merely for the ease of discussion, the design shown in Figure 6.2(a) will be referred to as a swimmer even thought it is a section within the pump, while the pump will refer to the overall system in Figure 6.2(e). The exact geometries of this system can be seen in Figure 6.2. Although the designed swimmer was based on that of Purcell's design, there are several different characteristics particularly with that of the links and hinges. Instead of flexible hinges the designed

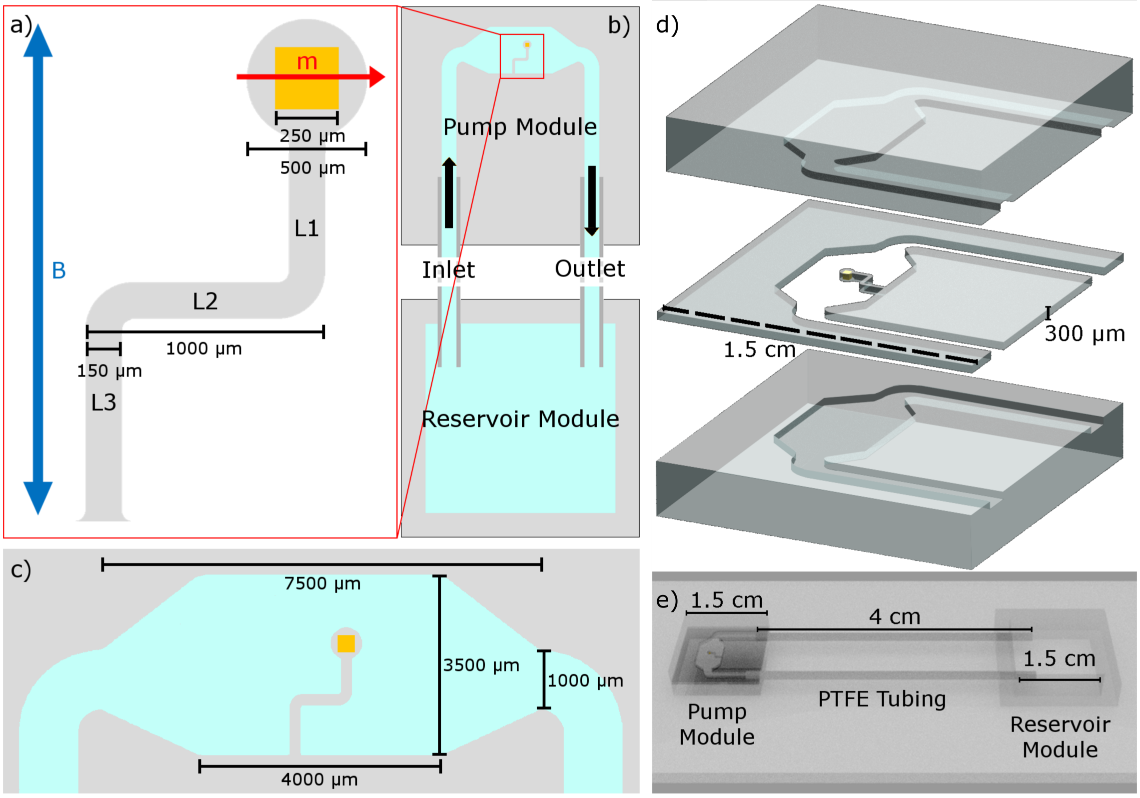

Figure 6.2: A diagram depicting the 3-linked pump, *(see next page for the full figure caption)*.

swimmer had elastic links which replace the role of the former, Figure 6.2(a), for ease of fabrication.

The behaviour of the created 3-linked pump was controlled by the elastic deformation in the design, similarly with the hinges in Purcell's swimmer. The average angle between the two pairs of links in the swimmer were required to change in order to create non-reciprocal motion, while only a single magnetic element is necessary to drive the motion. This is due to the fact that only the first link (the link closest to the magnetic head) needs to be actively driven, provided that the other links have an elastic restoring force. The elasticated links follow in phase behind the actively driven head to produce the non-reciprocal stroke cycle. As

Figure 6.2: This figure was adapted from [160]. For these diagrams gold is representative of the NdFeB 250 µm cubic magnet, grey is representative of the PDMS and blue is representative of a fluid. a) Shows the 3-linked swimmer with PDMS links labeled L1, L2 and L3. The gold region, the NdFeB 250 µm cubic magnet, has a red arrow indicating the direction of magnetisation while the blue arrow on the diagram indicates the direction of the uni-axial oscillating magnetic field. b) This is a cross-section diagram of the overall geometry of the enclosed pump. The red box points to where the swimmer is located. c) This shows a cross-sectional view of the pumping chamber where the swimmer is enclosed. d) This is a 3D rendering of an exploded projection of the pumping module of the device. The pumping module is made from three distinct layers and the middle layer contains the swimmer (a-c) e) A 3D rendering of the overall device. It shows how the pump module and reservoir module are arranged onto a glass slide and connected to each other via PTFE tubing.

previously mentioned, the discussed swimmer differs to that of Purcell's as it is fixed at the end of one link. This could be conceptualised as a third degree of freedom but it is not necessary for the non-reciprocal motion and this area of the swimmer is less mobile than that of others, due to the geometry.

While the general design has been discussed, particular materials for the components have not been introduced. The ferromagnetic head of the swimmer was comprised of a 250 µm cubic NdFeB magnet encased in PDMS, Figure 6.2(a). These are the same magnets used in Section 5.4. The swimmer's links and the pumping module were both formed of PDMS. The pumping module is fully enclosed with enough internal volume around the swimmer to allow the swimmer to move in-plane and drift out-of-plane without coming into contact with the boundary walls, Figure 6.2(c). The pumping module, PTFE tubing and reservoir module created an enclosed system which constitutes as a pump. Further details regarding the pump module, PTFE tubing and reservoir module layout can be found in Appendix B and [160].

6.3 Fabrication

The design of the fully enclosed pumping system can be seen in Figure 6.2(e). In order to produce the enclosed system, the device was separated into several different sections for the fabrication; the pumping module, reservoir module and the connecting tubing. These sections would later be connected together to form the enclosed system. The pumping and reservoir module were comprised of the

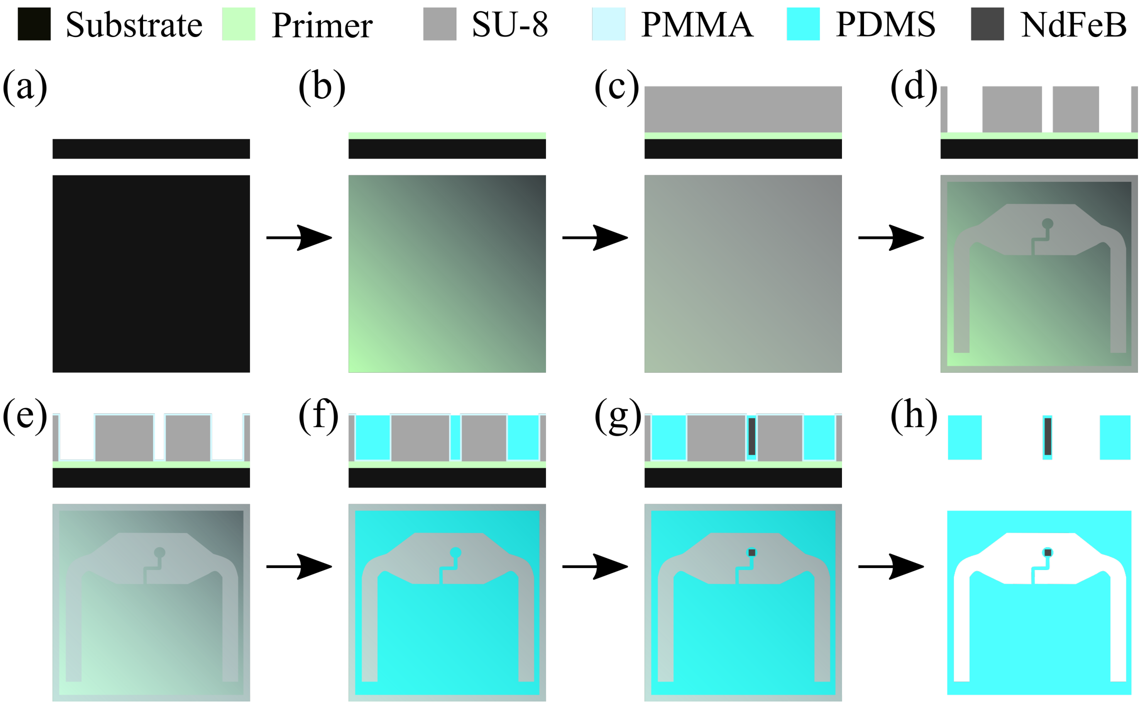

Figure 6.3: Fabrication of the middle section of the pumping module. For each stage there is a cross-sectional view above a top-down view. The height and width of the cross-sectional diagrams are not to scale with each other. a) Silicon wafer, b) hexamethyldisilazane (HMDS) based primer spun on, c) SU-8 preparation, d) Photolithographic step with development, e) polymethylmethacrylate (PMMA) spun on, f) uncured PDMS put into the mould, g) placing the NdFeB magnet into the uncured PDMS, h) Cure the PDMS using an oven and remove the structure from the mould.

silicon material PDMS. As such, the pumping and reservoir modules required certain moulds to shape the PDMS into the correct geometry.

The reservoir module had much larger feature sizes than that of the pumping module, therefore it was appropriate for the modules to be created using different techniques. A mould for the reservoir module was produced via a 3D printer with photopolymer resin. This method however was not suitable for the pumping module.

The fabrication of the pumping module was separated into three layers, as can be seen in Figure 6.2(d). The moulds for the upper and lower capping layers of the pumping module were both produced using an acrylic mould which was CNC machined. However, the middle layer of the pumping module, which consisted of the swimmer, required a more detailed fabrication process than other parts of the pump. This was due to the small, detailed structure of the swimmer and therefore, a more intricate mould is required.

The mould for the middle layer of the pumping module was created using lithographic techniques. The overall fabrication process of this middle layer is shown in Figure 6.3. Firstly a primer, hexamethyldisilizane (HMDS), was spin coated (at 4000 rpm) onto a 2 cm $\times$ 2 cm square of silicon wafer and baked (10 minutes at 95°C on a hot plate). This was to produce good wetting of the substrate by the later used SU-8 to improve substrate-resist adhesion, which is essential for obtaining homogeneous and stable coatings [161]. Next, the SU-8 3050 was spin coated onto the substrate (1500 rpm to produce $\sim$300 µm thickness) followed by a soft bake (45 minutes at 95°C on a flat-levelled hotplate).

The SU-8 was now prepared for exposure. The designed photo mask was printed on emulsion film by JD Photodata. The photomask was aligned with the wafer using a Kloe UV-Kub 2 masking optical system and exposed (UV 365 nm wavelength and 40 mW/cm^2 irradiance for 15 s). The substrate was then post-baked appropriately (5 minutes at 95°C on a hot plate). After this step, the SU-8 was developed (using propylene glycol methyl ether acetate (PGMEA) in a sonicator for 20 minutes) and cleaned (with isopropanol and N_2). The substrate was then ready for a sacrificial layer, which is crucial in removing the PDMS from the mould. The sacrificial layer used was polymethylmethacrylate (PMMA) 950K A4, which was spin coated onto the mould (4000 rpm) and baked (10 minutes at 100°C on a hot plate).

After the moulds for the three layers of the pumping module were produced, these moulds were filled with uncured PDMS (mixed 10:1 oligomer to curing agent) and cured (11 hours at 50°C in an oven) which would give an approximate elastic modulus of 1.6 MPa [154]. During the curing process, but before the middle layer was introduced to the oven, it was necessary to add a NdFeB magnet (250 µm cube) to the swimmer. The magnet was first dip-coated in PMMA, dried at room temperature before being manually inserted into the head of the swimmer in the middle layer of the pump. It was rotated to the desired orientation by application of an external magnetic field. The reservoir mould was also filled with PDMS and cured in an oven under the same conditions as the other moulds.

Once all three layers of the pumping module and the reservoir module were cured, they were removed from their respective moulds. The middle layer of the pumping module was removed by placing the substrate in acetone and providing agitation to remove the PMMA layer and allow the PDMS to be lifted from the substrate. After removal, these layers were manually aligned in a vertical stack (using an optical microscope) and additional uncured PDMS was used as an adhesive using the "stamp-and-stick" method [162]. It was cured at room temperature (for $\sim$ 48 hours) to avoid further heating of the pump and therefore maintaining a low elastic modulus. Once the PDMS was fully cured, this structure formed the completed pumping module.

The completed pumping module and reservoir module were each bonded at opposite ends of a glass slide with oxygen plasma treatment [163]. To link the two modules together PTFE tubing (inner diameter 860 µm) was inserted into both modules and sealed using uncured PDMS (and again cured for 48 hours at room temperature). The device was then completed and was able to be filled with fluid through the reservoir module using a needle and syringe.

6.4 Methods

High speed videos (1000 fps) of the experimental data were taken by Jacob L. Binsley, more details can be found in Appendix B and [160]. Some videos were taken of the swimmer itself to observe its behaviour, while others were of polystyrene tracer particles (15 µm diameter) in the channel to determine the flow speed generated by the device. After the experimental videos were taken, the images would go through an image analysis to determine the motion of the pump. This was mainly completed on the software 'Tracker' [2]. Firstly, the initial position of the centre of the pump's head or a particular tracer particles were recorded in the tracking software (e.g. frame 1). The position of the centre of the head or particular particles was automatically tracked by the software between frames as its position altered until the final frame. In this way it would be able to capture the position over multiple periods of the magnetic field oscillation. The final frame was set so that an integer number of periods of the driving field had occurred from the first frame (typically 1000 frames, 1 second, unless this was restricted). The maximum driving frequency in these experiments was limited to 60 Hz. This is due to the equipment used as the power was not sufficient to maintain the maximum field amplitude used at higher driving frequencies.

The velocity of the tracer particles can be calculated from the raw tracking data, where the velocity of a tracer particle is taken as the distance travelled over this integer number of periods. The peak fluid velocity, v_{peak}, is taken to be equal to the peak tracer particle velocity recorded as the particles are assumed to have equal velocity to the surrounding fluid. The maximum velocity of the fluid v_{peak} is known to occur at a consistent cross-sectional position at the centre of the channel. Therefore, this position is a consistent point of reference for the measurements.

The volumetric flow rate, Q, can be calculated from the peak fluid velocity v_{peak} as the channel cross section is known as the length, L_c, height, h and width w is known. For the channels used in this study, which are rectangular, the following two equations can be used [164]:

$$v_x(y,z) = \frac{4h^2\Delta P}{\pi^3\mu L_c}\sum_{N,odd}^{\infty}\frac{1}{N^3}\left[1-\frac{\cosh\left(N\pi\frac{y}{h}\right)}{\cosh\left(N\pi\frac{w}{2h}\right)}\right]\sin\left(N\pi\frac{z}{h}\right), \tag{6.1}$$

and

$$Q = \frac{h^3 w\Delta P}{12\mu L_c}\left[1-\sum_{N,odd}^{\infty}\frac{1}{N^5}\frac{192}{\pi^5}\frac{h}{w}\tanh\left(N\pi\frac{w}{2h}\right)\right]. \tag{6.2}$$

Where v_x is the velocity at any given position in the channel, ΔP is the pressure difference and μ is the dynamic viscosity. Here $h < w$ and y and z are the position vectors denoting a specified position within the cross section of the channel. The described equations were found by solving the Navier-Stokes equation analytically for a pressure induced steady-state fluid flow in an infinitely long, straight, rigid channel with a rectangular cross-sectional area. These equations, Equation (6.1), Equation (6.2) and $Q = Av_{average}$, where A is the cross-sectional area of the channel, can be used to a calculate a ratio of $v_{average}/v_{peak}$ given by

$$\frac{v_{average}}{v_{peak}} = \frac{\pi^3}{48} \frac{\left[1 - \sum_{N,odd}^{\infty} \frac{1}{N^5} \frac{192}{\pi^5} \frac{h}{w} \tanh\left(N\pi \frac{w}{2h}\right)\right]}{\sum_{N,odd}^{\infty} \frac{1}{N^3} \left[1 - \frac{\cosh\left(N\pi \frac{y}{h}\right)}{\cosh\left(N\pi \frac{w}{2h}\right)}\right] \sin\left(N\pi \frac{z}{h}\right)}. \tag{6.3}$$

For the geometry of the system, Equation (6.3) is calculated to be $\sim$ 0.4776. Due to this the peak velocity measurements need to only be multiplied by this ratio to obtain the average velocity and with addition to the channel cross section area, the volumetric flow rate.

6.5 Actuation & Swimming Motion

As previously mentioned, the swimmer was actuated via a hard ferromagnet connected to its head and a uniform, uni-axial oscillating magnetic field provided by a Helmholtz coil system. The magnet was orientated so that the magnetic moment was perpendicular to the external magnetic field. At this orientation the magnetic torque, which is the main force governing the motion, is at its maximum value. The duration of a period of the magnetic field's oscillation was equal to that of the swimmer's complete stroke cycle.

The actuation led to a deformation of the elastic beams, with the three links deforming out of phase with each other. The motion of the swimmer is reminiscent

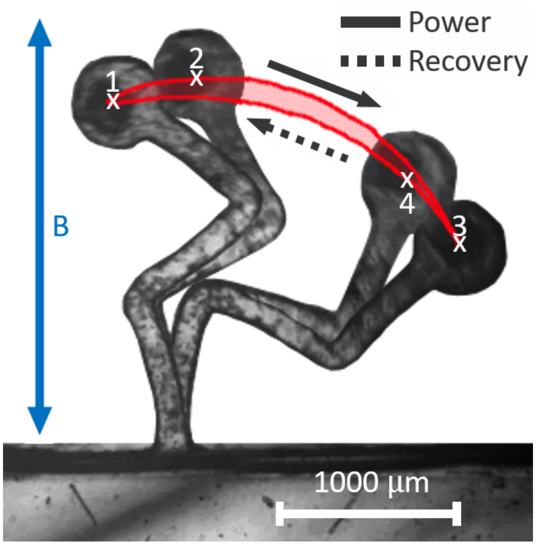

Figure 6.4: This indicates the hysteric pumping motion of the swimmer. It is four frames from a high speed video recording of the swimmer, labeled 1-4. The red line indicates the motion of the centre of the pump head. This image is taken from [160] and the image is adapted from data taken during experiments where the viscosity of the fluid is 0.001 kgm^{-1}s^{-1} and the driving field amplitude and frequency are 6 mT and 50 Hz respectively.

of that of Purcell's. This motion would be different to that of a swimmer that consists of a single flexible rod. Labeling the links, as in Figure 6.2, the motion of the swimmer can be discussed in the following paragraphs.

The predicted motion of the swimmer was shown in Figure 6.1(e) and the actual motion of the swimmer can be seen in Figure 6.4. There are two key differences between the predicted and actual motion of the swimmer. Firstly that the link L3 does in fact bend and secondly that bending occurs throughout the swimmer, however the majority of the deformation is within the links. These two aspects do not make a significant difference on the overall pump as the motion of is still asymmetric and it is still in the same category of swimmer as that of Purcell's design due to the other parallels that can be drawn.

An extension and contraction of the swimmer was observed in accordance with the direction of the generated torque. When a clockwise torque is generated, the swimmer goes through points $1 \rightarrow 2 \rightarrow 3$ which not only bends the swimmer towards the right, but also increases the average angle between links L1 and L2, describing a length extension of the system, Figure 6.4. The reverse is true of an anti-clockwise torque, the swimmer goes through points $3 \rightarrow 4 \rightarrow 1$. However, in this case, the extension and contraction of the length is much smaller as the pump deforms to the left.

Investigating the specific motion it was observed that the top-most link, L1, responds before the middle link, L2, as it is closer to the magnetic head. It appears that L1 was leading in phase and again there was a similar case between L2 and L3 where L2 leads the phase. Therefore, the desired non-reciprocal motion was achieved, this can be seen in Figure 6.4. The difference in phase between the links is the key factor in achieving this.

6.6 Results & Discussion

6.6.1 Hysteretic Area

As mentioned above, this overall motion is related to that of Purcell's swimmer. As the swimmer is pinned to the base, it was observed that the motion of the head exhibits a closed loop path and there is a hysterestic area enclosed, as shown in Figure 6.4. The result of this is that the swimmer goes through what can be thought of as a power stroke and a recovery stroke. This is where the fluid can be thought of as being pumped in both directions but the pumping in the direction of the power stroke is larger than the direction of the recovery stroke. This type of motion can be observed in biological cilia [165]. It is known that the area enclosed within the closed loop path difference between these two strokes of the cilia is proportional to the volume of the fluid pumped per cycle, this area is therefore an important figure of merit with respect to the pump response [121].

Continuing to look at the motion of the swimmer as in Section 6.5, the area contained in the closed loop path of the swimmer was investigated as a function of driving frequency for several different field amplitudes and viscosities, Figure 6.5. It was calculated as the median area over multiple pump cycles, with the standard deviation between these cycles taken as the uncertainty measurement. Due the frame rate and the nature of the path taken by the pump, at higher frequencies, fewer data points per oscillation period can be captured. For example, at a driving frequency of 10 Hz, 100 data points would be recorded per pump cycle, whereas at 50 Hz, only 20 points per cycle would be recorded. By looking at multiple periods it is possible to obtain a larger a spread of points across the closed loop for frequencies which do not give an integer when the frame rate is divided by the frequency. This is all due to sampling and therefore, the data is interpolated using a smoothing spline to better represent the physical realistic pump motion. However, due to the nature of the path taken by the pump, if too few data points are taken during a cycle, then linearly interpolating between them will result in

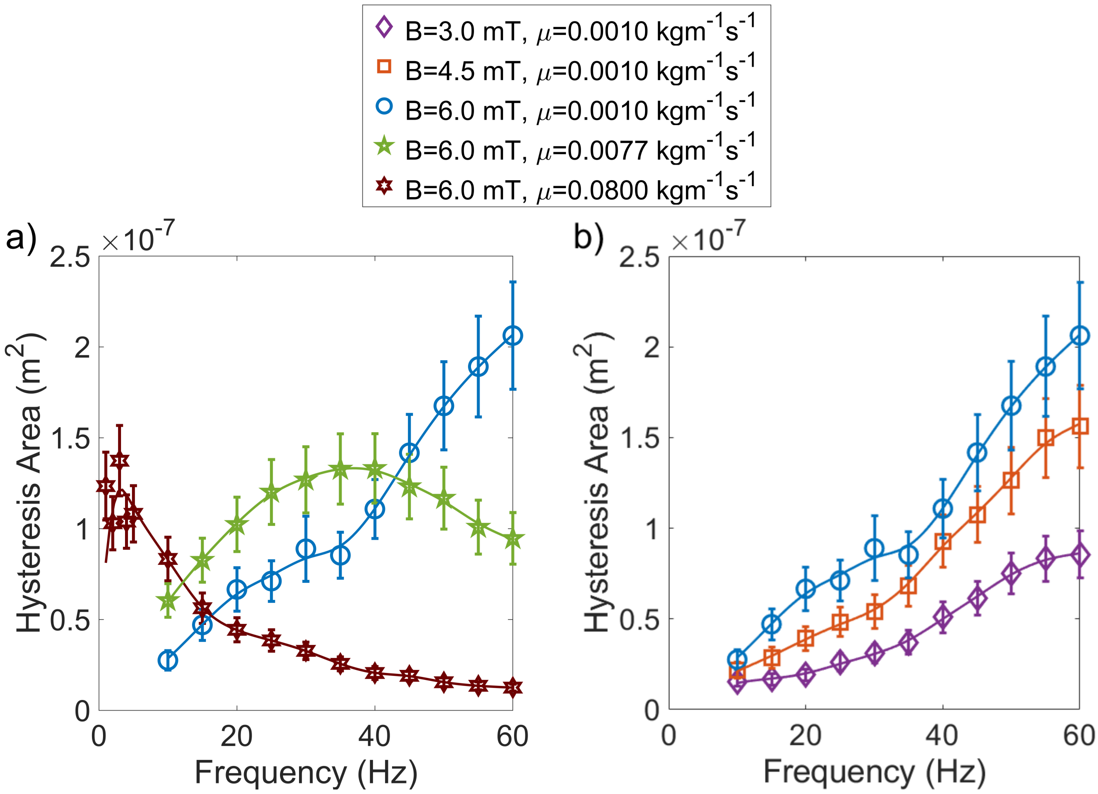

Figure 6.5: This shows area of the closed loop path of the swimmer head as a function of driving frequency. a) Shows the dependence on fluid viscosity with a constant field amplitude of 6 mT, b) shows the dependence on field amplitude with a constant dynamic viscosity of 0.001 kgm^{-1}s^{-1}. It is worth noting that the blue data points are the same in both (a) and (b). The plotted lines are a simple smoothing spline between the data points to act as a visual guide.

significantly under predicting the value of the enclosed area. Therefore it is necessary to interpolate between the data points with a smooth function, such as a smoothing spline.

Figure 6.5 contains the results of the hysteretic area measurements. At low frequencies, the hysteretic area enlarged with increasing frequency. This is clearly visible apart from $\mu = 0.08$ kgm^{-1}s^{-1}, where the viscosity is the largest used in this research. However, it is known that as the driving frequency tends to zero, the hysteretic area must also tend to zero. The maximum hysteretic area for $\mu = 0.08$ kgm^{-1}s^{-1} appears in the range of a few Hertz. Therefore, it can be concluded that the trend displayed by $\mu = 0.0077$ kgm^{-1}s^{-1} is similar to that of $\mu = 0.08$ kgm^{-1}s^{-1}. It is deduced that this trend of increasing the driving frequency expands the area of hysteresis until a maximum value of hysteretic area is reached. Following on from this point increasing the driving frequency further only reduces the area.

It can be seen from Figure 6.5(a) that the optimal driving frequency of the system strongly depends on the viscosity of the surrounding fluid. Firstly, the frequency at which the maximum hysteretic area is reached has an inverse relationship with viscosity. In addition to this, the magnitude of the maximum hysteretic area increases as the viscosity of the fluid decreases. This is due to the reduced drag force allowing the swimmer more ease of movement. In contrast to this, the field amplitude on the system is not shown to have a such a strong effect on the hysteretic area as that of the viscosity, see Figure 6.5(b). It does not alter that trend of the data, but field amplitude does increase the hysteretic area at any particular driving frequency. As can be expected, a greater field amplitude allows for greater maximum displacement of the pump from its original position, which widens and broadens the hysteresis. This is due to the increased torque force on the swimmer while other forces are kept similar.

This can be explained by looking at the dimensionless parameter known as the sperm compliance number, $\mathcal{S}_p$. The behaviour of a sperm-like swimmer has been studied analytically through the application of slender body theory. Slender body theory considers thin filaments moving through viscous fluids, far from any boundaries.

When examining a sperm-like swimmer with a magnetic head and a flexible tail analytically through the use of slender body theory, performing small amplitude motion, the sperm compliance number indicates the interaction between the provided force and the motion of a single tailed swimmer [99, 100, 166].

$$\mathcal{S}_p = L\left(\frac{\xi_\perp \omega}{E_b}\right)^{1/4}, \qquad \begin{pmatrix} \boldsymbol{F}_{head} \\ \boldsymbol{M}_{head} \end{pmatrix} = \mathcal{S}_p^4 \mathcal{R} \begin{pmatrix} \boldsymbol{u_{fh}} \\ \boldsymbol{\Omega} \end{pmatrix}. \tag{6.4}$$

Where the characteristic length scale L, the frequency of oscillation of the magnetic field ω, $\xi_\perp$ is the perpendicular fluid dynamic resistance coefficients, E_b is the Euler-Bernoulli filament of bending stiffness which is a constant of flagellum elastic stiffness. $\boldsymbol{F}_{head}$ and $\boldsymbol{M}_{head}$ represent the viscous drag force and the magnetic moment at the head respectively, while $\mathcal{R}$ is the dimensionless grand resistance matrix of the magnetic head, $\boldsymbol{u_{fh}}$ and $\boldsymbol{\Omega}$ represent the head velocity field.

An alteration in the sperm compliance number changes how the swimmer behaves [99, 100] and the resultant flow produced. Although this theory is not suitable to be applied in depth to experimental systems due to the necessary approximation of the system to be a series of high aspect ratio filaments and the boundary conditions, it provides a general overview of how the behaviour of the swimmer and resultant flows are expected to vary with geometric parameters.

As can be seen in Equation (6.4), increasing the driving frequency will increase $\mathcal{S}_p$. Increasing the viscosity of the fluid will also do this. Therefore, these together will accelerate the increasing sperm compliance number. Following this, a system of greater fluid viscosity will therefore exhibit a high sperm compliance number behaviour at low driving frequencies than larger. Altering the driving force in isolation does not alter it, but will have an impact on the flow. However, this impact is not a large as other parameters such as viscosity or driving frequency [99].

6.6.2 Investigating The Closed Loop Path

The shape of the hysteretic area which can be represented by the arclength and width can be investigated. The calculated arclength and width for three examples is shown in Figure 6.6(a-c). The power stroke and recovery stroke can be approximated as arcs. The arclength for a particular viscosity and frequency is taken to be the median path length of the power stroke over multiple pump cycles, with the standard deviation between these cycles being taken as the uncertainty measurement. Here, the width of the loop is similar to that of the width of a crescent-like or ellipsoidal-like shape. It was calculated using the following method. Any point on the power stroke path is a certain distance away from each point on the recovery path. Finding the minimum distance for each point in the power stroke to the recover path results in a series of distances. Finding the maximum of these distances can be thought of as the width of the loop. Again, the median over multiple pump cycles was used as the width, with the standard deviation between these cycles being taken as the uncertainty measurement.

The arclength and width of the closed loop drawn by the head of the swimmer were investigated for different driving frequencies, with various viscosities and

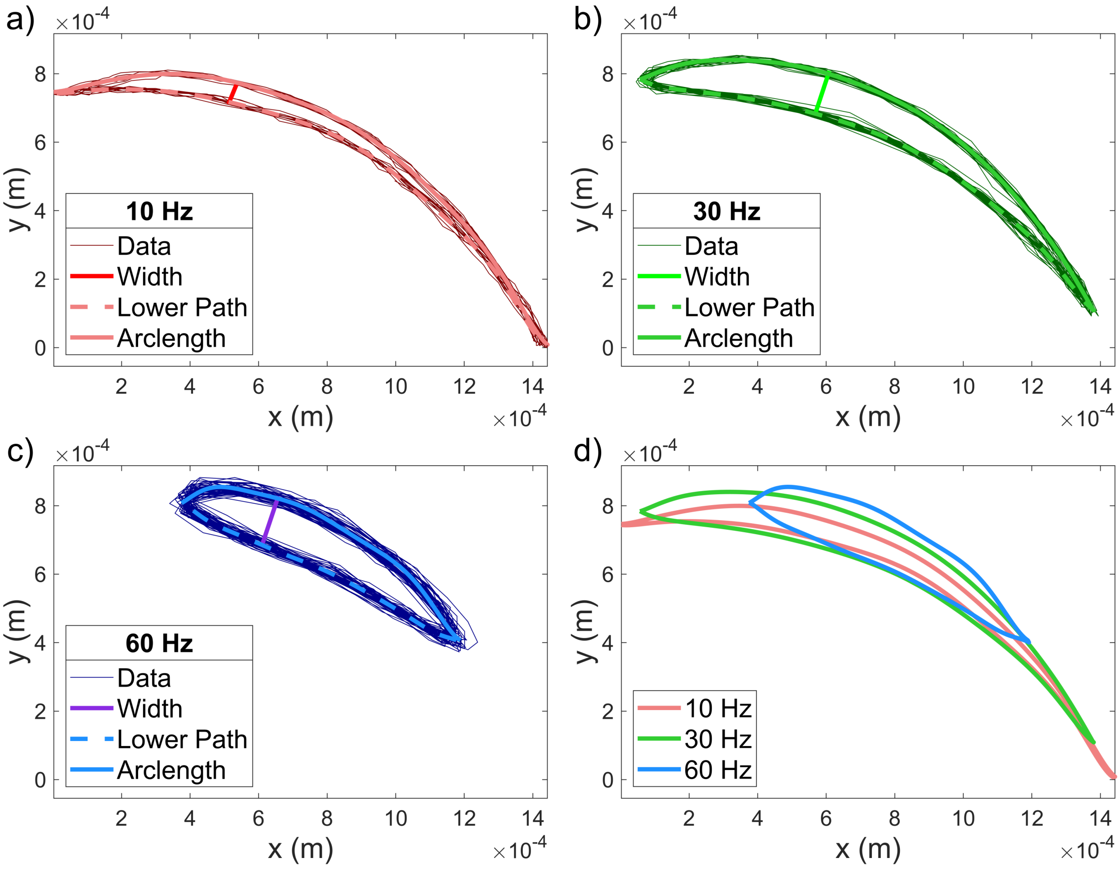

Figure 6.6: Investigating the closed loop path drawn by the head of the swimmer for the cases when the viscosity is 0.0077 kgm^{-1}s^{-1} and an actuation frequency of a) 10 Hz b) 30 Hz c) 60 Hz. The shape path is approximated to be two curves, with the upper curve being referred to as the arclength. d) Shows the approximated loops observed at frequencies 10 Hz, 30 Hz and 60 Hz.

field strengths. As can be seen from Figure 6.7, the viscosity of the fluid affects the shape of the closed loop more than the magnetic field. Looking particularly at the ratio between width and arclength with frequency in Figure 6.7(c), the different viscosities display very different trends while the distinct magnetic field results are very similar. Although, as can be seen Figure 6.7(d), the individual magnetic field ratios for the various frequencies differ slightly with the largest magnetic field displaying the largest ratio.

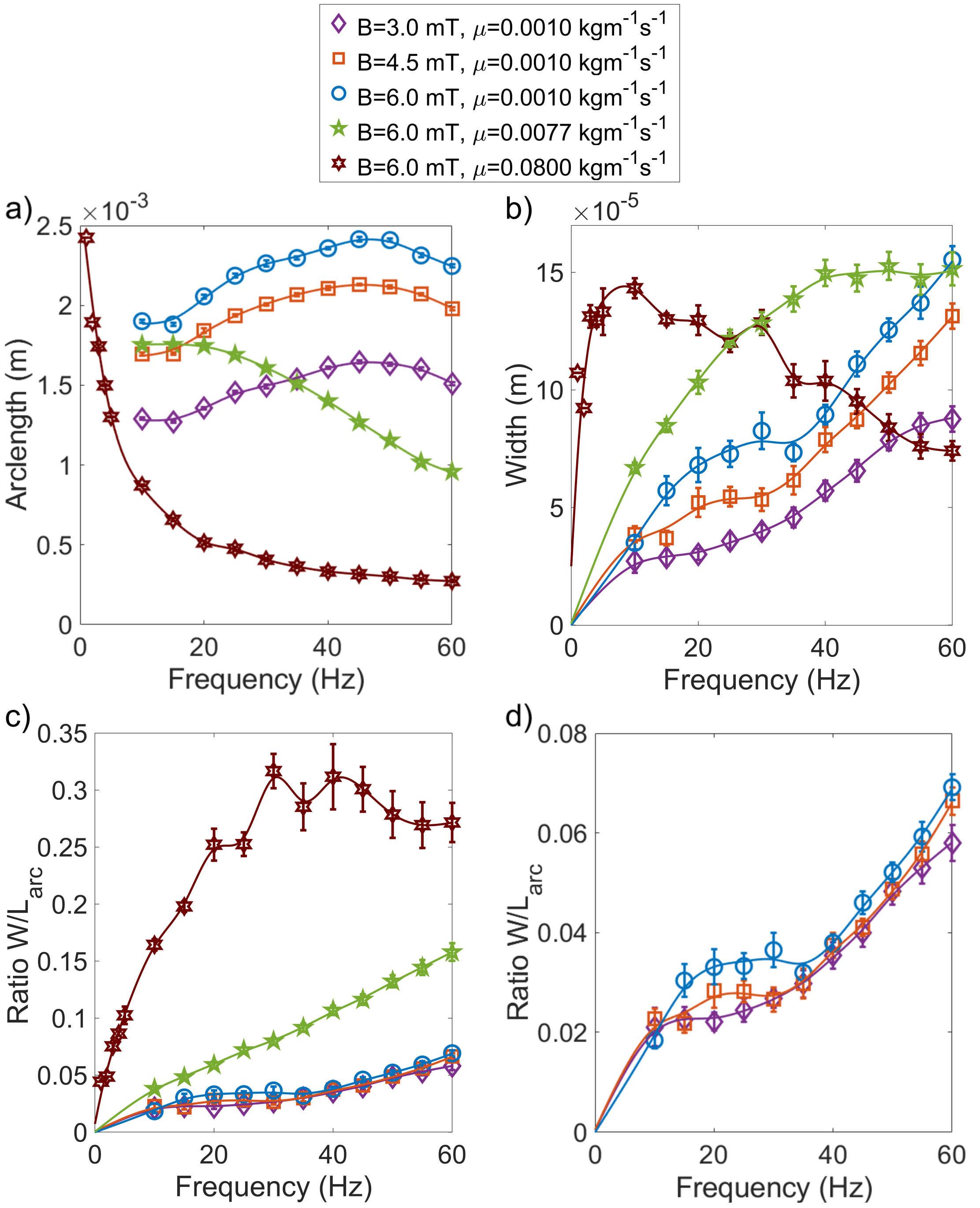

Figure 6.7: This shows shape dependence of the closed loop path of the swimmer head as a function of driving frequency. a) Shows the arclength dependence on frequency for various fluid viscosities and constant field amplitudes, b) shows the width dependence with frequency for the investigated fluid viscosities and field amplitudes. *(continued on next page)*

Figure 6.7: *(continued from previous page)* c) Shows the ratio of width (W) and arclength (L_{arc}) with frequency for the investigated fluid viscosities and field amplitudes. d) Is similar to (c) but only shows the investigations for various field amplitudes to be able to view this more clearly. The plotted lines are a simple smoothing spline between the data points to act as a visual guide.

Looking at Figure 6.5, Figure 6.6 and Figure 6.7 together, the general shape of the closed loop path can be understood further. Generally at low frequencies, the path drawn by the head displays a long sweeping arc, where the power stroke path is very similar to the recovery stroke path. The difference between the two paths widens as the frequency is increased and the path becomes more circular in shape. An example of this is shown in Figure 6.6(d) where the viscosity is 0.0077 kgm^{-1}s^{-1} and the paths for 10 Hz, 30 Hz and 60 Hz is shown.

This occurs until there is a significant decrease in arclength, (seen in μ=0.08 kgm^{-1}s^{-1}, $\sim$ 10 Hz) which also causes the width to decrease as well, due to the closer distance required to return to the initial position. It was predicted that the maximum arclength would occur at the lowest frequency and that as frequency increased, the arclength would decrease. This was predicted to be due the swimmers being unable to "keep up" with the driving frequency, so the head would not reach its maximum displacement (of that at lower frequency driving fields) before the magnetic field switched causing the swimmer's head to try to move in the opposite direction again and the closed loop path becomes more circular. However this only occurs when the viscosity is 0.0077 kgm^{-1}s^{-1} and 0.08 kgm^{-1}s^{-1}, which is when the Reynolds numbers are the lowest in this investigation.

Looking specifically again at the data with varying applied magnetic field strength with a viscosity of 0.001 kgm^{-1}s^{-1}, for all frequencies, the larger the magnetic field strength, the larger the arclength and the larger the width. However, for all the different magnetic field strengths, as the driving frequency increased so did the arclength until a maximum value was achieved (at $\sim$ 45-50 Hz). After this, as the driving frequency increased the arclength decreased. While in the range of the results, the width increased with frequency for the different magnetic field strengths. The similar trend is hypothesised to be due to their similar sperm compliance numbers. Having an increased arclength from that of at the lowest frequency is thought to be due to there being some time dependence in their motion. This is predicted to be the case as although their Reynolds' numbers are less than one, they are not as significantly below one compared to that of other results.

The different viscosity curves with a constant applied magnetic field strength (6 mT) displayed a maximum arclength (Figure 6.7(a)) and width (Figure 6.7(b)) at different frequencies to each other. The frequency at which the maximum arclength and width occurred at is inversely proportional to viscosity, similarly to hysteretic area (Figure 6.5(a)).

6.6.3 Flow Rates

From the video data tracking the tracer particles, the flow rate could be calculated (see B.2 and Section 6.4). This pump is able to produce flow rates in the range of -100 µl/h to 730 µl/h for the smallest viscosity investigated (0.001 kgm^{-1}s^{-1}).

The range was achieved only by altering the properties of the applied field.

Similarly to the area hysteresis results, as the frequency tends to zero so too does the flow rate. The flow produced is not a constant unidirectional flow but oscillates in both a positive and negative direction through each cycle. This is due to the recovery aspect of the stroke which moves fluid in the reverse direction of that of the power stroke. However, it does so less effectively which causes a non zero net flow.

In order to calculate the Reynolds number of a system, the velocity of the flow is required to be used. Taking the results from the experiments of different magnetic fields, (3 mT, 4.5 mT 6 mT) and a viscosity of 0.001 kgm^{-1}s^{-1}, the calculations come to the same value, which is $\sim 10^{-1}$. For the results when the viscosity is 0.0077 kgm^{-1}s^{-1} and 0.08 kgm^{-1}s^{-1} (both with a field amplitude of 6 mT) the Reynolds numbers are $\sim 10^{-2}$ and $\sim 10^{-4}$ respectively.

Observing the results shown in Figure 6.8, a few key points can be noticed. Firstly, there is a consistent region of negative flow produced for the smallest viscosity investigated (0.001 kgm^{-1}s^{-1}), it was seen at all investigated field amplitudes. The results also indicate such a region occurs when looking at the data with viscosity 0.0077 kgm^{-1}s^{-1}. This region of negative flow has not previously been documented for experimental Purcell-based systems. This effect is caused by the restrictions imposed on the system due to the close proximity of the boundary walls and at certain driving frequencies the negative flow direction can become favourable. This ability to have a flow rate in different directions without altering the geometry or any of the fixed properties of the system is noteworthy. By only

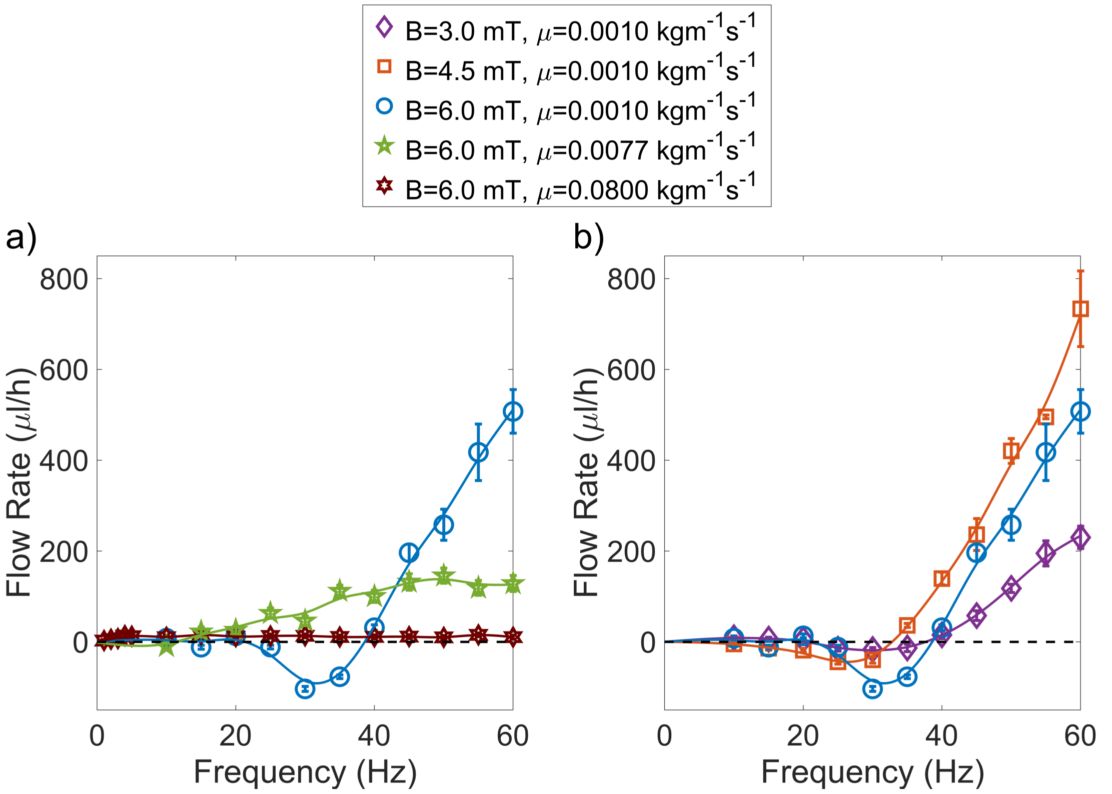

Figure 6.8: Shows the average volumetric flow rates produced at different driving frequencies when a) the fluid viscosity is varied and there is a constant field amplitude of 6 mT and b) the applied field is varied and there is a constant fluid viscosity of 0.001 kgm^{-1}s^{-1}. The dashed line on both graphs indicated a flow rate of 0 μl/h and the plotted lines on both is a simple smoothing spline between the data points to act as a visual guide.

altering the properties of the external actuation field the flow direction can change, this is an important factor to consider with regards to potential applications.

In Figure 6.8(a)), it can be seen in most cases that the larger the viscosity, the smaller the magnitude of the velocity. This is particularly apparent at frequencies above that of where the negative flow region is located ($f \geq 45$ Hz).

It can be observed that the peak flow rate is skewed more towards higher frequencies than that of the maximum area (seen most clearly where viscosity is 0.0077 kgm^{-1}s^{-1}). As the driving frequency increases thereafter, the pump completes more cycles in a set time period. At frequencies greater than at which the optimal hysteretic area occurs, the decrease in fluid displaced per cycle is counteracted by more cycles occurring within a certain time period. Looking at Figure 6.8(a), as the viscosity increases the magnitude of the maximum flow rate is reduced, similarly to maximum hysteretic area. In addition to this, by increasing the fluid viscosity the maximum flow rate occurs at lower driving frequencies.

Looking particularly at Figure 6.8(b)), it can be seen that there is not a linearly proportional relationship with field amplitude and flow rate (for a particular driving frequency) like there is with field amplitude and area enclosed by the head of the pump. The maximum flow rate occurs at the intermediate driving field amplitude (4.5 mT) rather than at the larger amplitude (6 mT) as might be expected. However the larger amplitude, 6 mT, is the amplitude which has the largest frequency range of negative flow direction. As the field amplitude increases the phase lag motion of the head is reduced. This is due to the fact that the force of torque increases compared to the opposing fluidic forces. This alters the moment in the cycle when the potential elastic energy is released. Therefore, an optimal driving amplitude is likely to exist in the context of maximising flow production within this system.

Using the data from the volumetric flow rates, it is worth looking at the volumetric flow rates per cycle, Figure 6.9. If the motion of the swimmer was constant regardless of the driving frequency, the same volumetric flow rates per cycle would

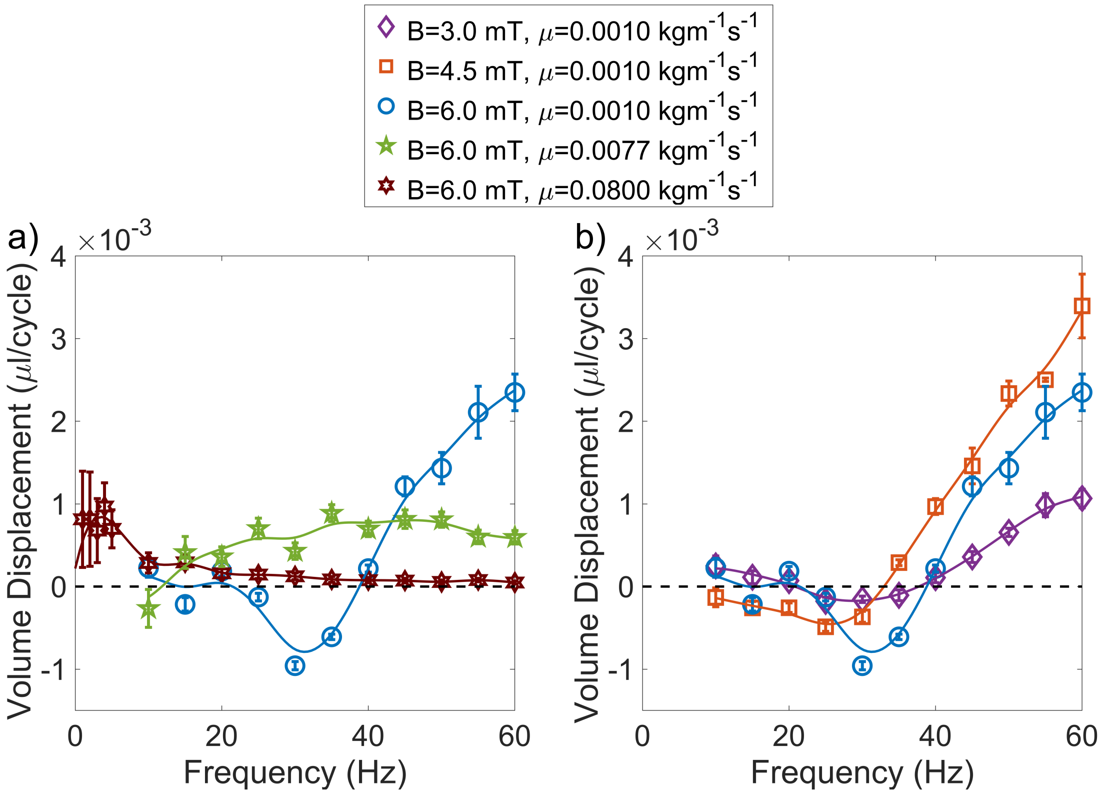

Figure 6.9: Shows the average volumetric flow rates per cycle produced at different driving frequencies a) when the fluid viscosity is varied and there is a constant field amplitude of 6 mT and b) when the applied field is varied and there is a constant fluid viscosity of 0.001 kgm^{-1}s^{-1}. The dashed line on both graphs indicated a flow rate of 0 µl/cycle and the plotted lines on both is a simple smoothing spline between the data points to act as a visual guide.

be expected across all the driving frequencies for a particular viscosity and field strength. As seen in Section 6.6.1 and Section 6.6.2, the driving frequency affects the motion of the swimmer. Therefore, it is not unexpected that the volumetric flow rates per cycle depends of the driving frequency.

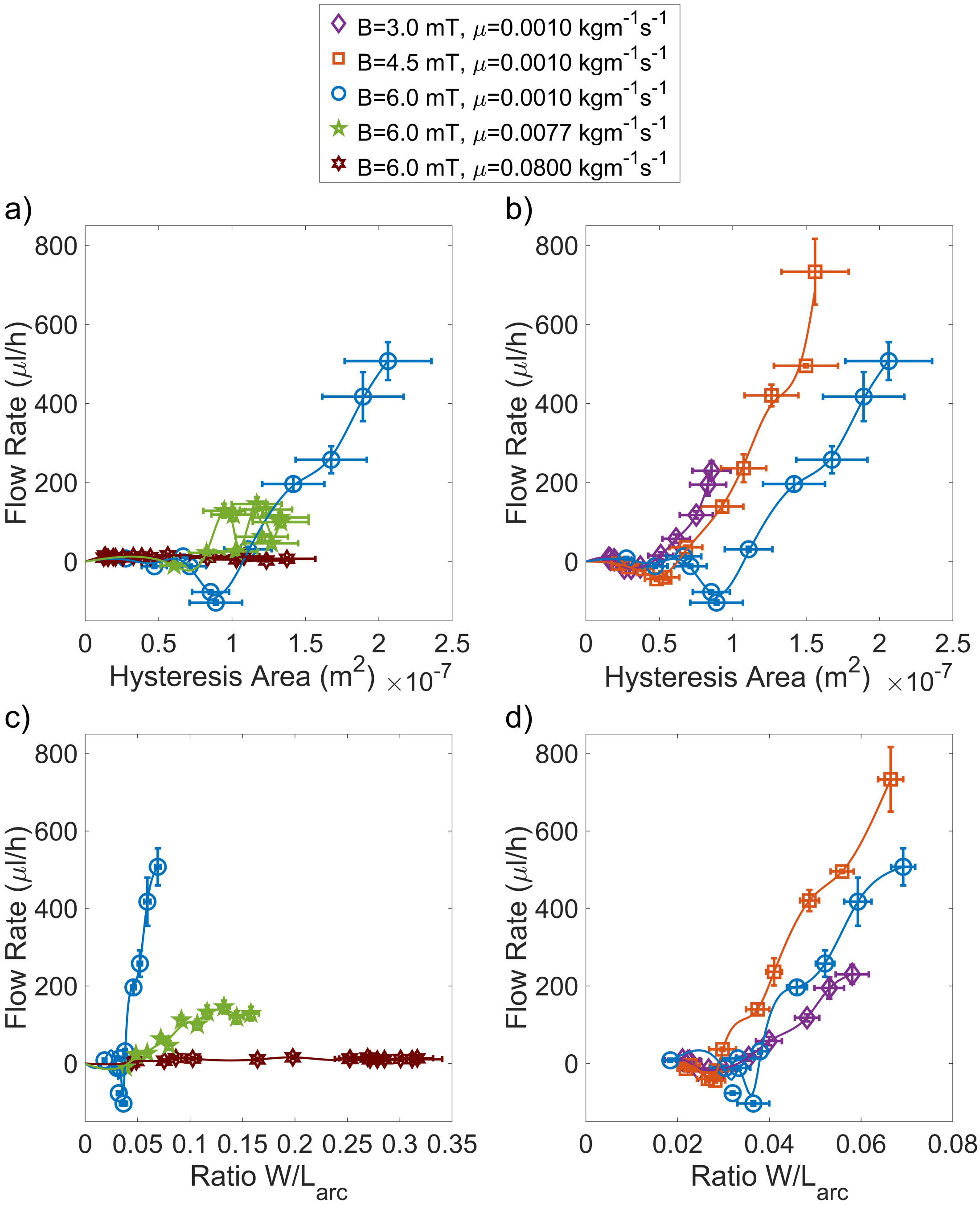

Figure 6.10: Comparing the average volumetric flow rates produced at different driving frequencies to the shape of the closed loop path drawn by the head of the swimmer, *(see next page for the full figure caption)*.

Figure 6.10: Shows the how average volumetric flow rates produced at different driving frequencies relates to the shape traced by the head of the swimmer. The dependence of hysteretic area when (a) the fluid viscosity (constant field amplitude of 6 mT) and (b) the applied field is varied (constant fluid viscosity of 0.001 kgm^{-1}s^{-1}). The dependence of the ratio of width/arclength (W/L$_{arc}$) when (c) the fluid viscosity is varied (field amplitude of 6 mT) and (d) the applied field is varied (constant fluid viscosity of 0.001 kgm^{-1}s^{-1}). There is a simple smoothing spline between the data points to act as a visual guide.

6.6.4 Comparing Flow Rates With The Closed-Loop Path

As can be seen looking from the data in Figure 6.5 and Figure 6.8 in Section 6.6.1 and Section 6.6.3 respectively, there was a certain relationship between the hysteretic area and the flow rate achieved. As Figure 6.10(a) and (b) show, there was a general trend, as hysteretic area increases so did the flow rate. However, there were additional factors such as the shape of the hysteresis which influences this relationship. This is represented in the dependence of the ratio of arclength and width compared with the flow rate, Figure 6.10(c) and (d). In this case the different magnetic field trends were much more similar to that of one another, while the behaviour at different viscosities still varied. It is worth noting that the the results with different viscosities where operating within different Reynolds numbers. In addition to this, the Reynolds number when the viscosity was 0.001 kgm^{-1}s^{-1} was $\sim$ 10^{-1}, while this is less than 1 and could be considered to be a low Reynolds number it is still relatively large. It is important to remember that Reynolds num-

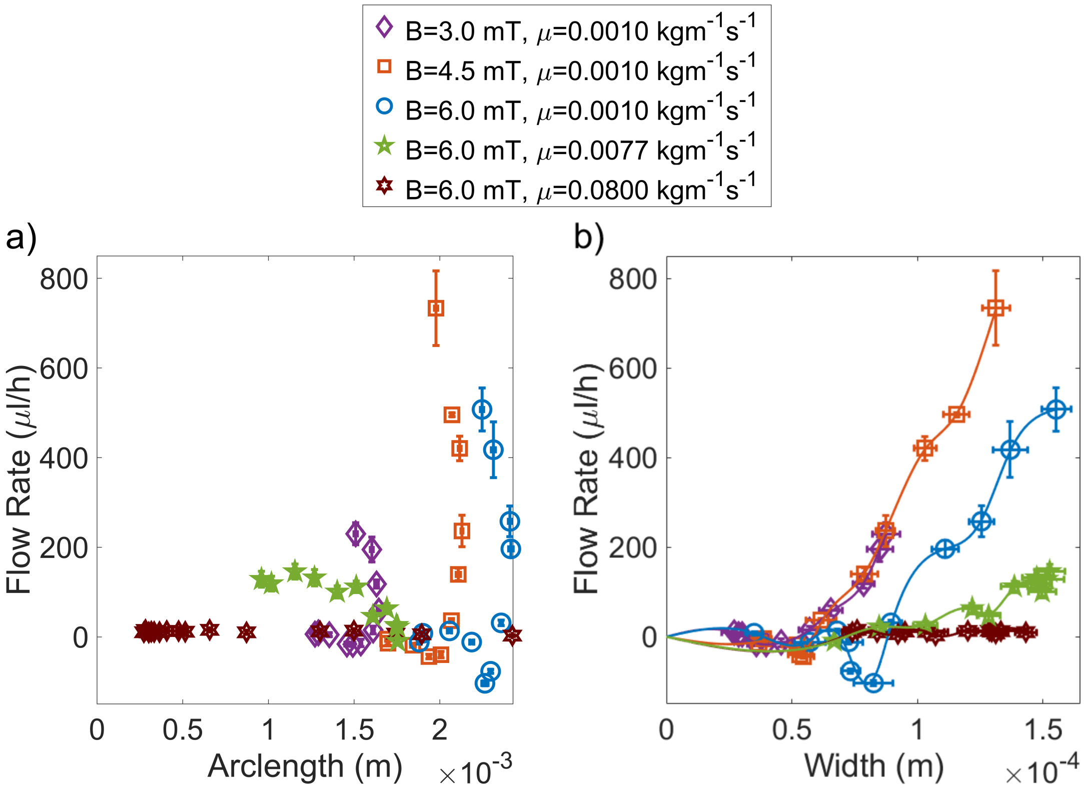

Figure 6.11: The relationship between average volumetric flow rate and a) the arclength and b) the width of the path traced by the head of the swimmer for various magnetic fields and viscosities, there is a simple smoothing spline between the data points to act as a visual guide.

ber is the ratio of inertial forces to viscous forces within a fluid and that different Reynolds numbers, even if the ratio is very small, would mean that the inertial forces have a different affect even if the viscous forces still dominate.

There are additional factors as the trends for different applied magnetic fields and viscosities are still separate. The relationship between the ratio of arclength and width with flow rate is a similar situation as hysteretic area, Figure 6.10(c) and Figure 6.10(d). However, in this case, the different magnetic field trends are much more similar, while the different viscosities still display very different trends.

The effect of width and arclength on the flow rate was investigated. As can be seen in Figure 6.11(a), there is little correlation between the arclength and the flow rate. It can only be observed that the larger flow rates only occur at the greater arclengths. However looking at the width, Figure 6.11(b), it can been seen that the width has an effect on the flow rate but other factors, such as viscosity and Reynolds number, also affects the flow.

To conclude, while the area enclosed by the head of swimmer and the corresponding properties are an important factor affecting the flow rate, other factors have also been investigated and observed to have a relationship with the flow rate, such as viscosity, Reynolds number and frequency.

6.7 Summary

This work has successfully created an asymmetric elasto-magnetic pumping device. This device is based on that of Purcell's 3-linked swimmer.

The peak flow was produced at an optimal driving frequency which is closely related to phase difference between the actuation of the links. This behaviour agrees with that of Purcell's 3-link swimmer as a maximum fluid velocity is observed at an optimal phase difference [99].

It's pumping is tuneable in terms of scale and is bidirectional, this is of interest as there is no need to alter the pumping system, instead only the magnetic field parameters, frequency and strength. The device has no physical connection to any external system (unlike most systems which use electric motors) and is self-contained. This is important as it has the possibility to open doors in new lab-on-a-chip technology. In addition to this, the pumping mechanism does not alter the fluid in any way through chemical reactions. The method of actuation can be generated via a single uni-axial magnetic coil system, minimising the complexity of the actuation equipment. While the fabrication time could be considered long, mainly due to the curing times, the process lends itself to batch manufacture. The pump can be fabricated as one piece with the rest of the microfluidic device. It could be integrated at the time of manufacture with minimal extra assembly required and the fabrication techniques are similar to that that are currently being used in microfluidics, to allow ease of integration. This device is the first experimental realisation of a Purcell-like pumping system and while the behaviour largely agrees with current research, it also exhibits behaviours which have not previously been observed.

Chapter 7

The Development of Elasto-Magnetic Paddles

7.1 Introduction

This chapter focuses on the further developments of elasto-magnetic paddle devices. This is separated into two main sections, fabrication advancements in the elasto-magnetic membrane and then experimental and theoretical results investigating the effect of magnetic orientation on the paddle system.

7.2 Advancements In The Elasto-Magnetic Membranes

This section will focus on methods of fabricating elasto-magnetic membranes with NdFeB. The membrane in Chapter 4 required a large number of steps and due to electrodeposition, it was not suitable to be used with NdFeB. However given the high anisotropic properties of this material and consequently the large torques that can be produced, it was desirable to incorporate NdFeB into elasto-magnetic membranes. Therefore, new designs were created using this material with the aim of reducing the fabrication time and maximising magnetic torque.

7.2.1 PDMS Network Embedded With SU-8 Pillars & NdFeB

Given the size constraints when using NdFeB, a method was created to produce an elasto-magnetic membrane with feature sizes of the order of 50 µm. This feature size was slightly larger than that of the devices discussed in Chapter 4, with the largest values at orders of several hundreds of micrometres. Given this large variation, there was a need for a thicker photo-resist, SU-8, as was used in Chapter 6.

NdFeB powder was a promising candidate for this research, partly used due to its popular use, as mentioned in Chapter 3. The NdFeB powder (purity 99%) used was provided by American Elements. Initial tests found that it could be embedded in a SU-8 structure, Figure 7.1(a). To achieve this, the powder was sprinkled on

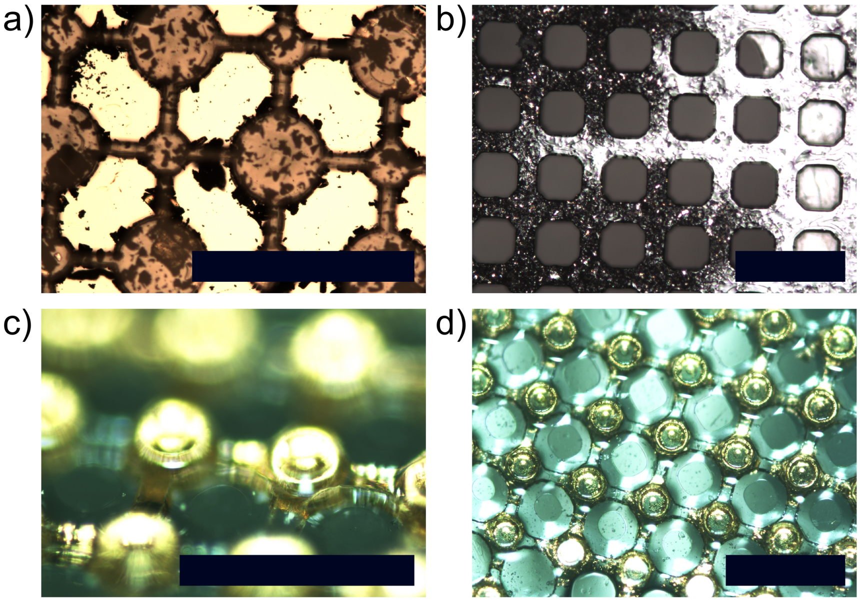

Figure 7.1: a) SU-8 structure embedded with NdFeB. b) PDMS and NdFeB structure produced with a SU-8 mould. c) SU-8 pillars within a PDMS network (Au is visible below the pillars). d) a top down view of (c). The scale bar in the bottom right corners of all of these pictures has a length of 500 µm.

the resist after it was spun on the substrate and then baked to embed the particles within the solid structure. The rest of the lithographic process was the same as that for SU-8 without the powder (similar to the process described in Section 6.3).

A further test was conducted to produce structure comprised of PDMS and NdFeB powder. The structure was able to be attached to a PDMS frame, Figure 7.1(b). In this procedure, the mould was first made using SU-8 and a sacrificial layer of PMMA was added. Then, the uncured PDMS was introduced to the mould and the NdFeB powder was again sprinkled on. Once the PDMS had cured, the structure was removed from the mould (via agitation in acetone to remove the sacrificial layer) and attached to a frame via the "stamp & stick" method [162]. As can be seen in Figure 7.1(b), the density of the powder is not uniform and the

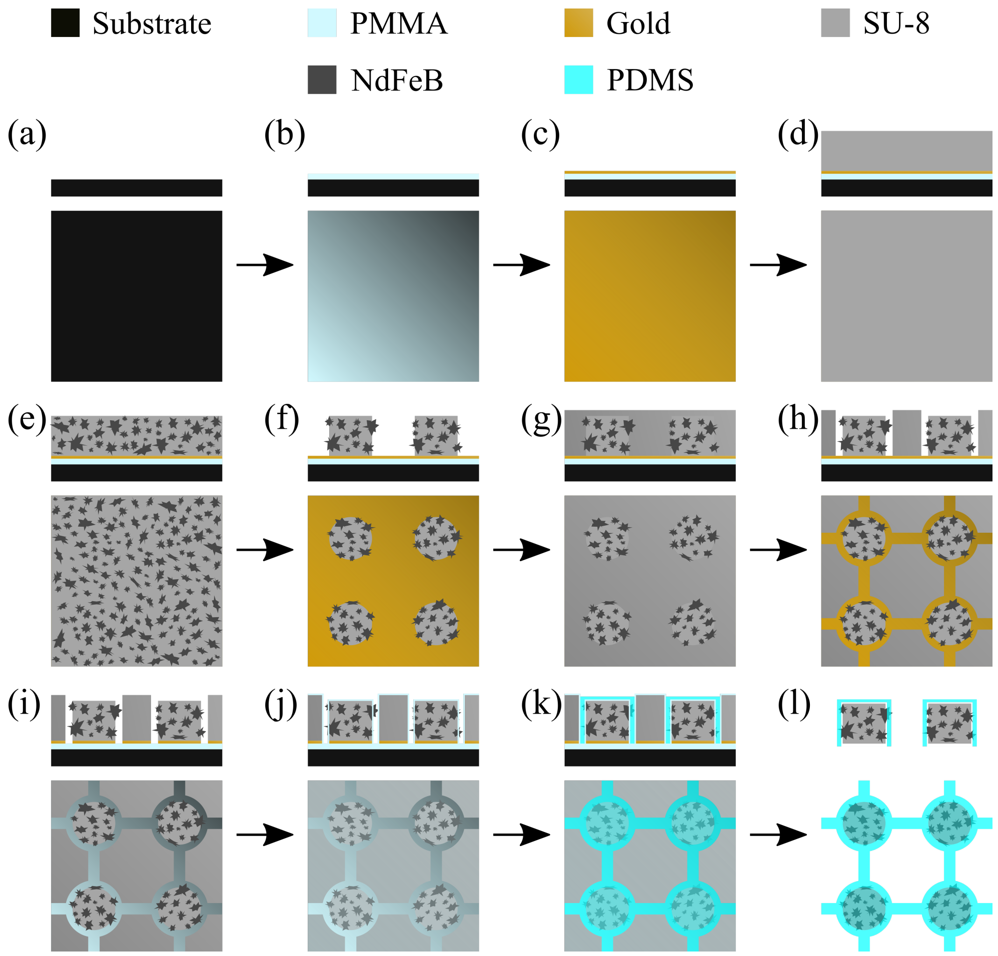

Figure 7.2: Diagram showing the fabrication steps to produce an NdFeB particle elasto-magnetic membrane. The upmost diagram for each letter shows the cross-section with the below diagram showing the view from directly above the sample. a) Si substrate b) with 600 nm PMMA spun on, c) followed by 50 nm of gold layered on top (via thermal evaporator). d) A layer of SU-8 is spun onto the substrate e) and the SU-8 is scattered with NdFeB particles. f) The lithographic step is completed, introduction of UV light, baking, developing etc. g) Another layer of SU-8 is spun on top. h) This lithographic step is completed to create a mould. i) A gold etchant is used. j) Another layer of PMMA is spun on the sample. k) Uncured PDMS is spun onto the sample to cover the mould. l) The membrane is removed from the mould via acetone and agitation.

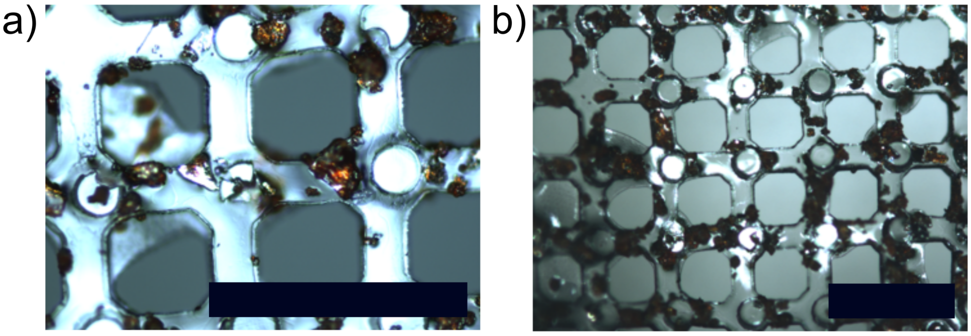

Figure 7.3: a) and b) are photographs of a PDMS network with SU-8 pillars and NdFeB powder. The scale bar in the bottom right corners of these pictures has a length of 500 µm.

location of the powder was unable to be added to specific positions using this method.

Following these tests, a design was created that consisted of pillars of SU-8 embedded with NdFeB powder attached to a PDMS network. A further test was completed to fabricate a PDMS network structure with SU-8 pillar, which can be seen in Figure 7.1(a) and (b). The theorised fabrication method of the elasto-magnetic SU-8, NdFeB and PDMS device is described in Figure 7.2.

Although a final device was produced, as can be seen in Figure 7.3, there were still some challenges to be overcome. The main issue being controlling the

location of the NdFeB. When creating the device, the powder became lodged between SU-8 elements and remained on the substrate. Due to this, the PDMS links also had powder particles within them. This was partly due to the size of the particles, as can be seen in Figure 7.3(a) some were of the order of 100 µm.

7.2.2 PDMS & NdFeB Cubic Magnets Membrane

Due to the success of using a SU-8 mould with PDMS and a manufactured NdFeB magnet to produce a pump (in Chapter 6), it was decided to use a similar process to fabricate the paddle system. The discs in this design were 500 µm, with axle widths of the order of 100 µm and the overall structure had distance of 10 mm between the first and sixth paddle.

The fabrication process was based on the methods used to create the middle section of the pump module discussed in Chapter 6. A SU-8 mould for the paddle design was created on silicon chip (2 cm $\times$ 2 cm). (The process of creating an SU-8 mould has already been discussed in Section 6.3.)

Following the mould creation procedure, a sacrificial layer was required before assembly of the device. A solution of PMMA:anisole was sprayed onto the mould, which resulted in a quick method to achieve a thin layer of PMMA. Following this, uncured PDMS was added with a syringe to the mould without introducing bubbles. It spread through the mould via capillary forces. Therefore, the thickness of the axles and discs in the paddle structure were consistent with the thickness of the mould. Then the cubic 250 µm NdFeB magnets were manually placed into the uncured PDMS discs and were orientated with a magnet. This was left at room temperature for the PDMS to cure with an external magnet to maintain the set orientation of the internal magnets. The paddle structure and mould can be seen at this point in Figure 7.4(d).

Once the PDMS had cured, the device was removed from its mould with acetone.

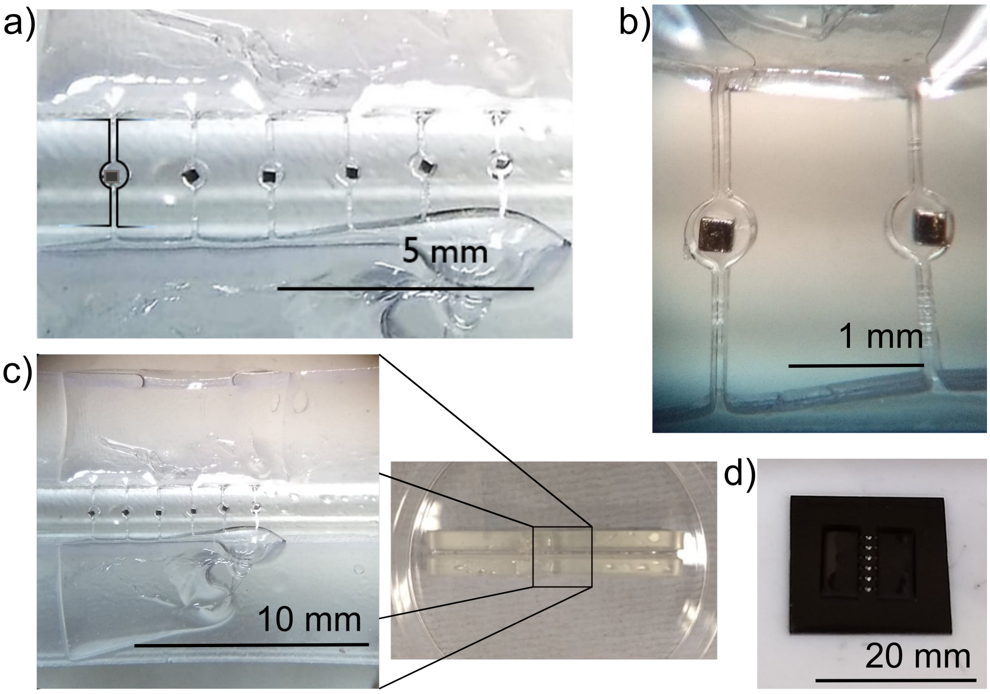

Figure 7.4: a) Showing The PDMS and NdFeB paddle device with a faded outline of the left most paddle. b) A closer view of two of the paddles. c) Showing the device attached to a 3D printed channel. d) A photograph of the SU-8 and silicon mould during the assembly of the device.

The structure can be seen in Figure 7.4(a) and (b). Due to the size of the device, it was able to be handled with tweezers without attaching to a frame, this was not the case with the previously discussed elasto-magnetic membranes. The device then needed to be attached to a 3D-printed channel. This was attempted using uncured PDMS via the "stamp & stick" method [162]. The structure on the channel can be seen in Figure 7.4(c).

Unfortunately this process was still relatively time consuming and the time gained was not a large benefit compared to the accuracy lost by the manual placement of the magnets. It did have the advantage that the moulds could be reused (unlike the electroplating method) but further research is needed to see if reusing the moulds has any disadvantageous effects. In addition to this, as the magnets would be added at the same time in the fabrication process they would all be orientated in the same direction. Therefore, any parameter alterations would need to be achieved by altering the PDMS structure. In order to alter the PDMS structure, a new SU-8 mould would need to be produced, which is the most time consuming part of the process. Other issues included the PDMS not being favorable to stick to the 3D printed material and the intricacies in manually placing the 250 µm magnetic into discs (diameter 500 µm, depth $\sim$ 300 µm). For these reasons, further research is required before this is a feasible method for producing paddle devices.

7.2.3 PDMS & NdFeB Powder Membrane

A new design combined both the two previously discussed methods in this chapter. The structure was similar to that of Section 7.2.2 but the magnetic component was inspired by Section 7.2.1.

As previously mentioned the NdFeB powder (purity 99%) was provided by American Elements and it has been seen that there was a significant range in the sizes of the particles. This was due to the manufacturing process, which used a 80 µm mesh to separate the particles. Therefore, it was advantageous to create a method utilising smaller particles.

A method was derived to separate the particles via static forces. First the original particles were placed on a glass slide. The slide was then tipped into a container and the particles with a lower mass would remain on the slide, allowing them to be collected. These smaller particles were then inserted into a PTFE tube (diameter 300 µm). The tube with the particles was then submerged into uncured PDMS which traveled through the tube and between the particles due to capillary forces, removing any air gaps. The tube was then baked on a heater at 150°C for 8 minutes to cure the PDMS. Once cured, the PDMS and NdFeB structure could be removed from the tube and cut into appropriate sizes (thickness $\sim$ 100 µm). An image of one of these structures can be seen in Figure 7.5(b). The magnetic properties of one of the PDMS-NdFeB discs was compared with that of one of the 250 µm manufactured magnets, Figure 7.5(a).

Similar to the previously discussed method, photolithography was used to form a mould via SU-8 on a silicon chip and PMMA was added to provide a sacrificial layer. The NdFeB-PDMS discs would be placed in the desired location in the SU-8 mould. Uncured PDMS would be incrementally added to the larger section of the mould. The uncured PDMS would flow to fill the axle mould channels and the area around the discs. It would fill up to the height of the mould due to surface tension. The mould with the PDMS and NdFeB-PDMS discs was then baked at 50°C for 11 hours. This would set the PDMS while maintaining it's elasticity. The device can be seen in Figure 7.5(d).

Similar to the previous method, the device could then be removed from its mould using acetone to remove the sacrificial layer and therefore, releasing the device. The structure could be magnetised using a VSM, as similarly executed in previous chapters. This device had the advantage that it could be manipulated in a certain

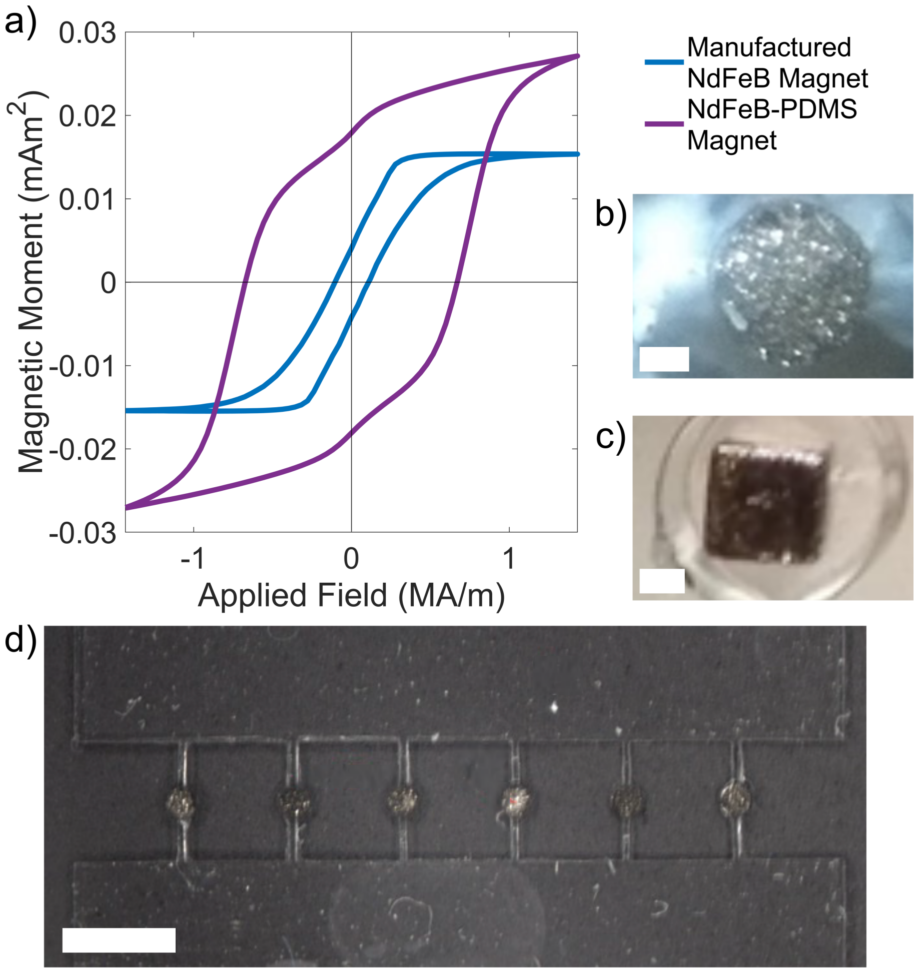

Figure 7.5: a) Hysteresis loop showing the differences between the PDMS-NdFeB powder magnet (300 µm diameter, ∼ 100 µm thick) and the cubic 250 µm NdFeB magnet (from SuperMagnetMan). b) An image of the PDMS-NdFeB powder magnet (300 µm diameter) with a scale bar indicating a width of 100 µm. c) An image of the manufactured cubic 250 µm NdFeB magnet with a scale bar indicating a width of 100 µm. d) A photograph of the PDMS and NdFeB device with a scale bar indicating 2 mm.

way before magnetising to cause the paddles' magnetic moments to be in different orientations.

While this method was able to produce elastic structures with NdFeB in a controlled location, there is still more research required to provide more consistency between the devices. There was a significant challenge in fabricating all the discs with a high concentration of NdFeB while maintaining consistency between them. One reason for this was that when submerging the tubing in the uncured PDMS, the PDMS would often carry some of the particles along the tubing, varying the concentration. In addition to this, cutting a cylinder of PDMS-NdFeB also brought some complications as it was done manually. One of the next steps in this work would be to control the mass of the powder, PDMS and the volume of the composition. Another, would be creating a method to ensure all the PDMS-NdFeB magnets would be cut to a consistent size.

7.3 Magnetic Orientation Of The Paddle Design

Chapter 5 discussed a series of ferromagnetic paddles with the same magnetic properties and different elastic properties actuated via a magnetic field. Initial investigations were performed in altering the magnetic properties of paddles which had the same elastic properties.

7.3.1 Theoretical Investigations

Theoretical studies were initially conducted to see if this was a feasible option for creating two degrees of freedom in the paddle system. The majority parameters remained the same as those described in Chapter 5 and Chapter A. The param-

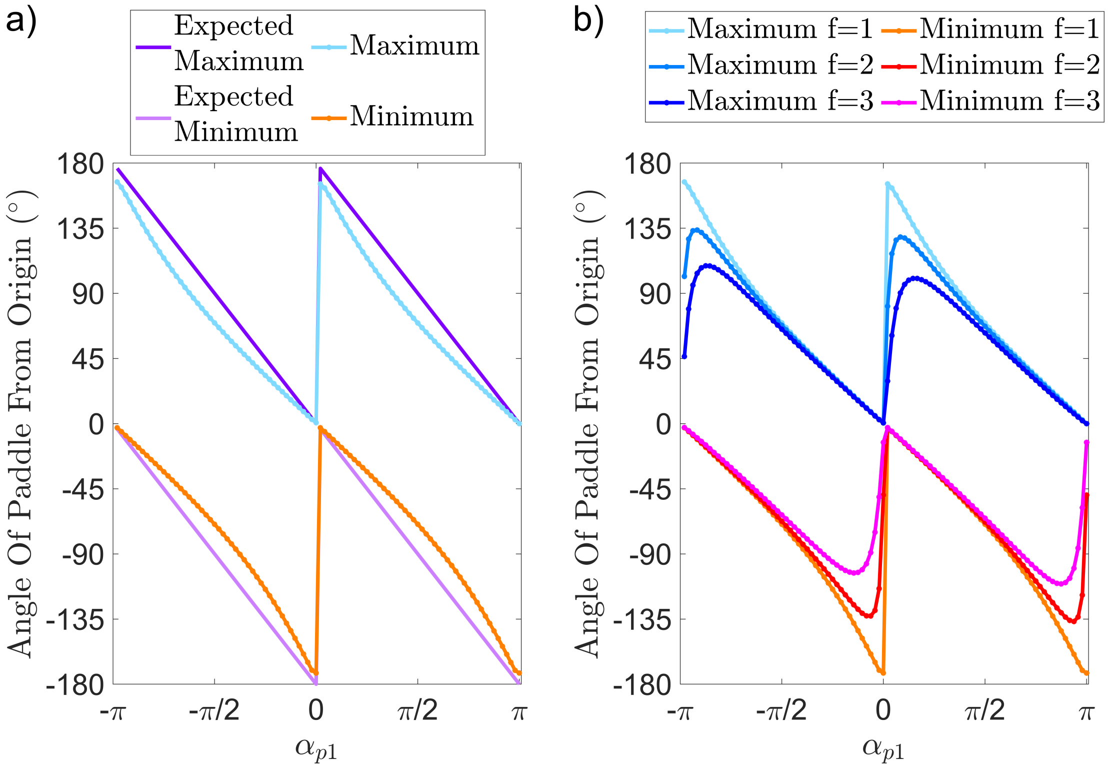

Figure 7.6: a) The dependence on the maximum and minimum angle of rotation from the origin when the orientation of the initial magnetic moment, α_{p1}, was varied between $-\pi$ and π and the dimensionless frequency was 1. The expected angle for a free disc is also shown. b) The variation in the maximum and minimum angles caused by different actuation frequencies 1, 2 and 3, with varying α_{p1}. In these graphs anti-clockwise rotation was displayed as positive angle, while clockwise, a negative.

eters which were altered were ℓ_{p1}, ℓ_{p2}, α_{p1} and α_{p2}, where α_{p1} and α_{p2} are the orientations of the initial magnetic moment of each of the paddles with respect to the $x-$ axis.

The orientation of the initial magnetic moment, α_{p1}, affected the rotational behaviour of the paddles, Figure 7.6. When $\alpha_{p1} > 0$ and the $x-$ component of the magnetic field was positive, the paddle rotated in a clockwise direction and when the $x-$ component of the field became negative, an anticlockwise direction. In the case when $\alpha_{p1} \leq 0$, the reverse was true. This caused a dramatic change in minimum and maximum angles in Figure 7.6(a) that can be seen when α_{p1} was risen from 0. The magnitude of the minimum and maximum angles was not as large as would be expected by an entirely free disc. This was caused by the fluidic drag and rotational stiffness forces acting on the paddles. Figure 7.6(a) shows the dependence of α_{p1} on the angles achieved by the paddles for different frequencies. Similar to the results seen in Section 5.3.5, varying the actuation frequency affects the behaviour of the paddles. As the frequency increased, the range of rotational angles for a particular α_{p1} became smaller.

The velocity generated by a system was investigated for varying values of α_{p1} and α_{p2}, when $\ell_{p1} = \ell_{p2} =$ 0.150 and f = 1, Figure 7.7. The value of frequency, ℓ_{p1} and ℓ_{p2} was chosen to allow for a large range of rotational angles to be achieved. As can be seen in Figure 7.7, the $x-$ component of the velocity is more critical than the $y-$component.

Firstly, the maximum speed calculated for this range of parameters was larger than that for the same frequency when ℓ_p was varied. This was thought to be due to the larger difference in angle that could be achieved in the current system. No flow was generated when α_{p1}=α_{p2}, due to the system only having one degree of freedom. The same is true when α_{p1}=$-\alpha_{p2}$, this occurs because the paddles are rotating in opposite directions but they are in-phase with each other. The velocity generated by a pair of α_{p1} and α_{p2} was equal in magnitude but opposing in direction to that of the same pair when their positions were reversed (e.i. $\boldsymbol{u}(\alpha_{p1} =$

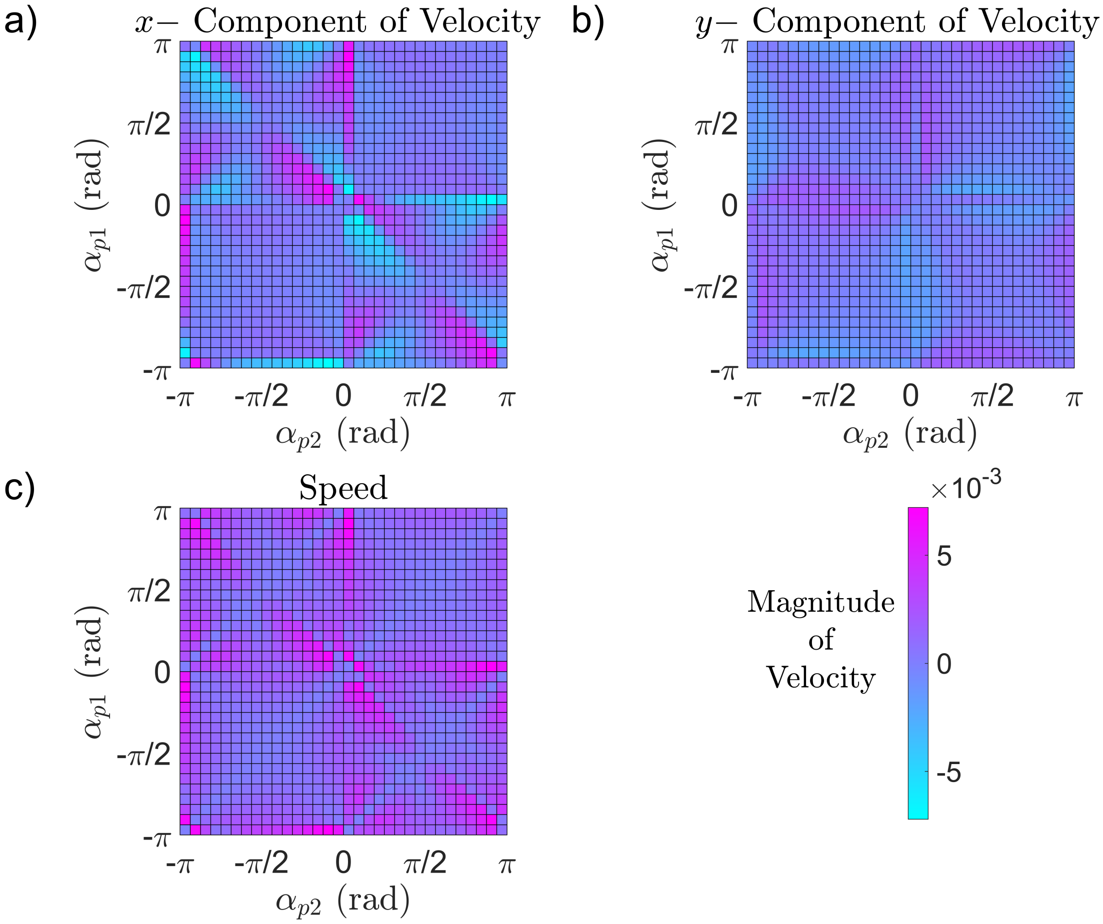

Figure 7.7: Surface plots indicating how varying α_{p1} and α_{p2} affects a) the $x-$component of the velocity, b) the $y-$component of the velocity and c) the speed of the generated flow when the frequency was set to 1 and $\ell_{p1} = \ell_{p2}$ =0.150.

$\Phi_1, \alpha_{p2} = \Phi_2$)=-$\boldsymbol{u}(\alpha_{p1} = \Phi_2, \alpha_{p2} = \Phi_1)$). This can be seen in Figure 7.7.

The generated velocity was the same in magnitude and direction when a pairs' movement was symmetrical to another's about a cycle. This symmetry was caused by the orientations of the magnetic moment and the almost uni-axial nature of the external magnetic field. The same velocity would occur for a pair when $\alpha_{p1} = \Phi_1$ & $\alpha_{p2} = \Phi_2$ and the pair $\alpha_{p1} = \Phi_3$ & $\alpha_{p2} = \Phi_4$, where $\Phi_3 = \Phi_1 \pm \pi$ and $\Phi_4 = \Phi_2 \pm \pi$. As can be seen Figure 7.6, these would achieve the same maximum and minimum angles. These angles would occur at different orientations of the magnetic field but this would not effect the generated velocity over a cycle.

The graphs in Figure 7.6 could be separated into four quadrants, when $\alpha_{p1} > 0$ & $\alpha_{p2} > 0$, $\alpha_{p1} < 0$ & $\alpha_{p2} > 0$, $\alpha_{p1} > 0$ & $\alpha_{p2} < 0$ and when $\alpha_{p1} < 0$ & $\alpha_{p2} < 0$. The generated velocities achieved in the quadrants $\alpha_{p1} > 0$ & $\alpha_{p2} > 0$ and $\alpha_{p1} < 0$ & $\alpha_{p2} < 0$ would be the same due to the similar behaviour exhibited by the paddles in these groups. This was also the case for $\alpha_{p1} < 0$ & $\alpha_{p2} > 0$ and $\alpha_{p1} > 0$ & $\alpha_{p2} < 0$. Therefore, only one of each of these two sections needs to be discussed further.

When $\alpha_{p1} > 0$ & $\alpha_{p2} > 0$, both of the paddles were rotating in the same direction as each other with the oscillating field (clockwise when the $x-$ component of the magnetic field was in the positive direction and anticlockwise when it was in the negative direction). However, when $\alpha_{p1} > 0$ & $\alpha_{p2} < 0$ they were rotating in opposite directions to each other, in one part of the cycle they would have a very large angle difference, whereas in the other, it would become very small. This action is reminiscent of a diaphragm pump. The generated speed was on average larger when the paddles were rotating in opposing directions than in the same direction.

Looking at the section when $\alpha_{p1} > 0$ & $\alpha_{p2} < 0$, particularly in Figure 7.7(a), it can be seen that the larger velocities were generated when the magnetic moments were close to the $x-$ axis. This was due to these pairs having the greatest maximum angles between them. The greatest speed achieved in this range of α_{p1} and α_{p2} was when α_{p1}=$\frac{\pi}{16}$ and α_{p2}=$-\frac{\pi}{8}$. Further research is required to validate this as

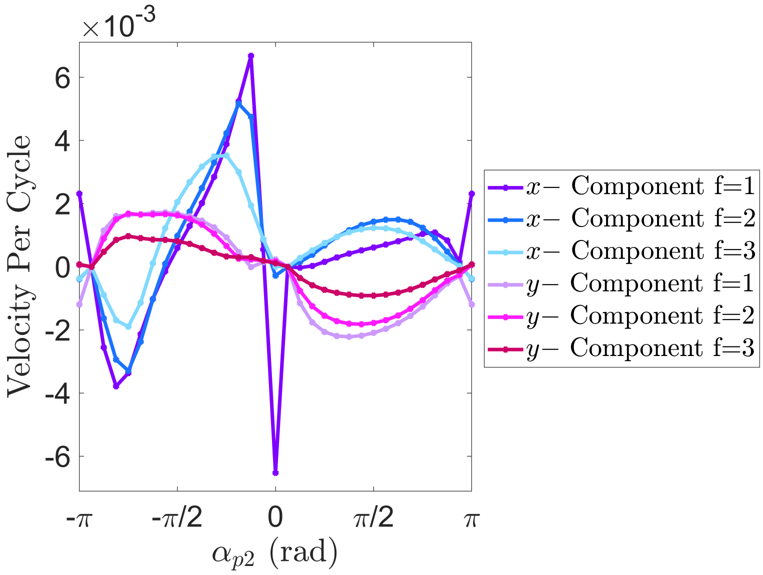

Figure 7.8: Varying α_{p2} when α_{p1}=$\frac{\pi}{16}$ for frequencies 1, 2 and 3, to observe the affects on the velocity.

the step-size of the investigated values of α_{p1} and α_{p2} was $\frac{\pi}{16}$.

The effect of frequency was investigated on the paddle system with varying α_{p1} and α_{p2}. When the frequency was changed from 1 to 2 and 3, the trends seen in the velocity dependence of α_{p1} and α_{p2} were still present. The maximum speed increased with frequency, while the values of α_{p1} and α_{p2} at which it occurred remained fairly consistent. However, the maximum speed per cycle decreased with frequency. This was predicted to be due to the decrease in the range of angles achieved for values of α_{p1} and α_{p2} close to the $x-$ axis at larger frequencies, as seen in Figure 7.6(b). In addition to this, at greater frequencies the velocity did not have such a rapid decline when α_{p1} and α_{p2} values were altered from the favourable pair. The rounding out of the maximum and minimum angles seen in Figure 7.6(b) could cause this effect.

Figure 7.8 shows the x and y components of velocity per cycle for frequencies 1, 2 and 3, when α_{p1}=$\frac{\pi}{16}$ and α_{p2} was varied. The magnitude of the velocity per cycle decreased as frequency was increased.

7.3.2 Experimental Investigations

Initial experimental investigations were conducted on the effect of magnetic orientation of the discs on the velocity of the flow. These have been conducted using the macro paddle design. The overall design and fabrication was similar to the structure discussed in Section 5.4. As the magnetic orientation of the paddles was required to be different, disc parts of the paddles were made separately. A separate 3D printed mould was created to allow the NdFeB magnets to be orientated by an external magnet and encased in the Polycraft silicone. After this was cured, the magnetic discs could be placed into a desired location in the 3D printed paddle moulds.The silicone could be added to the mould, completing the paddle device.

Similarly to Section 5.4, the structures were placed in a channel at the air-fluid interface. The fluid used in the channel was a solution of 50% glycerol and 50% water. The devices were actuated with a uni-axial oscillating magnetic field at frequencies 10-60 Hz with a strength of 6 mT (using the ABIOMATER system, Appendix C). Videos of the channel were taken and analysed using the software 'Tracker' [2] to obtain the generated flow rates. The experimental tests were performed by Tom Moynihan and the author of this thesis.

Figure 7.9 shows the effect of varying the actuation frequency on the velocity

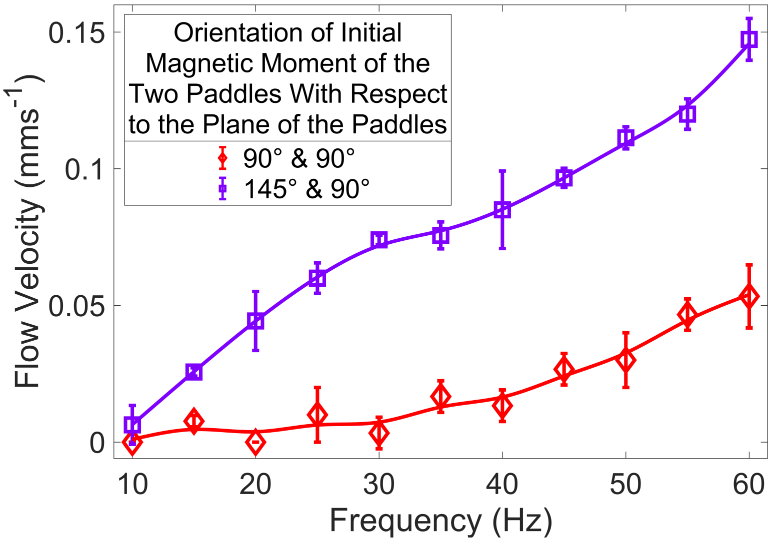

Figure 7.9: Average flow velocity as a function of frequency for a two paddle system with both axles 1.00 mm with the magnetic orientation of the second paddle 90° and the first being either 90° or 145° with respect to the plane of the paddles.

generated by two different paddle structures. In both of the structures, all the widths of the axles were 1.00 mm but the structures possessed different magnetic properties. In one, both paddles had the same magnetic orientation being out of plane, while in the other, one had 90° and the second 145° with respect to the plane of the paddles. It was found that for all frequencies the paddles with different magnetic orientations produced a larger velocity than the others. This was further emphasised as frequency increased.

Further experimental investigations are required to look into behaviour of the discs for varying magnetic moments. This is especially true when the orientation of the magnetic moments are at different angles with respect to one another.

7.4 Summary & Future Investigations

In this chapter, the current progress regarding the fabrication of the elasto-magnetic using NdFeB has been described as well as theoretical results indicating the affect of altering the magnetic orientation of the discs within the paddle structure. The future developments of this research can be separated into several sections.

Considering the research discussed in Chapter 4 and Section 7.2, advancements could still be made in fabricating an elasto-magnetic membrane. The majority of these suggested advancements have been mentioned in the discussed sections. One interesting development would be to create a method to produce NdFeB-PDMS magnets with consistent properties. The advantage of producing these magnets is that they could be made to the exact shape desired for the device (e.g. discs with a particular radius and thickness). The NdFeB-PDMS magnets could be fabricated by using a high particle density ratio with a consistent weight of the NdFeB powder, with powder particles within a certain range, a consistent weight of the uncured PDMS and a mould of consistent volume. These magnets could be added to larger SU-8 device moulds to be used in elasto-magnetic devices.

Chapter 5 discussed the development of a series of ferromagnetic paddles using the same magnetic properties and different elastic properties, while Section 7.3 focused on a similar structure but with the same elastic properties and different magnetic orientation of the discs. It has been shown by the theoretical investigations in Section 7.3.1 that producing a paddle systems with magnetic discs with very different magnetic orientations ($\alpha_{p1} > 0$ & $\alpha_{p2} < 0$ or $\alpha_{p1} < 0$ & $\alpha_{p2} > 0$)

produced a larger flow speed than when the angles were more similar. The next stage would be to experimentally produce devices with optimal magnetic orientations on a small scale. This would produce a challenge as the fabrication method used in Chapter 5 would not be suitable in its current stage. However, it may be possible to produce the structure and then orientate or bend the structure in a certain way to magnetise the magnetic materials in the desired orientations.

With regards to the work discussed in Chapter 6 on the three-linked pump, there are two separate areas for future investigations. The first is to alter the shape of the three-linked pump. The links in Purcell's three-linked swimmer does not bend and bending only occurs where two links join [1], this is not the case with the three-linked pump (Chapter 6). Therefore, it would be interesting to see the effect created by having smooth bends rather than corners. The three links would then become one sine-wave-shaped link. It has been previously mentioned that two degrees of freedom are required within a low Reynolds number system (Chapter 2). All links are bending in the three-linked pumps, which could be providing more than two degrees of freedom, therefore producing a similar pump with only two links may be possible. In both of these discussed ideas the fabrication techniques and actuation method would remain the same as the three-linked pump. The three-linked pump could also be integrated into a lab-on-a-chip device with other systems. An example of this could be aiding in controlled cell growth by cycling the nutrients around a closed circuit micro-channel.

Chapter 8

Conclusions

The aim of this thesis was to investigate magnetically actuated systems that are able to manipulate fluid in a low Reynolds number regime. This work was primarily focused on three different designs. The structures are created in such a way that the interactions between the magnetic, elastic and fluidic forces aim to create non-reciprocal motion. All of these designs were actuated by a predominantly uni-axial oscillating magnetic field.

The initial study was focused on the fabrication and experimental investigation of both anisotropically hard and soft ferromagnetic particles connected together via PDMS elastic links. The designs described were that of a 68 µm microswimmer and a membrane or network spanning 12 mm with feature sizes of the order of micrometers. Ellipsoidal CoNiP and circular Co particles were produced by electrodeposition to achieve diameters of 30 µm (major) and 10 µm (minor) and 10 µm, respectively, with a thickness in the range of 6–10 µm. The electrodeposition parameters have been optimized on deposition of CoNiP films to produce an out-plane coercivity for CoNiP elements of 54 kA/m. It has been successfully shown how these ferromagnetic elements can be incorporated into a microscale elastic structure. This was achieved via a multistage process with a number of photolithography steps, as well as electrodeposition and PDMS etching. As a proof-of-principle demonstration, the membrane was shown to deform in the presence of an oscillating magnetic field. While future challenges will focus on establishing the correct geometry and actuation for particular applications, this thesis has addressed major difficulties in device fabrication and establishes a strong basis for research in this area.

The second design was based on a series of magnetic paddles. Each paddle consisted of a disc, embedded with ferromagnetic material, and its associated elastic link/axle. The paddles were of the same magnetic nature but differing elastic properties. When actuated by an oscillating magnetic field while within a fluid, the magnetic paddles would initially experience the same magnetic torque and fluidic drag but different elastic forces, which led to a phase difference between the angles achieved by the paddle. Their rotational movement replicated that of a metachronal wave, which is reminiscent of the behaviour of cilia. An experimental device of this design was fabricated using lithographic techniques and electrodeposition. The structure consisted of 10 µm thick PDMS network divided into 650 µm × 500 µm cells. Each cell was composed of four 120 µm circular paddles with centre-to-centre spacing of 150 µm. Each paddle contained a hexagonal array of 6 µm thick, 10 µm diameter CoNiP cylinders with a pitch of 20 µm and was joined to a stiff frame by axle of widths of 3, 6, 9 and 12 µm. It was shown that the axle width of the paddle affected the maximum paddle rotation. These devices had the ability to generate flows with speeds up to 16 µms^{-1}.

To understand this design further a theoretical model was created. The model was able to reproduce experimental features of actuation and to predict design paradigms for generating flow in a low Reynolds number environment. Both the experimental and theoretical investigations agreed that a system of paddles with the same elastic and magnetic properties would not generate a flow whereas a system with different elastic properties would, providing both paddles were elastic enough to allow some rotation. They were also in agreement that altering the frequency affects the angle of rotation and therefore, the generated flow. Further theoretical investigations were conducted on the behaviour of the paddles over a cycle and the effect of paddle separation. For the dimensionless parameters investigated, the maximum speed was generated when the centre-to-centre separation was 0.9, the frequency was 1.4, ℓ_{p1} = 0.130 and ℓ_{p2} = 0.225, achieving maximum angles of 45° and 148° respectively. For the experimental device discussed in Section 5.2, this approximately corresponds to a separation of 135 µm, an actuation frequency of 21 Hz, with paddle axle widths of 13 µm and 35 µm. Considering the simplicity of the design and actuation method, devices such as these hold promise to be used as microfluidic pumps.

Chapter 6 was focused on an asymmetric elasto-magnetic system that provides a novel integrated pumping solution. The design is based on the concept of confining Purcell's 3-linked swimmer and attaching a magnetic head to it. An external magnetic field is used to drive the head and this causes the three links to deform out of phase with each other. The enclosed pumping system was comprised primarily of PDMS with PTFE tubing and a NdFeB magnet attached to the head of the pump. The more intricate parts of the design were fabricated using lithographic techniques with SU-8. When actuated, the properties of the closed loop of the head of the pump and the generated flow rate was investigated for different viscosities, actuation frequencies and field amplitudes. It was found that this system can provide tuneable fluid flow with a flow rate of up to 700 µlh^{-1}. The fluid flow could be reversed by adjusting the driving frequency. The flow rates achieved for the various frequencies and viscosities were compared with the properties of the closed loop path. It was found that the actuation frequency greatly influenced the motion of the head of the pump and this motion affected the generated flow. It is beneficial to the development of future technologies that properties of the actuating field of the device can vary the flow rate.

Chapter 7 discussed the further developments of elasto-magnetic paddle devices, focusing on the fabrication advancements and investigations on the effect of different magnetic orientations of paddles. Current progress has shown that NdFeB and PDMS paddle devices could be produced using SU-8 moulds. It has been shown by theoretical investigations that a paddle system with very different initial magnetic orientations could produce a larger flow rate than when the orientations were similar, when a uni-axial magnetic field was the actuation method for both designs. Initial experimental investigation conducted on a macro-paddle system also showed that different magnetic orientations of the paddles affects the flow produced. Within this chapter the future investigations for the work in this thesis were discussed.

Overall, in this thesis, it has been shown that elasto-magnetic devices could be used to control the flow of fluid in a low Reynolds number regime. These devices were all comprised of ferromagnets embedded within an elastic structure and activated by an oscillating magnetic field. While future research is required with regards to the challenges of implementing these structures in multi-functional microfluidic devices, the current designs discussed in this research establish many of the difficulties in this area regarding fabrication, design and actuation. This provides a strong basis for future technological applications.

References

[1] E. M. Purcell. Life at Low Reynolds Number. *American Journal of Physics*, 45(1):3–11, 1977.

[2] Douglas Brown. Tracker. `https://physlets.org/tracker/`, May 2017.

[3] Geoffrey Ingram Taylor. Film Notes For Low Reynolds Number Flows. *National Committee for Fluid Mechanics Films*, 1985.

[4] Eric Lauga and Thomas R. Powers. The Hydrodynamics Of Swimming Microorganisms. *Reports on Progress in Physics*, 72(9):096601, August 2009.

[5] Kathrin E. Peyer, Li Zhang, and Bradley J. Nelson. Bio-Inspired Magnetic Swimming Microrobots For Biomedical Applications. *Nanoscale*, 5:1259–1272, 2013.

[6] Jumril Yunas, Budi Mulyanti, Ida Hamidah, Muzalifah Mohd Said, Roer Eka Pawinanto, Wan Amar Fikri Wan Ali, Ayub Subandi, Azrul Azlan Hamzah, Rhonira Latif, and Burhanuddin Yeop Majlis. Polymer-Based MEMS Electromagnetic Actuator for Biomedical Application: A Review. *Polymers*, 12(5), 2020.

[7] Stefano Palagi, Dhruv P. Singh, and Peer Fischer. Light-Controlled Micromotors And Soft Microrobots. *Advanced Optical Materials*, 7(16):1900370, 2019.

[8] Maria Guix, Sonja M. Weiz, Oliver G. Schmidt, and Mariana Medina-Sánchez. Self-propelled micro/nanoparticle motors. *Particle & Particle Systems Characterization*, 35(2):1700382, 2018.

[9] Leilei Xu, Fangzhi Mou, Haotian Gong, Ming Luo, and Jianguo Guan. Light-Driven Micro/Nanomotors: From Fundamentals To Applications. *Chemical Society Reviews*, 46:6905–6926, 2017.

[10] Mariana Medina-Sánchez, Haifeng Xu, and Oliver G Schmidt. Micro- And Nano-Motors: The New Generation Of Drug Carriers. *Therapeutic Delivery*, 9(4):303–316, 2018. PMID: 29540126.

[11] J. E. Avron, O. Kenneth, and D. H. Oaknin. Pushmepullyou: An Efficient Micro-Swimmer. *New Journal of Physics*, 7:234, November 2005.

[12] Ali Najafi and Ramin Golestanian. Simple Swimmer At Low Reynolds Number: Three Linked Spheres. *Physical Review E*, 69:062901, June 2004.

[13] J. Stöhr and H. C. Siegmann. *Magnetism: From Fundamentals To Nanoscale Dynamics*. Springer Series in Solid-State Sciences. Springer Berlin Heidelberg, 2007.

[14] W. Gao and N. M. Sammes. *An Introduction To Electronic And Ionic Materials*. An Introduction to Electronic and Ionic Materials. World Scientific, 1999.

[15] A. G. Gurevich and G. A. Melkov. *Magnetization Oscillations And Waves*. Taylor & Francis, 1996.

[16] Carmen-Gabriela Stefanita. *Magnetism: Basics And Applications*. SpringerLink : Bücher. Springer Berlin Heidelberg, 2012.

[17] C. H. de Groot and Kees de Kort. Magnetoelastic Anisotropy In NdFeB Permanent Magnets. *Journal of Applied Physics*, 85(12):8312–8316, 1999.

[18] David M. Kirkwood, Gyana Pattanaik, and Giovanni Zangari. Electrodeposited CoNiP Films With Perpendicular Magnetic Anisotropy. *Journal of The Electrochemical Society*, 154(8):D363, 2007.

[19] T. L. Chow. *Introduction To Electromagnetic Theory: A Modern Perspective*. Jones and Bartlett Publishers, 2006.

[20] K. Yung, P. Landecker, and D. Villani. An Analytic Solution For The Force Between Two Magnetic Dipoles. *Physical Separation in Science and Engineering*, 9:39–52, 1998.

[21] Alexander A. Solovev, Yongfeng Mei, Esteban Bermúdez Ureña, Gaoshan Huang, and Oliver G. Schmidt. Catalytic Microtubular Jet Engines Self-Propelled By Accumulated Gas Bubbles. *Small*, 5(14):1688–1692, 2009.

[22] Yongfeng Mei, Gaoshan Huang, Alexander A. Solovev, Esteban Bermúdez Ureña, Ingolf Mönch, Fei Ding, Thomas Reindl, Ricky K. Y. Fu, Paul K. Chu, and Oliver G. Schmidt. Versatile Approach For Integrative And Functionalized Tubes By Strain Engineering Of Nanomembranes On Polymers. *Advanced Materials*, 20(21):4085–4090, 2008.

[23] Wei Gao, Sirilak Sattayasamitsathit, Jahir Orozco, and Joseph Wang. Highly Efficient Catalytic Microengines: Template Electrosynthesis Of Polyaniline/Platinum Microtubes. *Journal of the American Chemical Society*, 133(31):11862–11864, 2011. PMID: 21749138.

[24] Guanjia Zhao and Martin Pumera. Concentric Bimetallic Microjets By Electrodeposition. *RSC Advances*, 3(12):3963–3966, 2013.

[25] Walter F. Paxton, Kevin C. Kistler, Christine C. Olmeda, Ayusman Sen, Sarah K. St. Angelo, Yanyan Cao, Thomas E. Mallouk, Paul E. Lammert, and Vincent H. Crespi. Catalytic Nanomotors: Autonomous Movement Of Striped Nanorods. *Journal of the American Chemical Society*, 126(41):13424–13431, 2004. PMID: 15479099.

[26] Daniel Kagan, Percy Calvo-Marzal, Shankar Balasubramanian, Sirilak Sattayasamitsathit, Kalayil Manian Manesh, Gerd Uwe Flechsig, and Joseph Wang. Chemical Sensing Based On Catalytic Nanomotors: Motion-Based Detection Of Trace Silver. *Journal of the American Chemical Society*, 131(34):12082–12083, 2009. PMID: 19670862.

[27] Tung Chun Lee, Mariana Alarcón-Correa, Cornelia Miksch, Kersten Hahn, John G. Gibbs, and Peer Fischer. Self-Propelling Nanomotors In The Presence Of Strong Brownian Forces. *Nano Letters*, 14(5):2407–2412, 2014. PMID: 24707952.

[28] Jonathan R. Howse, Richard A. L. Jones, Anthony J. Ryan, Tim Gough, Reza Vafabakhsh, and Ramin Golestanian. Self-Motile Colloidal Particles: From Directed Propulsion To Random Walk. *Physical Review Letters*, 99(4):048102, July 2007.

[29] J. G. Gibbs and Y. P. Zhao. Autonomously Motile Catalytic Nanomotors By Bubble Propulsion. *Applied Physics Letters*, 94(16):163104, 2009.

[30] Larysa Baraban, Denys Makarov, Robert Streubel, Ingolf Mönch, Daniel Grimm, Samuel Sanchez, and Oliver G. Schmidt. Catalytic Janus Motors On Microfluidic Chip: Deterministic Motion For Targeted Cargo Delivery. *ACS Nano*, 6(4):3383–3389, 2012. PMID: 22424213.

[31] Wei Gao, Allen Pei, Xiaomiao Feng, Camille Hennessy, and Joseph Wang. Organized Self-Assembly Of Janus Micromotors With Hydrophobic Hemispheres. *Journal of the American Chemical Society*, 135(3):998–1001, 2013. PMID: 23286304.

[32] Yingjie Wu, Xiankun Lin, Zhiguang Wu, Helmuth Möhwald, and Qiang He. Self-Propelled Polymer Multilayer Janus Capsules For Effective Drug Delivery And Light-Triggered Release. *ACS Applied Materials & Interfaces*, 6(13):10476–10481, 2014. PMID: 24909305.

[33] Xing Ma, Kersten Hahn, and Samuel Sanchez. Catalytic Mesoporous Janus Nanomotors For Active Cargo Delivery. *Journal of the American Chemical Society*, 137(15):4976–4979, 2015. PMID: 25844893.

[34] Ana C. Hortelão, Tania Patiño, Ariadna Perez-Jiménez, Àngel Blanco, and Samuel Sánchez. Enzyme-Powered Nanobots Enhance Anticancer Drug Delivery. *Advanced Functional Materials*, 28(25):1705086, 2018.

[35] Wei Gao and Joseph Wang. Synthetic Micro/Nanomotors In Drug Delivery. *Nanoscale*, 6(18):10486–10494, 2014.

[36] Wei Gao, Allen Pei, and Joseph Wang. Water-Driven Micromotors. *ACS Nano*, 6(9):8432–8438, 2012. PMID: 22891973.

[37] Maria Guix, Anne K. Meyer, Britta Koch, and Oliver G. Schmidt. Carbonate-Based Janus Micromotors Moving In Ultra-Light Acidic Environment Generated By HeLa Cells In Situ. *Scientific Reports*, 6(October 2015):21701, 2016.

[38] Jinxing Li, Pavimol Angsantikul, Wenjuan Liu, Berta Esteban-Fernández de Ávila, Soracha Thamphiwatana, Mingli Xu, Elodie Sandraz, Xiaolei Wang, Jorge Delezuk, Weiwei Gao, Liangfang Zhang, and Joseph Wang. Micromotors Spontaneously Neutralize Gastric Acid For pH-Responsive Payload Release. *Angewandte Chemie - International Edition*, 56(8):2156–2161, 2017.

[39] Sheng Wang, Zhenzhen Jiang, Shenshen Ouyang, Zhipeng Dai, and Tao Wang. Internally/Externally Bubble-Propelled Photocatalytic Tubular Nanomotors For Ef-

ficient Water Cleaning. *ACS Applied Materials & Interfaces*, 9(28):23974–23982, 2017. PMID: 28650608.

[40] Fangzhi Mou, Yan Li, Chuanrui Chen, Wei Li, Yixia Yin, Huiru Ma, and Jianguo Guan. Single-Component TiO2 Tubular Microengines With Motion Controlled By Light-Induced Bubbles. *Small*, 11(21):2564–2570, 2015.

[41] Michael Ibele, Thomas E. Mallouk, and Ayusman Sen. Schooling Behavior Of Light-Powered Autonomous Micromotors In Water. *Angewandte Chemie - International Edition*, 48(18):3308–3312, 2009.

[42] Jizhuang Wang, Ze Xiong, Jing Zheng, Xiaojun Zhan, and Jinyao Tang. Light-Driven Micro/Nanomotor For Promising Biomedical Tools: Principle, Challenge, And Prospect. *Accounts of Chemical Research*, 51(9):1957–1965, 2018.

[43] Jeffrey L. Moran and Jonathan D. Posner. Phoretic Self-Propulsion. *Annual Review of Fluid Mechanics*, 49(1):511–540, 2017.

[44] Yan Li, Fangzhi Mou, Chuanrui Chen, Ming You, Yixia Yin, Leilei Xu, and Jianguo Guan. Light-Controlled Bubble Propulsion Of Amorphous TiO2/Au Janus Micromotors. *RSC Advances*, 6(13):10697–10703, 2016.

[45] Mingjun Xuan, Zhiguang Wu, Jingxin Shao, Luru Dai, Tieyan Si, and Qiang He. Near Infrared Light-Powered Janus Mesoporous Silica Nanoparticle Motors. *Journal of the American Chemical Society*, 138(20):6492–6497, 2016.

[46] Hong Ren Jiang, Natsuhiko Yoshinaga, and Masaki Sano. Active motion Of A Janus Particle By Self-Thermophoresis In A Defocused Laser Beam. *Physical Review Letters*, 105(26):1–4, 2010.

[47] Chaolei Huang, Jiu An Lv, Xiaojun Tian, Yuechao Wang, Yanlei Yu, and Jie Liu. Miniaturized Swimming Soft Robot With Complex Movement Actuated And Controlled By Remote Light Signals. *Scientific Reports*, 5(October):1–8, 2015.

[48] Stefano Palagi, Andrew G. Mark, Shang Yik Reigh, Kai Melde, Tian Qiu, Hao Zeng, Camilla Parmeggiani, Daniele Martella, Alberto Sanchez-Castillo, Nadia Kapernaum, Frank Giesselmann, Diederik S. Wiersma, Eric Lauga, and Peer Fischer. Structured Light Enables Biomimetic Swimming And Versatile Locomotion Of Photoresponsive Soft Microrobots. *Nature Materials*, 15(6):647–653, 2016.

[49] Ahmed Mourran, Hang Zhang, Rostislav Vinokur, and Martin Möller. Soft Microrobots Employing Nonequilibrium Actuation Via Plasmonic Heating. *Advanced Materials*, 29(2), 2017.

[50] Marvin C. Ziskin and Diana B. Petitti. Epidemiology Of Human Exposure To Ultrasound: A Critical Review. *Ultrasound in Medicine and Biology*, 14(2):91–96, 1988.

[51] Wei Wang, Luz Angelica Castro, Mauricio Hoyos, and Thomas E. Mallouk. Autonomous Motion Of Metallic Microrods Propelled By Ultrasound. *ACS Nano*, 6(7):6122–6132, 2012.

[52] Suzanne Ahmed, Wei Wang, Lamar O. Mair, Robert D. Fraleigh, Sixing Li, Luz Angelica Castro, Mauricio Hoyos, Tony Jun Huang, and Thomas E. Mallouk. Steering Acoustically Propelled Nanowire Motors Toward Cells In A Biologically Compatible Environment Using Magnetic Fields. *Langmuir*, 29(52):16113–16118, 2013.

[53] Andrew L. Balk, Lamar O. Mair, Pramod P. Mathai, Paul N. Patrone, Wei Wang, Suzanne Ahmed, Thomas E. Mallouk, J. Alexander Liddle, and Samuel M. Stavis. Kilohertz Rotation Of Nanorods Propelled By Ultrasound, Traced By Microvortex Advection Of Nanoparticles. *ACS Nano*, 8(8):8300–8309, 2014.

[54] Abi Berger. Magnetic Resonance Imaging. *BMJ*, 324(7328):35, 2002.

[55] R. D. Saunders. Biological Effects Of Magnetic Fields. *Journal of Radiological Protection*, 9(1):53–54, March 1989.

[56] L. E. Anderson. Biological Effects Of Magnetic Fields: Laboratory Studies. In *Proceedings of the 20th Annual International Conference of the IEEE Engineering in Medicine and Biology Society. Vol.20 Biomedical Engineering Towards the Year 2000 and Beyond (Cat. No.98CH36286)*, volume 6, pages 2791–2797, 1998.

[57] Domenico Formica and Sergio Silvestri. Biological Effects Of Exposure To Magnetic Resonance Imaging: An Overview. *BioMedical Engineering Online*, 3:1–12, 2004.

[58] D. J. Laser and J. G. Santiago. A Review Of Micropumps. *Journal of Micromechanics and Microengineering*, 14(6):R35–R64, April 2004.

[59] Yao Nan Wang and Lung Ming Fu. Micropumps And Biomedical Applications – A Review. *Microelectronic Engineering*, 195:121–138, 2018.

[60] L. J. Thomas and S. P. Bessman. Prototype For An Implantable Micropump Powdered By Piezoelectric Disk Benders. *Transactions - American Society for Artificial Internal Organs*, 21:516——522, 1975.

[61] W. J. Spencer, W. T. Corbett, L. R. Dominguez, and B. D. Shafer. An Electronically Controlled Piezoelectric Insulin Pump And Valves. *IEEE Transactions on Sonics and Ultrasonics*, 25(3):153–156, 1978.

[62] Peter Woias. Micropumps—Past, Progress And Future Prospects. *Sensors and Actuators B: Chemical*, 105(1):28–38, 2005.

[63] Jan G. Smits. Piezoelectric Micropump With Three Valves Working Peristaltically. *Sensors and Actuators A: Physical*, 21(1):203 – 206, 1990. Proceedings of the 5th International Conference on Solid-State Sensors and Actuators and Eurosensors III.

[64] H. T. G. van Lintel, F. C. M. van De Pol, and S. Bouwstra. A Piezoelectric Micropump Based On Micromachining Of Silicon. *Sensors and Actuators*, 15(2):153 – 167, 1988.

[65] Partha Kumar Das and A. B. M. Toufique Hasan. Mechanical Micropumps And Their Applications: A Review. *AIP Conference Proceedings*, 1851(1):020110, 2017.

[66] C. Joshitha, B. S. Sreeja, and S. Radha. A Review On Micropumps For Drug Delivery System. In *2017 International Conference on Wireless Communications, Signal Processing and Networking (WiSPNET)*, pages 186–190, 2017.

[67] Nam Trung Nguyen, Xiaoyang Huang, and Toh Kok Chuan. MEMS-Micropumps: A Review. *Journal of Fluids Engineering*, 124(2):384–392, May 2002.

[68] S. Mohith, P. Navin Karanth, and S. M. Kulkarni. Recent Trends In Mechanical Micropumps And Their Applications: A Review. *Mechatronics*, 60:34–55, 2019.

[69] K. E. Herold and A. Rasooly. *Lab On A Chip Technology: Fabrication And Microfluidics*. Lab on a Chip Technology. Caister Academic Press, 2009.

[70] Y. H. Ghallab and W. Badawy. *Lab-On-A-Chip: Techniques, Circuits, And Biomedical Applications*. Artech House integrated microsystems series. Artech House, 2010.

[71] Albert van den Berg and Loes Segerink. *Microfluidics For Medical Applications*. Royal Society of Chemistry, 2014.

[72] UK Government. Testing Coronavirus In The UK. `https://coronavirus.data.gov.uk/details/testing`, April 2021.

[73] Stephen C. Terry, John H. Herman, and James B. Angell. A Gas Chromatographic Air Analyzer Fabricated On A Silicon Wafer. *IEEE Transactions on Electron Devices*, 26(12):1880–1886, 1979.

[74] T. Honda, K. I. Arai, and K. Ishiyama. Micro Swimming Mechanisms Propelled By External Magnetic Fields. *IEEE Transactions on Magnetics*, 32(5):5085–5087, 1996.

[75] Li Zhang, Jake J. Abbott, Lixin Dong, Kathrin E. Peyer, Bradley E. Kratochvil, Haixin Zhang, Christos Bergeles, and Bradley J. Nelson. Characterizing The Swimming Properties Of Artificial Bacterial Flagella. *Nano Letters*, 9(10):3663–3667, 2009.

[76] Ambarish Ghost and Peer Fischer. Controlled Propulsion Of Artificial Magnetic Nanostructured Propellers. *Nano Letters*, 9(6):2243–2245, 2009.

[77] Mariana Medina-Sánchez, Lukas Schwarz, Anne K. Meyer, Franziska Hebenstreit, and Oliver G. Schmidt. Cellular Cargo Delivery: Toward Assisted Fertilization By Sperm-Carrying Micromotors. *Nano Letters*, 16(1):555–561, 2016.

[78] D. J. Bell, S. Leutenegger, K. M. Hammar, L. X. Dong, and B. J. Nelson. Flagella-like propulsion for microrobots using a nanocoil and a rotating electromagnetic field. In *Proceedings 2007 IEEE International Conference on Robotics and Automation*, pages 1128–1133, 2007.

[79] Li Zhang, Jake J. Abbott, Lixin Dong, Bradley E. Kratochvil, Dominik Bell, and Bradley J. Nelson. Artificial Bacterial Flagella: Fabrication And Magnetic Control. *Applied Physics Letters*, 94(6):2007–2010, 2009.

[80] Arthur W. Mahoney and Jake J. Abbott. Managing Magnetic Force Applied To A Magnetic Device By A Rotating Dipole Field. *Applied Physics Letters*, 99(13):1–4, 2011.

[81] Jamel Ali, U. Kei Cheang, Yigong Liu, Hoyeon Kim, Louis Rogowski, Sam Sheckman, Prem Patel, Wei Sun, and Min Jun Kim. Fabrication And Magnetic Control Of Alginate-Based Rolling Microrobots. *AIP Advances*, 6(12), 2016.

[82] Tianlong Li, Anning Zhang, Guangbin Shao, Mengshi Wei, Bin Guo, Guangyu Zhang, Longqiu Li, and Wei Wang. Janus Microdimer Surface Walkers Propelled by Oscillating Magnetic Fields. *Advanced Functional Materials*, 28(25):1–9, 2018.

[83] Jiangfan Yu, Lidong Yang, and Li Zhang. Pattern Generation And Motion Control Of A Vortex-Like Paramagnetic Nanoparticle Swarm. *The International Journal of Robotics Research*, 37(8):912–930, 2018.

[84] Peter J. Vach, Debora Walker, Peer Fischer, Peter Fratzl, and Damien Faivre. Pattern Formation And Collective Effects In Populations Of Magnetic Microswimmers. *Journal of Physics D: Applied Physics*, 50(11), 2017.

[85] Daniel Ahmed, Thierry Baasch, Nicolas Blondel, Nino Läubli, Jürg Dual, and Bradley J. Nelson. Neutrophil-Inspired Propulsion In A Combined Acoustic And Magnetic Field. *Nature Communications*, 8(1):1–8, 2017.

[86] Fernando Martinez-Pedrero and Pietro Tierno. Magnetic Propulsion Of Self-Assembled Colloidal Carpets: Efficient Cargo Transport Via A Conveyor-Belt Effect. *Physical Review Applied*, 3:051003, May 2015.

[87] Hui Xie, Mengmeng Sun, Xinjian Fan, Zhihua Lin, Weinan Chen, Lei Wang, Lixin Dong, and Qiang He. Reconfigurable Magnetic Microrobot Swarm: Multimode

Transformation, Locomotion, And Manipulation. *Science Robotics*, 4(28):1–15, 2019.

[88] Zhiguang Wu, Jonas Troll, Hyeon Ho Jeong, Qiang Wei, Marius Stang, Focke Ziemssen, Zegao Wang, Mingdong Dong, Sven Schnichels, Tian Qiu, and Peer Fischer. A Swarm Of Slippery Micropropellers Penetrates The Vitreous Body Of The Eye. *Science Advances*, 4(11):1–11, 2018.

[89] Ania Servant, Famin Qiu, Mariarosa Mazza, Kostas Kostarelos, and Bradley J. Nelson. Controlled In Vivo Swimming Of A Swarm Of Bacteria-Like Microrobotic Flagella. *Advanced Materials*, 27(19):2981–2988, 2015.

[90] Alexey Snezhko and Igor S. Aranson. Magnetic Manipulation Of Self-Assembled Colloidal Asters. *Nature Materials*, 10(9):698–703, 2011.

[91] A. Snezhko, M. Belkin, I. S. Aranson, and W.-K. Kwok. Self-Assembled Magnetic Surface Swimmers. *Physical Review Letters*, 102:118103, March 2009.

[92] Jiangfan Yu, Ben Wang, Xingzhou Du, Qianqian Wang, and Li Zhang. Ultra-Extensible Ribbon-Like Magnetic Microswarm. *Nature Communications*, 9(1):1–9, 2018.

[93] A. Snezhko, I. S. Aranson, and W.-K. Kwok. Surface Wave Assisted Self-Assembly of Multidomain Magnetic Structures. *Physical Review Letters*, 96:078701, February 2006.

[94] Fernando Martinez-Pedrero, Antonio Ortiz-Ambriz, Ignacio Pagonabarraga, and Pietro Tierno. Colloidal microworms propelling via a cooperative hydrodynamic conveyor belt. *Physical Review Letters*, 115:138301, September 2015.

[95] M. Koleoso, X. Feng, Y. Xue, Q. Li, T. Munshi, and X. Chen. Micro/Nanoscale Magnetic Robots For Biomedical Applications. *Materials Today Bio*, 8(October), 2020.

[96] Hideo Saotome, Takashi Okubo, and Yutaka Ikeda. A Novel Actuator With Nd-Fe-B Magnets Swimming Toward The Magnetic Field. *INTERMAG Europe 2002 - IEEE International Magnetics Conference*, 38(5):3009–3011, 2002.

[97] Bumjin Jang, Emiliya Gutman, Nicolai Stucki, Benedikt F. Seitz, Pedro D. Wendel-García, Taylor Newton, Juho Pokki, Olgaç Ergeneman, Salvador Pané, Yizhar Or, and Bradley J. Nelson. Undulatory Locomotion Of Magnetic Multilink Nanoswimmers. *Nano Letters*, 15(7):4829–4833, 2015.

[98] Rémi Dreyfus, Jean Baudry, Marcus L. Roper, Marc Fermigier, Howard a Stone, and Jérôme Bibette. Microscopic Artificial Swimmers. *Nature*, 437(7060):862–865, 2005.

[99] Hermes Gadêlha. On The Optimal Shape Of Magnetic Swimmers. *Regular and Chaotic Dynamics*, 18(1-2):75–84, 2013.

[100] H. Gadêlha, E. A. Gaffney, D. J. Smith, and J. C. Kirkman-Brown. Nonlinear Instability In Flagellar Dynamics: A Novel Modulation Mechanism In Sperm Migration? *Journal of the Royal Society Interface*, 7(53):1689–1697, 2010.

[101] Erik Gauger and Holger Stark. Numerical Study Of A Microscopic Artificial Swimmer. *Physical Review E - Statistical, Nonlinear, and Soft Matter Physics*, 74(2):1–10, 2006.

[102] Gábor Kósa, Péter Jakab, Gábor Székely, and Nobuhiko Hata. MRI Driven Magnetic Microswimmers. *Biomedical Microdevices*, 14(1):165–178, 2012.

[103] On Shun Pak, Wei Gao, Joseph Wang, and Eric Lauga. High-Speed Propulsion Of Flexible Nanowire Motors: Theory And Experiments. *Soft Matter*, 7(18):8169–8181, 2011.

[104] Veronika Magdanz, Islam S. M. Khalil, Juliane Simmchen, Guilherme P. Furtado, Sumit Mohanty, Johannes Gebauer, Haifeng Xu, Anke Klingner, Azaam Aziz, Mariana Medina-Sánchez, Oliver G. Schmidt, and Sarthak Misra. IRONSperm: Sperm-Templated Soft Magnetic Microrobots. *Science Advances*, 6(28):1–16, 2020.

[105] Wei Gao, Sirilak Sattayasamitsathit, Kalayil Manian Manesh, Daniel Weihs, and Joseph Wang. Magnetically Powered Flexible Metal Nanowire Motors. *Journal of the American Chemical Society*, 132(41):14403–14405, 2010.

[106] Kee Suk Ryu, Kashan Shaikh, Edgar Goluch, Zhifang Fan, and Chang Liu. Micro Magnetic Stir-Bar Mixer Integrated With Parylene Microfluidic Channels. *Lab on a Chip*, 4(6):608–613, 2004.

[107] T. Sawetzki, S. Rahmouni, C. Bechingera, and D. W. M. Marr. In Situ Assembly Of Linked Geometrically Coupled Microdevices. *Proceedings of the National Academy of Sciences of the United States of America*, 105(51):20141–20145, 2008.

[108] Masaya Hagiwara, Tomohiro Kawahara, Yoko Yamanishi, Taisuke Masuda, Lin Feng, and Fumihito Arai. On-Chip Magnetically Actuated Robot With Ultrasonic Vibration For Single Cell Manipulations. *Lab on a Chip*, 11(12):2049–2054, 2011.

[109] Masaya Hagiwara, Tomohiro Kawahara, Toru Iijima, and Fumihito Arai. High-Speed Magnetic Microrobot Actuation In A Microfluidic Chip By A Fine V-Groove Surface. *IEEE Transactions on Robotics*, 29(2):363–372, 2013.

[110] Peter Tseng, Jonathan Lin, Keegan Owsley, Janay Kong, Anja Kunze, Coleman Murray, and Dino Di Carlo. Flexible And Stretchable Micromagnet Arrays For Tunable Biointerfacing. *Advanced Materials*, 27(6):1083–1089, 2015.

[111] Fatemeh Nazly Pirmoradi, John K. Jackson, Helen M. Burt, and Mu Chiao. A Magnetically Controlled MEMS Device For Drug Delivery: Design, Fabrication, And Testing. *Lab on a Chip*, 11(18):3072–3080, 2011.

[112] Melvin Khoo and Chang Liu. Micro Magnetic Silicone Elastomer Membrane Actuator. *Sensors and Actuators, A: Physical*, 89(3):259–266, 2001.

[113] Fatemeh Pirmoradi, Luna Cheng, and Mu Chiao. A Magnetic Poly(dimethylesiloxane) Composite Membrane Incorporated With Uniformly Dispersed, Coated Iron Oxide Nanoparticles. *Journal of Micromechanics and Microengineering*, 20(1), 2010.

[114] Fatemeh Nazly Pirmoradi, John K. Jackson, Helen M. Burt, and Mu Chiao. On-Demand Controlled Release Of Docetaxel From A Battery-Less MEMS Drug Delivery Device. *Lab on a Chip*, 11(16):2744–2752, 2011.

[115] A. R. Shields, B. L. Fiser, B. A. Evans, M. R. Falvo, S. Washburn, and R. Superfine. Biomimetic Cilia Arrays Generate Simultaneous Pumping And Mixing Regimes. *Proceedings of the National Academy of Sciences of the United States of America*, 107(36):15670–15675, 2010.

[116] B. A. Evans, A. R. Shields, R. Lloyd Carroll, S. Washburn, M. R. Falvo, and R. Superfine. Magnetically Actuated Nanorod Arrays As Biomimetic Cilia. *Nano Letters*, 7(5):1428–1434, 2007.

[117] Jaakko V. I. Timonen, Christoffer Johans, Kyösti Kontturi, Andreas Walther, Olli Ikkala, and Robin H. A. Ras. A Facile Template-Free Approach To Magnetodriven,

Multifunctional Artificial Cilia. *ACS Applied Materials and Interfaces*, 2(8):2226–2230, 2010.

[118] Dirk Michael Drotlef, Peter Blümler, and Aránzazu Del Campo. Magnetically Actuated Patterns For Bioinspired Reversible Adhesion (Dry And Wet). *Advanced Materials*, 26(5):775–779, 2014.

[119] Nathan J. Sniadecki, Alexandre Anguelouch, Michael T. Yang, Corinne M. Lamb, Zhijun Liu, Stuart B. Kirschner, Yaohua Liu, Daniel H. Reich, and Christopher S. Chen. Magnetic Microposts As An Approach To Apply Forces To Living Cells. *Proceedings of the National Academy of Sciences of the United States of America*, 104(37):14553–14558, 2007.

[120] Srinivas Hanasoge, Matthew Ballard, Peter J. Hesketh, and Alexander Alexeev. Asymmetric Motion Of Magnetically Actuated Artificial Cilia. *Lab on a Chip*, 17(18):3138–3145, 2017.

[121] Srinivas Hanasoge, Peter J. Hesketh, and Alexander Alexeev. Microfluidic pumping using artificial magnetic cilia. *Microsystems and Nanoengineering*, 4(1), 2018.

[122] Srinivas Hanasoge, Peter J. Hesketh, and Alexander Alexeev. Metachronal Motion Of Artificial Magnetic Cilia. *Soft Matter*, 14(19):3689–3693, 2018.

[123] Hongri Gu, Quentin Boehler, Haoyang Cui, Eleonora Secchi, Giovanni Savorana, Carmela De Marco, Simone Gervasoni, Quentin Peyron, Tian Yun Huang, Salvador Pane, Ann M. Hirt, Daniel Ahmed, and Bradley J. Nelson. Magnetic Cilia Carpets With Programmable Metachronal Waves. *Nature Communications*, 11(1):1–10, 2020.

[124] Xiaoguang Dong, Guo Zhan Lum, Wenqi Hu, Rongjing Zhang, Ziyu Ren, Patrick R. Onck, and Metin Sitti. Bioinspired Cilia Arrays With Programmable Nonreciprocal Motion And Metachronal Coordination. *Science Advances*, 6(45), 2020.

[125] Mojca Vilfan, Anton Potočnik, Blaž Kavčič, Natan Osterman, Igor Poberaj, Andrej Vilfan, and Dušan Babič. Self-Assembled Artificial Cilia. *Proceedings of the National Academy of Sciences of the United States of America*, 107(5):1844–1847, 2010.

[126] Shuang Ben, Jun Tai, Han Ma, Yun Peng, Yuan Zhang, Dongliang Tian, Kesong Liu, and Lei Jiang. Cilia-Inspired Flexible Arrays For Intelligent Transport Of Viscoelastic Microspheres. *Advanced Functional Materials*, 28(16):1–7, 2018.

[127] Alain Truong, Guillermo Ortiz, Mélissa Morcrette, Thomas Dietsch, Philippe Sabon, Isabelle Joumard, Alain Marty, Hélène Joisten, and Bernard Dieny. Magneto-Optical Micromechanical Systems For Magnetic Field Mapping. *Scientific Reports*, 6(July):1–8, 2016.

[128] Madison L. Sheely. Glycerol Viscosity Tables. *Industrial and Engineering Chemistry*, 24(9):1060–1064, 1932.

[129] Brant A. Inman, Wiguins Etienne, Rainier Rubin, Richmond A. Owusu, Tiago R. Oliveira, Dario B. Rodriques, Paolo F. Maccarini, Paul R. Stauffer, Alireza Mashal, and Mark W. Dewhirst. The Impact Of Temperature And Urinary Constituents On Urine Viscosity And Its Relevance To Bladder Hyperthermia Treatment. *International Journal of Hyperthermia*, 29(3):206–210, 2013.

[130] David P. Arnold and Naigang Wang. Permanent magnets For MEMS. *Journal of Microelectromechanical Systems*, 18(6):1255–1266, 2009.

[131] Shan Guan and Bradley J. Nelson. Pulse-Reverse Electrodeposited Nanograin-sized CoNiP Thin Films And Microarrays For MEMS Actuators. *Journal of The Electrochemical Society*, 152(4):C190, 2005.

[132] Dimitri Kokkinis, Manuel Schaffner, and André R. Studart. Multimaterial Magnetically Assisted 3D Printing Of Composite Materials. *Nature Communications*, 6, 2015.

[133] K. M. Yin, S. L. Jan, and C. C. Lee. Current Pulse With Reverse Plating Of Nickel-Iron Alloys In A Sulphate Bath. *Surface and Coatings Technology*, 88(1-3):219–225, 1997.

[134] M. Ghaemi and L. Binder. Effects Of Direct And Pulse Current On Electrodeposition Of Manganese Dioxide. *Journal of Power Sources*, 111(2):248–254, 2002.

[135] M. S. Chandrasekar and Malathy Pushpavanam. Pulse And Pulse Reverse Plating-Conceptual, Advantages And Applications. *Electrochimica Acta*, 53(8):3313–3322, 2008.

[136] Shan Guan and Bradley J Nelson. Magnetic Composite Electroplating For Depositing Micromagnets. *Journal of Microelectromechanical Systems*, 15(2):330–337, 2006.

[137] B. Tury, M. Lakatos-Varsányi, and S. Roy. Effect Of Pulse Parameters On The Passive Layer Formation On Pulse Plated Ni-Co Alloys. *Applied Surface Science*, 253(6):3103–3108, 2007.

[138] Jue Chen and Lutz Rissing. Electroplating Hard Magnetic SmCo For Magnetic Microactuator Applications. *Journal of Applied Physics*, 109(7):07A766, 2011.

[139] P. Cojocaru, L. Magagnin, E. Gómez, and E. Vallés. Electrodeposition Of CoNi And CoNiP Alloys In Sulphamate Electrolytes. *Journal of Alloys and Compounds*, 503(2):454–459, 2010.

[140] F. Luborsky. High Coercive Force Films Of Cobalt-Nickel With Additions Of Group VA And VIB Elements. *IEEE Transactions on Magnetics*, 6(3):502–506, 1970.

[141] Chun Wu, Kai Wang, Donggang Li, Changsheng Lou, Yue Zhao, Yang Gao, and Qiang Wang. Tuning Microstructure And Magnetic Properties Of Electrodeposited CoNiP Films By High Magnetic Field Annealing. *Journal of Magnetism and Magnetic Materials*, 416:61–65, 2016.

[142] P. Cojocaru, L. Magagnin, E. Gomez, and E. Valles. Electrodeposition Of CoNiP Films With Modulated Magnetic Behaviour. *Transactions of the Institute of Metal Finishing*, 89(4):194–197, 2011.

[143] Nosang V. Myung, D. Y. Park, B. Y. Yoo, and Paulo T. A. Sumodjo. Development Of Electroplated Magnetic Materials For MEMS. *Journal of Magnetism and Magnetic Materials*, 265(2):189–198, 2003.

[144] Feodor Y. Ogrin, Peter G. Petrov, and C. Peter Winlove. Ferromagnetic Microswimmers. *Physical Review Letters*, 100(21):21812–21816, 2008.

[145] Andrew D. Gilbert, Feodor Y. Ogrin, Peter G. Petrov, and C. Peter Winlove. Theory Of Ferromagnetic Microswimmers. *The Quarterly Journal of Mechanics and Applied Mathematics*, 64(3):239–263, 2011.

[146] A. D. Gilbert, F. Y. Ogrin, P. G. Petrov, and C. P. Winlove. Motion And Mixing For Multiple Ferromagnetic Microswimmers. *European Physical Journal E*, 34(11), 2011.

[147] G. Bertotti. *Hysteresis In Magnetism: For Physicists, Materials Scientists, And Engineers*. Academic Press series in electromagnetism. Elsevier Science, 1998.

[148] Joshua K. Hamilton, Peter G. Petrov, C. Peter Winlove, Andrew D. Gilbert, Matthew T. Bryan, and Feodor Y. Ogrin. Magnetically Controlled Ferromagnetic Swimmers. *Scientific Reports*, 7:44142, 2017.

[149] Joshua K. Hamilton, Matthew T. Bryan, Andrew D. Gilbert, Feodor Y. Ogrin, and Thomas O. Myers. A New Class Of Magnetically Actuated Pumps And Valves For Microfluidic Applications. *Scientific Reports*, 8(1):1–12, 2018.

[150] K. Chouarbi, M. Woytasik, E. Lefeuvre, and J. Moulin. SmCo Micromolding In An Aqueous Electrolyte. In *Microsystem Technologies*, volume 19, pages 887–893, 2013.

[151] A. Walther, C. Marcoux, B. Desloges, R. Grechishkin, D. Givord, and N. M. Dempsey. Micro-patterning Of NdFeB And SmCo Magnet Films For Integration Into. *Journal of Magnetism and Magnetic Materials*, 321:590–594, 2009.

[152] M. D. Cooke, D. A. Allwood, D. Atkinson, G. Xiong, C. C. Faulkner, and R. P. Cowburn. Thin Single Layer Materials For Device Application. *Journal of Magnetism and Magnetic Materials*, 257(2-3):387–396, 2003.

[153] Shemaiah M. Weekes, Feodor Y. Ogrin, and William A. Murray. Fabrication Of Large-Area Ferromagnetic Arrays Using Etched Nanosphere Lithography. *Langmuir*, 20(25):11208–11212, 2004.

[154] I. D. Johnston, D. K. McCluskey, C. K. L. Tan, and M. C. Tracey. Mechanical Characterization Of Bulk Sylgard 184 For Microfluidics And Microengineering. *Journal of Micromechanics and Microengineering*, 24(3), 2014.

[155] Jinsheng Gao, D. Guo, S. Santhanam, and G. Fedder. Material characterization and transfer of large-area ultra-thin polydimethylsiloxane membranes. *Journal of Microelectromechanical Systems*, 24:2170–2177, 2015.

[156] Sedat Dogru, Bekir Aksoy, Halil Bayraktar, and B. Erdem Alaca. Poisson's ratio of pdms thin films. *Polymer Testing*, 69:375–384, 2018.

[157] Melissa P. Anenden, Martin Svehla, Nigel H. Lovell, and Gregg J. Suaning. Process Development For Dry Etching Polydimethylsiloxane For Neural Electrodes. In *33rd Annual International Conference of the IEEE Engineering in Medicine and Biology Society*, pages 2977–2980, 2011.

[158] M. T. Bryan, J. Garcia-Torres, E. L. Martin, J. K. Hamilton, C. Calero, P. G. Petrov, C. P. Winlove, I. Pagonabarraga, P. Tierno, F. Sagués, and F. Y. Ogrin. Microscale Magneto-Elastic Composite Swimmers At The Air-Water And Water-Solid Interfaces Under A Uniaxial Field. *Physical Review Applied*, 11(4):044019, 2019.

[159] Matthew T. Bryan, Elizabeth L. Martin, Aleksandra Pac, Andrew D. Gilbert, and Feodor Y. Ogrin. Metachronal Waves In Magnetic Micro-Robotic Paddles For Artificial Cilia. *Communications Materials*, 2(14):2–8, 2021.

[160] Jacob L. Binsley, Elizabeth L. Martin, Thomas O. Myers, Stefano Pagliara, and Feodor Y. Ogrin. Microfluidic Devices Powered By Integrated Elasto-Magnetic Pumps. *Lab on a Chip*, 20:4285–4295, 2020.

[161] A. del Campo and C. Greiner. SU-8: A photoresist for high-aspect-ratio and 3d submicron lithography. *Journal of Micromechanics and Microengineering*, 17(6):R81–R95, May 2007.

[162] Srinath Satyanarayana, Rohit N. Karnik, and Arunava Majumdar. Stamp-And-Stick Room-Temperature Bonding Technique For Microdevices. *Journal of Microelectromechanical Systems*, 14(2):392–399, 2005.

[163] Shantanu Bhattacharya, Arindom Datta, Jordan M. Berg, and Shubhra Gangopadhyay. Studies On Surface Wettability Of Poly(dimethyl) Siloxane (PDMS) And Glass Under Oxygen-Plasma Treatment And Correlation With Bond Strength. *Journal of Microelectromechanical Systems*, 14(3):590–597, 2005.

[164] Henrik Bruus. *Theoretical Microfluidics*. Oxford Master Series in Physics. OUP Oxford, 2007.

[165] Chris O'Callaghan, Kulvinder Sikand, and Mark A. Chilvers. Analysis Of Ependymal Ciliary Beat Pattern And Beat Frequency Using High Speed Imaging: Comparison With The Photomultiplier And Photodiode Methods. *Cilia*, 1:314–317, 2012.

[166] E. A. Gaffney, H. Gadêlha, D. J. Smith, J. R. Blake, and J. C. Kirkman-Brown. Mammalian Sperm Motility: Observation And Theory. *Annual Review of Fluid Mechanics*, 43:501–528, 2011.

[167] Joshua K. Hamilton, Andrew D. Gilbert, Peter G. Petrov, and Feodor Y. Ogrin. Torque Driven Ferromagnetic Swimmers. *Physics of Fluids*, 30(9):092001, September 2018.

[168] J. Happel and H. Brenner. *Low Reynolds Number Hydrodynamics With Special Applications To Particulate Media*. Mechanics of Fluids and Transport Processes. Springer Netherlands, 1983.

[169] L. D. Landau and E. M. Liftshitz. *Fluid Mechanics*. A-W series in advanced physics. Elsevier Science & Technology Books, 1959.

[170] B. J. Kirby. *Micro- And Nanoscale Fluid Mechanics: Transport In Microfluidic Devices*. Cambridge University Press, 2010.

[171] C. W. Oseen. *Neuere Methoden Und Ergebnisse In Der Hydrodynamik*. Mathematik und ihre Anwendungen in Monographien und Lehrbüchern. Akademische Verlagsgesellschaft, 1927.

[172] G. J. Hancock. The self-propulsion of microscopic organisms through liquids. *Proceedings of the Royal Society of London. Series A. Mathematical and Physical Sciences*, 217, 1953.

Appendix A

Elasto-Magnetic Paddles

A.1 Analytical model

To elucidate the mechanisms of the paddle membrane, Prof. Andrew D. Gilbert and I developed a minimal theoretical model. This model is based on previous simulations of magnetic swimmers [144–146, 167].

The geometry of this model consists of eight beads within a unit cell. These beads are connected together via links in the arrangement shown in Figure A.1. This is a 2D model and represents the system being viewed in a cross-sectional plane, which in the model is referred to as the (x, y) plane. The design in the model represents a repeated chain of two magnetic paddles (rather than the four that have been experimentally produced on a microscale), this is due to the computation time. Beads 1-4 form a backbone structure, with beads 5 and 6 connected to the backbone at bead 2 and similarly, beads 7 and 8 connected to bead 3.

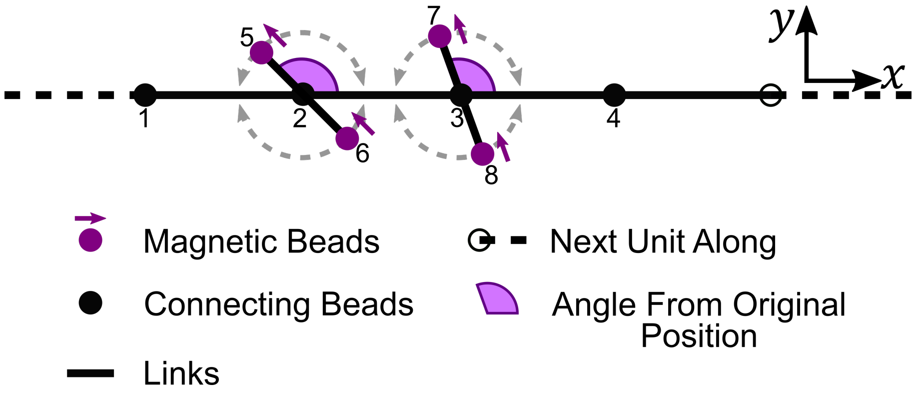

Figure A.1: Diagram showing theoretical representation of the paddle membrane, with numbered beads.

Therefore, the bead triplets 5–2–6 and 7–2–8 form the two rotating paddles on the backbone structure. Beads 5 and 6 correspond to the first paddle and beads 7 and 8 the second. The referred to backbone structure represents the frame the paddles are attached to via their PDMS axles. Beads 5–6 and 7–8 incorporate a hard magnetic moment aligned with their respective paddle orientations. The whole cell structure is repeated along the x-direction with periodic boundary conditions.

In this model, the non-dimensional equation of motion for the system of beads is solved, involving several different types of force. The five types are labelled *spring*, *bend*, *ext* (shorthand for *external magnetic*), *drag* and *interact* (shorthand for *fluid interaction*) and they are explained below. The beads have radii R_i and are centred at $\boldsymbol{r}_i(t) = (x_i, y_i)$; the centre of reaction [168] $\boldsymbol{\mathcal{X}}(t) = (X, Y)$ is given by:

$$\boldsymbol{\mathcal{X}} \sum_i R_i = \sum_i R_i \boldsymbol{r}_i. \tag{A.1}$$

The following is set $\boldsymbol{r}_{ij} = \boldsymbol{r}_i - \boldsymbol{r}_j$, $r_{ij} = |\boldsymbol{r}_{ij}|$, $\hat{\boldsymbol{r}}_{ij} = \boldsymbol{r}_{ij} {r_{ij}}^{-1}$ and $\tan\theta_{ij} = (y_i - y_j)(x_i - x_j)^{-1}$ which sets θ_{ij} to be the angle between $\boldsymbol{r}_{ij}$ and the x-axis. The

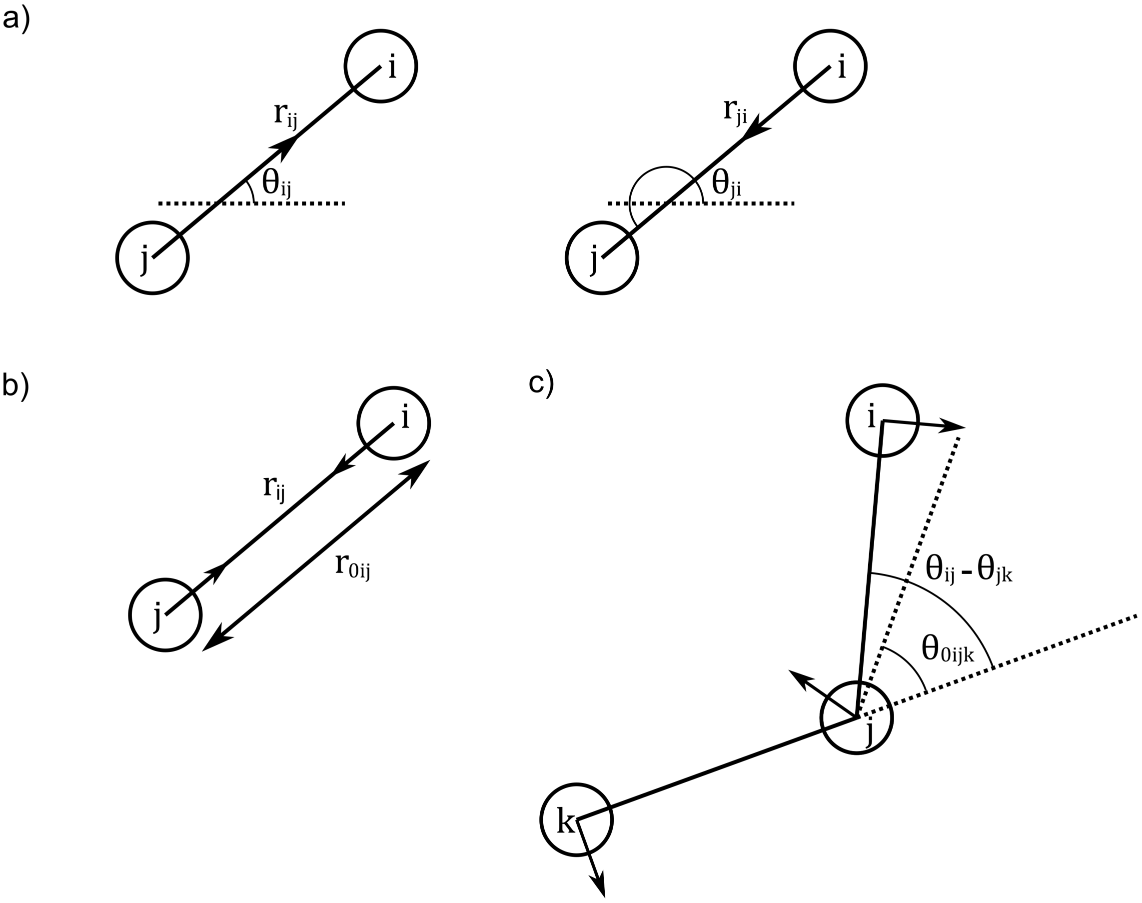

Figure A.2: Diagram showing how the distances and angles are set for the theoretical representation of the paddle membrane.

representation of this can be seen in Figure A.2. The motion of the beads is governed by:

$$\lambda_i \ddot{\boldsymbol{r}}_i = \boldsymbol{F}_{\mathrm{spring},i} + \boldsymbol{F}_{\mathrm{bend},i} + \boldsymbol{F}_{\mathrm{ext},i} + \boldsymbol{F}_{\mathrm{drag},i} + \boldsymbol{F}_{\mathrm{interact},i}, \tag{A.2}$$

with bead masses λ_i taken to be sufficiently small so the motion is effectively in an inertia-free Stokes regime (our results are insensitive to the values of λ_i in the limit $\lambda_i \to 0$).

The conservative forces are derived from potentials: the total elastic potential is the sum of potentials for each elastic link labelled (i, j) in the system:

$$V_{\text{spring}} = \sum_{i,j} V_{\text{spring},ij}, \qquad V_{\text{spring},ij} = \tfrac{1}{2} k_{ij} (r_{ij} - r_{0ij})^2, \tag{A.3}$$

where r_{0ij} is the link's natural length and k_{ij} is the spring constant. The code maintains a list of all elastic links for $k_{ij} \neq 0$ and at each time step calculates and assigns the elastic force for the ith bead, (The code assigns the opposite force to the jth bead)

$$\boldsymbol{F}_{\text{spring},i} = k_{ij} (r_{ij} - r_{0ij}) \hat{\boldsymbol{r}}_{ij}. \tag{A.4}$$

As well as elastic forces between selected pairs of beads, forces that resist bending are imposed. This is taken to represent the widths of the paddle's PDMS axles. For any pairs of links, (i, j) and (j, k) that are joined at bead j, these bending forces oppose any change in the angle $\theta_{ij} - \theta_{jk}$ from a specified relaxed value. Summing over all triples (i, j, k) for which this effect is included, the bending forces are derived from the potential

$$V_{\text{bend}} = \sum_{i,j,k} V_{\text{bend},ijk}, \qquad V_{\text{bend},ijk} = -\ell_{ijk} \cos(\theta_{ij} - \theta_{jk} - \theta_{0ijk}). \tag{A.5}$$

Where ℓ_{ijk} is the bending stiffness and θ_{0ijk} is the natural angle to which the angle $\theta_{ij} - \theta_{jk}$ relaxes to in the absence of other forces. Since $\cos\Phi = 1 - \Phi^2/2 + \cdots$, the potential is quadratic for small angles, but then acts as a “soft” spring for larger angles. As the potential is 2π-periodic in the angles, it avoids at the outset any numerical problems if an angle jumps by 2π in the simulations. The code maintains a list of triples (i, j, k) for which $\ell_{ijk} \neq 0$ and at each time-step assigns forces to the 3 particles:

$$\boldsymbol{F}_{\text{bend},i} = \ell_{ijk}\sin(\theta_{ij} - \theta_{jk} - \theta_{0ijk})r_{ij}^{-2}[(y_i - y_j)\boldsymbol{i} - (x_i - x_j)\boldsymbol{j}], \tag{A.6}$$

$$\begin{aligned}\boldsymbol{F}_{\text{bend},j} = \ell_{ijk}\sin(\theta_{ij} - \theta_{jk} - \theta_{0ijk})\Big[&r_{ij}^{-2}[-(y_i - y_j)\boldsymbol{i} + (x_i - x_j)\boldsymbol{j}] \\ &+ r_{jk}^{-2}[-(y_j - y_k)\boldsymbol{i} + (x_j - x_k)\boldsymbol{j}]\Big],\end{aligned} \tag{A.7}$$

$$\boldsymbol{F}_{\text{bend},k} = \ell_{ijk}\sin(\theta_{ij} - \theta_{jk} - \theta_{0ijk})r_{jk}^{-2}[(y_j - y_k)\boldsymbol{i} - (x_j - x_k)\boldsymbol{j}]. \tag{A.8}$$

Note that (naturally) these give no net force and no net torque on the system.

The external magnetic field $\boldsymbol{B}_{\text{ext}}$ drives the elasto-magnetic membrane directly through a potential term, which is imposed for all magnetised beads in the system,

$$V_{\text{ext}} = \sum_i V_{\text{ext},i}, \qquad V_{\text{ext},i} = -\boldsymbol{m}_i \cdot \boldsymbol{B}_{\text{ext}} = -m_i\, B_{\text{ext}}\, b(t)\cos[\alpha_i + \alpha_{0i} + \theta_{ij} - \psi(t)], \tag{A.9}$$

where the field has a magnitude of $B_{\text{ext}}b(t)$ and angle $\psi(t)$ to the x-axis. In Equation (A.9), m_i is the magnetic moment of each magnetic bead ($i = 5$–8), α_{0i} is the angle of easy axis with respect to the angle of a particular link (i, j) (with a choice of j made for each magnetised bead i so as to fix its orientation, here j being the bead at the centre of each paddle).

The bead's magnetic field is taken to be at an angle α_i to the bead's easy axis. The angles α_{0i}, α_i θ_{ij} are shown in Supplementary Figure A.3. In this model α_{0i} is set to be 0 for beads $i = 6, 8$ and π for beads $i = 5, 7$; this is so that all the magnetic beads to have an in-plane easy axis in the same orientation. The

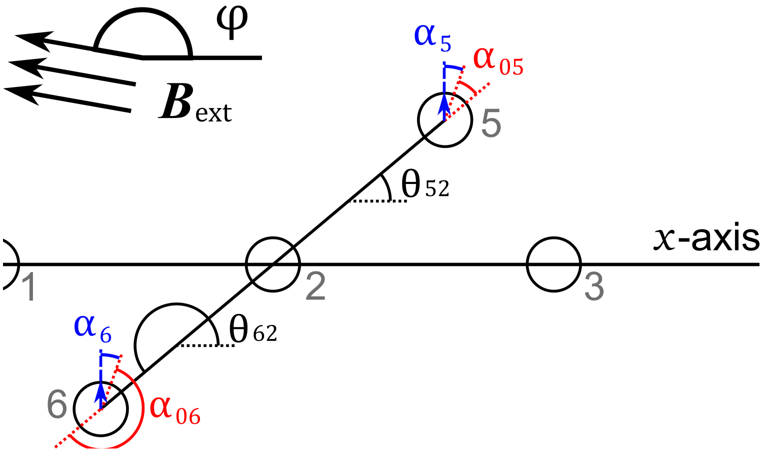

Figure A.3: This diagram indicates how the various angles, α_{0i} and α_i related to the first paddle (beads 2, 5 and 6).

magnetic force on bead i is given by

$$\boldsymbol{F}_{\text{ext},i} = m_i B_{\text{ext}} b \sin[\alpha_i + \alpha_{0i} + \theta_{ij} - \psi(t)] r_{ij}^{-2} [(y_i - y_j)\boldsymbol{i} - (x_i - x_j)\boldsymbol{j}]. \qquad \text{(A.10)}$$

An equal and opposite force is imposed on the appropriate bead j, involving a net magnetic torque on the system in general. In this model, B_{ext} is a constant and $b(t)$ and $\psi(t)$ are dimensionless. The field is mainly in the x-direction but has a weak elliptical component, $\boldsymbol{B}_{\text{ext}} = B_{\text{ext}}(b_x, b_y)$ with

$$\boldsymbol{B}_{\text{ext}} = B_{\text{ext}}(\beta \sin \omega t, \alpha \cos \omega t), \qquad \text{(A.11)}$$

where β = 1.00 and α=0.01. The weaker elliptical component exists to mimic the fact that in experimental situations, systems aren't aligned perfectly along the x-axis, so there is always some magnetic torque. Without this in the model, if the paddle was perfectly aligned along the x-axis and the field was oscillating in the x direction only, there would be no force due to torque and therefore, the paddle would remain still.

The bead's magnetic field angle α_i is governed by the following equation,

$$\Gamma\dot{\alpha}_i = (1-\kappa_i)b\sin[\psi(t)-\alpha_i-\alpha_{0i}-\theta_{ij}] - \kappa_i \sin 2\alpha_i. \tag{A.12}$$

Here Γ is a very fast internal magnetic time-scale and κ represents how magnetically "hard" or "soft" the magnetic bead is. When $\kappa = 1$ the magnetic bead is entirely magnetically hard which means its field direction is fixed along the easy axis α_{0i}. When $\kappa = 0$ the bead is entirely magnetically soft which means that its field direction completely follows that of the external magnetic field. In the model the magnetic beads are set to be predominantly magnetically hard while the internal magnetic dynamics still play a small role, taking $\kappa = 0.9$. In this model, there is no magnetic interaction between the beads themselves, that is to say no magnetic dipole component is included. The only magnetic interaction is between each bead and the external magnetic field. This is because the magnetic forces are quite short range compared with the fluid interactions that are included (discussed later in this section).

The forces $\boldsymbol{F}_{\text{spring},i}$, $\boldsymbol{F}_{\text{bend},i}$, and $\boldsymbol{F}_{\text{ext},i}$ are derived from their potentials above and incorporated into equation (A.2). The forces due to the fluid interactions are not derived from potentials. The fluid interactions are related to Stokes flow equations which are valid when the Reynolds number is $\ll 1$.

The bead radii are considered to be very small compared to the natural length of the connecting links ($R_i \ll r_{p0}$), therefore, the force on each bead from the surrounding fluid may be expressed as [168, 169]:

$$\boldsymbol{F}_{\text{fluid},i} = \boldsymbol{F}_{\text{drag},i} + \boldsymbol{F}_{\text{interact},i} = -6\pi\mu R_i \dot{\boldsymbol{r}}_i + 6\pi\mu R_i \sum_j \frac{3}{4}\frac{R_j}{r_{ij}}\left(\hat{\boldsymbol{r}}_{ij}\hat{\boldsymbol{r}}_{ij} + I_n\right)\cdot\dot{\boldsymbol{r}}_j, \tag{A.13}$$

where I is the identity matrix. Equation (A.13) includes the Stokes drag ($\boldsymbol{F}_{\mathrm{drag},i} = -6\pi\mu R_i \dot{\boldsymbol{r}}_i$) the total force of viscous and resultant pressure forces on a sphere in a low Reynolds number regime.

$\boldsymbol{F}_{\mathrm{drag},i}$ is the drag force on bead i moving in a stationary fluid. However because of the motion of other beads labelled by j, there will be a local flow near the spherical bead i. At leading order a bead j will generate a stokeslet, the fluid solution by a point force ($\boldsymbol{F}_\delta$) in a Stokes regime. The stokeslet is the primary Green's function of Stokes flow, given by [170]

$$\boldsymbol{J}(\boldsymbol{r}) = \frac{1}{8\pi\mu}\left(\frac{I_n}{r} + \frac{\boldsymbol{r}\boldsymbol{r}}{r^3}\right). \tag{A.14}$$

The stokeslet was first derived by Oseen in 1927 [171] and was named by Hancock in 1953 [172]. The solution for the velocity of the flow (with the speed vanishing at infinity) is

$$\boldsymbol{u}(\boldsymbol{r}) = \boldsymbol{F}_\delta \cdot \boldsymbol{J}(\boldsymbol{r}). \tag{A.15}$$

Bead i experiences drag in the flow that is the sum of these stokeslets from beads labelled by j, and this gives Equation (A.13).

Here and further on, the term when $i = j$ is excluded. These are the leading terms in an expansion in the small parameter $\epsilon = R/r_{p0} \ll 1$, where R is the average bead radius. Note that at this level of approximation, the motion of the centre of reaction is given by

$$6\pi\mu\Big(\sum_i R_i\Big)\dot{\boldsymbol{\mathcal{X}}} = \sum_i \boldsymbol{F}_{\mathrm{interact},i} = \sum_{i,j} \frac{9\pi}{2}\,\frac{\mu R_i R_j}{r_{ij}}\,(\hat{\boldsymbol{r}}_{ij}\hat{\boldsymbol{r}}_{ij} + I_n)\cdot\dot{\boldsymbol{r}}_j. \tag{A.16}$$

Note that all the $\boldsymbol{F}_{\mathrm{drag},i}$ forces cancel each other out, therefore fluid interactions need to be included for motion to occur.

This concludes the description of the forces in equation (A.2) which then may be time-stepped numerically using a standard routine for a stiff system (since the masses are taken to be very small). The function `ode15s` was used in Matlab.

The parameters controlling the system are $\{\lambda_i,\, R_i,\, k_{ij},\, r_{0ij},\, \ell_{ijk},\, \theta_{0ijk},\, m_i,\, \alpha_{0i},\, \kappa_i,\, \Gamma,\, B_{\mathrm{ext}},\, \omega,\, \mu\}$. In order to non-dimensionalise, the following basic length, time and mass scales are used:

$$r_{p0} = L, \qquad \omega^{-1} = \mathcal{T}, \qquad k_0\omega^{-2} = \mathcal{M}, \tag{A.17}$$

where k_0 is a typical value of the k_{ij} and r_{p0} a typical value of the r_{0ij}. These are used to define the dimensionless variables, denoted by a star, with unstarred quantities for the dimensional variables:

$$\begin{aligned}
x_i &= Lx_i^*,\\
y_i &= Ly_i^*,\\
t &= \mathcal{T}t^*,\\
R_i &= RR_i^* = \epsilon LR_i^*,\\
r_{0ij} &= r_{p0}r_{0ij}^* = Lr_{0ij}^*,\\
k_{ij} &= k_0k_{ij}^* = \frac{\mathcal{M}}{\mathcal{T}^2}\,k_{ij}^*,\\
\ell_{ijk} &= k_0r_{p0}^2\ell_{ijk}^* = \frac{\mathcal{M}L^2}{\mathcal{T}^2}\,\ell_{ijk}^*,\\
m_i &= m_0m_i^*,\\
\lambda_i &= \lambda\lambda_i^*.
\end{aligned} \tag{A.18}$$

Here R is a typical value for R_i, λ for λ_i and m_0 for m_i. It is convenient to define key dimensionless parameters:

$$\begin{aligned} \epsilon &= \frac{R}{L}, \\ \varpi &= \epsilon \frac{L\mathcal{T}}{\mathcal{M}} 6\pi\mu, \\ \upsilon &= \frac{\lambda}{\varpi^2 \mathcal{M}}, \\ A_{ext} &= m_0 B_{\text{ext}} \frac{\mathcal{T}^2}{\mathcal{M}L^2}, \\ \varsigma &= \frac{\Gamma}{\varpi \mathcal{T}}. \end{aligned} \tag{A.19}$$

Dropping the stars, the dimensionless equation of motion for a bead i in this system now takes the form

$$\upsilon\varpi^2\lambda_i \ddot{\boldsymbol{r}}_i = \boldsymbol{F}_{\text{spring},i} + \boldsymbol{F}_{\text{bend},i} + \boldsymbol{F}_{\text{ext},i} + \boldsymbol{F}_{\text{drag},i} + \boldsymbol{F}_{\text{interact},i}, \tag{A.20}$$

with the elastic forces $\boldsymbol{F}_{\text{spring},i}$ and bending forces $\boldsymbol{F}_{\text{bend},i}$ having an unchanged form, and

$$\boldsymbol{F}_{\text{ext},i} = m_i A_{\text{ext}} b \sin[\alpha_i + \alpha_{0i} + \theta_{ij} - \psi(t)] r_{ij}^{-2} [(y_i - y_j)\boldsymbol{i} - (x_i - x_j)\boldsymbol{j}], \tag{A.21}$$

$$\boldsymbol{F}_{\text{drag},i} + \boldsymbol{F}_{\text{interact},i} = -\varpi R_i \dot{\boldsymbol{r}}_i + \frac{3}{4}\epsilon\varpi \sum_j \frac{R_i R_j}{r_{ij}} (\hat{\boldsymbol{r}}_{ij}\hat{\boldsymbol{r}}_{ij} + I_n) \cdot \dot{\boldsymbol{r}}_j. \tag{A.22}$$

Equation (A.12) governing the magnetic moment orientation α_i becomes

$$\varsigma\varpi\dot{\alpha}_i = (1 - \kappa_i) b \sin[\psi(t) - \alpha_i - \alpha_{0i} - \theta_{ij}] - \kappa_i \sin 2\alpha_i. \tag{A.23}$$

Again, with the stars removed, the dimensionless quantities which govern the system are specified as $\{\lambda_i,\ R_i, k_{ij},\ r_{0ij},\ \ell_{ijk},\ \theta_{0ijk},\ m_i,\ \alpha_{0i},\ \kappa_i,\ A_{\text{ext}},\ \varpi,\ \upsilon,\ \epsilon,\ \varsigma\}$. However in the investigations ℓ_{ijk} and α_{0i} are the predominant variables that are altered once the geometry is set ($\ell_{ijk} = 0.125$–0.225 in Chapter 5 and $\alpha_{0i} = 0$–2π in Chapter 7). The dimensionless parameters for the simulations are used, listed in Table A.1 and $\{r_{0ij}, \theta_{0ijk}, \alpha_{0i}\}$ are controlled by the set geometry. These values are found by using typical dimensional parameters in Section 5.2, ($L = 150$ µm, $\omega = 2\pi \times 15$ s^{-1}, $B_{\text{ext}} = 2.4$ mT, $k_0 = 3 \times 10^{-4}$ N m^{-1}, $m_0 = 2.4 \times 10^{-9}$ Am^2, $\mu = 3.7 \times 10^{-2}$ Pa s, which is for a mixture of glycerol and water.)

Table A.1: Values of the dimensionless parameters used in the model.

Variable	Value
ϖ	0.89
υ	1×10^{-5}
A_{ext}	0.86
ϵ	0.025
ς	1×10^{-5}
k_{ij}	50
R_i	1
m_i	1
λ_i	1
κ_i	0.9

It should be noted that the idealised model is only expected to allow qualitative comparison with the experiments.

A.2 Additional Theoretical Results

In order to fully understand the paddle design, an array of parameters were varied to ensure the validity of the theoretical results and eliminate other possible causes

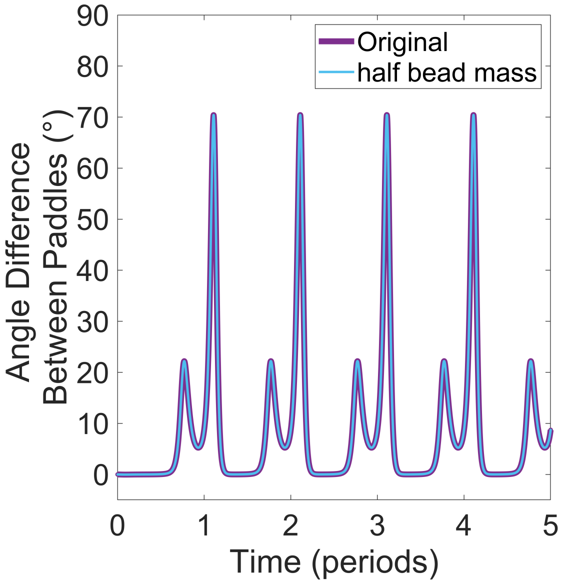

Figure A.4: Shows the difference in angle between the paddles when the mass of the beads is the model is halved.

that could be affecting the results.

These results are all comparing the angle difference between the two paddles for different parameters. ℓ_{p1} was set to 0.1349 and ℓ_{p2} to 0.1522, these values were chosen because they reproduce the maximum rotation observed in the experimental device for axle widths of 3 µm and 6 µm respectively. The original theoretical setup's time dependence of the difference in paddle angles can be seen in Figure 5.6.

As can be seen from Figure A.4, altering the mass of the beads in the model does not alter the paddles motion. The value for the spring constants of the links, k_{ij} and the bending stiffness for the backbone beads, ℓ_{ijk} when i, j and k are all values 1-4, was set to be suitably stiff to ensure a stable connecting structure that was not contributing to the cause of the non-reciprocal motion. In the results, both k_{ij} and the backbone ℓ_{ijk} was set to 50. Looking at Figure

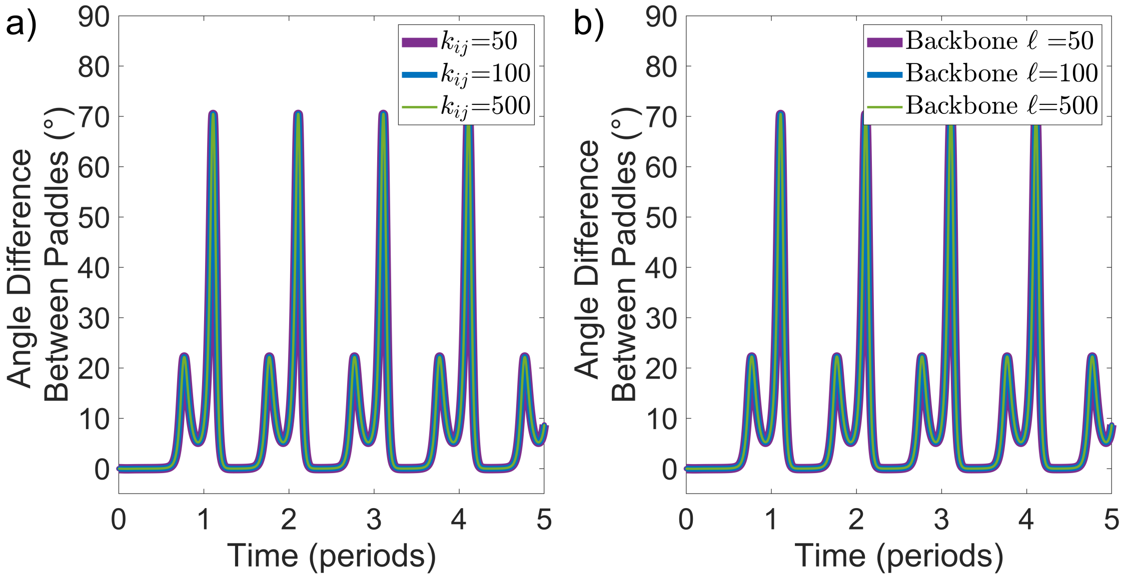

Figure A.5: a) Shows the difference in angle between the paddles when varying large values of k_{ij} which is a spring constant term for all the links. b) Shows the difference in angle between the paddles when varying large values of ℓ_{ijk} for the backbone bead triplets.

A.5(a) and (b), it can be seen that dramatically increasing these values does not alter the behaviour of the paddles. Therefore, this value of 50 was suitable for the other investigations. However, it is worth noting that dramatically decreasing these values would change the behaviour of the system but it was not further investigated here.

The initial position of the paddles was altered to confirm that the movement was not due to the paddles being perfectly in-line with the actuating magnetic field which is not feasible in experiments. In Figure A.6(a), the initial position of the paddles were altered and the easy axis of the paddles was still inline with that of the x direction. This graph indicates that this does not change the overall behaviour of the paddles. Figure A.6(b) compares the difference in angle when

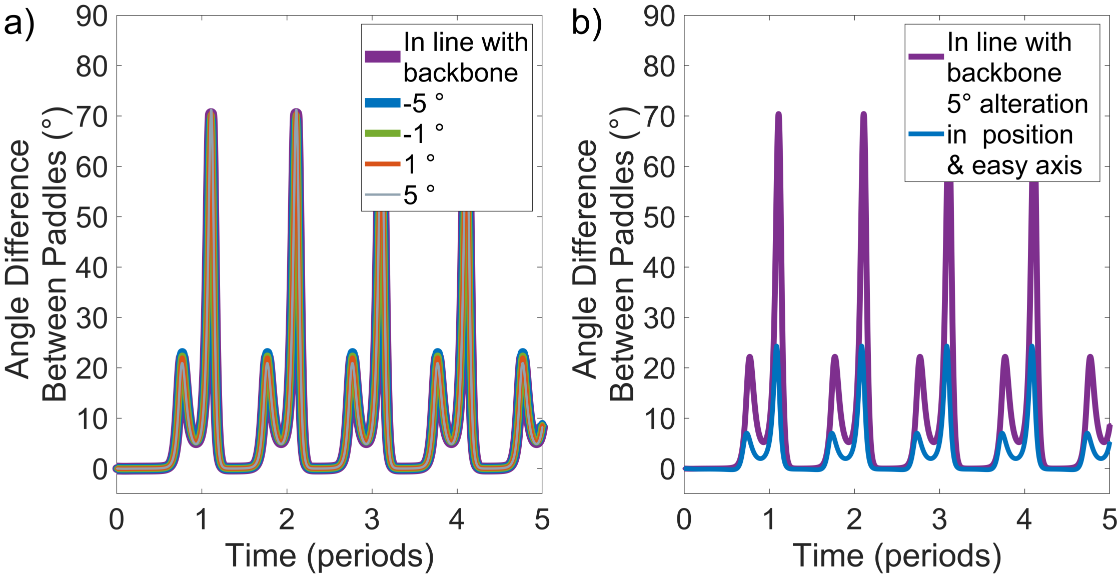

Figure A.6: a) Shows the difference in angle between the paddles when varying initial orientations of the paddles by a small angle. b) Shows the difference in angle between the paddles when the initial orientation of the disc and easy axis is altered by a small angle.

the paddles have small difference in position and orientation of easy axis. As could be expected this does alter the behaviour of the paddles more than the other parameters previously looked at.

In the earlier results κ was set to be 0.9 so the paddles act as hard magnets but the magnetic moment is not totally fixed to the easy axis. Figure A.7 shows the behaviour of the paddles if $\kappa = 1$. The peaks of the angle difference is slightly larger, which could be expected by this change but the general behaviour of the paddles was not altered.

In the experimental system the device was driven solely by a uni-axial oscillating magnetic field. In this theoretical model the field is mainly in the x-direction ($\beta = 1$) but it has a weak elliptical component ($\alpha = 0.01$). This is required to

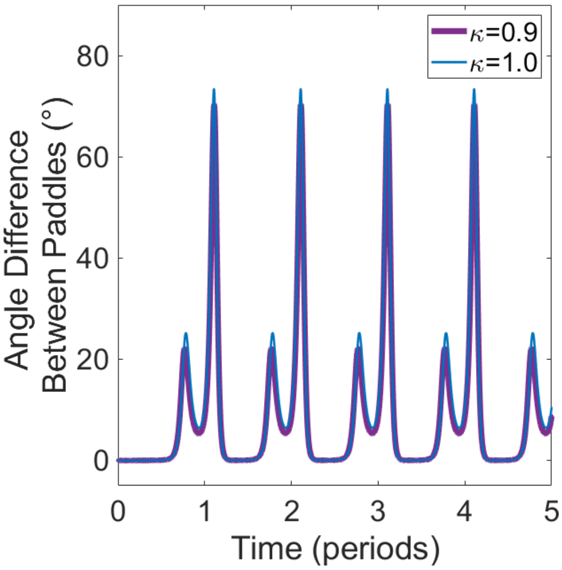

Figure A.7: Shows the difference in angle between the paddles when κ = 1.0 compared to κ=0.9 which was used in the other results.

initiate a torque on the paddles when their magnetic moment is in-line with the x directional magnetic field but in the opposite direction. It was investigated that rather than having an elliptical field, instead utilising a dampening y component of the magnetic field. As can be seen in Figure A.8 this was not suitable as after the second period the paddles returned to their initial position as the y component of the magnetic field was no longer large enough to produce sufficient torque to cause the paddles to rotate against the fluidic and elastic forces. Therefore, the magnetic field required a consistent oscillating y component.

The y component of the magnetic field was varied as shown in Figure A.9. The value of the y component made a considerable difference on the behaviour of the paddles as could be expected. When $\beta = 1$ and $\alpha = 0.1$, it formed more of a rotating field and for the paddles investigated this overcame the elastic forces and the paddles continually rotated in one direction for the periods looked at (five

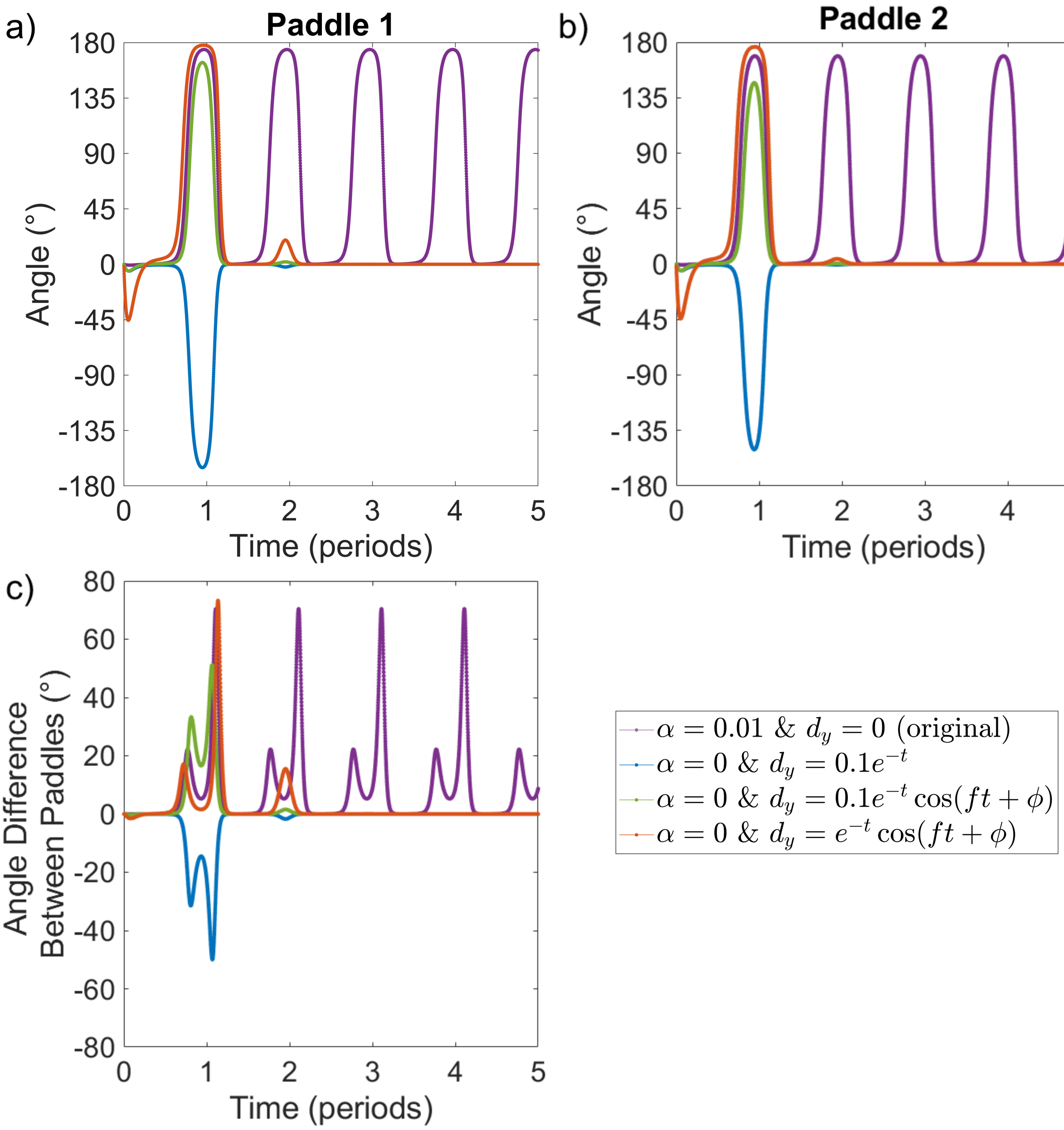

Figure A.8: a) Shows the angle of the first paddle and b) angle of the second paddle and c) the difference in angle when having a y directional magnetic field that dampens instead using $\alpha = 0.01$ which is the amplitude of the oscillating y field.

periods).

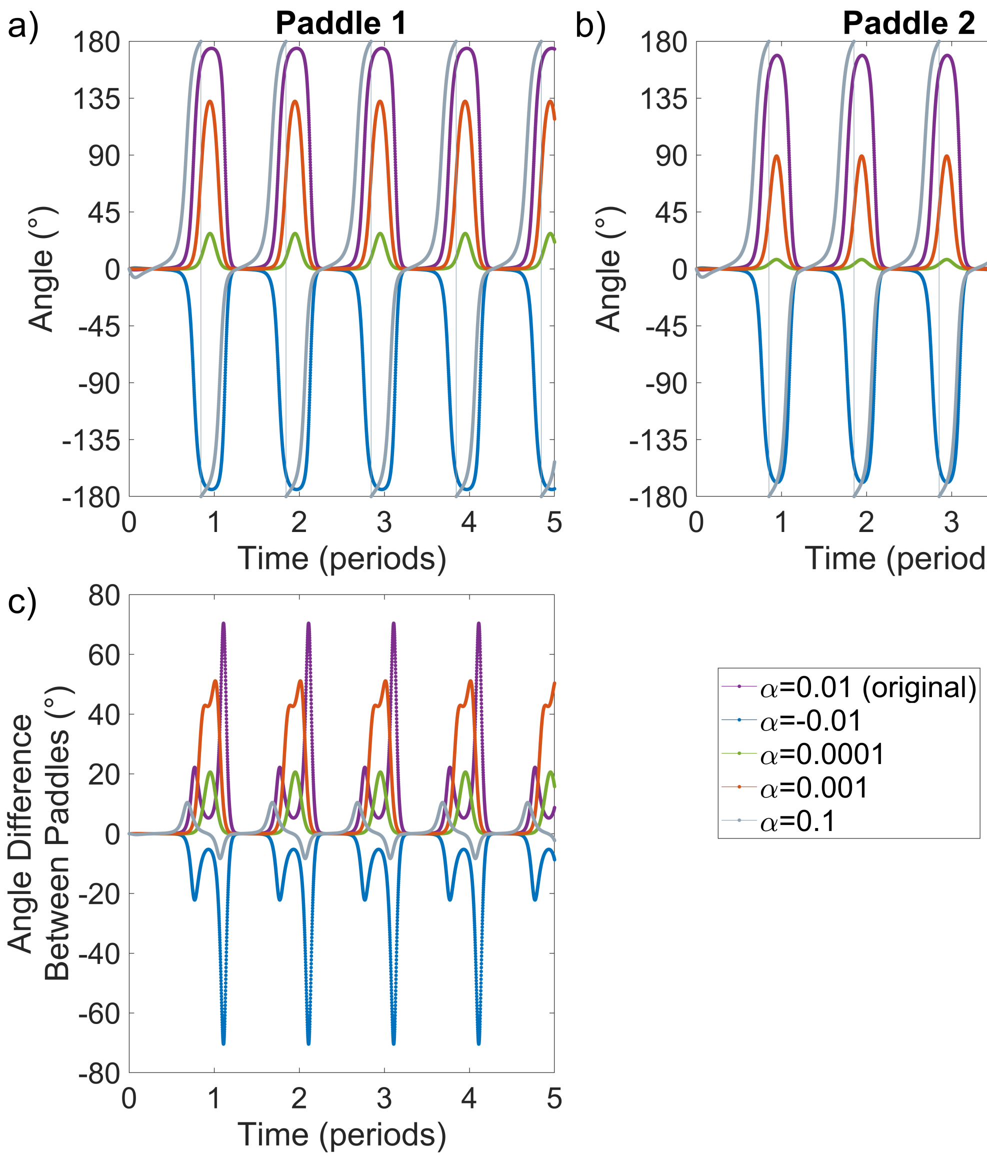

Figure A.9: a) Shows the angle of the first paddle when varying α. b) Shows the angle of the second paddle when varying α. c) Shows the difference in angle between the paddles when varying α.

Appendix B

Single-Ferromagnetic Elasto-Magnetic Pump

B.1 Pump Geometry

The swimmer's three elastic PDMS links were 150 µm in width and 300 µm thick. Links L2 and L3 were 1000 µm in length (from the centre of the bend to centre of the bend). The link L1 was shorter to cause the centre of the bend to the centre of the head to be 1000 µm. The diameter of the head that encases the 250 µm cubic NdFeB magnet was 500 µm and was also 300 µm in thick. The overall pumping chamber volume (including the swimmer) was $\sim$ 20 mm^3. Both the inlet and outlet of the chamber were square channels with a width of 1000 µm and a depth of 900 µm.

The channel was centred at the swimmer layer (300 µm) but the upper and lower layers acted to extend its height by 300 µm each side. The pumping module was 1.5 cm × 1.5 cm. The pumping module itself was connected to the reservoir module via PTFE tubing which had a length of 4 cm and internal diameter of 860 µm. This reservoir module was a large, open cup structure with internal side-length of 1.5 cm which was not fully enclosed and allows for fluid and tracer particles to be readily introduced, removed or replaced in this system.

As mentioned in Chapter 6, Jacob L. Binsley. designed the enclosed pump system encasing the swimmer that has been described above and further details can be found in [160].

B.2 Taking Raw Flow Data

As mentioned in Chapter 6, Jacob L. Binsley recorded the raw data provided by the pump described below and further details can be found in [160].

The device could be filled with an appropriate mixture of water and glycerol to obtain the desired viscosities used in Chapter 6 and 15 µm diameter polystyrene microbeads ((Sigma-Aldrich, 74964) were added to aid the observation of the flow. This was added via the reservoir module. The device was placed in the centre of the single axis Helmholtz coil in the ABIOMATER system, Appendix C. The pump was actuated by the Helmholtz coil providing a sinusoidal, oscillating magnetic field perpendicular to the orientation of the NdFeB magnet. During the experiments the driving field amplitude and frequency was varied between 3 mT to 6 mT and 1 Hz to 60 Hz respectively.

The channel could be videoed with the aid of the ABIOMATER system's microscope (with a 10x magnification optic) and high speed camera (1000 fps). This data was then analysed with the open source software 'Tracker' [2]. The pump motion was measured using the same method but with the use of a 2.5x magnification optic instead, to enable a larger field of view.

Appendix C

ABIOMATER System

The ABIOMATER system was produced Platform Kinetics, which was in collaboration with the University of Exeter. A photograph of part of the system is shown in Figure C.1. This system was built to actuate swimmer/devices via a magnetic field and to have imaging instrumentation and software. This key feature of this system was the a Helmholtz coil system and microscope. The system produced sinusoidal, oscillating magnetic fields with strengths up to 25 mT for frequencies of 1-300 Hz. The system had an observation area of 50 mm × 50 mm.

A PC interface was created to control the frequency, amplitude and phase of the magnetic fields. A microscope was built around the Helmholtz coil assembly with an extended optical path to reach into the centre of the coils. The upright microscope was configured with epi-illumination to support Olympus objectives (MPLFLN2.5x, 2.5x, MPLFLN10x 10x, and MPLFLN20x 20x magnification optics have been used). A high-speed camera (MotionBLITZ EoSens mini1 monochro-

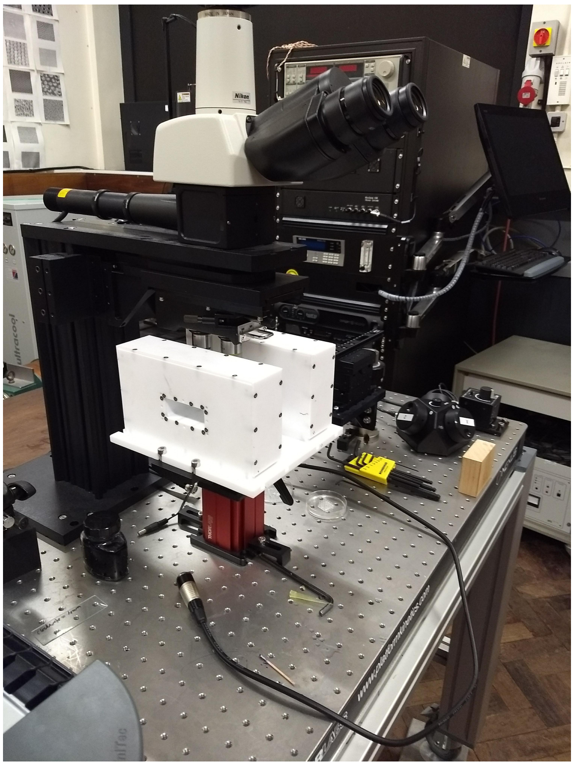

Figure C.1: A photograph of the ABIOMATER system produced by Platform Kinetics.

matic) was also attached to the microscope system which could achieve a frame rate up to 1000 fps.